Light Hadron Spectrum from Lattice QCD Simulations with 2+1 Flavours

Robert John Tweedie

Doctor of Philosophy

The University of Edinburgh
2006

Abstract

This thesis describes the calculation of masses and matrix elements using lattice QCD. Exploratory results are presented for the hadron mass spectrum and pseudoscalar meson decay constants using a mixed action formalism where the sea and valence actions are different. Improved staggered sea quarks are used and HYP-smeared overlap valence quarks. A method for matching the sea and valence quark masses is proposed. Good signals on 10 configurations at one lattice spacing and two different sets of sea quark masses are obtained.

Results are presented for light meson masses, nucleon masses and pseudoscalar meson decay constants in 2+1 flavour domain wall QCD with the DBW2 and Iwasaki gauge actions. This formalism preserves chiral symmetry at finite lattice spacing. The lattices used have linear sizes in the range 1.6 to 2.2fm and u and d quark masses as low as one quarter of the strange quark mass. All data were generated on the QCDOC machines at the University of Edinburgh and Brookhaven National Laboratory. Despite large residual masses and a limited number of sea quark mass values with which to perform chiral extrapolations, our results agree with experiment and scale within errors.

Acknowledgements

I would like to thank my supervisors, Richard Kenway and Ken Bowler, for their support during my PhD and Richard for careful reading and comments on this thesis. My thanks goes to Chris Maynard for all his help over the duration of my PhD and for providing the answers to more "stupid" questions than I care to admit to having asked. I would also like to recognise the roll of all the other members of the PPT group in Edinburgh in making my time here both entertaining and enjoyable and for providing useful discussions and distractions (particularly during midnight feasts). I would particularly like to thank those whose help and advice has been invaluable to me over the last three years and those who have worked and/or continue to work on the QCDOC project in Edinburgh.

I would like to thank all my friends in Edinburgh who have made my non-working hours fun and my brothers Neil, Blair and Ewen for keeping me amused.

Finally and most importantly I am deeply indebted to Gillian for all her love and support over the last three years and for keeping my sanity intact and my Mum and Dad for their love, patience, support and encouragement and I dedicate this thesis to them.

Contents

Chapter 1

Introduction

At present there is a very successful model of particle interactions called the Standard Model [1]. This theory incorporates quantum electrodynamics (QED), the Glashow-Weinberg-Salam theory of electroweak processes and quantum chromodynamics or QCD. The combined quantum field theories are described by a Lagrangian possessing an $SU(3)_c \otimes SU(2)_L \otimes SU(1)_Y$ gauge symmetry.

QCD is a theory of strong interactions between coloured particles: the quarks and gluons. Neither of these two types of particles have ever been observed on their own. The observed spectrum in nature is made up of hadrons. These are composite particles, mesons and baryons, composed of bound states of quarks and gluons. These bound states may be classified according to symmetries. Hadrons are built out of quarks, three quarks in a baryon and two quarks (one quark and one anti-quark) in a meson. This is because the hadrons are colour singlets and must transform trivially under $SU(3)_c$. Consequently a complete understanding of the strong interaction requires a theoretical explanation of the mass spectrum.

The strong interactions are governed by a non-abelian gauge group and hence possess the property of asymptotic freedom. At large energies the coupling constant of QCD is small and this lends itself to analysis by perturbative methods. These

have been used to successfully predict particle phenomena. At low energies the coupling constant of QCD is $\mathcal{O}(1)$ and much larger than that of the electromagnetic or weak theories. This causes problems when doing calculations in QCD as perturbative methods fail. Instead a non-perturbative approach, such as Lattice QCD, is required. Chapter 2 describes some of the theoretical challenges faced when attempting to perform QCD calculations on a space-time lattice of discrete points.

Wilson [2] first proposed lattice QCD in 1974 as a mechanism for studying the confinement of quarks. It provides a numerical way of testing low energy QCD by calculating the mass spectrum of the lightest hadrons and then comparing them with experimentally observed values. Lattice QCD calculations may also be used as a predictive tool for phenomenologically interesting quantities which are unmeasurable directly by experiment, for example proton decay. In semi-leptonic meson decays the scattering matrix may be factorised into a leptonic piece and a hadronic piece where the hadronic piece can be parameterised in terms of the momentum and a decay constant. This pseudoscalar decay matrix element may be compared to the experimentally obtained value providing another test of low energy QCD.

Over the last decade there has been a shift of emphasis from quenched calculations, where a rather drastic approximation was made due to computational constraints, to dynamical simulations where one, two or three of the light quarks in the theory have been included. Results from high statistics simulations [3] identified errors associated with the quenched approximation: predicted hadron masses in the continuum limit, particularly those containing strange quarks, differ from the corresponding experimental results by up to 10%. Moving to dynamical simulations reduces these discrepacies, however, the increased computational cost of including these quarks is large and increases with decreasing quark mass. Most recent simulations including dynamical quarks have included only two flavours

due to algorithmic reasons (for a review see [4]). Including the third dynamical quark, the strange quark, has only recently become feasible. Although the quarks are now included in the simulation we also require the correct chiral and flavour symmetries of the underlying theory to be reproduced. Including the correct chiral and flavour symmetries adds yet more computational cost.

In chapter 4 exploratory hadron spectrum calculations are performed where the valence action uses Ginsparg-Wilson fermions [5] which have the correct chiral and flavour symmetries but are computationally expensive. The quarks used in the configurations are generated with the improved staggered action which is computationally cheaper than the Ginsparg-Wilson type quarks. This has the advantage that the configurations may have very light dynamical quarks. The simplest states of the light hadron spectrum, mesons and baryons, and the pseudoscalar decay matrix element for both light and heavy-light states have been measured. However, using a different action for the valence and sea quarks means it is not straightforward to interpret the results. Some of the issues with mixed actions are discussed in more detail in chapter 4.

Recent algorithmic improvements and increased computational power has allowed simulations with 2+1 flavours of quark and a softly broken realisation of chiral symmetry. The symmetry breaking is controlled by a parameter which is independent of the lattice spacing. For domain wall quarks the breaking is controlled by the length of the fifth dimension. Where the breaking is small, its effects amount to an additive quark mass renormalisation by m_{res}. Chapter 5 presents initial results for hadron masses and pseudoscalar meson decay constants using 2+1 flavour domain wall QCD. This has been possible due to recent increased computational resources and theoretical improvements. The domain wall action is used to simulate both the sea and valence quarks and is a Ginsparg-Wilson type action preserving the correct chiral and flavour symmetries. The ensembles generated were primarily intended to explore the available parameter space for

a larger production run. As such the ensembles are relatively small, have been generated with several different β values, have different gauge actions and are relatively small in volume. However, even with these drawbacks it is still possible to calculate the light hadron spectrum and pseudoscalar decay constants obtaining results which are consistent with experiment and scale within large errors.

Chapter 2

Background theory

Lattice QCD is now more than thirty years old and is the subject of many books [6, 7, 8, 9] and lecture series [10, 11, 12, 13, 14]. This chapter outlines some of the basic concepts and pitfalls encountered when attempting to describe QCD using a lattice of space-time points.

2.1 Path Integral Approach

Lattice QCD calculations rely on the Feynman path integral approach [15, 16]. Path integrals may be used to calculate the expectation values of all the physical observables of a quantum field theory. The QCD expectation value of some observable $\mathcal{O}[\psi, \bar{\psi}, A_\mu]$ constructed from the time ordered product of the fields of the theory, ψ, $\bar{\psi}$ and A_μ in the Feynman path integral formalism is given by

$$\langle 0|\{\hat{\mathcal{T}}\hat{\mathcal{O}}[\psi, \bar{\psi}, A_\mu]\}|0\rangle = \frac{1}{\mathcal{Z}} \int \mathcal{D}\psi \mathcal{D}\bar{\psi} \mathcal{D}A_\mu \mathcal{O}[\psi, \bar{\psi}, A_\mu] e^{iS[\psi, \bar{\psi}, A_\mu]} \tag{2.1}$$

where $\mathcal{Z}$ is the partition function given by

$$\mathcal{Z} = \int \mathcal{D}\psi \mathcal{D}\bar{\psi} \mathcal{D}A_\mu e^{iS[\psi, \bar{\psi}, A_\mu]} \tag{2.2}$$

and S is the action of the theory related to the Lagrangian density, $\mathcal{L}(\psi, \bar{\psi}, A_\mu)$ by

$$S[\psi, \bar{\psi}, A_\mu] = \int d^4x \mathcal{L}(\psi, \bar{\psi}, A_\mu). \tag{2.3}$$

The integral (2.1) is over all field values $\psi(x), \bar{\psi}(x)$ and $A_\mu(x)$ for all values of x and hence is over an infinite number of degrees of freedom since space-time is continuous. It is therefore necessary to introduce a regulator and a simple but rigorous way of doing this is to introduce a lattice of points in space and time.

As the functional integral is complex and strongly oscillating, evaluation of the integral numerically is difficult. To circumnavigate this problem calculations are performed in Euclidean space rather than Minkowski space. This will be discussed in section 2.3. The remainder of this chapter is concerned with the particular form of the action for QCD. In particular the basic details of how QCD may be regularised using a lattice of space-time points will be discussed.

2.2 Continuum Quantum Chromodynamics

In the Standard Model it is the principle of gauge invariance that describes the fundamental interactions between particles. A gauge theory is a theory which is invariant under a set of local transformations, i.e. transformations that can vary in space and time. The strong interactions are invariant under colour SU(3) transformations. All observed hadrons are singlets of the SU(3) group. This gauge theory is called quantum chromodynamics, or QCD, as it is concerned with the colour quantum numbers of the quarks and the gluons.

Quarks $\psi^a(x)$ ($a = 1, 2, 3$ for the three different colours) are fermions in the fundamental representation of the colour SU(3) gauge group. Furthermore, the quarks carry flavour degrees of freedom which are independent of the colour. The flavours form generations, each of which having two components. At present six

flavours have been discovered giving three generations, (u,d), (c,s), and (t,b). The Dirac Lagrangian for non-interacting fermions is given by

$$\mathcal{L} = \sum_{f=u,\ldots,t} \bar{\psi}_f^i(x)(i\gamma^\mu \partial_\mu - m_f)\psi_f^i(x) \tag{2.4}$$

where the index $i, j = 1, 2, 3$ denotes the colour of the quark field, f is flavour, $\mu = 0, \ldots, 3$ is the Minkowski space-time index, ψ is a 4-component spinor and the conjugate field $\bar{\psi}$ is given by

$$\bar{\psi} = \psi^\dagger \gamma_0. \tag{2.5}$$

To extend this theory to include interactions, one demands that $\mathcal{L}$ is invariant under a local phase transformation of the fields

$$\psi(x) \rightarrow \psi'(x) \equiv S(x)\psi(x) \tag{2.6}$$

$$\bar{\psi}(x) \rightarrow \bar{\psi}'(x) \equiv \bar{\psi}(x)S^\dagger(x) \tag{2.7}$$

$$S(x) \equiv e^{i\alpha_a(x)\frac{\lambda^a}{2}} \tag{2.8}$$

where $\alpha_a(x)$, $a = 1, \ldots, 8$, are a set of arbitrary SU(3) group parameters, λ^a, $a = 1, \ldots, 8$ are the Gell-Mann matrices, the generators of the fundamental representation of SU(3) and the colour indices on the quark fields have been suppressed for clarity. The Gell-Mann matrices are a set of linearly independent 3×3 matrices satisfying the commutation relation

$$\left[\frac{\lambda^a}{2}, \frac{\lambda^b}{2}\right] = i f_{abc} \frac{\lambda^c}{2}, \tag{2.9}$$

where f_{abc} are the structure constants of SU(3), and are normalised according to

$$Tr\lambda^a\lambda^b = 2\delta^{ab}. \tag{2.10}$$

The parameter $\alpha_a(x)$ depends on x, hence this transformation is local - depends on space and time. The mass term in the Lagrangian density (2.4) is trivially invariant under the local gauge transformation (2.6), however, applying this transformation to the gradient piece of the Lagrangian density (2.4) we observe

$$\partial_\mu \psi(x) \rightarrow \partial_\mu(S(x)\psi(x)) = S(x)\left[\partial_\mu \psi(x) + S^{-1}(x)(\partial_\mu S(x))\psi(x)\right] \tag{2.11}$$

i.e. that $\partial_\mu \psi(x)$ transforms non-covariantly.

In order for the Lagrangian density to remain invariant under the gauge symmetry we require that the derivative transform covariantly, i.e.

$$D_\mu \psi(x) \rightarrow D'_\mu \psi'(x) = S(x)(D_\mu \psi(x)). \tag{2.12}$$

To satisfy this requirement a covariant derivative defined by

$$D_\mu \psi(x) = (\partial_\mu + igA_\mu(x))\psi(x) \tag{2.13}$$

is introduced together with eight vector Yang-Mills gauge fields, $A_\mu(x)$ defined by

$$A_\mu(x) = A^a_\mu(x)\tau_a \tag{2.14}$$

where for SU(3) $\tau_a = \frac{\lambda_a}{2}$. g is the gauge coupling. These vector gauge fields are hermitian $A^\dagger_\mu(x) = A_\mu(x)$. The gauge fields are required to transform under the gauge symmetry as

$$\begin{aligned} A_\mu(x) &\rightarrow S(x)A_\mu(x)S^{-1}(x) + \frac{i}{g}\left(\partial_\mu S(x)\right)S^{-1}(x) \\ &= S(x)\left[A_\mu + \frac{i}{g}S^{-1}(x)\left(\partial_\mu S(x)\right)\right]S^{-1}(x). \end{aligned} \tag{2.15}$$

Using the above transformation we note

$$\begin{aligned} D_\mu \psi(x) &\rightarrow D'_\mu \psi'(x) \\ &= (\partial_\mu + igA'_\mu(x))\psi'(x) \\ &= (\partial_\mu + ig\left(S(x)\left[A_\mu + \frac{i}{g}S^{-1}(x)\left(\partial_\mu S(x)\right)\right]S^{-1}(x)\right)S(x)\psi(x) \\ &= S(x)(\partial_\mu + igA_\mu(x))\psi(x) \\ &= S(x)D_\mu \psi(x) \end{aligned} \tag{2.16}$$

as required for covariance, i.e. we have that $D_\mu \psi(x) \rightarrow D'_\mu \psi'(x) = S(x)(D_\mu \psi(x))$. We have arrived at a Lagrangian density

$$\mathcal{L} = \sum_{f=u,\ldots,t} \bar{\psi}^i_f(x)(i\gamma^\mu D^{ij}_\mu - m_f \delta^{ij})\psi^j_f(x) \tag{2.17}$$

which is invariant under the full gauge transformation

$$\psi(x) \rightarrow \psi'(x) \equiv S(x)\psi(x) \tag{2.18}$$

$$\bar{\psi}(x) \rightarrow \bar{\psi}'(x) \equiv \bar{\psi}(x)S^{\dagger}(x) \tag{2.19}$$

$$S(x) \equiv e^{i\alpha_a(x)\frac{\lambda^a}{2}} \tag{2.20}$$

$$A_\mu(x) \rightarrow S(x)\left[A_\mu + \frac{i}{g}S^{-1}(x)\left(\partial_\mu S(x)\right)\right]S^{-1}(x). \tag{2.21}$$

A kinetic piece for the Lagrangian density is required in order to have propagating gauge fields. To construct a kinetic term for the vector field $A_\mu(x)$, we need to construct a field strength tensor $F_{\mu\nu}(x)$, which we define in the usual way as the commutator of the covariant derivative

$$F_{\mu\nu}\psi(x) \equiv -\frac{i}{g}\left[D_\mu, D_\nu\right]\psi(x). \tag{2.22}$$

To maintain the gauge invariance of the Lagrangian density we require the gauge field strength tensor to transform according to the adjoint representation under local gauge transformations

$$F'_{\mu\nu} = S(x)F_{\mu\nu}S^{-1}(x). \tag{2.23}$$

The vector gauge transformation given in equation (2.15) can be shown to be sufficient [17, 18] to satisfy equation (2.23). The gauge invariant kinetic term for the gauge fields (also known as the Yang-Mills piece) is thus

$$\mathcal{L}_{YM} = -\frac{1}{4}F^a_{\mu\nu}F^{\mu\nu}_a. \tag{2.24}$$

We have arrived at our final expression for the Lagrangian density describing the strong interaction

$$\mathcal{L} = -\frac{1}{4}F^a_{\mu\nu}F^{\mu\nu}_a + \sum_{f=u,\ldots,t}\bar{\psi}^i_f(x)(i\gamma^\mu D^{ij}_\mu - m_f\delta^{ij})\psi^j_f(x). \tag{2.25}$$

The Lagrangian density is invariant under local SU(3) gauge transformations and describes three equal mass Dirac fields (the 3 colours of a given quark flavour) in interaction with eight massless vector fields (the gluons). The gluons are

required to be massless as a term proportional to $A^a_\mu A^\mu_a$ breaks gauge invariance. The Yang-Mills term in the Lagrangian density, in sharp contrast to the abelian case, contains interaction terms

$$-g f_{abc}(\partial_\mu A^a_\nu) A^b_\mu A^c_\nu + \frac{1}{4} g^2 f_{abc} f_{ade} A^b_\mu A^c_\nu A^d_\mu A^e_\nu. \tag{2.26}$$

The interactions are necessary to ensure gauge invariance: non-abelian gauge fields are therefore necessarily self-interacting.

2.3 Continuation from Minkowski to Euclidean space

The complex exponents in equations (2.1) and (2.2) and resulting oscillatory behaviour make numerical evaluation of the integrals impossible. Wick rotating the action to a Euclidean time metric

$$\eta_{\mu\nu} = \begin{pmatrix} 1 & 0 & 0 & 0 \\ 0 & 1 & 0 & 0 \\ 0 & 0 & 1 & 0 \\ 0 & 0 & 0 & 1 \end{pmatrix} \tag{2.27}$$

from the Minkowski metric is one solution to this problem. The following set of transformations relate the coordinates, fields and Dirac gamma matrices in the Minkowski metric, M, to those in the Euclidean metric, E

$$x^M_0 \to -i x^E_4 \qquad A^M_0 \to -i A^E_4 \tag{2.28}$$

$$\gamma^M_0 \to \gamma^E_4 \qquad d^4x^M \to -i d^4x^E \tag{2.29}$$

$$\gamma^M_i \to -i\gamma^E_i \qquad \not{D}_M \to i \not{D}_E \tag{2.30}$$

$$\partial^M_0 \to i\partial^E_4 \tag{2.31}$$

and

$$\bar{\psi}^M_f(x)(i\not{D} - m)\psi^M_f(x) \to -\bar{\psi}^E_f(x)(\not{D}^E + m)\psi^E_f(x). \tag{2.32}$$

Applying these transformations to the Lagrangian density in equation (2.25) gives the following change in the action

$$\begin{aligned} S_{QCD} &\rightarrow i\int d^4x^E\{\frac{1}{4}\mathrm{Tr}F^E_{\mu\nu}F^E_{\mu\nu} + \sum_f \bar{\psi}^E_f(\not{D}^E + m_f)\psi^E_f\} \\ &= iS^E_{QCD} \end{aligned} \tag{2.33}$$

and therefore the partition function given by equation (2.1) in Euclidean space is

$$\mathcal{Z}^E_{QCD} = \int \mathcal{D}\psi\mathcal{D}\bar{\psi}\mathcal{D}A_\mu e^{-S^E_{QCD}}. \tag{2.34}$$

The partition function is now weighted by the factor $e^{-S^E_{QCD}}$, and is similar to those found in statistical mechanics (with appropriate Boltzmann factor). Provided S^E_{QCD} is a real valued function of the field variables and is bounded from below the functional integral is numerically tractable. The Green functions defined in chapter 3 are replaced by the corresponding correlation functions. For the Euclidean theory to properly describe the Minkowski theory, reflection positivity must be satisfied. A description of reflection positivity may be found in [8]. In the rest of this thesis the index E will be dropped as we will be working in Euclidean space unless stated otherwise.

2.4 Dirac fermions on the lattice

The path integral has not been given a precise mathematical meaning. To do this we introduce an isotropic hypercubic space-time lattice, $\mathcal{V}$, with lattice spacing a, and the continuum space-time index x_μ is replaced by a discrete hypercubic index n_μ.

$$\mathcal{V} = \{x \in \mathbb{R}^4 | n_\mu = \frac{x_\mu}{a} \in \mathbb{Z}, \mu = 1,2,3,4\} \tag{2.35}$$

where $n_\mu = 1 \ldots (L-1)$ for $\mu = 1,2,3$ and $n_\mu = 1 \ldots (T-1)$ for $\mu = 4$ where L and T are the linear spatial and time extent of the lattice respectively. In doing this we note that the fermion fields $\psi(x)$ are now defined only on the lattice

sites. For numerical simulation we scale our parameters by the lattice spacing according to their canonical dimensions. Derivatives become finite differences and the integration over Euclidean space-time in the action is replaced by the sum over all sites on the lattice. This procedure may be summarised as

$$x_\mu \rightarrow an_\mu \tag{2.36}$$

$$\psi_\alpha(x) \rightarrow \frac{1}{a^{\frac{3}{2}}}\hat{\psi}_\alpha(n) \tag{2.37}$$

$$\bar{\psi}_\alpha(x) \rightarrow \frac{1}{a^{\frac{3}{2}}}\hat{\bar{\psi}}_\alpha(n) \tag{2.38}$$

$$\partial_\mu\psi(x) \rightarrow \frac{1}{a^{\frac{5}{2}}}\hat{\partial}_\mu\hat{\psi}(n) \tag{2.39}$$

$$m \rightarrow \frac{1}{a}\hat{m} \tag{2.40}$$

$$\int d^4x \rightarrow a^4\sum_n \tag{2.41}$$

and $\hat{\partial}_\mu$ is the antihermitian lattice derivative defined by

$$\hat{\partial}_\mu\hat{\psi}_\alpha(n) = \frac{1}{2}\left[\hat{\psi}_\alpha(n+\hat{\mu}) - \hat{\psi}_\alpha(n-\hat{\mu})\right] \tag{2.42}$$

where $\hat{\mu}$ is a unit vector in the μ direction. i.e. $\hat{\mu} = (\hat{x}, \hat{y}, \hat{z}, \hat{t})$. In the following the hats on the lattice quantities will be dropped.

Applying this transformation to the Euclidean free fermion action

$$S_F = \int d^4x\bar{\psi}(x)(\gamma_\mu\partial_\mu + m)\psi(x) \tag{2.43}$$

leads to

$$S_F = \sum_{n,\mu}\frac{1}{2}\bar{\psi}(n)\gamma_\mu\left[\psi(n+\hat{\mu}) - \psi(n-\hat{\mu})\right] + \sum_n m\bar{\psi}(n)\psi(n) \tag{2.44}$$

where the spinor indices have been suppressed. This discretisation of the action has led to bilinear terms in the fermionic fields at different points in space-time, $\bar{\psi}(n)\psi(n+\hat{\mu})$ for example. As in the continuous case we would like the action to be invariant under a local gauge transformation

$$\psi(n) \rightarrow S(n)\psi(n) \tag{2.45}$$

$$\bar{\psi}(n) \rightarrow \bar{\psi}(n)S^\dagger(n). \tag{2.46}$$

The mass term is trivially invariant under such a transformation

$$\bar{\psi}(n)\psi(n) \rightarrow \bar{\psi}(n)S^{\dagger}(n)S(n)\psi(n) \rightarrow \bar{\psi}(n)\psi(n), \tag{2.47}$$

however, the bilinear term with fermionic fields at different points in space time is not gauge invariant under the same local gauge transformation

$$\bar{\psi}(n)\psi(n+\hat{\mu}) \rightarrow \bar{\psi}(n)S^{\dagger}(n)S(n+\hat{\mu})\psi(n+\hat{\mu}). \tag{2.48}$$

The essential problem is that we are trying to compare two fields at two different points when the colour 'co-ordinate axes' are changing as we move about. To resolve this we need to parallel transport one field to the same point as the other before they can be properly compared. To this end we introduce the quantity

$$\mathcal{O}(x,y) = \bar{\psi}(x)e^{ig\int_x^y A_\mu(z)dz_\mu}\psi(y) \tag{2.49}$$

where the line integral is carried out along a path C connecting x and y. As in the continuum case it will be shown that a new vector field, $A_\mu(x)$, is required in order to maintain gauge invariance. Under the gauge transformation $\mathcal{O}(x,y)$ can be shown to transform [7, 19] as

$$\mathcal{O}(x,y) = \bar{\psi}(x)S^{\dagger}(x)S(x)e^{ig\int_x^y A_\mu(z)dz_\mu}S^{\dagger}(y)S(y)\psi(y). \tag{2.50}$$

The quantity $\mathcal{O}(x,y)$ is gauge invariant. In the discrete case we replace $\mathcal{O}(x,y)$ by

$$\mathcal{O}(n,m) = \bar{\psi}(n)U(n,m)\psi(m) \tag{2.51}$$

where $U(n,m)$ is

$$U(n,m) = e^{ig\int_n^m A_\mu(z_n)dz_{n_\mu}} \tag{2.52}$$

and we can write in the limit of small a

$$U(n,n+\hat{\mu}) \equiv U_\mu(n) = e^{iagA_\mu(n)} \approx 1 + iagA_\mu(n) \tag{2.53}$$

where $A_\mu(n)$ is the gauge potential on site n. Hence in the discretised version we have that

$$\bar{\psi}(n)U_\mu(n)\psi(n+\hat{\mu}) \tag{2.54}$$

is gauge invariant. Note that $U(n, n+\hat{\mu}) = U^{\dagger}(n+\hat{\mu}, n)$ i.e. that $U(n, n+\hat{\mu})$ is a directed quantity which may be represented graphically as in figure 2.4. Under a local gauge transformation $U_{\mu}(n)$ transforms as

$$U_{\mu}(n) \rightarrow S(n)U_{\mu}(n)S^{\dagger}(n+\hat{\mu}). \tag{2.55}$$

In contrast to the quark fields, $\psi(x)$, discussed earlier, the group elements, $U(n, n+\hat{\mu})$, live on the links connecting two neighbouring sites, hence, they are sometimes referred to as link variables. The above considerations suggest that to arrive at a gauge-invariant expression for the fermionic action on the lattice we should make the following substitution to the derivative piece of the action

$$\partial_{\mu}\psi(n) \rightarrow D_{\mu}\psi(n) \equiv \frac{1}{2}\left[U_{\mu}(n)\psi(n+\hat{\mu}) - U_{\mu}^{\dagger}(n-\hat{\mu})\psi(n-\hat{\mu})\right] \tag{2.56}$$

Putting this all together gives us a discretised gauge invariant version of the fermion action

$$\begin{aligned} S_F &= \sum_{n,\mu} \frac{1}{2}\bar{\psi}(n)\gamma_{\mu}\left[U_{\mu}(n)\psi(n+\hat{\mu}) - U_{\mu}^{\dagger}(n-\hat{\mu})\psi(n-\hat{\mu})\right] \\ &+ \sum_{n} m\bar{\psi}(n)\psi(n). \end{aligned} \tag{2.57}$$

It is important to realise that the form of the lattice action is not unique. We have merely chosen the simplest one. The following section discusses the implications of this choice of fermion action.

2.5 Fermion Doubling

The only requirement that any lattice action should fulfil is that it reproduces the correct classical expression in the naive continuum limit (scaling the variables with a appropriately and taking $a \rightarrow 0$). However, it is also very desirable that it possesses as many continuum symmetries as possible.

The lattice version of the fermion action given in equation (2.44) may be written in a more compact notation as

$$S_F = \sum_{n,l,\alpha,\beta} \bar{\psi}_\alpha(n) M_{\alpha\beta}(n,l) \psi_\beta(l) \tag{2.58}$$

where

$$M_{\alpha\beta}(n,l) = \sum_\mu \frac{1}{2}(\gamma_\mu)_{\alpha,\beta} \left[\delta_{l,n+\hat{\mu}} - \delta_{l,n-\hat{\mu}}\right] + m\delta_{ln}\delta_{\alpha\beta} \tag{2.59}$$

is the fermionic matrix. The free field propagator, $S^{-1}_{\alpha\beta}(p)$, can be calculated in momentum space from the inverse of the fermion matrix by Fourier transformation

$$M_{\alpha\beta}(n,l) = \int_{-\pi}^{\pi} \frac{d^4p}{(2\pi)^4} S^{-1}_{\alpha\beta}(p) e^{ip.(n-l)} \tag{2.60}$$

with

$$S^{-1}(p) = \sum_\mu i\gamma_\mu \text{sin}p_\mu + m. \tag{2.61}$$

From $S^{-1}(p)S(p) = 1$ we have that

$$S(p) = \frac{m - i\gamma_\mu s_\mu}{m^2 + s^2}, \quad s_\mu = \text{sin}p_\mu. \tag{2.62}$$

Rewriting in physical units the propagator becomes

$$S(p) = \frac{\frac{1}{a}\{am - i\sum_\mu \gamma_\mu \text{sin}(ap_\mu)\}}{\frac{1}{a^2}\{(am)^2 + \sum_\mu \text{sin}^2(ap_\mu)\}} \tag{2.63}$$

which gives the continuum result

$$S(p) = \frac{m - i\gamma_\mu p_\mu}{m^2 + p^2} + \mathcal{O}(a^2) \tag{2.64}$$

in the limit $a \to 0$. The continuum propagator has a pole at $p_4 = i\omega = i\sqrt{\vec{p}^2 + m^2}$ corresponding to a Dirac particle. The pole is near the zeros of the sine function at the origin $ap_\mu = 0$. However, there are fifteen other regions, at the edges of the Brillouin zone, where $\text{sin}(ap_\mu)$ takes a finite value in the limit $a \to 0$. In d space-time dimensions this corresponds to 2^d species of fermion. This is the phenomenon of fermion doubling. To obtain the correct continuum limit these extra fermion species require to be eliminated.

Several possible methods for eliminating these extra fermion species have been proposed. The next few sections will discuss some of these proposals.

2.6 Wilson Fermion Action

One possible solution to the fermion doubling problem was proposed by Wilson [2]. His suggestion was to ameliorate the effects of species doubling at the expense of breaking chiral symmetry explicitly on the lattice. His method involved adding a term to the fermion action which raises the masses of the unwanted doublers to values of order the cutoff - hence decoupling them from the continuum physics. The additional term vanishes in the naive continuum limit, however, it breaks chiral symmetry (see section 2.8). For free fermions the mass term in equation (2.44) is replaced by

$$\begin{aligned} m\sum_n \bar{\psi}(n)\psi(n) &\rightarrow m\sum_n \bar{\psi}(n)\psi(n) + \frac{r}{2}\sum_{n,\mu}\bar{\psi}(n)\partial^2\psi(n) \\ &= m\sum_n \bar{\psi}(n)\psi(n) \\ &+ \frac{r}{2}\sum_{n,\mu}\bar{\psi}(n)\left[\psi(n+\hat{\mu}) + \psi(n-\hat{\mu}) - 2\psi(n)\right] \\ &= (m+4r)\sum_n \bar{\psi}(n)\psi(n) \\ &- \frac{r}{2}\sum_{n,\mu}\left[\bar{\psi}(n)\psi(n+\hat{\mu}) + \bar{\psi}(n)\psi(n-\hat{\mu})\right] \end{aligned} \tag{2.65}$$

where the lattice laplacian ∂^2 is defined by $\partial^2\psi(n) = \psi(n+\hat{\mu}) + \psi(n-\hat{\mu}) - 2\psi(n)$. This has the effect of replacing the mass, m, in the inverse propagator in momentum space by

$$m + \frac{r}{a}\sum_\mu (1 - \cos(ap_\mu)) \equiv \mathcal{M}(p) \tag{2.66}$$

in lattice units. The propagator is then given by

$$S(p) = \frac{\frac{1}{a}\{a\mathcal{M}(p) - i\sum_\mu \gamma_\mu \sin(ap_\mu)\}}{\frac{1}{a^2}\{(a\mathcal{M}(p))^2 + \sum_\mu \sin^2(ap_\mu)\}}. \tag{2.67}$$

For any fixed value of p_μ we have that $\mathcal{M}(p)$ approaches m for $a \to 0$. Near the corners of the Brillouin zone $\mathcal{M}(p)$ diverges as the lattice spacing tends to zero. The doubling problem has been eliminated at the expense of the chiral symmetry for $m = 0$ which is now broken. The chiral symmetry is recovered in the continuum limit but the chiral and continuum limits cannot be decoupled. In fact Nielson and Ninomiya [20] showed in their *no go theorem* that it is impossible to define a local hermitian lattice theory which has no doublers and is chirally symmetric.

Redefining parameters, the Wilson action is often expressed in terms of the hopping parameter

$$\kappa = \frac{1}{2m + 8r} \tag{2.68}$$

as

$$\begin{aligned} S_F^W &= \sum_n \{\bar{\psi}(n)\psi(n) \\ &+ \kappa \sum_\mu \bar{\psi}(n)\left[(\gamma_\mu - r)\psi(n+\hat{\mu}) - (\gamma_\mu + r)\psi(n-\hat{\mu})\right]\}. \end{aligned} \tag{2.69}$$

The Wilson action has discretisation errors of $\mathcal{O}(a)$ which may be suppressed by the addition of a clover term $\sim \bar{\psi}\sigma_{\mu\nu}F^{\mu\nu}\psi$ [21] which also breaks chiral symmetry.

2.7 The Staggered Fermion Action

J. Kogut and L. Susskind [22, 23, 7] proposed the staggered fermion action as another way of dealing with the lattice doubling problem. They interpreted the additional fermion doublers as different "flavours" and proposed to eliminate them by exploiting the fact that spin-diagonalisation can be used to reduce the degrees of freedom from 16 down to 4. Staggered fermions $\chi(n)$ are related to the fields $\psi(n)$ via

$$\psi(n) = T_n\chi(n), \quad \bar{\psi}(n) = \bar{\chi}(n)T_n^\dagger \tag{2.70}$$

where

$$T_n = \gamma_1^{n_1}\gamma_2^{n_2}\gamma_3^{n_3}\gamma_4^{n_4} \tag{2.71}$$

is a 4×4 unitary matrix diagonalising all the γ-matrices in the naive form of the fermion action

$$T^\dagger(n)\gamma_\mu T(n+\mu) = \eta_\mu(n)\mathbb{I}. \tag{2.72}$$

$\eta_\mu(n)$ are complex numbers and $\mathbb{I}$ is the unit matrix. The phase factors $\eta_\mu(n)$ satisfy

$$\eta_\mu(n) = (-1)^{n_1+\ldots+n_{\mu-1}}, \quad \eta_1(n) = 1 \tag{2.73}$$

which do not have a spinor index. As the different spin components of χ decouple its spin index may be dropped leaving only a colour index. In the new fields formulation the staggered fermion action acquires the form

$$\begin{aligned} S_F^{st} &= \sum_{n,\mu} \bar{\chi}(n) \left\{ \frac{1}{2}\eta_\mu(n) \left[U_\mu(n)\chi(n+\mu) - U_\mu^\dagger(n-\mu)\chi(n-\mu) \right] \right\} \\ &+ m \sum_n \bar{\chi}(n)\chi(n). \end{aligned} \tag{2.74}$$

This action is diagonal in the Dirac indices and the different spin components are decoupled. The 16-fold degeneracy is thus reduced to 4-fold. The resulting fermion action describes 4 flavours of Dirac fermions. In order to simulate a single quark the quark determinant in the path integral (2.148) is replaced by a fourth root. The staggered action (2.74) allows large flavour changing strong interactions at $\mathcal{O}(a^2)$ which are not present in QCD. In order to deal with these effects the gauge piece of the action (see section 2.12) is modified by the addition of three, five and/or seven link staple terms. These modifications lead to the so-called family of improved staggered actions.

2.8 Chiral symmetry on the lattice

If we consider the continuum massless Euclidean action

$$S_E = \int d^4x \bar{\psi} \not{D} \psi \tag{2.75}$$

then this action remains invariant under the field transformation

$$\psi \to e^{\alpha\gamma_5}\psi, \quad \bar{\psi} \to \bar{\psi}e^{\alpha\gamma_5}. \tag{2.76}$$

This condition may also be written

$$\{\gamma_5, \not{D}\} = 0. \tag{2.77}$$

This is what is meant by chiral symmetry.

Chiral symmetry can be recovered on the lattice without doublers if we only insist that the symmetry holds on shell. In this case the field transformation becomes

$$\psi \to e^{\alpha\gamma_5\left(1-\frac{a}{2}\not{D}\right)}\psi, \quad \bar{\psi} \to \bar{\psi}e^{\alpha\gamma_5\left(1-\frac{a}{2}\not{D}\right)} \tag{2.78}$$

and hence the Dirac operator must be invariant under

$$\not{D} \to e^{\alpha\gamma_5\left(1-\frac{a}{2}\not{D}\right)} \not{D} e^{\alpha\gamma_5\left(1-\frac{a}{2}\not{D}\right)} = \not{D} \tag{2.79}$$

For an infinitesimal transformation ($\alpha << 1$) this gives us the Ginsparg-Wilson (GW) relation [5]

$$\gamma_5\not{D} + \not{D}\gamma_5 = \{\gamma_5, \not{D}\} = a\not{D}\gamma_5\not{D}. \tag{2.80}$$

This relation replaces equation (2.77) with a weaker condition which clearly restores the chiral symmetry in the continuum limit $a \to 0$. Having dropped the condition that γ_5 anticommutes with $\not{D}$ the conflict with the Nielson-Ninomiya theorem is avoided.

Now that we understand how to remove the doublers while at the same time preserve the chiral symmetry on shell, it remains to find an operator, $\not{D}$, that satisfies the GW relation.

2.9 Chirally symmetric operators

A possible operator that satisfies the Ginsparg-Wilson relation was proposed by Neuberger [24]. The construction of the operator begins by writing $\not{D}$ as

$$a\not{D} = 1 + \gamma_5 V \tag{2.81}$$

which we are able to do without loss of generality. This can be thought of as defining V. The form of V is constrained to be Hermitian by the γ_5 hermiticity of $\not{D}$ and to be unitary by multiplying the Ginsparg-Wilson relation on the left by γ_5

$$\not{D} + \not{D}^\dagger = a\not{D}^\dagger\not{D} \tag{2.82}$$

so that

$$\frac{1}{a}(1+\gamma_5 V) + \frac{1}{a}(1+V^\dagger\gamma_5) = \frac{a}{a^2}(1+V^\dagger\gamma_5)(1+\gamma_5 V) \tag{2.83}$$

$$2 + \gamma_5 V + V\gamma_5 = 1 + \gamma_5 V + V\gamma_5 + V^2 \tag{2.84}$$

$$\Rightarrow V^2 = 1. \tag{2.85}$$

In order to satisfy the Ginsparg-Wilson relation V must be both Hermitian and unitary. The product $\gamma_5 V$ is also unitary but is neither Hermitian or anti-Hermitian. This means that the eigenvalues of $\gamma_5 V$ are given by $\lambda = e^{i\alpha}$ and therefore the eigenvalues of $aD = 1 + \gamma_5 V$ are given by $\lambda_{aD} = 1 + e^{i\alpha}$ and lie on the unit circle centered on (1,0) in the complex plane (see figure 2.1).

Neuberger proposed that V should take the form

$$V = \frac{\gamma_5(aD_W - 1)}{\sqrt{(aD_W - 1)^\dagger(aD_W - 1)}} \tag{2.86}$$

where D_W is any valid lattice Dirac operator and often taken to be the Wilson Dirac operator. V can be shown to satisfy both unitarity and hermiticity for any D_W which is γ_5 Hermitian.

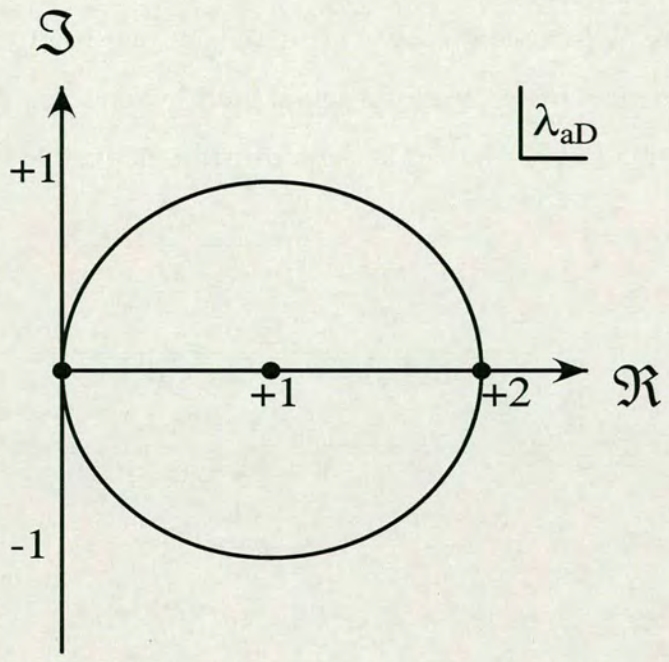

Figure 2.1: The eigenvalues of $aD = 1 + \gamma_5 V$ in the real-imaginary plane.

Substituting this into equation (2.81) gives

$$a\not{D} = 1 + \frac{(aD_W - 1)}{\sqrt{(aD_W - 1)^\dagger (aD_W - 1)}} \tag{2.87}$$

$$= 1 + \gamma_5 \frac{\gamma_5 (aD_W - 1)}{\sqrt{[\gamma_5 (aD_W - 1)]^\dagger \gamma_5 (aD_W - 1)}} \tag{2.88}$$

$$= 1 + \gamma_5 \frac{\gamma_5 (aD_W - 1)}{\sqrt{[\gamma_5 (aD_W - 1)]^2}} \tag{2.89}$$

where the fact that $H = [\gamma_5 (aD_W - 1)]$ is Hermitian has been used in the last step. This expression may be written as

$$a\not{D} = 1 + \gamma_5 sgn(H) \tag{2.90}$$

where

$$sgn(x) = \frac{x}{\sqrt{x^2}} \tag{2.91}$$

is the matrix *sgn* function. For a matrix this is defined as diagonalising the matrix and then taking the sign of the eigenvalues. Neuberger's operator satisfies the

Ginsparg-Wilson relation by construction. It may be observed that the Neuberger operator gives the correct continuum limit by replacing D_W with $\not{\partial} + a\partial^2 + \mathcal{O}(a^2)$ in equation (2.89) where $\not{\partial}$ is the continuum derivative $\gamma_\mu \partial_\mu$. This gives

$$\begin{aligned} a\not{D} &= 1 + \gamma_5 \frac{\gamma_5(a\not{\partial} + a^2\partial^2 + \mathcal{O}(a^3) - 1)}{\sqrt{\left[\gamma_5(a\not{\partial} + a^2\partial^2 + \mathcal{O}(a^3) - 1)\right]^2}} \\ &= 1 + \frac{(a\not{\partial} + a^2\partial^2 - 1) + \mathcal{O}(a^3)}{\sqrt{\gamma_5(a\not{\partial} + a^2\partial^2 - 1 + \mathcal{O}(a^3))\gamma_5(a\not{\partial} + a^2\partial^2 - 1 + \mathcal{O}(a^3))}} \\ &= 1 + \frac{(a\not{\partial} + a^2\partial^2 - 1) + \mathcal{O}(a^3)}{\sqrt{(-a\not{\partial} + a^2\partial^2 - 1 + \mathcal{O}(a^3))(a\not{\partial} + a^2\partial^2 - 1 + \mathcal{O}(a^3))}} \\ &= 1 + \frac{(a\not{\partial} + a^2\partial^2 - 1) + \mathcal{O}(a^3)}{\sqrt{1 - 2a^2\partial^2 + \mathcal{O}(a^3)}} \\ &= 1 + (a\not{\partial} + a^2\partial^2 - 1 + \mathcal{O}(a^3))(1 - 2a^2\partial^2 + \mathcal{O}(a^3))^{-\frac{1}{2}} \\ &= 1 + (a\not{\partial} + a^2\partial^2 - 1 + \mathcal{O}(a^3))(1 + a^2\partial^2 + \mathcal{O}(a^3)) \\ &= a\not{\partial} + \mathcal{O}(a^3). \end{aligned} \tag{2.92}$$

Provided D_W gives the correct continuum limit $\not{D}$ will also give the correct continuum limit. Note that the leading order correction to the Neuberger operator is $\mathcal{O}(a^2)$. Since the overlap fermion is invariant under the lattice chiral transformation it does not mix with dimension five operators which are not chirally invariant. Therefore there is no $\mathcal{O}(a)$ or $\mathcal{O}(ma)$ error. The massive Neuberger operator may be defined by

$$aD_{\text{ov}}(m_q) = (1 + \frac{am_q}{2}) + (1 - \frac{am_q}{2})\gamma_5 sgn(\gamma_5(aD_W - 1)) \tag{2.93}$$

which gives the continuum Dirac operator with bare quark mass m_q by similar arguments to those in equation (2.92). As well as having a mass term for the quarks we are simulating a mass term may also be added to the auxiliary action D_W. D_W may have near zero eigenvalues. This causes problems when inverting the matrix as the condition number (given by the ratio of the norm of the largest eigenvalue to the norm of the smallest eigenvalue) blows up. However, since we only require the signs of the eigenvalues of D_W we are free to add any mass parameter ρ to D_W without affecting the continuum limit. Carefully choosing

ρ can decrease the computational cost of the simulation. Replacing $(aD_W - 1)$ by $(aD_W - \rho)$ requires a rescaling of $\not{D}$ since in taking the continuum limit as in equation (2.92) we find

$$\lim_{a\to 0} \gamma_5 sgn\left[\gamma_5((aD_W - \rho))\right] \to \frac{a\not{\partial} - \rho}{\rho}. \tag{2.94}$$

The correct continuum limit can be achieved by rescaling equation (2.90) by ρ so that

$$a\not{D} = \rho\left(1 + \gamma_5 sgn\left[\gamma_5(aD_W - \rho)\right]\right). \tag{2.95}$$

For the massive case this gives

$$aD_{\rm ov}(m_q, \rho) = \rho(1 + \frac{am_q}{2\rho}) + \rho(1 - \frac{am_q}{2\rho})\gamma_5 sgn(\gamma_5(aD_W - \rho)) \tag{2.96}$$

which is sometimes written

$$aD_{\rm ov}(\mu) = \rho(1 + \mu) + \rho(1 - \mu)\gamma_5 sgn(H) \tag{2.97}$$

where $\mu = \frac{am_q}{2\rho}$. This is the form of the overlap operator that will be used to simulate the valence quarks in chapter 4.

2.10 Domain wall fermions

A class of five dimensional actions satisfying the Ginsparg-Wilson relation have been proposed of which the domain wall fermion action [25] is one. The domain wall fermion action removes the doublers while preserving the chiral symmetry away from the continuum limit. Kaplan showed that the light chiral modes can be produced in a d dimensional theory as surface states coupled to a domain wall in a $d + 1$ dimensional theory. The formulation introduces an extra space-time dimension in order to separate the chiral and continuum limits. This extra dimension will be denoted s and Lorentz indices $\mu, \nu, \ldots$ label the four physical directions as before. The Dirac operator in 4+1 dimensions is given by

$$D(x, s) = \gamma_\mu \partial_\mu + \gamma_5 \partial_5 + m(s) \tag{2.98}$$

where the fermion mass, $m(s)$, has the shape of a domain wall, that is a monotonic function of s with the asymptotic form

$$\lim_{s\to\pm\infty} m(s) = \pm m_{\pm}, \quad m_{\pm} > 0 \tag{2.99}$$

where the reason for the subscripts will become apparent. This is shown schematically in figure 2.2. Since the mass vanishes at $s = 0$ one might expect to find

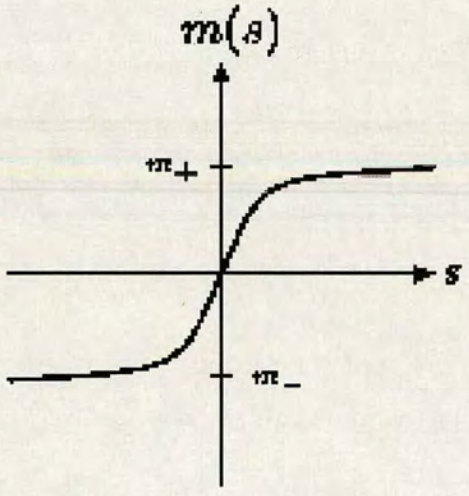

Figure 2.2: Qualitative shape of the fermion mass function. The prototype of such a function is $m(s) = M\tanh(Ms)$ for a step function of height M and width $1/M$.

massless states bound to the defect. In four dimensions the Dirac equation describing massless propagation is given by

$$\gamma_\mu \partial_\mu \psi(x, s) = 0 \tag{2.100}$$

so in order to describe massless propagation along the defect the "zeromode" would have to satisfy

$$D(x, s)\psi(x, s) = \gamma_\mu \partial_\mu \psi(x, s). \tag{2.101}$$

Substituting a trial function of the form

$$\psi^{\pm}(x,s) = e^{ip.x}\phi_{\pm}(s)u_{\pm}, \tag{2.102}$$

where the $u_{\pm}$ are constant spinors satisfying $\gamma_5 u_{\pm} = \pm u_{\pm}$, into the five dimensional Dirac equation

$$D(x,s)\psi(x,s) = 0 \tag{2.103}$$

and using equation (2.100) gives that the functions $\phi_{\pm}(s)$ must satisfy

$$\left[\pm\partial_s + m(s)\right]\phi_{\pm}(s) = 0. \tag{2.104}$$

The solutions to equation (2.104) are

$$\phi_{\pm}(s) = exp(\mp\int_0^s m(s')ds'). \tag{2.105}$$

While the solution $\phi_-(s)$ grows exponentially at large $|s|$, the solution $\phi_+(s)$ is normalisable. Physically this corresponds to a single, positive chirality massless fermion bound to the mass defect.

Shamir [26] proposed a variant of Kaplan fermions known as surface fermions. He defined the free theory on a semi-infinite five dimensional lattice to have the five dimensional action

$$S = S_4 + S_5 \tag{2.106}$$

where S_4 is the usual four dimensional Wilson action summed over the fifth direction s with the coefficient of the Wilson term set to one

$$\begin{aligned} S_4 &= \sum_{x,\mu,s\geq 0} \bar{\psi}(x,s)\gamma_\mu\partial_\mu\psi(x,s) + M_5\sum_{x,s\geq 0}\bar{\psi}(x,s)\psi(x,s) \\ &+ \frac{1}{2}\sum_{x,\mu,s\geq 0}\bar{\psi}(x,s)\partial^2\psi(x,s) \end{aligned} \tag{2.107}$$

where M_5 is is normally called the domain wall height and corresponds to the height of the step function. S_5 is given by

$$\begin{aligned} S_5 &= \sum_{x,s\geq 0}\bar{\psi}(x,s)\gamma_5\partial_5\psi(x,s) + \frac{1}{2}\sum_{x,s\geq 0}\bar{\psi}(x,s)\partial_5^2\psi(x,s) \\ &+ \frac{1}{2}\sum_x\bar{\psi}(x,0)\gamma_5\psi(x,1) + \frac{1}{2}\sum_x\bar{\psi}(x,0)(\psi(x,1) - 2\psi(x,0)). \end{aligned} \tag{2.108}$$

With this action he showed that the propagator is given by

$$G_{R,L}(s,s';p) = G_0(s,s';p) + K_{R,L}(s';p)e^{-\alpha(p)s} \tag{2.109}$$

where

$$\begin{aligned}
G_0(s,s';p) &= \frac{e^{-\alpha(p)|s-s'|}}{2b(p)\sinh\alpha(p)} && (2.110)\\
K_R(s';p) &= -\frac{e^{-\alpha(p)(s'+2)}}{2\sinh\alpha(p)} && (2.111)\\
K_L(s';p) &= \frac{e^{-\alpha(p)(s'+2)}}{2\sinh\alpha(p)}\frac{b(p)-e^{\alpha(p)}}{b(p)-e^{-\alpha(p)}} && (2.112)\\
2\cosh\alpha(p) &= \frac{1+b(p)^2+\tilde{p}^2}{b(p)} && (2.113)\\
\tilde{p}_\mu &= \sin p_\mu && (2.114)\\
b(p) &= 1 - M_5 + \sum_\mu (1-\cos(p_\mu)). && (2.115)
\end{aligned}$$

Importantly $K_L(s';p)$ has a pole at zero momentum coming from the existence of a chiral bound state stuck to the wall. Indeed it may be observed that as p vanishes $\alpha \to -\ln b$.

For the case of a finite fifth dimension $0 \leq s \leq L_s - 1$ and including a term that couples the fermions at $s = 0$ and $s = L_s - 1$ it can be shown [26] that the propagator describes both a left-handed massless mode bound to the wall at $s = 0$ and a right-handed massless mode bound to the wall at $s = L_s$. These states of opposite chiralities mix between the walls and decrease exponentially away from the walls (see figure 2.3). Therefore the mixing is exponentially suppressed with the size of the fifth dimension and chiral violations are proportional to the size of the mixing.

Including interactions the domain wall fermion action developed by Narayanan and Neuberger [27, 28] and by Furman and Shamir [26, 29] is given by

$$S_F^{DW} = \bar{\Psi}_{x,s} D_{x,s,x',s'} \Psi_{x',s'} \tag{2.116}$$

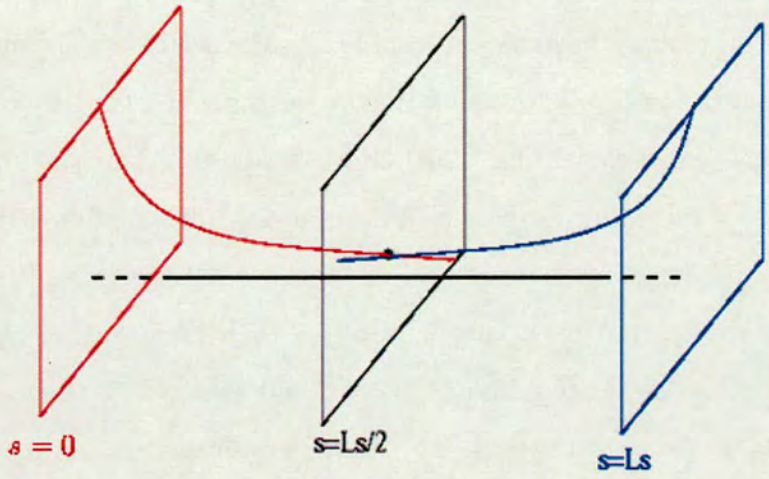

Figure 2.3: The domain walls are separated by L_s. The mixing between the modes decays exponentially in the fifth direction.

where the spatial indices have been subscripted so the five dimensional fermion field is given by $\Psi(x,s) \equiv \Psi_{x,s}$ and the domain wall fermion Dirac operator, D, is given by

$$D_{x,s;x',s'} = \delta_{s,s'} D^{\parallel}_{x,x'} + \delta_{x,x'} D^{\perp}_{s,s'} \tag{2.117}$$

$$\begin{aligned} D^{\parallel}_{x,x'} &= \frac{1}{2}\sum_{\mu=1}^{4}\left[(1-\gamma_\mu)U_{x,\mu}\delta_{x+\hat{\mu},x'} + (1+\gamma_\mu)U^{\dagger}_{x',\mu}\delta_{x-\hat{\mu},x'}\right] \\ &\quad +(M_5-4)\delta_{x,x'} \end{aligned} \tag{2.118}$$

$$D^{\perp}_{s,s'} = P_L M_{s,s'} + P_R M^{\dagger}_{s,s'} - \delta_{s,s'}, \tag{2.119}$$

where $P_L = \frac{1}{2}(1-\gamma_5)$, $P_R = \frac{1}{2}(1+\gamma_5)$ and M is an $L_s \times L_s$ matrix

$$M_{s,s'} = \delta_{s+1,s'} - m_f \delta_{s,L_s-1}\delta_{0,s'} = \begin{pmatrix} 0 & 1 & 0 & \cdots & 0 \\ 0 & 0 & 1 & \cdots & 0 \\ \cdots & \cdots & \cdots & \cdots & \cdots \\ 0 & 0 & 0 & \cdots & 1 \\ -m_f & 0 & 0 & \cdots & 0 \end{pmatrix}. \tag{2.120}$$

The value of the five dimensional quark mass or domain wall height, M_5, determines how many flavours are coupled to the walls. m_f is the four dimensional bare quark mass which explicitly couples the $s = 0$ and $s = L_s - 1$ walls hence mixing the two chiralities. The delta functions, $\delta_{s,s'}$, are assumed to have period L_s. $D^{\parallel}_{x,x'}$ takes the form of a Wilson action with modified mass term which is replicated across each of the slices in the fifth dimension. The modified mass makes the modes heavy and suppresses their propagation along the 4-d slices. The number of heavy fermions is $\sim L_s$ and as $L_s \to \infty$ these lead to a bulk type infinity in the path integral. This may be cancelled by adding a five dimensional Pauli Villars field with a heavy mass [30, 31]. The $D^{\perp}_{s,s'}$ describes the propagation in the fifth dimension. It can loosely be thought of as describing the coupling between the five dimensional slices. The gauge fields are replicated along the fifth dimension

$$U_{\mu \leq d}(x, s) = U_\mu(x) \quad U_{d+1}(x, s) = \mathbb{I} \tag{2.121}$$

and as such couple to the fermions in the natural way.

The four dimensional fermion fields, $\psi(x)$, are constructed from the five dimensional fermion field, $\Psi(x, s)$, by projection of the different chiralities on the walls [29]

$$\psi(x) = P_{\mathrm{L}}\Psi(x, 0) + P_{\mathrm{R}}\Psi(x, L_s - 1) \tag{2.122}$$

$$\bar{\psi}(x) = \bar{\Psi}(x, L_s - 1)P_{\mathrm{L}} + \bar{\Psi}(x, 0)P_{\mathrm{R}}. \tag{2.123}$$

The domain wall fermion action may be shown to be related in the $L_s \to \infty$ limit to the Neuberger or overlap action described in section 2.9 (see for example [32, 33]). As such, the domain wall fermion action may be shown to have discretisation errors of $\mathcal{O}(a^2)$.

2.11 The anomalous or residual quark mass

Due to the finite extent of L_s, and the direct coupling via the quark mass m_f between the fermion fields on the walls, the modes coupled to the $s = 0$ and $s = L_s - 1$ walls are mixed. The effect of the violation in chiral symmetry due to the finite L_s is to shift the bare mass, m_f, by some small additive piece m_{res}, the residual or anomalous mass. In the following we assume that the m_f are equal for $f = 1, \ldots, N_f$ (The case for non-equal quark masses is discussed in [34]). In order to quantify the size of the symmetry breaking we examine the Ward-Takahashi identity for domain wall fermions.

The chiral transformation is defined to rotate the fermions in the two half spaces along the s direction with opposite charges

$$\delta\Psi(x,s) = +iQ(s)\epsilon^a\frac{\lambda^a}{2}\Psi(x,s) \tag{2.124}$$

$$\delta\bar{\Psi}(x,s) = -i\bar{\Psi}(x,s)Q(s)\epsilon^a\frac{\lambda^a}{2} \tag{2.125}$$

$$Q(s) = \text{sgn}((L_s-1)-2s) = \text{sgn}\left(\frac{L_s-1}{2}-s\right) \tag{2.126}$$

where ϵ^a is a transformation parameter. The axial current corresponding to this transformation is given by [29]

$$\mathcal{A}^a_\mu(x) = \sum_{s=0}^{L_s-1} Q(s)\mathcal{J}^a_\mu(x,s), \tag{2.127}$$

where

$$\begin{aligned}\mathcal{J}^a_\mu(x,s) &= \overline{\Psi}(x,s)\left(\frac{1-\gamma_\mu}{2}\right)U_\mu(x)\frac{\lambda^a}{2}\Psi(x+\hat{\mu},s) \\ &- \overline{\Psi}(x+\hat{\mu},s)\left(\frac{1+\gamma_\mu}{2}\right)U^\dagger_\mu(x)\frac{\lambda^a}{2}\Psi(x,s).\end{aligned} \tag{2.128}$$

The divergence of the axial current has two contributions

$$\sum_{\mu=1}^{4}\partial_\mu\mathcal{A}^a_\mu(x) = 2m_f\mathcal{J}^a_5(x,L_s-1) + 2\mathcal{J}^a_5(x,\frac{L_s}{2}) \tag{2.129}$$

where $\partial_\mu f(x) = f(x) - f(x - \hat{\mu})$ is a finite difference operator and $\mathcal{J}_5^a(x,s)$ is given by

$$\mathcal{J}_5^a(x,s) = \tag{2.130}$$
$$\begin{cases} \overline{\Psi}(x,s)P_L\frac{\lambda^a}{2}\Psi(x,s+1) - \overline{\Psi}(x,s+1)P_R\frac{\lambda^a}{2}\Psi(x,s) & 0 \le s < L_s - 1 \\ \overline{\Psi}(x,L_s-1)P_L\frac{\lambda^a}{2}\Psi(x,0) - \overline{\Psi}(x,0)P_R\frac{\lambda^a}{2}\Psi(x,L_s-1) & s = L_s - 1 \end{cases}$$

In terms of the four dimensional fermion fields (2.122) the current $\mathcal{J}_5^a(x,L_s-1)$ may be written as

$$\mathcal{J}_5^a(x,L_s-1) = \bar{\psi}(x)\gamma_5\frac{\lambda^a}{2}\psi(x) = P^a(x) \tag{2.131}$$

which is the common pseudoscalar density. The second term, $\mathcal{J}_5^a(x,\frac{L_s}{2})$, which vanishes in the $L_s \to \infty$ limit [29] is due to the coupling of left and right handed light surface states at the midpoint of the fifth dimension. The modified axial Ward-Takahashi identity is thus given by

$$\begin{aligned} \sum_{\mu=1}^{4}\partial_\mu\langle\mathcal{A}_\mu^a(x)\bar{\psi}(0)\gamma_5\frac{\lambda^a}{2}\psi(0)\rangle &= 2m_f\langle\bar{\psi}(x)\gamma_5\frac{\lambda^a}{2}\psi(x)\bar{\psi}(0)\gamma_5\frac{\lambda^a}{2}\psi(0)\rangle \\ &+ 2\langle\mathcal{J}_5^a(x,\frac{L_s}{2})\bar{\psi}(0)\gamma_5\frac{\lambda^a}{2}\psi(0)\rangle \\ &- \delta_{x,0}\langle\bar{\psi}(0)\psi(0)\rangle. \end{aligned} \tag{2.132}$$

The above equation may be compared with the Ward-Takahashi identity for the effective continuum theory in the continuum limit. The sum of the two currents in equation (2.132) is proportional to an effective quark mass, $m_{\text{eff}} = m_f + m_{\text{res}}$, times the pseudoscalar density with the anomalous quark mass, m_{res} defined by

$$\mathcal{J}_5^a(x,\frac{L_s}{2}) \equiv m_{\text{res}}\mathcal{J}_5^a(x,L_s-1) = m_{\text{res}}P^a(x). \tag{2.133}$$

In practice the residual mass term is computed by means of the ratio [35, 36, 37]

$$m_{\text{res}} = \frac{\Sigma_{\vec{x},\vec{y}}\langle\mathcal{J}_5^a(\vec{y},t,\frac{L_s}{2})P^a(\vec{x},0)\rangle}{\Sigma_{\vec{x},\vec{y}}\langle P^a(\vec{y},t)P^a(\vec{x},0)\rangle}. \tag{2.134}$$

where t is suitably large so that the effects of low-energy long-distance physics are dominant.

2.12 The Gauge Action

To complete the construction of the lattice action, we need to construct a lattice kinetic term for A_μ analogous to equation (2.24) which should be gauge invariant and be a function of the link variables only. The simplest gauge invariant objects that we can build from the link variables are formed by taking the trace of an ordered product of gauge links forming a closed loop, referred to as a Wilson loop. The smallest, and simplest, example of this is the plaquette (see figure 2.4). Rewriting $U(n, n+\hat{\mu}) \equiv U_\mu(n)$, the plaquette is given by

$$U_{\mu\nu}(n) = U_\mu(n)U_\nu(n+\hat{\mu})U_\mu^\dagger(n+\hat{\nu})U_\nu^\dagger(n) \tag{2.135}$$

which can be seen to be gauge invariant by considering the transformation properties of $U_\mu(n)$ under a local gauge transformation given by equation (2.55). It

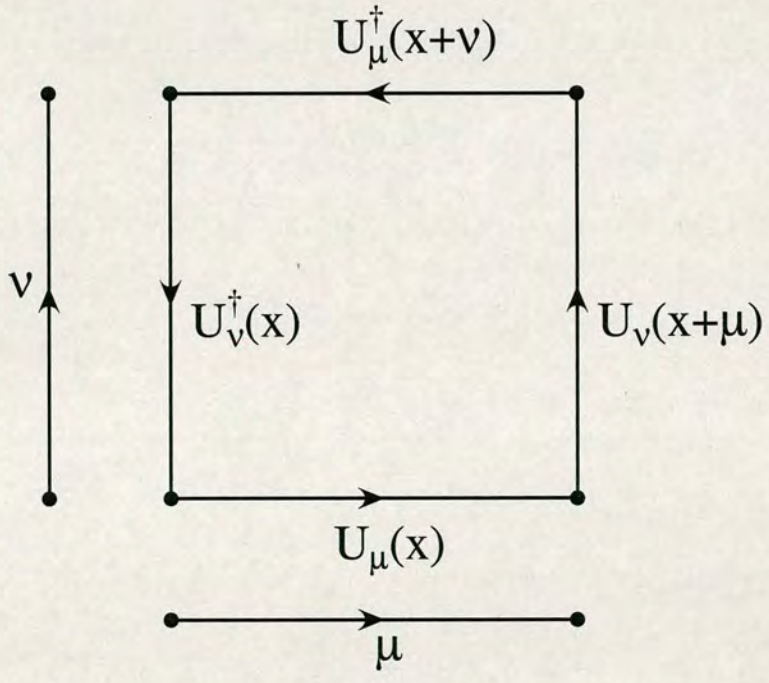

Figure 2.4: The plaquette.

is clear that we should focus on the smallest possible loops because of the local

structure of the integrand in equation (2.24). This helps with locality of the quantum field theory and proof of reflection positivity (See for example [8]). The path ordering is important as the $U_\mu(n)$ are matrices which do not commute. Although we have defined the quantity $U_{\mu\nu}(n)$ we have not yet seen what it corresponds to in the continuum theory. To that end we substitute

$$U_\mu(n) = e^{iagA_\mu(n)} \tag{2.136}$$

into equation (2.135) and obtain

$$U_{\mu\nu}(n) = e^{iagA_\mu(n)} e^{iagA_\nu(n+\hat{\mu})} e^{-iagA_\mu(n+\hat{\nu})} e^{-iagA_\nu(n)}. \tag{2.137}$$

Expanding this expression in powers of a for small a using

$$A_\mu(n+\hat{\nu}) = A_\mu(n) + a\partial_\nu A_\mu(n) + \mathcal{O}(a^2) \tag{2.138}$$

and repeated use of the Baker-Campbell-Hausdorff formula,

$$e^A e^B = e^{A+B+\frac{1}{2}[A,B]+\cdots}, \tag{2.139}$$

where the dots correspond to terms involving 2 or more commutators, gives

$$U_{\mu\nu}(n) = e^{ia^2 g F_{\mu\nu}(n)} \tag{2.140}$$

where $F_{\mu\nu}(n)$ is given by

$$F_{\mu\nu}(n) = \partial_\mu A_\nu - \partial_\nu A_\mu + ig[A_\mu, A_\nu] + \mathcal{O}(a^2). \tag{2.141}$$

A simple expansion of equation (2.140) gives

$$U_{\mu\nu}(n) = 1 + ia^2 g F_{\mu\nu}(n) - \frac{g^2 a^4}{2} F_{\mu\nu}(n) F_{\mu\nu}(n) + \mathcal{O}(a^6) \tag{2.142}$$

and therefore we write the lattice version of the kinetic term for the gauge fields in the action as

$$S_G = \frac{\beta}{3} \sum_{\mu<\nu} Re\mathrm{Tr}(1 - U_{\mu\nu}(n)) \tag{2.143}$$

where the trace is over the colour indices, the sum is over all plaquettes on the lattice with $\mu < \nu$ and where the gauge coupling, g, has been written in terms of the dimensionless constant, $\beta = \frac{6}{g^2}$ for SU(3), in order to give the correct continuum action in the limit $a \to 0$. β is the single input parameter for a Yang-Mills calculation (whether on the lattice or not) involving only gluon fields. In principle there is also the θ parameter, however, experimentally it is observed that $\theta \sim 0$ (strong CP problem). The lattice spacing is not explicit anywhere, and its value in physical units is unknown until after the calculation. This will depend on the bare coupling constant.

2.13 Improved gauge actions

Although the gauge action (2.143) reproduces the correct continuum limit expression, it was obtained up to discretisation errors of $\mathcal{O}(a^2)$. This is the simplest choice that can be made for the gauge action. Improved gauge actions attempt to reduce the $\mathcal{O}(a^2)$ discretisation error further by adding additional higher order terms to the action to make it closer to the continuum theory at non-zero lattice spacing. After the plaquette, the next simplest higher order terms that can be added to the action are terms involving Wilson loops created from six links instead of four. There are three topologically distinct six link Wilson loops. These go by the names rectangle, bent rectangle, and parallelogram (see figure 2.5). These are denoted $\mathcal{P}_1^{(6)}$, $\mathcal{P}_2^{(6)}$, $\mathcal{P}_3^{(6)}$, respectively. The lattice gauge action may therefore be written as

$$S_G = \beta\{c_0^{(4)}(g^2)\mathcal{P}^{(4)} + \sum_{i=1,\ldots,3} c_i^{(6)}(g^2)\mathcal{P}_i^{(6)}\} \tag{2.144}$$

in terms of the plaquette, $\mathcal{P}^{(4)}$, and the three six link loops. The leading order term in the expansion of all Wilson loops is $\mathcal{O}^{(4)} = F_{\mu\nu}F_{\mu\nu}$ and corrections begin at $\mathcal{O}(a^2)$, hence the lattice action (2.144) will have the correct form in the limit

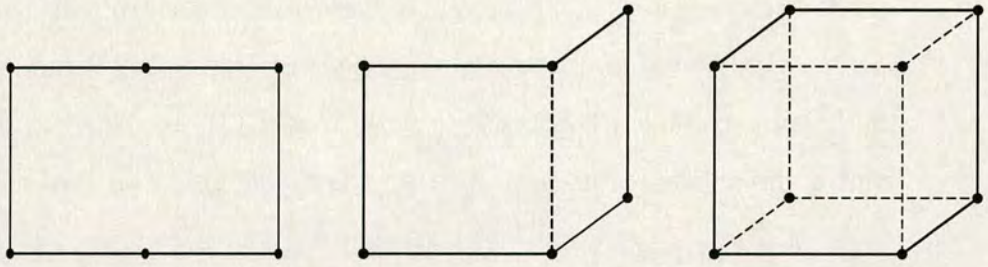

Figure 2.5: Six link loops: the rectangle, the bent rectangle and the parallelogram or chair.

$a \to 0$ with corrections of $\mathcal{O}(a^2)$.

The Doubly Blocked Wilson (DBW2) and Iwasaki actions are examples of improved actions where the discretisation error in the Wilson action is improved by adding the next simplest loop ,the rectangle, $\mathcal{P}_1^{(6)}$. These actions are renormalisation group improved actions in a two parameter space (c_0, c_1). The coefficient in front of the $\mathcal{P}_1^{(6)}$ term is obtained by studying block transformations in perturbation theory. The form of the action is given by

$$S_G[U] = -\frac{\beta}{3}\left[(1-8\,c_1)\sum_{n;\mu<\nu} P[U]_{n,\mu\nu} + c_1 \sum_{n;\mu\neq\nu} R[U]_{n,\mu\nu}\right] \tag{2.145}$$

$$R[U]_{n,\mu\nu} = U_\mu(n)U_\mu(n+\mu)U_\nu(n+2\mu)U_\mu^\dagger(n+\mu+\nu)U_\mu^\dagger(n+\nu)U_\nu^\dagger(n),$$

where $P[U]_{n,\mu\nu}$ and $R[U]_{n,\mu\nu}$ represent the real part of the trace of the path ordered product of links around the 1×1 plaquette and 1×2 rectangle, respectively, in the μ,ν plane at the point n, and $\beta \equiv 6/g^2$ with g the bare coupling constant. The coefficient $c_0 = (1-8c_1)$. For the DBW2 gauge action [38, 39], the coefficient c_1 is chosen to be -1.4069, while for the Iwasaki gauge action [40, 41] $c_1 = -0.331$.

2.14 Monte Carlo Integration

We are interested in calculating the mass spectrum and matrix elements using lattice QCD. The starting point for any such calculation is the path integral expectation value of an observable $\mathcal{O}$

$$\langle \mathcal{O} \rangle = \frac{1}{\mathcal{Z}_{\mathrm{LQCD}}} \int \prod_f \mathcal{D}U \mathcal{D}\bar{\psi}_f \mathcal{D}\psi_f \mathcal{O} e^{-S_{\mathrm{LQCD}}[U,\psi,\bar{\psi}]} \tag{2.146}$$

where the partition function, $\mathcal{Z}_{\mathrm{LQCD}}$, is given by

$$\mathcal{Z}_{\mathrm{LQCD}} = \int \prod_f \mathcal{D}U \mathcal{D}\bar{\psi}_f \mathcal{D}\psi_f e^{-S_{\mathrm{LQCD}}[U,\psi,\bar{\psi}]} \tag{2.147}$$

and the lattice action, S_{LQCD}, is given by $S_{\mathrm{LQCD}}[U,\psi,\bar{\psi}] = S_F[U,\psi,\bar{\psi}] + S_G[U]$ for some choice of fermionic and gauge action. In general, the observable $\mathcal{O}$ will be some function $\mathcal{O}(\psi,\bar{\psi},U)$ of the quark, antiquark and gauge fields, and the action S_{LQCD} is assumed to be a real function of the field variables bounded from below. The assumption of a real action means that we have a positive fermion determinant, which restricts the class of allowed fermionic theories. The path integral may be formally defined on a discrete space-time lattice. Since the fermionic piece of the action, S_F, is bilinear in the Grassmann valued quark fields, the fermionic integration can be carried out analytically (see appendix A) and produces a determinant of the fermionic matrix for each flavour of quark field

$$\langle \mathcal{O} \rangle = \frac{1}{\mathcal{Z}_{\mathrm{LQCD}}} \int \mathcal{D}U \det(M^u[U]) \det(M^d[U]) \det(M^s[U]) \mathcal{O} e^{-S_G} \tag{2.148}$$

where in the flavour product, we have included the up, down, and strange quarks as they are the lightest three quarks in our theory and contribute most to the physics that we wish to study. We denote the number of quarks used in our theory as N_{sea}. Since $m_u \approx m_d \equiv m_l$, this can be written as

$$\langle \mathcal{O} \rangle = \frac{1}{\mathcal{Z}_{\mathrm{LQCD}}} \int \mathcal{D}U \left[\det(M^l[U])\right]^2 \det(M^s[U]) \mathcal{O} e^{-S_G}. \tag{2.149}$$

The integration is now only over the gauge degrees of freedom. The fermionic contribution is now contained in the highly non-local term $\det M^i[U]$ for $i = u, d, s$.

In the case of most lattice field systems of interest, the number of integration variables is extremely large, and therefore we must turn to statistical methods to evaluate the ensemble average. The fermion determinant may be dealt with in several ways. Firstly, we can re-express it to obtain an effective gauge action

$$S_{\text{eff}}[U] = S_G[U] - \ln \det M[U] \tag{2.150}$$

$$= S_G[U] - \text{Trln} M[U] \tag{2.151}$$

and perform all simulations with this effective action. Secondly, we could write this fermionic determinant as a Gaussian integral over bosonic variables ϕ (known as pseudofermions)

$$\det M[U] = \int D\phi^\dagger(x) D\phi(x) e^{-\phi_x^\dagger M_{xy}^{-1} \phi_y}. \tag{2.152}$$

This is the method employed for the Hybrid Monte-Carlo algorithm (section 2.16). In this case, the action is re-written as an effective action

$$S_{\text{eff}}[U, \phi, \phi^\dagger] = S_G[U] + \phi_x^\dagger M_{xy}^{-1}[U] \phi_y. \tag{2.153}$$

This effective action includes an inverse of the fermion matrix. In practice $M^\dagger M$ is used rather than M for algorithmic reasons (M is real but not positive definite). This has the advantage that we are able to deal with both of the light quark fields (that of the u and d quarks), to the extent that they are degenerate, together.

Quark masses simulated are much larger than those found experimentally due to the large computational cost of light sea quarks and because finite volume effects are larger for lighter sea quarks.

The expectation value of an observable $\mathcal{O}$ may be computed by the following sum

$$\langle \mathcal{O} \rangle \approx \frac{1}{N} \sum_{i=1}^{N} \mathcal{O}[U_i] \tag{2.154}$$

where the U_i are configurations chosen with the appropriate probability weight. Thus, in the path integral case (2.148) we calculate the expectation value of an

observable $\mathcal{O}$ as

$$\langle \mathcal{O} \rangle \approx \frac{1}{N} \sum_{i=1}^{N} \frac{1}{\mathcal{Z}_{\mathrm{LQCD}}} e^{-S_G[U_i]} \prod_f \det M^f [U_i] \mathcal{O}[U_i] \tag{2.155}$$

where here the product is over the quark flavours $f = u, d, s$. Since most configuration will have an action which is very large, only a small fraction of them will make a significant contribution to the above sum. To alleviate this problem instead of choosing all configurations with equal weight, a more efficient method consists of generating a sequence of link configurations with probability distribution given by the Boltzmann weight

$$P[U] = \frac{1}{\mathcal{Z}_{\mathrm{LQCD}}} e^{-S_G[U_i]} \prod_f \det M^f [U_i] . \tag{2.156}$$

This is known as importance sampling. If the sequence of configurations generated has this probability distribution, then the ensemble average, $\langle \mathcal{O} \rangle$, may be approximated by equation (2.154) where $\{U\}_i$, $i = 1, \ldots, N$ denote the configurations generated with the appropriate Boltzmann weight.

2.15 Metropolis algorithm and Markov chains

Metropolis [42] algorithms generate a sequence of configurations, C_i, $i = 1, \ldots, N$, where C_{i+1} is generated from C_i stochastically according to some transition probability $P(C_i \to C_j)$. This sequence of configurations is known as a Markov chain. The chain will converge to the desired probability distribution if it fulfils two important conditions. Firstly, updating algorithms should fulfil detailed balance, a sufficient but not necessary condition. Given the transition probability $P(A \to B)$, for going from configuration A to B detailed balance asserts that

$$W[A]P(A \to B) = W[B]P(B \to A) \tag{2.157}$$

where $W[A]$ and $W[B]$ represent the distribution we wish to sample e.g. $e^{-S(A)}$.

The second important condition that updating algorithms should respect is ergodicity, i.e. it has to be possible to reach any other configuration with the updating step. In terms of transition probability, this reads for any pair of configurations

$$P(A \to B) > 0. \tag{2.158}$$

This is known as strong ergodicity. Every elementary step does not have to fulfil this strong condition, because if enough of these elementary steps are combined to a bigger step, it is sufficient that this bigger step fulfils the strong ergodicity condition. If these two conditions are satisfied it can be shown that the Markov process generates a unique equilibrium distribution.

The Metropolis algorithm [42], is a way of constructing a Markov process that satisfies detailed balance and is in principle applicable to any system. The rule for generating the configurations in a sequence follows

- Let A be the configuration we wish to update
- Suggest a new configuration A' with transition probability $P_0(A \to A')$
- Accept A' if $e^{-S[A']} > e^{-S[A]}$ (i.e. the action has been lowered)
- If the action has been increased, generate a random number R in the interval [0,1] and accept A' if $R \leq \frac{e^{-S[A']}}{e^{-S[A]}}$

It is the conditional acceptance in the last step that allows the system to increase its action. While classical configurations correspond to a minima of the action, the quantum system is allowed to move away from the classical configurations. The algorithm can be shown to satisfy detailed balance [7].

This provides us with a rule for how to select the next configuration in a Markov chain given the configuration immediately preceding it.

In general, the Metropolis algorithm is computationally too costly when it comes to simulations including dynamical fermions. This is because the action depends

non-locally on the co-ordinates and in this case the ratio $\frac{e^{-S[A']}}{e^{-S[A]}}$ will no longer be determined by nearest neighbour interactions. To take fermions into account, we require more efficient algorithms which allow an update to the entire lattice at once, rather than one gauge link at a time. The algorithm of choice for dynamical fermion simulations is the Hybrid Monte Carlo Algorithm (HMC).

2.16 Hybrid Monte Carlo

The Hybrid Monte Carlo algorithm (HMC) [43] is one method for performing dynamical fermion simulations. The HMC algorithm constructs a Markov process satisfying detailed balance with respect to the desired probability distribution and is ergodic, as is required for it to converge to the desired equilibrium distribution.

The algorithm requires the introduction of fictitious momenta conjugate to the link variables U so that the Hamiltonian for the system may be written as

$$H[P,U,\phi] = \frac{1}{2}\sum_{\mu,j} P_{\mu,j}^2 + S[U,\phi] \tag{2.159}$$

where $S[U,\phi]$ plays the rôle of a potential and is given by equation (2.153). The expectation value of some observable $\mathcal{O}(U,\phi)$ can then be written as

$$\langle \mathcal{O} \rangle = \frac{1}{\mathcal{Z}} \int \mathcal{D}P\mathcal{D}U\mathcal{D}\phi\mathcal{D}\phi^\dagger \mathcal{O}(U,\phi) e^{-H[P,U,\phi]} \tag{2.160}$$

where the partition function is now given by

$$\mathcal{Z} = \int \mathcal{D}P\mathcal{D}U\mathcal{D}\phi\mathcal{D}\phi^\dagger e^{-H[P,U,\phi]}. \tag{2.161}$$

The Hamiltonian (2.159) defines a dynamical system, constrained to be conservative, due to the lack of any explicit time dependence in the Hamiltonian. The variables satisfy Hamilton's equations with respect to a (fictitious) "molecular dynamics" time τ. The basic HMC algorithm is

1. Choose an initial configuration of U and P fields, (U, P), at $\tau = 0$.

2. Generate a field ϕ by taking it at random from an appropriate probability distribution (see for example [44, 45]).

3. Molecular dynamics: use Hamilton's equations of motion to evolve deterministically P and U for some time ($N_{md}\delta\tau$) while holding ϕ fixed to obtain a new gauge configuration (U', P').

4. Accept the new configuration with probability

$$p = \min\left(1, \exp\left(-\Delta H\right)\right) \tag{2.162}$$

   where ΔH is the change in the Hamiltonian due to the molecular dynamics step.

5. Regenerate a new set of P's randomly as before.

6. Go to step 2 with the new/old configuration of U's depending on the accept/reject step.

The algorithm depends only on the molecular dynamics step size, $\delta\tau$, and the number of molecular dynamics steps we take, N_{md}, also called the trajectory length. This process satisfies detailed balance and ergodicity [43, 44].

2.17 2+1 flavour simulations and the RHMC algorithm

In chapter 5 results for simulations with two degenerate light flavours of quark and one heavier quark will be presented. The Hybrid Monte Carlo algorithm, and the various refinements which have been applied to it since its inception, has been the algorithm of choice for most recent calculations. However, it does have some

drawbacks, most notably that the algorithm cannot efficiently generate ensembles of configurations with only a single quark flavour present. This is because the operator $\mathcal{M} \equiv M^\dagger M$ must be included in the action rather than just M in equation (2.153). For Wilson fermions this corresponds to a two flavour theory. Historically this has not been a problem since the up and down quarks are usually treated as degenerate and generally calculations have been performed using mass parameters much much heavier than the strange quark mass, meaning there has been little point in performing simulations with 2+1 flavours.

The resolution to the problem of simulations with 2+1 flavours of quarks has been to use the inexact R algorithm [46] or the Polynomial Monte Carlo algorithm [47, 48, 49]. An alternative method proposed recently, and the one used in this work is the RHMC algorithm [50, 51].

The RHMC algorithm replaces the function of the fermion matrix by a rational approximation over the spectral interval of the matrix. For example, to deal with the "1" in our 2+1 flavour simulation we require the action to have a term

$$\phi^\dagger (M^\dagger M)^{-\frac{1}{2}} \phi = \phi^\dagger \mathcal{M}^{-\frac{1}{2}} \phi. \tag{2.163}$$

In the RHMC algorithm a rational approximation is made

$$r(\mathcal{M}) \approx \mathcal{M}^{-\alpha} \tag{2.164}$$

where the rational function is given by

$$r(x) = \frac{p_n(x)}{p_d(x)} \tag{2.165}$$

where $p_j(x)$ is a degree j polynomial. The coefficients of these polynomials used to generate an optimal rational approximation to a given function over some finite range are found using the Remez algorithm [52]. For the special case of the (inverse) square root function with minimum relative errors the rational coefficients can be calculated analytically [53]. Once the rational approximation has

been found it may be expressed in product representation as

$$r(\mathcal{M}) = \alpha_0 \frac{\prod_{k=1}^{n}(\mathcal{M}+\gamma_k)}{\prod_{k=1}^{d}(\mathcal{M}+\beta_k)}. \tag{2.166}$$

by finding the roots. It is found that in this notation the shifts, γ_k and β_k, are always positive. To evaluate this function applied to a source vector, ϕ, is very expensive as d inverses would require to be found. This is normally done with Krylov subspace iterative solver methods (for example see [54, 55]). However, any rational function can be written as a polynomial quotient plus the sum of a series of partial fractions

$$r(\mathcal{M}) = \alpha_0 + \sum_{k=1} n \frac{\alpha_k}{\mathcal{M}+\kappa_k}. \tag{2.167}$$

If we assume that the degree of the numerator and denominator are equal ($n = d$) then α_0 will just be a constant. To evaluate this function applied to a source vector, ϕ, also requires d inversion operations, however, as all the denominator monomials are acting on a common vector and all the κ_k are real valued and positive this allows the use of a multi-shift solver to perform the matrix inversions simultaneously [56].

The fermion determinant is thus written

$$\det \mathcal{M}^{\alpha} = \int \mathcal{D}\phi^{\dagger}\mathcal{D}\phi e^{-\phi^{\dagger} r^2(\mathcal{M})\phi} \det[\mathcal{M}^{\alpha} r_{mc}^2(\mathcal{M})] \tag{2.168}$$

where $r_{mc}(x)$ is an approximation to $x^{-\alpha/2}$ over the spectral range of the fermion matrix. The reason for using r_{mc}^2 for the approximation rather than r_{mc} is to allow for a pseudofermion heatbath to be used. If the approximation is chosen to be good enough then the matrix $\mathcal{M}^{\alpha} r_{mc}^2(\mathcal{M})$ will be close to the unit matrix and therefore easy to invert. Indeed, if the approximation is chosen appropriately then the determinant factor in equation (2.168) may be set equal to unity without fear of bias and a conventional Metropolis acceptance test may be used. It is worth noting that in practice a lower order approximation $r_{md}(x)$ is used in the molecular dynamics step than in the accept/reject step ($r_{mc}(x)$) to increase the

speed of the algorithm. This is because the evaluation of the force term in the action requires two Krylov iterative solves. Any errors incurred through the lower order approximation may be stochastically corrected for in the accept/reject step. With the above modifications the RHMC algorithm proceeds in a similar way to the HMC algorithm of section 2.16 where step 2 requires an additional fermion refreshment for the "1" field.

2.18 Autocorrelation length

When generating configurations as a Markov chain there is some amount of time, know as the thermalisation time, before the system has reached an equilibrium state. At this point the system will have converged on the desired probability distribution. The number of trajectories required for thermalisation and to ensure a large enough correlation length between configurations depends on

- the algorithm used
- the observable being studied
- values of bare parameters.

Once thermalised, a system should have lost all knowledge of where it started and all expectation values must be independent of the starting condition.

Once the system has reached equilibrium we may use the thermalised configurations in order to measure our observables. In practice, the number of such configurations is finite, but if the sequence generated by the algorithm constitutes a representative set, then the ensemble average

$$\langle \mathcal{O} \rangle = \frac{\int \mathcal{D}U \mathcal{O}[U] e^{-S_G}}{\int \mathcal{D}U e^{-S_G}} \tag{2.169}$$

will be given by the sum (2.154) and the error in the mean will be of order $(\frac{1}{\sqrt{N}})$. Subsequent configurations generated in a Markov chain have knowledge of previous configurations so, in practice, the configurations generated sequentially are not statistically independent. This must be measured and taken into account when performing analysis. Considering an ensemble of N measurements of some observable, A $\{A_i, i = 1 \ldots N\}$, then in the limit of a large number of configurations the mean value can be approximated by

$$\bar{A} \approx \langle A \rangle \equiv \frac{1}{N} \sum_{i=1}^{N} A_i. \tag{2.170}$$

In order to measure the statistical dependence we define the integrated autocorrelation time [57, 58]

$$\tau_A^{int} = \frac{1}{2} \sum_{-\infty}^{\infty} \rho_A(t) = \frac{1}{2} + \sum_{t=1}^{\infty} \rho_A(t) \quad \tau >> 1 \tag{2.171}$$

where the autocovariance function, $\rho(t)$, is

$$\rho_A(t) = \frac{\Gamma_A(t)}{\Gamma_A(0)}, \quad \rho_A(t) \overset{t \to \infty}{\propto} e^{-\frac{t}{\tau_{exp}}} \tag{2.172}$$

and the autocovariance of an observable A is

$$\Gamma_A(t) = \langle (A_s - \langle A \rangle)(A_{s+t} - \langle A \rangle) \rangle. \tag{2.173}$$

Equation (2.172) defines the exponential autocorrelation time, τ_{exp}. The subscripts t and s in equation (2.173) label the configuration time and the outer average is over all pairs separated by t. The autocovariance function has the property that $\rho(t)=\rho(-t)$ which was used to obtain the expression for the integrated autocorrelation time.

It will be shown in section 3.17 that this definition of integrated autocorrelation time implies that statistically independent configurations are separated by $2\tau_A^{int}$. In practice we truncate the sum (2.171) at some finite value, t_{max}, and define the cumulative autocorrelation time to be

$$\tau_A^{cum} = \frac{1}{2} + \sum_{t=1}^{t_{max}} \rho_A(t). \tag{2.174}$$

This will be a good approximation to τ_{int} in the limit that t_{max} has been chosen large enough. A plot of τ_A^{cum} versus t_{max} should exhibit a plateau for large enough t_{max}.

Chapter 3

Correlation functions and data analysis

The aim of lattice QCD calculations is to extract numerical values for masses and matrix elements which can be contrasted with experimentally observed values. In this chapter I outline the basic principles required in the calculation of masses and matrix elements associated with meson and baryon states and discuss some of the techniques used to extract numerical values. I begin with a discussion of the quark propagator, the building block of two point correlation functions.

3.1 The quark propagator

Recalling equation (2.146) the expectation value of a bilinear $\psi(x)\bar{\psi}(y)$ may be written as

$$\langle \psi(x)\bar{\psi}(y) \rangle = \frac{1}{\mathcal{Z}_{\mathcal{LQCD}}} \int DUD\psi D\bar{\psi}\psi(x)\bar{\psi}(y)e^{-S_{\mathcal{LQCD}}[U,\psi,\bar{\psi}]} \tag{3.1}$$

and performing the (Grassmann) integration over the fermionic degrees of freedom and using Wick's contraction as in appendix A gives

$$\langle \psi(x)\bar{\psi}(y)\rangle = \frac{1}{\mathcal{Z}}\int DU \prod_f \det M_f[U] e^{-S_G[U]} M^{-1}(x,y;U) \tag{3.2}$$

where M is the fermion matrix from equation (2.58). Given the gauge fields are weighted appropriately with the factor

$$\frac{1}{\mathcal{Z}_{\mathcal{LQCD}}}\int DU \prod_f \det M_f[U] e^{-S_G[U]}, \tag{3.3}$$

in order to evaluate the integral we require to evaluate the inverse of the fermion matrix, or quark propagator, on each gauge configuration. The quark propagator is the building block for the more complicated correlation functions to follow. The quark propagator, G, is defined through the equation

$$M^{ab}_{\alpha\beta}(x,y;U) G^{bc}_{\beta\gamma}(y,0;U) = \delta(x,0)\delta_{\alpha\gamma}\delta^{ac} \tag{3.4}$$

where we have identified $G^{bc}_{\beta\gamma}(x,y;U) \equiv M^{-1bc}_{\beta\gamma}(x,y;U)$. The Greek indices label the spin components and the Latin indices label the colour components. The solution of the above equation is computationally intensive as the matrix M is large and sparse. In practice this equation is solved for each of the twelve spin-colour components separately using the iterative solver algorithms [54, 55].

Due to the relation between the fermion matrix and the propagator the (discrete) symmetries of the fermion matrix are shared by the propagator. Applying the discrete Lorentz transformations, parity ($\mathcal{P}$), charge conjugation ($\mathcal{C}$), time reversal ($\mathcal{T}$), hermiticity ($\mathcal{H}$), together with the combined transformation ($\mathcal{CPH}$) it can be seen that the quark propagator transforms as

$$\mathcal{P} : G(x,y;U) \rightarrow \gamma_4 G(x^P, y^P; U^P)\gamma_4 \tag{3.5}$$

$$\mathcal{T} : G(x,y;U) \rightarrow \gamma_4\gamma_5 G(x^T, y^T; U^T)\gamma_5\gamma_4 \tag{3.6}$$

$$\mathcal{C} : G(x,y;U) \rightarrow \gamma_4\gamma_2 G^T(x,y;U^C)\gamma_2\gamma_4 \tag{3.7}$$

$$\mathcal{H} : G(x,y;U) \rightarrow \gamma_5 G^\dagger(y,x;U)\gamma_5 \tag{3.8}$$

$$\mathcal{CPH} : G(x,y;U) \rightarrow C\gamma_4\gamma_5 G^\dagger(y^P, x^P; U^C)\gamma_5\gamma_4 C^{-1} \tag{3.9}$$

for a given background configuration U. These relations are very useful when discussing the properties of correlation functions.

3.2 Correlation functions

In order to test our theory against physical values obtained by experiment we are interested in calculating observables, for example, the mass spectrum, decay constants, and other matrix elements. These can be calculated using correlation functions, or correlators, constructed from interpolating quantum field operators whose form depends on the particular observable one wishes to study. Two point correlation functions are a subset of these correlation functions defined to be the vacuum expectation value of the time ordered product of two interpolating quantum field operators at two times

$$\begin{aligned} C_{AB}\left(\vec{x},t;\vec{0},0\right) &= \langle 0|\hat{T}\{\Theta_A(\vec{x},t)\overline{\Theta}_B(\vec{0},0)\}|0\rangle & (3.10)\\ &= \langle \Theta_A(\vec{x},t)\overline{\Theta}_B(\vec{0},0)\rangle & (3.11)\\ &= \frac{1}{\mathcal{Z}}\int DUD\psi D\overline{\psi}\Theta_A(x)\overline{\Theta}_B(0)e^{-S_{LQCD}} & (3.12) \end{aligned}$$

where $\overline{\Theta}_B(0)$ is a creation operator at source and $\Theta_A(x)$ an annihilation operator at sink and A and B label the particular form of the operator.

3.3 Meson correlation functions

A meson operator is generically written in a form bilinear in the quark fields

$$\Theta_M(x) = \bar{\psi}_i(x)\Gamma\psi_j(x) \tag{3.13}$$

where i,j are flavour indices and the colour and spinor indices have been suppressed. Γ is taken to be one of the sixteen possible Dirac gamma matrices

belonging to the Clifford algebra and depends on which state we wish to measure. Discussion of the choice of the matrix Γ will be postponed to section 3.5. The corresponding creation operator is given by

$$\overline{\Theta}_M(x) = \bar{\psi}_j(x)\bar{\Gamma}\psi_i(x) \tag{3.14}$$

where $\bar{\Gamma} = \gamma_4\Gamma^\dagger\gamma_4$. Substituting (3.13) and (3.14) into equation (3.10), and including the spinor (Greek) and colour (Latin) indices explicitly, the two point correlation function for creating a generic meson at the source and then annihilating it at the sink becomes

$$\begin{aligned} C_{MM}(x;0) &= \langle 0|\hat{T}\{\Theta_M(x)\overline{\Theta}_M(0)\}|0\rangle \qquad (3.15)\\ &= \langle 0\left|\hat{T}\{\bar{\psi}^a_{i,\alpha}(x)\Gamma_{\alpha\beta}\psi^a_{j,\beta}(x)\bar{\psi}^b_{j,\gamma}(0)\bar{\Gamma}_{\gamma\delta}\psi^b_{i,\delta}(0)\}\right|0\rangle \\ &= \frac{1}{\mathcal{Z}}\int DUD\overline{\psi}D\psi\Gamma_{\alpha\beta}\bar{\Gamma}_{\gamma\delta}\bar{\psi}^a_{i,\alpha}(x)\psi^a_{j,\beta}(x)\bar{\psi}^b_{j,\gamma}(0)\psi^b_{i,\delta}(0)e^{-S_{LQCD}[U,\psi,\bar{\psi}]}. \end{aligned}$$

Performing the Wick contractions of the Grassmann valued quark fields and recalling from appendix A that we can perform the integral over the Grassmann valued quark and anti-quark fields analytically

$$\begin{aligned} C_{MM}(x;0) &= \frac{1}{\mathcal{Z}}\int DUD\overline{\psi}D\psi\Gamma_{\alpha\beta}\bar{\Gamma}_{\gamma\delta}\,[\,\overbrace{\psi^a{}_{j,\beta}(x)\bar{\psi}^a_{i,\alpha}}(x)\overbrace{\psi^b{}_{i,\delta}(0)\bar{\psi}^b_{j,\gamma}}(0) \qquad (3.16)\\ &- \overbrace{\psi^a{}_{j,\beta}(x)\bar{\psi}^b_{j,\gamma}}(0)\overbrace{\psi^b{}_{i,\delta}(0)\bar{\psi}^a_{i,\alpha}}(x)\,]\,e^{-S_{LQCD}[U,\psi,\bar{\psi}]} \\ &= \frac{1}{\mathcal{Z}}\int DU\mathrm{Tr}_{sc}\{\delta_{ji}G^{aa}_{\beta\alpha}(x,x;U)\Gamma_{\alpha\beta}\}\mathrm{Tr}_{sc}\{\delta_{ij}G^{bb}_{\delta\gamma}(0,0;U)\bar{\Gamma}_{\gamma\delta}\} \\ &- \mathrm{Tr}_{sc}\{G^{ba}_{\delta\alpha}(0,x;U)\Gamma_{\alpha\beta}G^{ab}_{\beta\gamma}(x,0;U)\bar{\Gamma}_{\gamma\delta}\}\prod_f^{N_{sea}}\det M^f[U]e^{-S_G[U]} \\ &= \langle\mathrm{Tr}_{sc}\{\delta_{ji}G^{aa}_{\beta\alpha}(x,x;U)\Gamma_{\alpha\beta}\}\mathrm{Tr}_{sc}\{\delta_{ij}G^{bb}_{\delta\gamma}(0,0;U)\bar{\Gamma}_{\gamma\delta}\}\rangle_U \\ &- \langle\mathrm{Tr}_{sc}\{G^{ba}_{\delta\alpha}(0,x;U)\Gamma_{\alpha\beta}G^{ab}_{\beta\gamma}(x,0;U)\bar{\Gamma}_{\gamma\delta}\}\rangle_U \end{aligned}$$

where the trace is over the spin and colour indices only and $\langle\rangle_U$ denotes integration over the gauge fields U which have been weighted appropriately with $\frac{1}{\mathcal{Z}}\prod_f^{N_{sea}}\det M^f[U]e^{-S_G[U]}$ where N_{sea} is the number of quark masses in our simulation. $G^{ab}_{\beta\gamma}(x,0;U)$ is the quark propagator evaluated on each gauge configuration. The third and fifth lines in equation (3.16) contain a delta function

of the quark flavours and hence these terms only contribute when the operator (3.13) is constructed using two quarks with the same flavour. For a flavour singlet operator the two point function (3.16) will consist of a connected piece and a disconnected piece (See figure 3.1 (left)). The quark propagator is dependent on both the quark fields and the gauge field and therefore must be calculated on each configuration. The disconnected piece requires the calculation of an all-to-all propagator, $G(x, x; U)$. This is computationally very costly and hence in most calculations the disconnected piece is ignored. For flavour non-singlet mesons the disconnected piece is not present.

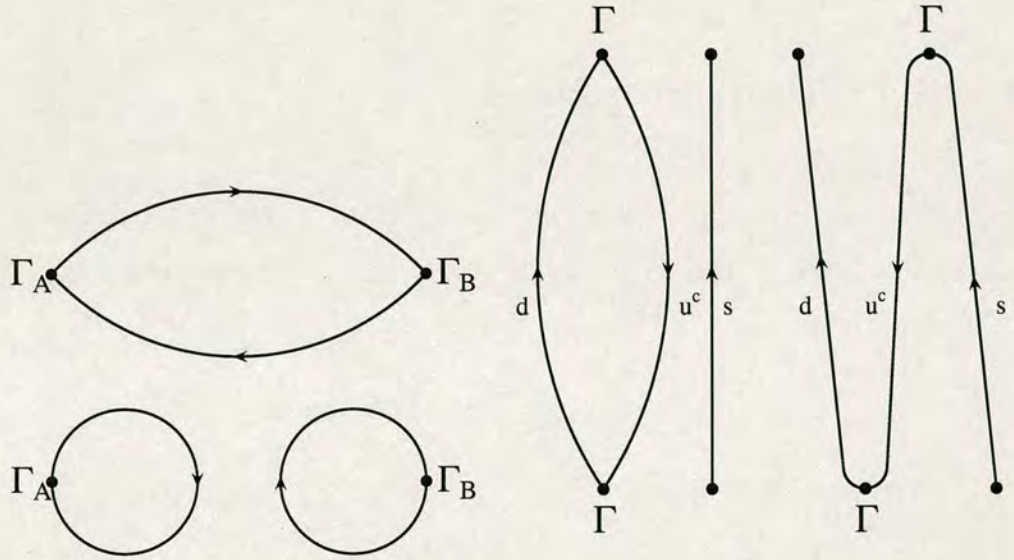

Figure 3.1: **LEFT:** Connected and disconnected meson correlator contractions formed by taking the trace over spin and colour indices. Each line represents a quark propagator and the dots denote the insertion points for the Dirac gamma matrices. **RIGHT:** Two different types of contractions for baryon correlators.

In the case where we neglect the disconnected term in equation (3.16) we must still compute two point-to-all propagators: one for the quark $(0 \to x)$ and one for the antiquark $(x \to 0)$, given by $G(0, x; U)$ and $G(x, 0; U)$ respectively (see equation(3.4)). This can be simplified by using the hermiticity of the quark

propagator

$$G^{ab}_{\beta\gamma}(0,x;U) = (\gamma_5)_{\beta\eta} G^{\dagger ab}_{\eta\rho}(x,0;U)(\gamma_5)_{\rho\gamma} \tag{3.17}$$

where the adjoint is defined with respect to the spinor and colour indices which allows us to rewrite equation (3.16) in terms of one propagator

$$C_{MM}(x;0) = -\langle \mathrm{Tr}_{sc}\{\gamma_5 G^\dagger(x,0;U)\gamma_5 \Gamma G(x,0;U)\bar{\Gamma}\}\rangle_U \tag{3.18}$$

where the indices have been suppressed for clarity. This means we require one inversion of the fermion matrix per configuration for degenerate quarks.

3.4 Hadron masses

Although we have derived the form of the two point function for a generic meson the extraction of the meson masses is worthy of some comment. Defining the delta functions

$$\delta_{\vec{x}\vec{x}'} = \frac{1}{N^3}\sum_{\vec{p}} e^{i\vec{p}.(\vec{x}-\vec{x}')} \tag{3.19}$$

$$\delta_{\vec{p}\vec{p}'} = \frac{1}{N^3}\sum_{\vec{x}} e^{i\vec{x}.(\vec{p}-\vec{p}')} \tag{3.20}$$

and the Fourier transform of a function $f(\vec{x},t)$ as

$$f(\vec{x},t) = \frac{1}{N^3}\sum_{\vec{p}} f(\vec{p},t)e^{i\vec{x}.\vec{p}} \tag{3.21}$$

$$f(\vec{p},t) = \sum_{\vec{x}} f(\vec{x},t)e^{-i\vec{p}.\vec{x}} \tag{3.22}$$

where periodic spatial boundary conditions mean the momentum is quantised in units of $ap_i = \frac{2\pi n_i}{L}$, $i = 1,2,3$, where $n_i = 0,\ldots N-1$ is an integer and $L = Na$ the spatial extent of the lattice. The momenta, due to the introduction of the lattice, are restricted to the Brillouin zone $[0, \frac{2\pi}{a}]$. An equivalent formulation is to restrict the momenta to $[-\frac{\pi}{a}, \frac{\pi}{a}]$. The discrete Fourier transform is used to

project out the momentum. Taking $t > 0$ and the discrete Fourier transform of equation (3.15)

$$\begin{aligned} C_{MM}(\vec{p}, t; \vec{0}, 0) &= \sum_{\vec{x}} C_{MM}(\vec{x}, t) e^{-i\vec{x}.\vec{p}} \\ C_{MM}(\vec{p}, t; \vec{0}, 0) &= \sum_{\vec{x}} \langle 0|\Theta_M(x)\bar{\Theta}_M(0)|0\rangle e^{-i\vec{x}.\vec{p}} \end{aligned} \tag{3.23}$$

and then inserting a complete set of eigenstates of the Hamiltonian

$$\hat{1} = \frac{1}{N^3} \sum_{n,\vec{q}} \frac{1}{2E_n(\vec{q})} |n, \vec{q}\rangle\langle n, \vec{q}| \tag{3.24}$$

normalised for a lattice of finite spatial extent as

$$\langle m, \vec{q}|n, \vec{p}\rangle = 2E_n(\vec{p}) N^3 \delta_{mn} \delta_{\vec{q},\vec{p}} \tag{3.25}$$

gives

$$C_{MM}(\vec{p}, t; \vec{0}, 0) = \sum_{n,\vec{q},\vec{x}} \frac{e^{-i\vec{p}.\vec{x}}}{2E_n(\vec{q})N^3} \langle 0|\Theta_M(x)|n, \vec{q}\rangle\langle n, \vec{q}|\bar{\Theta}_M(0)|0\rangle. \tag{3.26}$$

Applying the translation operator ζ,

$$\Theta(x) = e^{(Ht - i\vec{Q}.\vec{x})}\Theta(0)e^{-(Ht - i\vec{Q}.\vec{x})} = e^{\zeta}\Theta(0)e^{-\zeta} \tag{3.27}$$

where H and Q are the lattice Hamiltonian and three momentum respectively to equation (3.26) gives

$$C_{MM}(\vec{p}, t) = \sum_{n,\vec{q},\vec{x}} \frac{e^{-i\vec{p}.\vec{x}}}{2E_n(\vec{q})N^3} \langle 0|e^{(Ht - i\vec{Q}.\vec{x})}\Theta_M(0)e^{-(Ht - i\vec{Q}.\vec{x})}|n, \vec{q}\rangle\langle n, \vec{q}|\bar{\Theta}_M(0)|0\rangle. \tag{3.28}$$

Noting that

$$e^{-Ht}|n, \vec{q}\rangle = e^{-E_n t}|n, \vec{q}\rangle \tag{3.29}$$

where $E_n(\vec{q})$ is the energy eigenvalue of the state $|n, \vec{q}\rangle$ and equivalently

$$e^{i\vec{Q}.\vec{x}}|n, \vec{q}\rangle = e^{i\vec{q}.\vec{x}}|n, \vec{q}\rangle \tag{3.30}$$

equation (3.28) becomes

$$C_{MM}(\vec{p}, t) = \sum_{n,\vec{q},\vec{x}} \frac{e^{-E_n t} e^{-i(\vec{p}-\vec{q}).\vec{x}}}{2E_n(\vec{q})N^3} \langle 0|\Theta_M(0)|n, \vec{q}\rangle\langle n, \vec{q}|\bar{\Theta}_M(0)|0\rangle. \tag{3.31}$$

Substituting for the delta function (3.19) and performing the sum over $\vec{q}$

$$C_{MM}(\vec{p},t) = \sum_n \frac{e^{-E_n t}}{2E_n(\vec{p})} \left|\langle 0|\Theta_M(0)|n,\vec{p}\rangle\right|^2 . \tag{3.32}$$

Considering this equation at zero momentum

$$C_{MM}(\vec{0},t) = \sum_n A_n e^{-m_n t} \tag{3.33}$$

where

$$A_n = \frac{Z^2}{2m_n} = \frac{\left|\langle 0|\Theta_M(0)|n,\vec{0}\rangle\right|^2}{2m_n} \tag{3.34}$$

and allows the extraction of the masses of the states. The ground state mass of the particles and matrix elements with the ground state can be obtained by looking at the large time exponential decay of the time sliced correlator at zero momentum

$$\lim_{t\to\infty} C_{MM}(\vec{0},t) \to A_0 e^{-m_0 t}. \tag{3.35}$$

The matrix elements obtained from A_0 will are required in order to evaluate pseudoscalar decay constants discussed in section 3.11.

As we have a finite volume which is anti-periodic in time equation (3.27) is replaced with

$$\Theta(x) = e^{(Ht - i\vec{Q}.\vec{x})}\Theta(0)e^{-(H(T-t) - i\vec{Q}.\vec{x})} \tag{3.36}$$

where T is the time extent of the lattice. We now have a backward propagating state and the two-point function is properly given by

$$\lim_{t\to\infty} C_{MM}(\vec{0},t) \to C_0 \left[e^{-m_0 t} + \sigma_1\sigma_2 e^{-m_0(T-t)}\right] \tag{3.37}$$

where the factor $\sigma_1\sigma_2$ depends on the time reversal symmetry of the two operators in the correlation function. The time reversal symmetry of operators is discussed further in section 3.5 and the values are given in table 3.1. In order to extract masses and matrix elements from the correlators the function (3.37) is fitted to the correlators. For example, in the case of a pseudoscalar, $\eta_1\eta_2 = 1$ and $C_{MM}(\vec{0},t)$ is given by

$$C_{MM}(\vec{0},t) \to 2C_0 e^{-\frac{m_0 T}{2}} \cosh\left[m_0\left(\frac{T}{2} - t\right)\right]. \tag{3.38}$$

3.5 Interpolating operators for mesons

In section 3.3 the general two point correlation function for mesons was derived using a generic operator $\Theta_M(x)$. There is no unique correspondence between particle states and operators so all we require is that the operator have non-zero overlap with the state in question. This can be achieved by requiring the operator to have the same flavour content and same J^{PC} quantum numbers as the state in question where J is the total angular momentum and P and C correspond to the operators symmetry under parity and charge conjugation respectively.

Considering the general two point correlator

$$\begin{aligned} C^{BA}(\vec{p},t) &= \sum_{\vec{x}} e^{-i\vec{p}.\vec{x}} \langle \bar{\psi}_2(x)\Gamma_B\psi_1(x)\bar{\psi}_1(0)\Gamma_A\psi_2(0)\rangle_U \\ &= -\sum_{\vec{x}} e^{-i\vec{p}.\vec{x}} \langle \mathrm{Tr}(G_2(0,x;U)\Gamma_B G_1(x,0;U)\Gamma_A) b\rangle_U \end{aligned} \tag{3.39}$$

we wish to address the possible physical states that may be obtained. The transformation properties of the gamma matrices Γ_A and Γ_B under the discrete symmetries given by equations (3.5-3.9) allows us to deduce whether the correlator is even or odd in its time variable, even or odd in its momenta, how it behaves under charge conjugation and whether the correlator is real or imaginary.

For each element of the Dirac algebra, Γ_A, we define signs, σ, depending on its transformation property under the discrete symmetries associated with $\mathcal{T}$, $\mathcal{P}$, $\mathcal{C}$ and $\mathcal{CPH}$

$$\gamma_4\gamma_5\Gamma_A\gamma_5\gamma_4 = \sigma_A^{\mathcal{T}}\Gamma_A \tag{3.40}$$

$$\gamma_4\Gamma_A\gamma_4 = \sigma_A^{\mathcal{P}}\Gamma_A \tag{3.41}$$

$$\gamma_4\gamma_2\Gamma_A^T\gamma_2\gamma_4 = \sigma_A^{\mathcal{C}}\Gamma_A \tag{3.42}$$

$$C\gamma_4\gamma_5\Gamma_A\gamma_5\gamma_4 C^{-1} = \sigma_A^{\mathcal{CPH}}\Gamma_A^* \tag{3.43}$$

in analogy with equations (3.5-3.9). The particular values of the σ's for the different Γ matrices are presented in table 3.1.

	1	γ_i	γ_4	$\gamma_i\gamma_j$	$\gamma_i\gamma_4$	$\gamma_i\gamma_5$	$\gamma_4\gamma_5$	γ_5
$\sigma_A^{\mathcal{T}}$	+	+	-	+	-	-	+	-
$\sigma_A^{\mathcal{P}}$	+	-	+	+	-	+	-	-
$\sigma_A^{\mathcal{C}}$	+	-	+	-	-	+	+	+
$\sigma_A^{\mathcal{CPH}}$	+	-	+	+	-	+	-	-

Table 3.1: Signs describing the transformation for particular choices of gamma matrices under the discrete transformations $\mathcal{T}$, $\mathcal{P}$, $\mathcal{C}$ and $\mathcal{CPH}$.

The above discussion implies the following for equation (3.39)

- if $\sigma_A^{\mathcal{T}}\sigma_B^{\mathcal{T}} = \pm 1$ $C^{BA}(\vec{p},t)$ is even(odd) in t
- if $\sigma_A^{\mathcal{P}}\sigma_B^{\mathcal{P}} = \pm 1$ $C^{BA}(\vec{p},t)$ is even(odd) in $\vec{p}$
- if $\sigma_A^{\mathcal{C}}\sigma_B^{\mathcal{C}} = \pm 1$ $C^{BA}(\vec{p},t)$ is even(odd) under C-parity
- if $\sigma_A^{\mathcal{CPH}}\sigma_B^{\mathcal{CPH}} = \pm 1$ $C^{BA}(\vec{p},t)$ is real (imaginary).

This allows us to select operators having the same J^{PC} numbers as the physical states we wish to measure. Table 3.2 lists some possible choices for the interpolating operators.

3.6 Interpolating operators for baryons

Relativistic baryon operators involve the charge conjugation matrix, $C = \gamma_4\gamma_2$, which has the properties

$$C^\dagger = C^{-1} = C^T = -C \tag{3.44}$$

$$C\gamma_\mu C^{-1} = -\gamma_\mu^T \tag{3.45}$$

Bilinear	J^{PC}	Operator(s)	meson state (MeV)
Scalar (S)	0^{++}	$\bar{\psi}^{q_1}(x)\psi^{q_2}(x)$	$a_0(980)$
	0^{+-}	$\bar{\psi}^{q_1}(x)\gamma_4\psi^{q_2}(x)$	
Pseudoscalar (PS)	0^{-+}	$\bar{\psi}^{q_1}(x)\gamma_5\psi^{q_2}(x)$	$\pi(140), K(490)$
		$\bar{\psi}^{q_1}(x)\gamma_4\gamma_5\psi^{q_2}(x)$	
Vector (V)	1^{--}	$\bar{\psi}^{q_1}(x)\gamma_i\psi^{q_2}(x)$	$\rho(770), K^*(892), \phi(1020)$
		$\bar{\psi}^{q_1}(x)\gamma_i\gamma_4\psi^{q_2}(x)$	
Axial (A)	1^{++}	$\bar{\psi}^{q_1}(x)\gamma_i\gamma_5\psi^{q_2}(x)$	$a_1(1260)$
Tensor (T)	1^{+-}	$\bar{\psi}^{q_1}(x)\gamma_i\gamma_j\psi^{q_2}(x)$	$b_1(1235)$

Table 3.2: Quark bilinear interpolating operators describing meson states.

so that the spinors transform as

$$\psi \to \psi^C = \eta_C C\bar{\psi}^T \tag{3.46}$$

$$\bar{\psi} \to \bar{\psi}^C = \eta_C^* \psi^T C \tag{3.47}$$

with η_C an unobservable phase. Baryons are then constructed from operators of the form

$$B_{\Gamma,k,\delta}(x) = \epsilon_{abc}\left(\left(\bar{\psi}^C_{i,\alpha}(x)\right)^a \Gamma^{\alpha\beta}\psi^b_{j,\beta}(x)\right)\psi^c_{k,\delta}(x) \tag{3.48}$$

where i, j, k label the flavours, a, b, c label the colours, and α, β, δ are Dirac indices. To describe the baryons these operators must have a non-vanishing overlap with the baryon states. This requires them to have the same quantum numbers as the baryon states and to transform correctly under Lorentz and parity transformations. The baryon operators (3.48) are colour singlets and have one free spinor index necessary for describing spin-$\frac{1}{2}$ octet and spin-$\frac{3}{2}$ decuplet baryons. The basic interpolating operators used to describe the octet and decuplet baryons are given in table 3.3. Appendix B shows for the nucleon operator, $N_{1,\alpha}$, why

Channel	Operator	$I(J^P)$	Lightest state(s)(MeV)
Nucleon	$N_{1,\alpha} = \epsilon_{abc}\left(u^{a,T}C\gamma_5 d^b\right)u^c_\alpha$ $N_{2,\alpha} = \epsilon_{abc}\left(u^{a,T}C\gamma_4\gamma_5 d^b\right)u^c_\alpha$	$\frac{1}{2}(\frac{1}{2}^{\pm})$	N(940),N(1535)
Delta-$\frac{3}{2}$	$\Delta^{3/2}_{i,\alpha} = \epsilon_{abc}\left(u^{a,T}C\gamma_i u^b\right)u^c_\alpha$	$\frac{3}{2}(\frac{3}{2}^{\pm})$	$\Delta(1232), \Delta(1700)$
Delta-$\frac{1}{2}$	$\Delta^{1/2}_{4,\alpha} = \epsilon_{abc}\left(u^{a,T}C\gamma_4 u^b\right)u^c_\alpha$	$\frac{3}{2}(\frac{1}{2}^{\pm})$	$\Delta(1750), \Delta(1900)$

Table 3.3: Three quark interpolating operators describing baryons and their relationship to the lightest particle states. The flavour content of the quarks has been made explicit.

this is a good choice of operator to describe the nucleon(proton) state by considering some of its symmetry transformation properties. In order to get the flavour symmetry of the operators correct it is necessary to take linear combinations of these operators, for example, the nucleon operator is given by (up to some normalisation)

$$B_{N,\alpha}(x) = (d^{T,a}(x)C\gamma_5 u^b)d^c_\alpha(x)\epsilon_{abc} + (d^{T,a}(x)C\gamma_5 d^b)u^c_\alpha(x)\epsilon_{abc} \tag{3.49}$$

which is antisymmetric under interchange of the first two quarks. Details of how to construct the appropriate linear combinations for the other octet and decuplet baryon states can be found in [8, 59, 60, 10, 61]. The baryon operators given in table 3.3 do not have a definite parity. They couple to both the negative and positive parity states, transforming under parity as

$$\mathcal{P}B_{\Gamma,k,\delta}(x_4,\vec{x})\mathcal{P} = \gamma_4 B_{\Gamma,k,\delta}(x_4,-\vec{x}). \tag{3.50}$$

Given the representation of $\gamma_4 = \mathrm{diag}(1,1,-1,-1)$, this shows that the upper two spinor components of B transform with positive parity while the lower two transform with negative parity. These states can be projected out using the projection operators

$$P_\pm = \frac{1}{2}(1 \pm \gamma_4). \tag{3.51}$$

The delta baryon operator

$$D_{\gamma_\mu,\alpha}(x) = (u^{T,a}(x)C\gamma_\mu u^b)u^c_\alpha(x)\epsilon_{abc} \tag{3.52}$$

couples to the spin-$\frac{1}{2}$ and spin-$\frac{3}{2}$ states. To obtain an operator to represent the spin-$\frac{3}{2}$ decuplet baryon only the spin-$\frac{3}{2}$ part of the operator must be projected out. This is carried out by noticing that the operator with $\gamma_\mu = \gamma_4$ projects onto a pure spin-$\frac{1}{2}$ state. Appendix D gives details of the construction of these projection operators. The spin-$\frac{3}{2}$ correlators are constructed by averaging over the correlators constructed from the operators with the three spatial gamma matrices, γ_i, and then subtracting the appropriate spin-$\frac{1}{2}$ correlator

$$C_{\Delta^{3/2}\bar{\Delta}^{3/2}}(t) = \frac{1}{3}\sum_i C_{\Delta_i\bar{\Delta}_i} - \frac{1}{3}C_{\Delta_4\bar{\Delta}_4}. \tag{3.53}$$

This is performed after the projection onto a state of definite parity. As the delta baryon operator is symmetric under interchange of any two quarks (as $(C\gamma_\mu)^T = C\gamma_\mu$) it can be used to study the Δ, Σ^*, Ξ^* and Ω baryons by using non-degenerate combinations of quark flavours. Further details of this can be found in [59, 10].

3.7 Baryon correlation functions

Once a choice of baryon operator has been made the construction of the baryon correlators follows in a similar manner to that of the mesons (see section 3.3). Appendix C gives an example baryon correlator calculation in the case of a nucleon(proton). The correlator contractions for the spin-$\frac{1}{2}$ octet can be split into two types. These are denoted 'Σ like' and 'Λ like'. The '$\Sigma(\Lambda)$ like' correlators correspond to the wave function of the state being symmetric(antisymmetric) in u and d quark flavours. These correlators can be written in terms of two contractions. The u and d quarks could be contracted into a closed loop while the

propagator for the s quark carries the spin quantum numbers of the baryon or there could be an ordered contraction of three quarks. These are depicted in figure 3.1(right). On calculating the correlation function for a 'Σ like' correlator the other 'Σ like' correlators: the proton, neutron, Σ^+, Σ^-, Ξ^0 and Ξ^- may be obtained by appropriate substitution of quark flavours. Similar considerations may be applied for decuplet baryon correlation functions [10].

In section 3.4 the functional form of a meson two-point correlator was calculated. The functional form of the baryon two-point correlator is more complicated as the baryon operators couple to states of both positive and negative parity and the fermionic states have a spin degree of freedom, s. In analogy with section 3.4 using a similar notation to that found in [62] the states are defined as $|n, \vec{p}, s, P\rangle$ where n labels the distinct mass states as in the mesonic case, $\vec{p}$ the momentum, s the spin and P the parity: either $+$ or $-$. With this nomenclature the forward propagating states at zero three momentum can be factorised as

$$\langle 0|N^i_\sigma(0)|n, \vec{p}, s, P\rangle = C^{N^i}_P u_\sigma(M^P_n, \vec{p}, s) \tag{3.54}$$

$$\langle 0|\Delta^j_\sigma(0)|n, \vec{p}, s, P\rangle = C^{\Delta}_P u_{\sigma,j}(M^P_n, \vec{p}, s) \tag{3.55}$$

for spin-$\frac{1}{2}$ and spin-$\frac{3}{2}$ respectively. For spin-$\frac{1}{2}$ $i \in \{1, 2\}$, while for spin-$\frac{3}{2}$ j runs over the three spatial indices. $u_\sigma(p, s)$ and $u_{\sigma,j}(p, s)$ are Dirac and Rarita-Schwinger [63] polarisation spinors respectively. The backward propagating anti-particle states can be related to the above results by charge conjugation. The asymptotic form of the baryon two-point correlator

$$C_{B\bar{B}}(t) = \sum_{\vec{x}} \langle 0|B(\vec{x}, t)\bar{B}(0)|0\rangle \tag{3.56}$$

then follows from inserting a complete set of states (as in section 3.4) and performing the spin sum over the Dirac or Rarita-Schwinger spinors [64] at zero three momentum given by

$$\sum_s u(\vec{0}, s)\bar{u}(\vec{0}, s) = \frac{1}{2}(1 + \gamma_4) \tag{3.57}$$

$$\sum_s u_j(\vec{0},s)\bar{u}_j(\vec{0},s) = \frac{2}{3}.\frac{1}{2}(1+\gamma_4). \tag{3.58}$$

The asymptotic form of the two-point correlator is given by

$$\begin{aligned} C_{B\bar{B}}(t) \overset{T,t\to\infty}{\to} & (1+\gamma_4)\left[D_{B^+}e^{-M_{B^+}t} + D_{B^-}e^{-M_{B^-}(T-t)}\right] \\ + & (1-\gamma_4)\left[D_{B^+}e^{-M_{B^+}(T-t)} + D_{B^-}e^{-M_{B^-}t}\right] \end{aligned} \tag{3.59}$$

where $B = N_1, N_2$ or Δ. The positive and negative parity contributions to the correlator can then be projected out using the projection operator (3.51) to give

$$C^{\pm}_{B\bar{B}}(t) = \mathrm{Tr}(P_{\pm}C_{B\bar{B}}(t)) \overset{T,t\to\infty}{\to} D_{B^{\pm}}e^{-M_{B^{\pm}}t} + D_{B^{\mp}}e^{-M_{B^{\mp}}(T-t)}. \tag{3.60}$$

Unlike the meson two-point function case there is no time reflection symmetry, as the forward and backward propagating exponentials are dependent on different mass values. The positive and negative parity correlators for baryon are related by

$$C^{+}_{B\bar{B}}(t) = -C^{-}_{B\bar{B}}(T-t). \tag{3.61}$$

3.8 Effective mass plots

In order to decide where the ground state dominates the sum (3.35) it is often useful to examine effective mass plots. The effective masses for mesons and baryons are defined in terms of the averaged timesliced correlator (3.95) by

$$m^{\mathrm{eff}}_{\mathrm{meson}}(t) = \cosh^{-1}\left[\frac{C(t-1)+C(t+1)}{2C(t)}\right], \tag{3.62}$$

$$m^{\mathrm{eff}}_{\mathrm{baryon}}(t) = \ln\left[\frac{C(t+1)}{C(t)}\right]. \tag{3.63}$$

These functions should plateau as t increases. The onset of the plateau gives an indication as to where the contribution from the excited states has decayed away and therefore the interval over which to fit for the groundstate.

3.9 Smearing

The previous sections have shown how meson and baryon functions may be created from quark propagators. The operators used to make the correlation functions were required to have a non-zero overlap with the state to be measured, i.e. have the correct J^{PC} quantum numbers. Increasing the overlap of these operators is a way of improving the signal from the data. In equations(3.37) and (3.60) the correlator was written as a sum of exponentials and the ground state was extracted from the behaviour at large Euclidean times. Enhancing the signal of the ground state relative to the first excited state by increasing the ground state amplitude (and decreasing the excited state amplitude) has the benefit that the ground state will dominate the sum at smaller Euclidean times and give a better signal to noise ratio.

A standard procedure for increasing the contribution from a state involves modifying some or all of the fermion fields in the operator by convolving the quark field at the source or sink (or both) with an appropriate smearing function

$$\psi_S(\vec{x},t) \rightarrow \sum_{\vec{y}} \Upsilon(\vec{x},\vec{y},t)\psi(\vec{y},t), \quad \bar{\psi}_S(\vec{x},t) \rightarrow \sum_{\vec{y}} \bar{\psi}(\vec{y},t)\Upsilon^{\dagger}(\vec{y},\vec{x},t) \tag{3.64}$$

where the smearing function, Υ, at source and sink need not necessarily be the same. The smearing function may depend on the gauge configuration and is usually chosen in such a way as to model the spatial distribution of the wavefunction of the state to be measured as the mesons and baryons themselves are actually extended objects. This modifies the quark propagators constructed from these quark fields. The quark propagator smeared at source is given by

$$\begin{aligned} G_U^{SL}(x_4,\vec{x};y_4,\vec{y}) &= \frac{1}{\mathcal{Z}}\int D\bar{\psi}D\psi\psi(x_4,\vec{x})\bar{\psi}_S(y_4,\vec{y})e^{-S_F[\psi,\bar{\psi},U]} \\ &= \sum_{\vec{z}} G(x_4,\vec{x};y_4,\vec{z})\Upsilon^{\dagger}(\vec{y},\vec{z},y_4) \end{aligned} \tag{3.65}$$

where $G(x_4,\vec{x};y_4,\vec{y})$ is the usual local quark propagator (given by equation (3.4)) and the subscript U indicates that this is evaluated on each gauge configuration.

The dependence of the smearing function on the gauge configuration is implicit. The sink-smeared quark propagator is given by

$$\begin{aligned} G_U^{LS}(x_4, \vec{x}; y_4, \vec{y}) &= \frac{1}{\mathcal{Z}} \int D\bar{\psi} D\psi \psi_S(x_4, \vec{x}) \bar{\psi}(y_4, \vec{y}) e^{-S_F[\psi, \bar{\psi}, U]} \\ &= \sum_{\vec{z}} \Upsilon(\vec{x}, \vec{z}, x_4) G(x_4, \vec{z}; y_4, \vec{y}) \end{aligned} \tag{3.66}$$

and smearing can of course be done at both source and sink

$$\begin{aligned} G_U^{SS}(x_4, \vec{x}; y_4, \vec{y}) &= \frac{1}{\mathcal{Z}} \int D\bar{\psi} D\psi \psi_S(x_4, \vec{x}) \bar{\psi}_S(y_4, \vec{y}) e^{-S_F[\psi, \bar{\psi}, U]} \\ &= \sum_{\vec{z}} \Upsilon(\vec{x}, \vec{z}, x_4) G^{SL}(x_4, \vec{z}; y_4, \vec{y}). \end{aligned} \tag{3.67}$$

This allows the smeared propagators to be derived from the local propagator $G(x_4, \vec{x}; y_4, \vec{y})$. In most practical cases the source is constructed on a single timeslice and it is therefore computationally cheaper to perform source smearing than sink smearing which requires smearing at every annihilation point. It is observed in general that the signal from timesliced correlators constructed from propagators smeared at source are less noisy than those constructed from propagators smeared at sink. The smearing functions used in this work are wall smeared sources [65] and hydrogen-like wavefunction smeared sources [66, 67].

Recall in equation (3.4) we restricted ourselves to the case of requiring the elements of G with a fixed space-time source at the origin. Having used iterative solver methods to obtain the local quark propagator the sink-smeared propagator can be obtained by simply convolving the local propagator with the smearing function as in equation (3.66). The source-smeared case is not as simple as from equation (3.65) the propagator $G(x_4, \vec{z}; y_4, \vec{z})$ is required for all relevant $\vec{z}$. Rather than create an all-to-all propagator, which is computationally expensive, it is more efficient to replace the point source with a smeared source in equation (3.4) and solve the matrix equation

$$M(x, y; U) G^{SL}(y, 0; U) = \Upsilon^{\dagger}(x_4, \vec{x}, \vec{0}) \tag{3.68}$$

using iterative methods. The spin and colour indices have been dropped for clarity. Having done this the SS propagator can be obtained by convolution with the smearing function using equation (3.67). Source and sink smeared correlators for the mesons and baryons can then be constructed by replacing some of the local-local propagators in equations (3.18) and (C.29) with smeared ones.

3.10 Renormalisation

In the specific case of calculating matrix elements on the lattice the result will depend on the lattice spacing a. However, any physical result should not depend on the value of the lattice spacing chosen. Therefore the bare parameters in the theory must be redefined in such a way that the results remain finite as the lattice spacing is removed. The renormalised operator $\mathcal{O}_R$ is defined through a rescaling of the bare operator $\mathcal{O}$ by

$$\mathcal{O}_R(\mu) = Z_{\mathcal{O}}(a\mu)\mathcal{O}(a) \tag{3.69}$$

such that the renormalised matrix element remains finite in the limit $a \to 0$. The a dependence of the operator is absorbed into the renormalisation constant $Z_{\mathcal{O}}$. The renormalised operator will depend on the scale μ which was introduced into the theory in order to keep the results dimensionally correct.

For certain operators symmetry arguments lead to simplifications that allow non-perturbative evaluation of some renormalisation constants through the use of Ward identities. The renormalisation constant Z_A, which is required in the calculation of the pseudoscalar decay constant in section 3.11, is one such constant.

The continuum chiral symmetry for n_f flavours of degenerate quarks

$$\psi(x) \to e^{i\alpha_a T^a \gamma_5}\psi(x) \quad \bar{\psi}(x) \to \bar{\psi}(x)e^{i\alpha_a T^a \gamma_5} \tag{3.70}$$

where T^a is the generator of the flavour symmetry group $SU(n_f)$ leads to the

axial Ward identity

$$Z_A\langle\partial_\mu A^a_\mu\Omega\rangle = 2Z_m m_q Z_P\langle P^a\Omega\rangle \tag{3.71}$$

where $A^a_\mu = \bar{\psi}\gamma_\mu\gamma_5 T^a\psi$ and $P^a = \bar{\psi}\gamma_5 T^a\psi$ are the local axial and pseudoscalar currents respectively, m_q is the bare quark mass and Z_A, Z_P and Z_m are their respective renormalisation constants.

Denoting the scalar current $S^a = \bar{\psi}T^a\psi$ and noting that a mass term of the form $m\bar{\psi}\psi$ in the Lagrangian must be renormalisation group invariant means that $Z_m^{-1} = Z_S$ where Z_S is the renormalisation constant for the scalar current. The scalar and pseudoscalar currents are in the same chiral multiplet. This can be seen by applying the infinitesimal chiral transformation

$$\delta\psi = i\alpha_b T^b\gamma_5\psi, \quad \delta\bar{\psi} = \bar{\psi}iT^b\alpha_b\gamma_5 \tag{3.72}$$

to the scalar and pseudoscalar currents which gives

$$\delta S^a = -if_{abc}\alpha_b P^c, \quad \delta P^a = -if_{abc}\alpha_b S^c. \tag{3.73}$$

As these currents transform as a doublet $Z_P = Z_S$. Substituting these relations into equation (3.71) and choosing the functional Ω to be the pseudoscalar operator allows the evaluation of Z_A

$$Z_A = \frac{2m_q\langle 0|P|P\rangle}{\langle 0|\partial_\mu A_\mu|P\rangle}. \tag{3.74}$$

On the lattice there is a weaker on-shell chiral symmetry (as described in section 2.9) given by

$$\psi(x) \to e^{i\alpha_a T^a\gamma_5(1-\frac{a}{2}\not{D})}\psi(x) \quad \bar{\psi}(x) \to \bar{\psi}(x)e^{i\alpha_a T^a(1-\frac{a}{2}\not{D})\gamma_5}. \tag{3.75}$$

In this case the Ward identity is given by

$$Z'_A\langle\partial_\mu A'^a_\mu\Omega\rangle = 2Z_m m_q Z'_P\langle P'^a\Omega\rangle \tag{3.76}$$

where A'^a_μ and P'^a are the lattice axial and pseudoscalar currents

$$A'^a_\mu = \bar{\psi}\gamma_\mu\gamma_5\left(1-\frac{a}{2}\not{D}\right)T^a\psi, \quad P'^a = \bar{\psi}\gamma_5\left(1-\frac{a}{2}\not{D}\right)T^a\psi. \tag{3.77}$$

It may be shown [68, 69] that the lattice currents transform under the lattice chiral symmetry (3.75) in the same way as their local counterparts transform in the continuum. The lattice infinitesimal chiral transformations corresponding to equation (3.75) are given by

$$\delta\psi = i\alpha_b T^b \gamma_5 \left(1 - \frac{a}{2}\not{\mathcal{D}}\right)\psi, \quad \delta\bar{\psi} = \bar{\psi} i T^b \alpha_b \left(1 - \frac{a}{2}\not{\mathcal{D}}\right)\gamma_5 \tag{3.78}$$

and with these transformations the scalar and pseudoscalar currents transform as

$$\delta S'^a = -i f_{abc} \alpha_b P'^c, \quad \delta P'^a = -i f_{abc} \alpha_b S'^c. \tag{3.79}$$

Therefore, as in the continuum case S and P transform as a doublet and $Z_{S'} = Z_{P'}$. It may be shown [68], up to lattice artefacts, that the lattice renormalisation constants coincide with their continuum counterparts and therefore even at finite lattice spacing $Z_S = Z_P$.

Finally, noting that the mass dependent term in the Lagrangian may be written in the form

$$m\bar{\psi}\left(1 - \frac{a}{2}\not{\mathcal{D}}\right)\psi \tag{3.80}$$

we have that $Z_m^{-1} = Z_S$ as in the continuum case. With these relations between the renormalisation constants, holding both in the continuum and at finite lattice spacing, it is possible to evaluate Z_A through equation 3.74.

3.11 Pseudoscalar decay constant

In semi-leptonic meson decays the scattering matrix can be factorised into a leptonic piece and a hadronic piece where the hadronic piece can be parameterised in terms of the momentum and decay constant. In this section three different methods to extract the pseudoscalar decay constant, f_{PS}, from combinations of two-point correlation functions will be outlined. The differences between the

methods lies in the correlator chosen to extract the relevant matrix element. The pseudoscalar decay constant is given by the equation

$$Z_A\langle 0|\bar{\psi}\gamma_4\gamma_5\psi|P(\vec{0})\rangle \equiv f_{PS}m_{PS} \tag{3.81}$$

where $\bar{\psi}$ and ψ are the Hilbert space quark operators, and m_{PS} is the pseudoscalar meson mass. With our normalisations the pseudoscalar decay constant, f_{PS}, is found experimentally to be approximately 130 MeV [70].

3.11.1 Method A: Evaluation of f_{PS} using the local pseudoscalar density correlator

In order to evaluate the pseudoscalar decay constant using only the pseudoscalar density correlator

$$C_{PP}(t) = \sum_{\vec{x}}\langle P^a(\vec{x},t)P^a(\vec{0},0)\rangle \tag{3.82}$$

we begin with the axial Ward identity

$$Z_A\partial_\mu A_\mu = 2Z_m m_q Z_P P \tag{3.83}$$

where $A_\mu = \bar{\psi}\gamma_\mu\gamma_5\psi$ and $P = \bar{\psi}\gamma_5\psi$. Inserting a complete set of states into equation (3.83), noting that $Z_m^{-1} = Z_P$ (see section 3.10), and considering only the temporal current (i.e. the zero momentum correlators) allows us to extract Z_A

$$Z_A = \frac{2m_q|\langle 0|P|P\rangle|}{m_{PS}|\langle 0|A_4|P\rangle|}. \tag{3.84}$$

Substituting for Z_A in equation (3.81) gives the following expression for f_{PS}

$$\begin{aligned} f_{PS}^{PP} &= \frac{2m_q|\langle 0|P|P\rangle||\langle 0|A_4|P\rangle|}{m_{PS}^2|\langle 0|A_4|P\rangle|} \\ f_{PS}^{PP} &= \frac{2m_q|\langle 0|P|P\rangle|}{m_{PS}^2}. \end{aligned} \tag{3.85}$$

The matrix element and mass required to evaluate the decay constant is obtained from fits to the pseudoscalar density correlator as described in section 5.11.1.

3.11.2 Z_A

For the remaining two methods of calculating f_{PS} an explicit calculation of the renormalisation constant Z_A in equation (3.81) is required. The renormalisation factor Z_A is found from comparing the amplitudes of two-point functions $C(t)$ and $L(t)$ defined as the correlators of the pseudoscalar density with the partially conserved and local axial currents respectively

$$C(t+\frac{1}{2}) = \sum_{\vec{x}} \langle \mathcal{A}_4(\vec{x},t) P(\vec{0},0) \rangle \tag{3.86}$$

$$L(t) = \sum_{\vec{x}} \langle A_4(\vec{x},t) P(\vec{0},0) \rangle \tag{3.87}$$

where $\mathcal{A}_\mu$ is the conserved axial current given in equation (2.127). The $\frac{1}{2}$ in the argument of $C(t+\frac{1}{2})$ comes from the fact that the conserved axial current $\mathcal{A}_\mu(x)$ is not the current at lattice site x but instead the current carried by the link between x and $x+\hat{\mu}$. Appropriate arithmetic averages are taken in order to account for the fact that $C(t+\frac{1}{2})$ and $L(t)$ are not at the same location. $Z_A(t)$ is defined as

$$Z_A = \frac{C(t+\frac{1}{2}) + C(t-\frac{1}{2})}{4L(t)} + \frac{C(t+\frac{1}{2})}{(L(t)+L(t+1))}. \tag{3.88}$$

For t suitably large the ratio $\frac{C(t)}{L(t)}$ behaves like a constant which can be identified with Z_A. Both of the terms in equation (3.88) estimate this value without $\mathcal{O}(a)$ errors. The average of these two terms, as in equation (3.88), further suppress $\mathcal{O}(a^2)$ lattice artifacts [35].

3.11.3 Method B: Evaluation of f_{PS} using the axial-axial correlator

This method requires the temporal (zero momentum) two-point local axial-axial current

$$C_{A_4A_4}(t) = \sum_{\vec{x}} \langle A_4^a(\vec{x},t) A_4^a(\vec{0},0) \rangle \tag{3.89}$$

where $A_4 = \bar{\psi}\gamma_4\gamma_5\psi$. Inserting a complete set of states and using the obtained renormalisation constant Z_A allows the evaluation of the pseudoscalar decay constant from

$$f_{PS}^{AA} = \frac{Z_A|\langle 0|A_4|P\rangle|}{m_{PS}}. \tag{3.90}$$

The matrix element and mass required to evaluate the decay constant is obtained from fits to the local axial-axial correlator as described in section 5.11.3.

3.11.4 Method C: Evaluation of f_{PS} using the local axial correlator

In this method we use a ratio of the two-point local axial current

$$C_{A_4P}(t) = \sum_{\vec{x}} \langle A_4^a(\vec{x}, t)P^a(\vec{0}, 0)\rangle \tag{3.91}$$

to the pseudoscalar density current (3.82). Given the renormalisation constant Z_A, considering only the temporal (zero momentum) currents and inserting a complete set of states in both equation (3.91) and (3.82) allows the evaluation of the pseudoscalar decay constant from

$$f_{PS}^{AP} = \frac{Z_A|\langle 0|P|P\rangle|}{m_{PS}} \times \frac{|\langle 0|A_4|P\rangle||\langle P|P|0\rangle|}{|\langle 0|P|P\rangle||\langle P|P|0\rangle|}. \tag{3.92}$$

Both the two-point local axial current and the pseudoscalar density current are required in order to extract the required matrix elements and masses from fits. This is described in section 5.11.4.

3.12 Fitting methods and statistical analysis

As discussed in section 2.14 the expectation value of some operator, $\mathcal{O}$, can be estimated by an average over an ensemble of gauge configurations and gives rise

to a set of correlation functions $C_k(t_i), k = 1, \ldots, N$ for an ensemble with N statistically independent configurations. The case of gauge configurations which are not statistically independent will be considered later. The large time behaviour of these correlation functions can be parameterised by some model function, $f(\vec{a}, t_i)$, where $\vec{a}$ is the set of parameters to be determined. Examples of these functions for mesonic and baryonic correlators are given in equations (3.37) and (3.60) respectively. The aim is to find the best fit between these model functions and the data. The standard procedure for doing this is to minimise the χ-squared function

$$\chi^2(a) = \sum_{i,j=1}^{N_D} \left(\bar{C}(t_i) - f(\vec{a}, t_i)\right) \Omega_{ij}^{-1} \left(\bar{C}(t_j) - f(\vec{a}, t_j)\right) \tag{3.93}$$

which depends on the model parameters, $\vec{a}$ and the N_D data points. The matrix, Ω, is the symmetric covariance matrix and can be estimated by

$$\Omega_{ij} = \frac{1}{N(N-1)} \sum_{k=1}^{N} \left(C_k(t_i) - \bar{C}(t_i)\right) \left(C_k(t_j) - \bar{C}(t_j)\right). \tag{3.94}$$

The covariance matrix describes the distribution of the data around the mean value

$$\bar{C}(t_i) = \frac{1}{N} \sum_{k=1}^{N} C_k(t_i). \tag{3.95}$$

The diagonal elements of the covariance matrix can be taken as estimates of the variances on the sample mean and are related to the standard errors on the means, σ_i, by

$$\sigma_i = \sqrt{\Omega_{ii}} \tag{3.96}$$

In this way the χ^2 function takes into account correlations in the data between different timeslices. The function χ^2 measures how closely the data resembles the model function. Indeed, when minimising the χ^2 function, a good fit to the data is indicated by a $\chi^2/\upsilon \sim 1$ where υ is the number of degrees of freedom, (N_D - number of fit parameters). Large values of χ^2/υ indicate a poor fit while small values can indicate that the errors in the data have been overestimated.

The fitted values are the parameter values which minimise the χ^2 function. In practice the correlation matrix

$$\rho_{ij} = \frac{\Omega_{ij}}{\sigma_i \sigma_j} \tag{3.97}$$

is used rather than the covariance matrix. This is more stable having $\rho_{ii} = 1$ and values between +1 for totally correlated data to -1 for totally anti-correlated data with $\rho_{ij} = 0$ being a necessary condition for the data at t_i and t_j to be statistically independent. The process of minimisation of the χ^2 function is implemented using an algorithm such as the Marquardt-Levenberg algorithm [71].

3.13 Error Estimation

The χ^2 minimisation technique gives a prescription for calculating the "best fit" values, however, an estimate of the error on these parameters is required. The bootstrap technique [72] is one such method. This involves constructing N_B sub-ensembles of N correlators including repetitions randomly selected from the set of N correlators. The mean of each sub-ensemble can then be calculated

$$\bar{C}^B(t_i) = \frac{1}{N} \sum_{j=1}^{N} C_j^B(t_i). \tag{3.98}$$

The χ^2 minimisation technique can then be applied in turn to each of the sub-ensembles of correlators. This results in a set of N_B parameter values, $(\vec{a}^B)_k$, $k = 1, \ldots, N_B$, which are distributed and hopefully peaked about the best parameter values from the fit to the full dataset. The mean value of the N_B parameter values can be estimated from

$$\bar{a}_i^B = \frac{1}{N_B} \sum_{j=1}^{N_B} a_{ji}^B \tag{3.99}$$

where the index i labels the parameter number, and the variance from

$$\left(\sigma^B(a_i)\right)^2 = \frac{1}{N_B - 1} \sum_{j=1}^{N_B} \left[a_{ji}^B - \bar{a}_i^B\right]^2. \tag{3.100}$$

The advantage of the bootstrap sampling method is that it does not assume any prior form for the distribution of the correlation functions. Therefore, in practice, a confidence level is defined. For a 68% confidence level the lower interval bound a_i^L is defined by 16% of the sub-ensemble parameter values a_{ji}^B being less than the lower interval bound, $a_{ji}^B < a_i^L$ and 16% being greater than the higher bound $a_{ji}^B > a_i^H$.

Another technique for estimating the error is Jackknife. This differs from the bootstrap method described above only in that N_J sub-ensembles are created by removing from each sub-ensemble one particular measurement (so each sub-ensemble has size $N-1$ where the full ensemble is made of N measurements). This is equivalent to removing the contribution from one gauge configuration to a correlator. The mean values for the data on sub-ensemble n is therefore written

$$\bar{C}_n^J(t_i) = \frac{1}{N_J - 1} \sum_{j \neq n} C_j(t_i). \tag{3.101}$$

3.14 Fitting functions of correlators

In some cases, the model function is a fit to some function of several correlator types. For example, the residual mass calculation in section 5.8 requires the ratio of two correlator types. It is worth noting at this point that in most cases when dealing with ratios we are interested in the ratio of the ensemble averages, not the ensemble average of the ratios

$$\frac{\langle \mathcal{A} \rangle}{\langle \mathcal{B} \rangle} \neq \left\langle \frac{\mathcal{A}}{\mathcal{B}} \right\rangle. \tag{3.102}$$

Consider the general case where we wish to model some function of n correlators, $D(t) = f(C_1(t), \ldots, C_n(t))$. The ensemble averages of these n correlators can be estimated using equation (3.95) giving an estimate for the function $D(t_i)$

$$\bar{D}(t_i) = f(\bar{C}_1(t), \ldots, \bar{C}_n(t)). \tag{3.103}$$

Minimisation of the χ^2 function requires a covariance matrix, Ω. However, in this case we no longer have an ensemble of correlators. The covariance matrix is estimated using a jackknife procedure by calculating $\bar{D}_m(t_i), m = 1, \ldots, N$ where one measurement m has been removed in turn. The jackknife estimate of the covariance matrix is then given by

$$\Omega_{ij} = \frac{(N-1)}{N} \sum_{m=1}^{N} \left(\bar{D}_m(t_i) - \bar{D}_\star(t_i)\right) \left(\bar{D}_m(t_j) - \bar{D}_\star(t_j)\right) \tag{3.104}$$

where

$$\bar{D}_\star(t_i) = \frac{1}{N} \sum_{m=1}^{N} \bar{D}_m(t_i) \tag{3.105}$$

is the average of $\bar{D}_m(t_i)$ over all the jackknife samples. Otherwise the error estimation and parameter extraction proceed as described above.

3.15 Fitting to bootstrapped data

In many situations, for example when performing chiral extrapolations, a fit where the data, $y(q_i)$, input to the fit are bootstrap sets, $y_b(q_i), b = 1, \ldots, N_B$, is required where b runs over the distinct bootstrap results. First the covariance matrix is estimated

$$\Omega_{ik} = \frac{1}{N_B - 1} \sum_{j=1}^{N_B} \left(a_{ji}^B - \bar{a}_i^B\right) \left(a_{jk}^B - \bar{a}_k^B\right) \tag{3.106}$$

and then the correlation matrix as in equation (3.97). The upper and lower confidence limits, $a^H(q_i)$ and $a^L(q_i)$, are then calculated using the bootstrap data at each q_i. The covariance matrix is finally estimated by

$$\rho_{ij} = \delta a(q_i) \Omega_{ij} \delta a(q_j) \tag{3.107}$$

where

$$\delta a(q_i) = \frac{1}{2} \left(a^H(q_i) - a^L(q_i)\right). \tag{3.108}$$

Best fit values for the model parameters are then determined in the usual way by minimising χ^2 for the data $y(q_i)$. The errors are estimated by fitting the model to the data from each bootstrap subset $y_b(q_i)$ to build up bootstrap distributions for the fit parameters. Confidence intervals are determined as usual.

3.16 Goodness of fit

Although the value of χ^2 gives an indication of the quality of the fit, i.e. how well the data is modelled by the function, another useful quantity is the Q value given by

$$Q\left(\frac{v}{2},\frac{\chi^2}{2}\right)=\frac{1}{\Gamma(\frac{v}{2})}\int_{\frac{\chi^2}{2}}^{\infty}e^{-t}t^{\frac{v}{2}-1}dt=\frac{\Gamma(\frac{v}{2},\frac{\chi^2}{2})}{\Gamma(\frac{v}{2})} \tag{3.109}$$

where Γ is the gamma function. The Q value is the probability that the value of χ^2 returned from the minimisation (assuming that the errors on the data are normally distributed) exceeds a particular χ^2 by chance. Low values of Q usually signify that the model function does not describe the data well or that the size of the errors are too small. However, if the errors on the data are not normally distributed very low values of Q do not necessarily signify a bad fit. Values of Q close to 1 indicate that the fit is perhaps too good or that the errors on the data have been overestimated. Ideally the value should be around $\frac{1}{2}$.

3.17 Statistically dependent data

Assuming that measurements, A, on each configuration of an ensemble are statistically independent, the sample average, $\overline{A}$, is given by equation (3.95). The sample average is an estimator of the ensemble average $\overline{\overline{A}}$ or mean value which is equal to the expectation value $\overline{\overline{A}}=\langle A\rangle$. Given a set of measurements on statistically independent configurations the sample average is normally distributed

around the mean value with variance

$$\sigma^2_{\overline{A}} = \frac{1}{N_{meas}-1}\left(\overline{A^2} - \overline{A}^2\right) \tag{3.110}$$

where N_{meas} is the sample size. This is a consequence of the central limit theorem [73]. This error estimate is too optimistic as in general subsequent configurations generated have some dependence on previous ones. Assuming for simplicity that $\overline{\overline{A}} = \langle A \rangle = 0$ then $\langle \overline{A} \rangle = \sum_{i=1}^{N_{meas}} \langle A_i \rangle = \langle A \rangle = 0$. The variance of this estimator is then given by

$$\sigma^2_{\overline{A}} = \langle \left(\overline{A} - \langle \overline{A} \rangle\right)^2 \rangle = \langle \overline{A}^2 \rangle = \frac{1}{N^2_{meas}} \sum_{i=1}^{N_{meas}} \sum_{j=1}^{N_{meas}} \langle A_i A_j \rangle \tag{3.111}$$

$$= \frac{1}{N^2_{meas}} \left\{ \sum_{i=1}^{N_{meas}} \langle A_i^2 \rangle + 2 \sum_{i=1}^{N_{meas}-1} \sum_{j=i+1}^{N_{meas}} \langle A_i A_j \rangle \right\} \tag{3.112}$$

$$= \frac{1}{N_{meas}} \langle A^2 \rangle \left\{ 1 + \frac{2}{N_{meas}} \sum_{k=1}^{N_{meas}} (N-k) \rho_A^{s=1}(k) \right\}, \tag{3.113}$$

where

$$\rho^{s=1}(k) = \frac{\Gamma_A^{s=1}(k)}{\Gamma_A(0)} = \frac{\langle A_k A_1 \rangle}{\langle A^2 \rangle}. \tag{3.114}$$

In equation (3.113) the factor of $(N-k)$ comes from a counting argument by noting that $\langle A_1 A_3 \rangle = \langle A_2 A_4 \rangle = \ldots \langle A_n A_{n+2} \rangle$ etc. $\Gamma_A(t)$ is the autocovariance given in equation (2.173). In terms of the autocorrelation the true variance of $\overline{A}$ can be shown to be [8, 74]

$$\sigma^2_{\overline{A}} \simeq \frac{2\tau_{int,A}}{N_{meas}} \left(\overline{A^2} - \overline{A}^2\right) \tag{3.115}$$

where $\tau_{int,A}$ is the integrated autocorrelation time defined in equation (2.171). This result tells us that on average $2\tau_{int,A}$ correlated measurements are needed to reduce the variance by the same amount as a single truly independent measurement. Correct error estimates on statistically dependent configurations can therefore be made by scaling the errors calculated by the appropriate factor of the integrated autocorrelation time. A second method for dealing with configurations which are not statistically independent will be outlined in section 5.3.

Chapter 4

Mixed Actions

4.1 Introduction

In this chapter mixed actions will be defined and some of the motivation for using mixed actions will be discussed. The implications of simulating QCD using mixed actions will be considered. In the mixed action framework a method for matching the valence quark mass to the sea quark mass is proposed and demonstrated in a simpler case on UKQCD clover data. Exploratory results for the hadron mass spectrum and pseudoscalar meson decay constants using a mixed action formalism are then presented.

4.2 Motivation

To predict phenomenological quantities from lattice QCD with high precision requires the ability to simulate with light dynamical quarks. Ginsparg-Wilson fermions (see section 2.8) have the correct chiral and flavour symmetries. However, they are computationally expensive compared to improved staggered quarks

(see section 2.7). In the $N_f = 2 + 1$ improved staggered programme the square root of the fermion determinant is employed to reduce the number of dynamical flavours from four to two for the up and down quarks, and the fourth root is taken to reduce the number of flavours from four to one for the strange quark [75]. Ensembles of gauge field configurations are then generated with these fractional power determinants as weight factors. There is no known local action to which this model corresponds.

A mixed action is defined as one where the action used to generate the ensemble of gauge configurations, or sea quark action, is different from the valence quark action used to determine hadronic observables on those configurations. This corresponds to choosing a different kernel (M) for the determinant than in the inverse in equation (3.2). Current $N_f = 2+1$ improved staggered simulations have a mixed action because the four-flavour staggered Dirac operator, D_{st}, is used to generate the valence quark propagators rather than a local operator equivalent to that used in the ensemble weight. Unless a local operator can be found such that

$$\det D_{\mathrm{local}} \equiv (\det\{D_{\mathrm{st}} + m\})^{1/4} \tag{4.1}$$

mixed actions are inevitable in the improved staggered programme. The commonly used Chebyshev polynomial approximation to the square root of $(D_{\mathrm{st}} + m)$ is not the required operator as it has been shown to be non-local [76, 77, 78]. That $(D_{\mathrm{st}} + m)^{1/4}$ is non-local does not imply that D_{local} does not exist, but serves as a warning, since the obvious candidate for such an operator fails.

In the rest of this chapter it is assumed that some D_{local} exists so that the improved staggered ensembles are generated with an action in the same universality class as QCD. For the case where the valence quark action is manifestly different from that of the sea, the valence action that has the best chiral properties is chosen, that is, overlap valence quarks on an improved staggered sea. In [79] a local Symanzik action and the corresponding low-energy chiral effective Lagrangian

are constructed for a general Ginsparg-Wilson valence action with Wilson sea quarks. Some of their considerations apply to more general mixed actions and, in particular, to overlap valence quarks on a staggered quark sea.

Neuberger's overlap operator [24] was described in section 2.9 and is given by

$$aD_{\rm ov}(\mu) = \rho(1+\mu) + \rho(1-\mu)\gamma_5\epsilon(H_{\rm W}) \tag{4.2}$$

where $H_{\rm W}$ is the Hermitian Wilson operator

$$H_{\rm W}(-\rho) = \gamma_5(aD_{\rm W} - \rho) \tag{4.3}$$

with mass parameter $0 \leq \rho \leq 2$, and $\epsilon(H_{\rm W})$ is the matrix sign function of $H_{\rm W}$. The mass parameter μ is related to the bare quark mass am_q through

$$\mu = \frac{am_q}{2\rho} \tag{4.4}$$

although we will ignore this below and write $D_{\rm ov}(m_0)$. The expectation value of some observable $\mathcal{O}$ in a model where the ensemble has been generated as $2+1$ flavours of staggered quarks, with overlap valence quarks is

$$\begin{aligned}\langle\mathcal{O}\rangle &= \frac{1}{\mathcal{Z}}\int \mathcal{D}U \left(\det\left\{D_{\rm st}[U]+m_{ud}\right\}\right)^{1/2}\left(\det\left\{D_{\rm st}[U]+m_s\right\}\right)^{1/4} e^{-S_G[U]} \\ &\quad \times\mathcal{O}\left[\frac{\delta}{\delta\bar{\eta}_i},\frac{\delta}{\delta\eta_i},U\right] e^{-\bar{\eta}_i\{D_{\rm ov}[U](m_i)\}^{-1}\eta_i}\Big|_{\bar{\eta}_i=\eta_i=0},\end{aligned} \tag{4.5}$$

where U are the gauge fields, $\mathcal{Z}$ is the partition function, $\{\bar{\eta}_i,\eta_i\}$, $i=1,\cdots,N_f$, are the valence quark sources and S_G is the gauge action. The real parts of the eigenvalues of $D_{\rm ov}$ are positive and bounded from below by the valence quark masses m_i, assuming $m_i > 0$. The expectation values are equal to those of a local field theory with action given by

$$\begin{aligned}S &= S_G[U] + \sum_{l=ud}\bar{\chi}_l\left(D_{\rm local}[U]+m_{ud}\right)\chi_l + \bar{\chi}_s\left(D_{\rm local}[U]+m_s\right)\chi_s \\ &\quad + \sum_i\left\{\bar{q}_i D_{\rm ov}[U](m_i)q_i + \phi_i^+ D_{\rm ov}[U](m_i)\phi_i\right\}\end{aligned} \tag{4.6}$$

where the χ fields are the one-component staggered sea quark fields, and the q fields are the overlap valence quark fields. The ϕ fields are pseudofermion sea

fields introduced to cancel the determinant of the overlap operator [80]. For practical purposes the model can be regarded as having an exact $SU(N_f|N_f)_L \otimes SU(N_f|N_f)_R \otimes U(1)_V$ symmetry when $m_i = 0$ for $i = 1, \cdots, N_f$ [81]. Restricting to transformations only in the valence quark sector, the infinitesimal chiral rotation is given by

$$\begin{aligned} \delta q &= i\epsilon\tau\gamma_5 \left(1 - \frac{1}{2}D_{\text{ov}}\right) q \\ \delta\bar{q} &= i\epsilon\bar{q} \left(1 - \frac{1}{2}D_{\text{ov}}\right) \gamma_5\tau \end{aligned} \tag{4.7}$$

and possesses the correct $U(1)_A$ anomaly and an index theorem [82, 83] (for a review see [69]).

For $N_f = 3$, this model is in the same universality class as QCD when the sea and valence quark masses are matched. At non-zero lattice spacing, the separate chiral symmetries for sea and valence quarks ensure that the lightest pseudoscalar meson mass vanishes at $m_{\text{val}} = m_{\text{sea}} = 0$. This implies that the bare quark masses are related by

$$m_{\text{val}} = \zeta(a) m_{\text{sea}} \tag{4.8}$$

where $\zeta \to 1$ as $a \to 0$. To date $N_f = 2 + 1$ simulations with staggered valence quarks using fractional determinants of the staggered sea [75] have set $\zeta(a) = 1$. However, it is not obvious that this is the appropriate matching condition for overlap valence quarks on a staggered sea (or, for that matter, for staggered valence quarks).

4.3 Matching the quark masses

To match the sea and valence quark masses to their experimental values one would have to find an experimentally known hadronic state whose mass depended strongly on the sea quark masses. In principle, the η' is one such hadron. The sea

quark mass could be tuned until the η' has the correct experimental mass, whilst tuning the valence quark mass of the flavour non-singlet pseudoscalar meson correlator to the pion mass. In practice, this is rather difficult, as the η' requires very high statistics calculations. An alternative would be to relate the bare sea and valence quark masses to each other via equation (4.8), and then tune the flavour non-singlet mesons to their experimental values in the usual way.

When the sea quark mass is infinite, *i.e.* quenched, Bardeen *et al.* [84, 85] have demonstrated numerically that the model violates unitarity. This violation has also been observed numerically in partially quenched two flavour QCD and demonstrated in partially quenched chiral perturbation theory by [86]. We perform a similar analysis and show the same unitarity violation occurs when $m_{\text{val}} < m_{\text{sea}}$. Our results suggest a criterion for matching the sea and valence quark masses. The quark masses can be tuned by varying the valence quark mass to see when these partially quenched pathologies appear for a given sea quark mass. This determines when the valence quark is lighter than the sea quark.

Bardeen *et al.* [84, 85] show that the scalar correlator,

$$C_{SS}(t) = \sum_{\vec{x}} e^{-\vec{p}\cdot\vec{x}} \langle \bar{\psi}(x)\psi(x)\bar{\psi}(0)\psi(0)\rangle, \tag{4.9}$$

is sensitive to this quenched pathology because it couples to an $\eta' - \pi$ intermediate state. Shown in figure 4.1 are two of the diagrams which contribute to the η' propagator. Diagram a), the "hairpin", has a negative coefficient. In full QCD, diagram b), with a series of vacuum bubbles, cancels the effect of the hairpin diagram, so there is no negative contribution. In quenched QCD, only the hairpin diagram contributes, so the intermediate $\eta' - \pi$ state couples with a negative spectral weight. This gives the scalar correlator a negative value. In partially quenched QCD the situation is more complicated. The bubble in diagrams b) depends only on the sea quark mass, whereas the connected quark-flow lines

Figure 4.1: Quark-flow diagrams contributing to the η' propagator.

depend only on the valence quark mass. Heuristically at least, the size of the contribution from diagrams b) can been thought of in the following way. When the sea quark mass is smaller than the valence quark mass, diagrams b) have a larger positive contribution than the negative contribution from diagram a). When the sea quark mass is heavier than the valence quark mass, diagram b) has a smaller contribution than a), which means the $\eta' - \pi$ intermediate state couples to the scalar correlator with a negative weight. By monitoring the sign of the scalar correlator as the valence quark mass is varied it should be possible to match the sea and valence quark masses.

To demonstrate this method, we examined the scalar correlator on the UKQCD $N_f = 2$ clover data sets [87, 88], where the sea and valence quarks have the same action. So whether the valence quark mass is heavier or lighter than the sea is known. This data was generated with the Wilson plaquette gauge action and the clover quark action, where the coefficient of the Sheikholeslami-Wohlert term [21] was determined non-perturbatively [89]. For all data sets $\beta = 5.2$ and the volume is $L^3 \times T = 16^3 \times 32$. The values of the hopping parameter for the sea and valence quark masses, and the number of configurations are shown in Table 4.1.

The relatively poor signal-to-noise ratio for the scalar correlator implies the need for a large number of configurations. To improve the statistical resolution, we used a ratio of correlation functions, as the statistical fluctuations are correlated. In particular, we considered the ratio

$$R(t) = \frac{C_{PP}(t) - C_{SS}(t)}{C_{PP}(t)} \tag{4.10}$$

where PP denotes the pseudoscalar correlator. At sufficiently large times the ground states will dominate and R is then

$$R(t) = 1 - \left(\frac{A_{SS}}{A_{PP}}\right)\left(\frac{e^{-m_S t} + e^{-m_S(T-t)}}{e^{-m_P t} + e^{-m_P(T-t)}}\right). \tag{4.11}$$

At the mid-point of the lattice

$$R(T/2) = 1 - \frac{A_{SS}}{A_{PP}} e^{-\Delta m T/2} \tag{4.12}$$

where $\Delta m = m_S - m_P$ is the mass splitting between the scalar and pseudoscalar states. For a large enough lattice time extent, T, this ratio tends to unity at the mid-point.

However, when the valence quark mass is lighter than the sea quark mass, the $\eta' - \pi$ state couples to the scalar correlator with a negative weight. Thus, a signal for the valence quark mass being lighter than the sea is $R > 1$. Figure 4.2 shows the ratio for different sea and valence quark masses. The open circle and filled square both have the sea and valence quark masses equal, and R tends to unity at the mid point of the lattice. For the filled circles, $R > 1$ as $t \approx T/2$ at the 2σ level, a signal for partial quenching, and indeed this data set has $m_{\text{val}} < m_{\text{sea}}$. This effect is clearly dependent on the sea quark mass, as the open and filled circles both have the same valence quark mass.

Also shown in Table 4.1 is the result of fitting equation (4.11) to the data. Clearly the ratio A_{SS}/A_{PP} is not a very well-determined quantity. However, it seems clear that this ratio being negative is a signal at the $1 - 2\sigma$ level that the data is partially quenched. Figure 4.3 shows both the scalar correlator and the ratio (4.11). At lighter quark mass and with fewer configurations, the fit results become rather dependent on the fit range chosen, but combining the fit information and examining these plots, it is clear that for $\kappa_{\text{sea}} = 0.13565$, $\kappa_{\text{val}} = 0.13580$ there is a signal for the negative weight state, and for $\kappa_{\text{val}} = 0.13565$ this signal is absent. A precise matching of the sea and valence quark masses will be difficult to achieve, because the signal for the scalar ground state at large times for light quarks seems

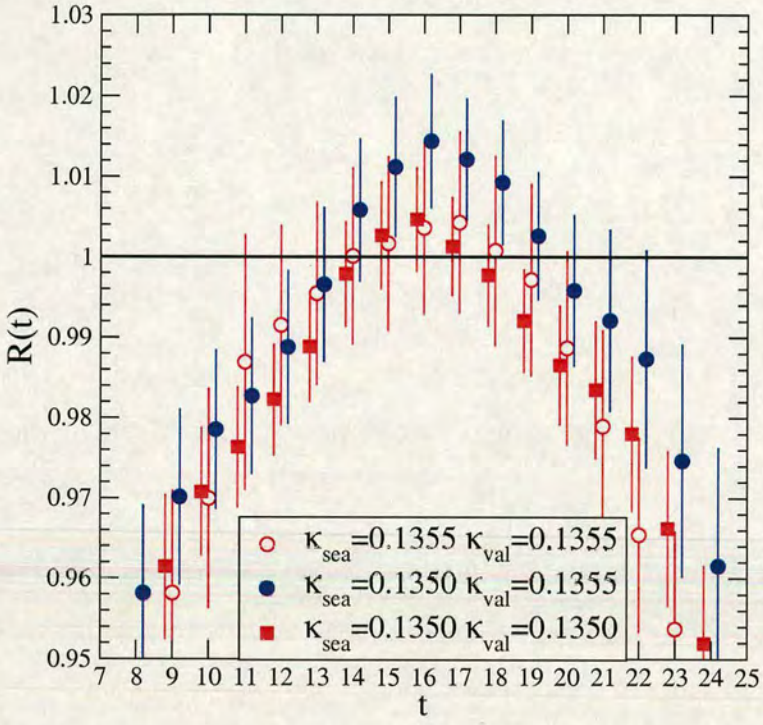

Figure 4.2: $R(t)$ in equation (4.11) versus Euclidean time, t.

to disappear into the noise. When the valence quark mass is lighter than the sea, the signal for the negative weight $\eta' - \pi$ state is fairly strong. However, our results suggest that it is possible, in principle, (equivalently with very high statistics) to match the valence and sea quark masses. This is necessary to make sense of simulations with mixed actions when at least one of the sea or valence quark masses is out-with the chiral regime and matching to chiral perturbation theory is problematic.

4.4 Overlap valence quarks on a staggered sea

In this section the results of an exploratory study using overlap valence quarks on MILC $N_f = 2 + 1$ improved staggered configurations [90] is discussed. The simplest states of the light hadron spectrum, mesons and baryons, and the pseu-

κ_{sea}	κ_{val}	Nconfig	$m_{\text{val}} : m_{\text{sea}}$	A_{SS}/A_{PP}
0.13500	0.13400	202	$>$	0.6(1)
	0.13450	202	$>$	190(50)
	0.13500	202	$=$	0.0(2)
	0.13550	202	$<$	$-0.00015(5)$
0.13550	0.13500	208	$>$	1.2(2)
	0.13550	208	$=$	0.0(1)
0.13565	0.13550	141	$>$	1.5(5)
	0.13565	141	$=$	5.0(10)
	0.13580	141	$<$	$-0.00014(14)$
0.13580	0.13565	137	$>$	0.06(4)
	0.13580	137	$=$	0.0(1)
	0.13595	137	$<$	$-0.003(2)$

Table 4.1: UKQCD dynamical clover ($N_f = 2$) data sets for $\beta = 5.2$.

doscalar decay matrix element for both light and heavy-light states have been measured. Due to a lack of computational resources, the number of configurations analysed was small. This prevented any realistic attempt at matching the sea and valence quark masses as described in section 4.3. Whilst the results presented below appear encouraging, the low statistics means they must be regarded as purely illustrative of the effectiveness of a mixed action approach.

4.5 Smearing

The overlap operator is only local for gauge configurations which are "smooth enough" [91]. The MILC configurations used in this analysis are relatively coarse with a lattice spacing of $a \sim 0.125$ fm. It is therefore expected that smoothing the gauge configurations by smearing should improve the localisation of the

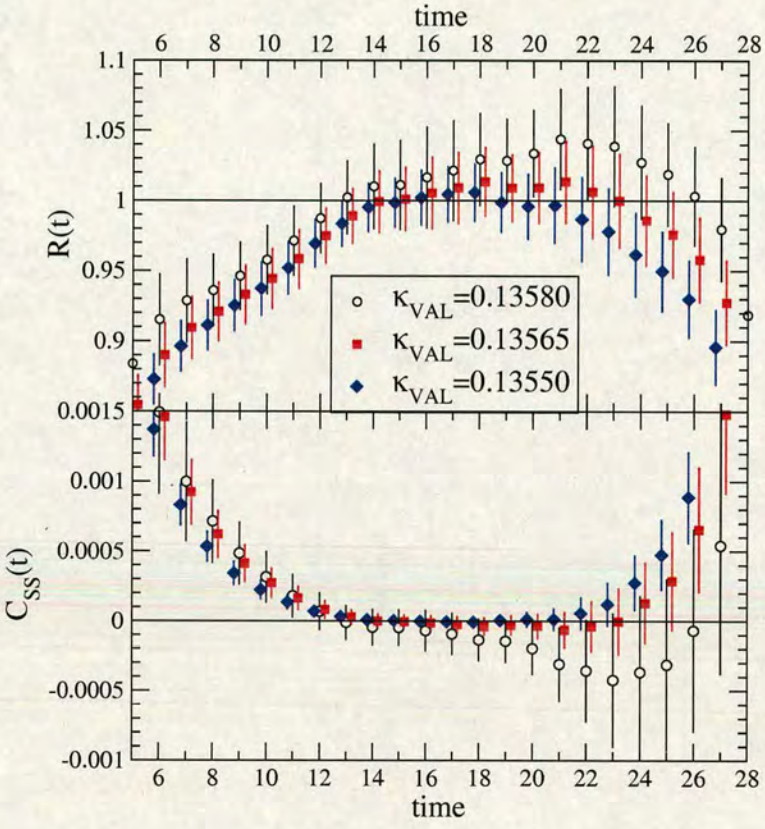

Figure 4.3: $R(t)$ and $C_{SS}(t)$ versus t for $\kappa_{\text{sea}} = 0.13565$.

overlap operator. Moreover, smoothing the gauge fields by "HYP-smearing" [92] can improve the spectral properties of the Wilson-Dirac operator [93], which reduces the amount of computation required in the solver used to apply $\epsilon(H_{\text{W}})$. Indeed, it was observed that HYP-smearing the gauge configuration does speed up the inversions. The effect of HYP-smearing the configurations is effectively to smear the operator measured. Furthermore, the low-lying eigenvalues of the staggered operator "mimic" the eigenvalue spectrum of the overlap operator when the configurations are smoothed in this way [94, 95, 96] suggesting that a smoothly behaved matching condition may exist for light quark masses.

To examine the effect of multiple iterations of HYP-smearing, the quark-antiquark potential was studied using 624 quenched UKQCD configurations at $\beta = 5.93$

with a volume of $16^3 \times 32$. The smearing parameters used were $\alpha_1 = 0.75$, $\alpha_2 = 0.60$, and $\alpha_3 = 0.35$ [92]. Planar Wilson loops were used to extract the quark-antiquark potential, which was fitted to

$$V(r) = V_0 + \sigma r - \frac{\kappa}{r}. \tag{4.13}$$

Figure 4.4 shows the effect of multiple iterations of HYP-smearing on quark-antiquark potential and on the string tension, σ. As shown in figure 4.4 repeated

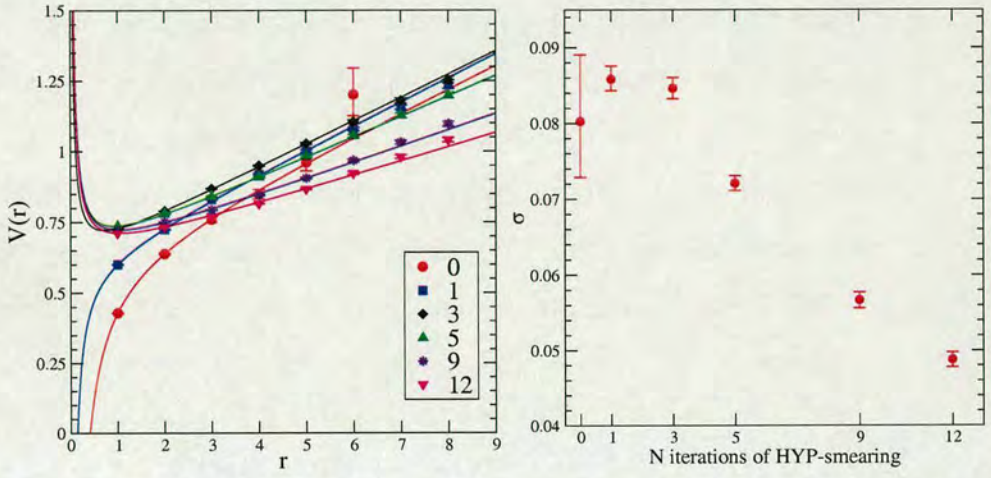

Figure 4.4: The effect of the number of HYP-smearing iterations on **LEFT:** the quark-antiquark static potential and **RIGHT:** the long-range potential as measured by σ using 624 quenched UKQCD configurations with volume $16^3 \times 32$.

HYP-smearing quickly altered the short-distance behaviour, while the medium-to-long distance behaviour remained relatively unchanged for a small number ($\lesssim$ 3) of iterations. The effect on the potential of smoothing configurations has been studied many times before, following the work of Teper [97]. Recently Durr [98] has carried out an extensive study for different actions and different smearings. The limited study performed here agrees with these previous results. It was concluded that three or less iterations of HYP-smearing does not significantly alter the long range potential and thus the spectrum.

4.6 Simulation parameters

The overlap propagator calculations were performed on ten configurations from each of two improved staggered ensembles with a volume of $20^3 \times 64$ produced by the MILC collaboration [90]. One ensemble had $am_s = 0.05$, $am_l = 0.03$ and the other had $am_s = 0.05$, $am_l = 0.02$. Both had a lattice spacing $a \simeq 0.125$ fm ($\approx 1.5GeV$) obtained from the static quark potential [90] and linear size $L \simeq 2.5$ fm. Three iterations of HYP-smearing were applied to each configuration. The 32 lowest eigenmodes were projected out in order to reduce the condition number and speed up the convergence of the solver. The overlap operator from the SZIN code [99] was used to calculate propagators. These were created with seven different valence quark masses using the overlap multi-mass solver: four light and three heavy [56, 100]. Some of these results have been previously reported in [101].

4.7 The light hadron spectrum

Simultaneous fits were performed to three different correlators: the pseudoscalar density correlator C_{PP}, the axial-axial correlator C_{AA} and the axial-pseudoscalar correlator C_{AP} using the fit form

$$C(t) = \begin{cases} \frac{Z_{PP}^2}{2E_0}\left(e^{-E_0 t} + e^{-E_0(T-t)}\right) & \text{for } C_{PP}(t) \\ \frac{Z_{AA}^2}{2E_0}\left(e^{-E_0 t} + e^{-E_0(T-t)}\right) & \text{for } C_{AA}(t) \\ \frac{Z_{PP}Z_{AA}}{2E_0}\left(e^{-E_0 t} - e^{-E_0(T-t)}\right) & \text{for } C_{AP}(t) \end{cases} \tag{4.14}$$

in order to extract the pseudoscalar meson mass. Figure 4.5 shows a typical effective mass plot with fit. The fluctuations in the effective mass are larger than the apparent statistical errors, but this is probably due to underestimation of the variance on ten configurations. Similar fluctuations have also been observed in high statistics runs [102]. Tables 4.3 and 4.4 give the values extracted from the fits. In the case of the heavy-heavy correlators the signal is very poor and

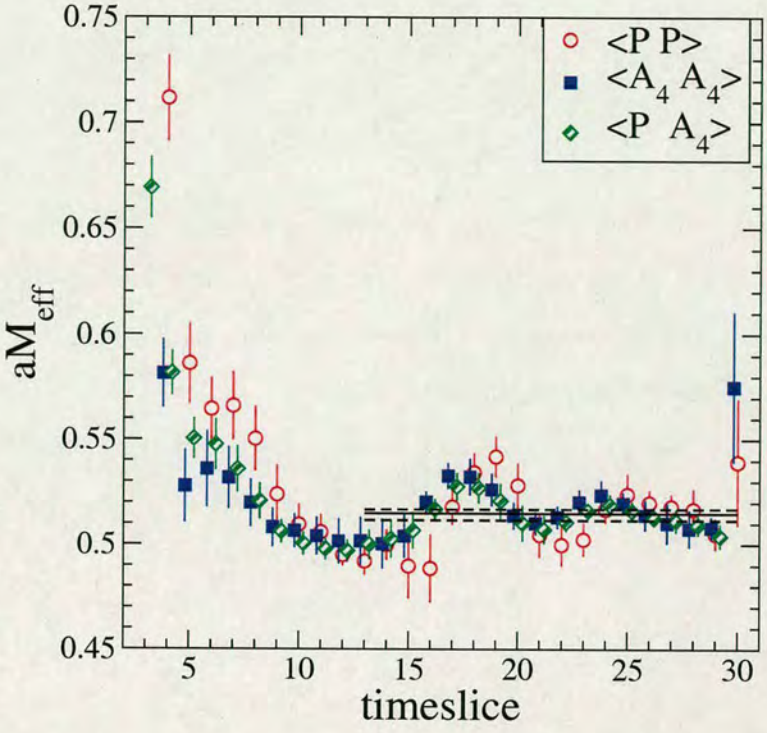

Figure 4.5: Pseudoscalar meson effective mass and simultaneous uncorrelated fit to three correlators ($P = \bar{q}\gamma_5 q$, $A_4 = \bar{q}\gamma_4\gamma_5 q$). The squares and diamonds are slightly offset horizontally for clarity.

therefore only limited results for these correlators are given.

A partially quenched analysis was carried out, that is the sea quark mass was held fixed whilst varying the valence quark mass. Since we had multiple input valence masses, non-degenerate meson correlators could be constructed. Shown in figure 4.6 is the two-dimensional fit performed to $(aM_{PS})^2$ versus valence masses m_{q_1} and m_{q_2}, which allowed evaluation of the average u and d quark mass, $\hat{m}$, from

$$M_\pi^2 = B\,(m_{q_1} + m_{q_2}) + A = 2B\hat{m} + A \tag{4.15}$$

where M_π is the physical pion mass. The chiral symmetry of the operator should make $(aM_{PS})^2$ vanish at zero quark mass. We do not constrain the fit to satisfy this condition, but within the limited statistics the parameter A is consistent with

zero. This in turn allowed us to evaluate the strange quark mass, m_s, from

$$M_K^2 = B\,(m_s + \hat{m}) + A \tag{4.16}$$

where M_K is the physical kaon mass. Table 4.7 gives the value of the unrenormalised (lattice) normal and strange quark masses together with the intercept A from the above analysis. These were obtained using only the four lightest and three heaviest quarks on both seas.

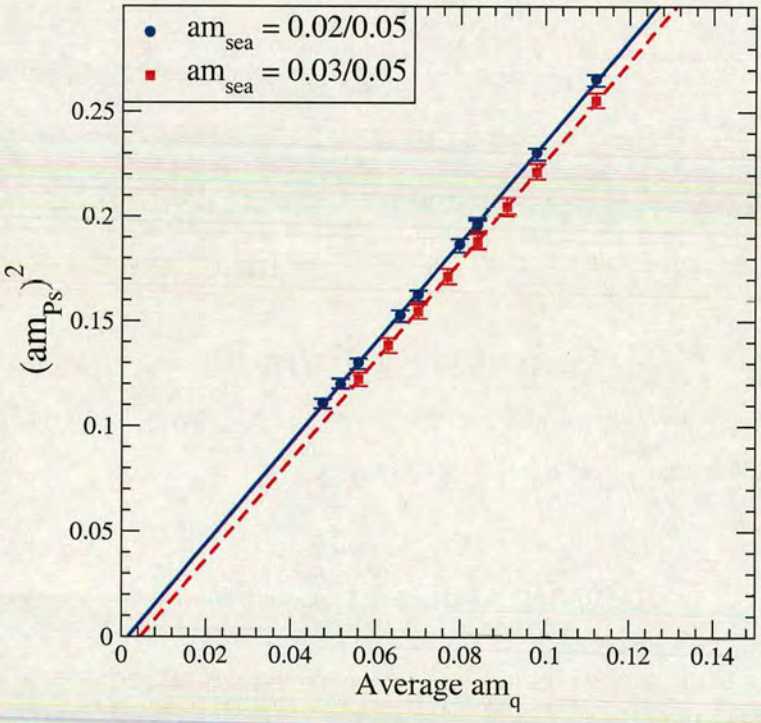

Figure 4.6: The square of the pseudoscalar meson mass vs bare overlap quark mass.

The masses of the nucleon and delta baryon was also determined. The signal for the nucleon mass is very clean. Figure 4.7 shows the effective mass of the nucleon for the two operators

$$N_1(x) = \varepsilon_{ijk}(\psi_i^T C\gamma_5\psi_j)\psi_k \tag{4.17}$$

$$N_2(x) = \varepsilon_{ijk}(\psi_i^T C\gamma_4\gamma_5\psi_j)\psi_k. \tag{4.18}$$

The mass of the nucleon was obtained from a single exponential fit to the average of these two channels and is given in table 4.5 together with the value obtained in the chiral limit using the four lightest quark masses. It is remarkable that we can see a signal for the negative parity partner of the nucleon on as few as ten configurations. This suggests that, despite their relative cost per propagator compared with staggered quarks, overlap valence quarks may be the most cost effective way to extract precision light baryon physics from improved staggered configurations. Figure 4.8 shows the nucleon (upper plot) and decuplet (lower

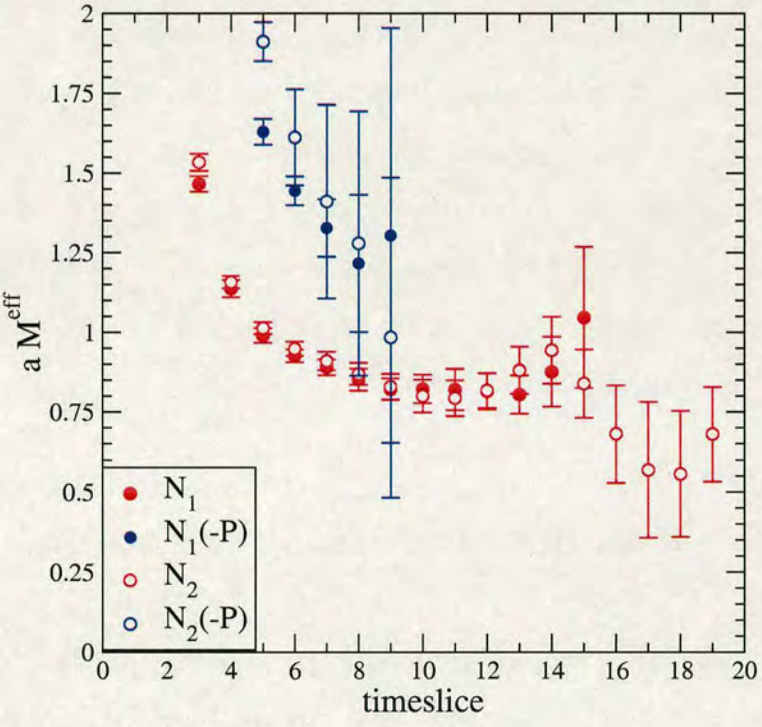

Figure 4.7: Nucleon effective mass for the heavier sea quarks, with $am_q = 0.056$ (equation 4.4). The blue symbols show the negative parity excitation.

plot) masses versus the pseudoscalar meson mass squared. The decuplet mass given in table 4.6 is obtained from a single exponential fit and the value in the chiral limit is found from an uncorrelated linear fit to the data using the lightest four quark masses. The result of this uncorrelated linear fit is shown by the lines in figure 4.8. The values calculated by the MILC collaboration [90] on their

corresponding full ensembles are shown by open symbols. Both the nucleon and decuplet baryon masses from the overlap operator are significantly lower although, *a priori*, we don't know how to match the horizontal scales. The cut-off effects for the different formalisms will be different and, unless the matching function in equation (4.8) is very different from one, this suggests that the cut-off effects for the overlap baryons are smaller. The nucleon mass shows some sea quark mass dependence, but the decuplet mass shows no variation. With ten configurations and relatively heavy sea quark masses, any trend is hard to spot. In the lower plot, the vertical dashed-dotted line shows the estimate of the $\eta_{s\bar{s}}$ mass squared, as measured by the overlap operator on these configurations. The horizontal dotted line is the physical Ω^- mass in lattice units. Within large statistical uncertainties, this determination of the Ω^- mass at fixed lattice spacing agrees with the experimental value. Again, this may suggest that cut-off effects with overlap fermions are smaller than with staggered fermions, but, with data at only one lattice spacing, this remains speculation.

4.8 Pseudoscalar decay constant

The pseudoscalar decay constant, f_{PS}, is defined in equation (3.81). In this section the method described in sections 3.11.1 and 5.11.1 was used to calculate the pseudoscalar decay constant. This method requires only C_{PP}, the pseudoscalar density correlator, in order to compute a renormalised f_{PS}.

Once again, we performed a 2-d linear fit to the light non-degenerate pseudoscalars to calculate f_{PS} in the chiral limit (see tables 4.8 and 4.9) and extracted the ratio of f_K/f_π (see table 4.2). Figure 4.9 shows the pseudoscalar meson decay constant plotted against the pseudoscalar meson mass squared in physical units where the lattice spacing was obtained from the MILC analysis of the static quark potential [90]. The value of f_K/f_π increases slightly with decreasing light

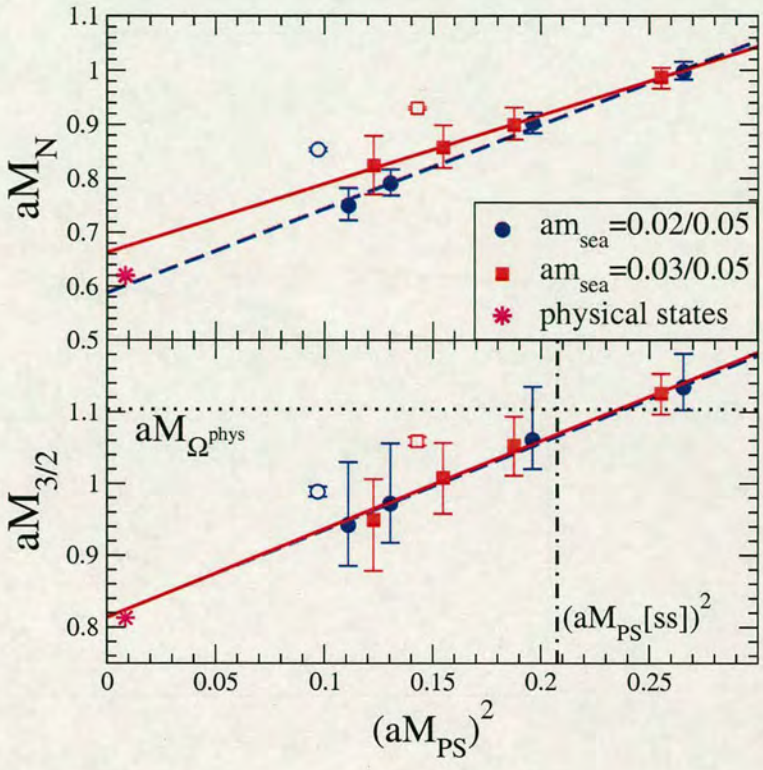

Figure 4.8: The nucleon and decuplet baryon mass versus $(aM_{PS})^2$ for the two ensembles. The open symbols show the baryon masses measured on the full ensemble with staggered valence quarks [90]. The lower plot shows the physical Ω^- mass in lattice units, where the lattice spacing is set by r_0 taken from the reference above.

sea quark mass (see table 4.2) in the right direction to agree with experiment. This movement towards the experimental value is also evident from the slight change of the gradient with sea quark mass in figure 4.9.

4.9 Charm Physics

Heavy quark propagators essentially come for free in the overlap propagator calculation through the use of a multi-mass solver. However, lattice artefacts are

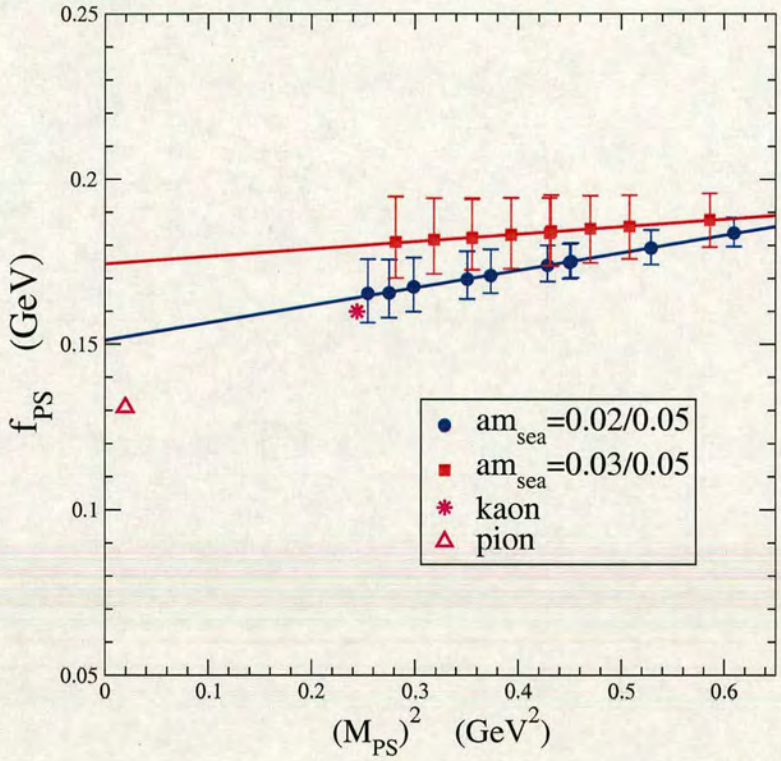

Figure 4.9: f_{PS} versus M_{PS}^2 for the two ensembles.

Sea Quarks	f_K/f_π	f_{Ds} (MeV)
$am_{\text{sea}} = 0.03/0.05$	1.03(3)	226(14)
$am_{\text{sea}} = 0.02/0.05$	1.08(4)	232(11)
Experiment [70]	1.22(1)	266(32)

Table 4.2: Pseudoscalar meson decay constants.

$\mathcal{O}(am_q)^2$ and the heaviest input valence quark mass used is $am_q = 0.896$, so $(am_q)^2 \sim 0.8$. With the lattice spacing of $a^{-1} \sim 1.5$GeV, the calculation is at best on the limit of simulating charm. Due to the rapid decay in Euclidean time, we require double precision.

These heavy quark propagators were used to calculate the mass of heavy-light

pseudoscalar states and heavy-light pseudoscalar decay constants which were extrapolated in the light quark mass holding the heavy quark mass fixed

$$aM_{Hl}(m_{q_l}) = Cm_{q_l} + D \tag{4.19}$$

$$af_{Hl}(m_{q_l}) = Em_{q_l} + F. \tag{4.20}$$

Using the previously obtained value of the strange quark mass

$$aM_{Hs} \equiv aM_{Hl}(m_{q_l} = m_s) \tag{4.21}$$

$$af_{Hs} \equiv af_{Hl}(m_{q_l} = m_s) \tag{4.22}$$

were obtained for each of the 3 heaviest quark masses (see tables 4.10 and 4.11). f_{Ds} was then calculated using the physical value of $M_{Ds} = 1968.5$MeV [70]. The value of f_{Ds} increases with decreasing light sea quark mass, in the direction of the experimental value, as can be seen from the change of gradients in figure 4.10. The short distance behaviour of the potential has been altered by repeated smearing. As heavy quarks in quarkonium feel the short distance potential, this repeated smearing may be a source of worry. Indeed, examining the heavy-heavy correlator for the heaviest quark mass we do not see the effective mass reaching a plateau. It might be expected that a heavy-light state feels the effect of the short distance potential less. Indeed the effective mass for the heavy-light correlator reaches a plateau. This suggests that the heavy-light states are not suffering so much from the modified short-distance behaviour. In any future work using fewer iterations of smearing would be anticipated.

4.10 Recent developments

Recently A. Hasenfratz [103] has argued that if staggered fermions describe QCD in the continuum limit there has to be an underlying flavor symmetric Ginsparg-Wilson action that is equivalent to the staggered action up to lattice artifacts.

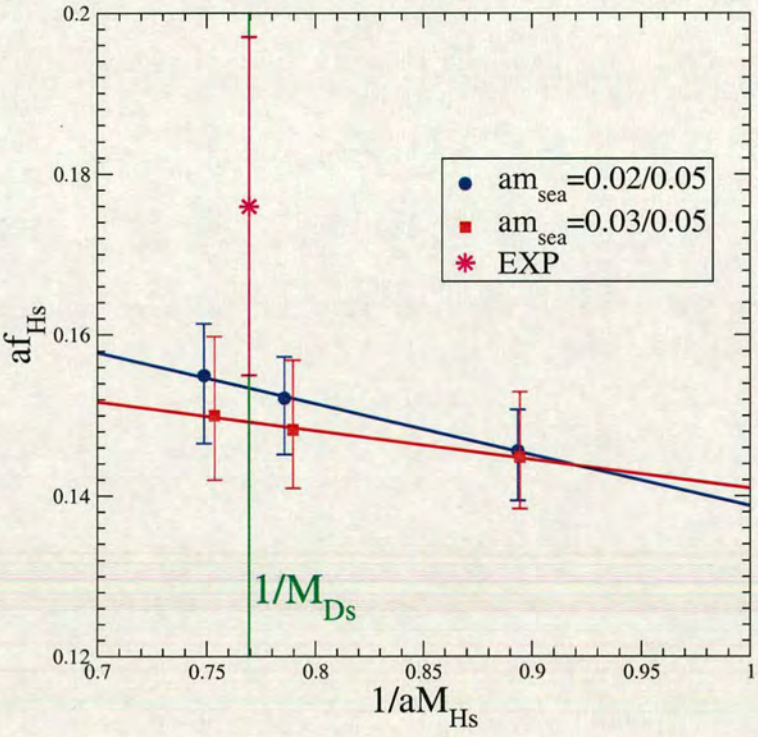

Figure 4.10: f_{Hs} vs inverse heavy-strange pseudoscalar meson mass.

She argues that if 4-taste staggered fermions describe 4-flavour QCD in the continuum limit then at any finite lattice spacing the fermion mass of the underlying chiral 4-flavour theory differs from the mass of the staggered action not only in a multiplicative but by an additive term as well. This additive mass, she suggests, is a lattice artefact and should go away in the continuum limit. In [104] it is shown that staggered chiral perturbation theory predicts that the topological susceptibility scales with the taste singlet (heaviest) pion while in her paper she shows that measurements of the topological susceptibility clearly indicate a mass shift. It is therefore interesting to consider this shift in the context of mixed actions.

In [105] the mass differences between the different tastes of pseudoscalar mesons on the lattices used in this chapter are listed. Converting this difference into lattice units, the difference between the Goldstone and taste-singlet pseudoscalar

mesons squared is given by

$$((M_{PS}^{Singlet})^2 - (M_{PS}^{Goldstone})^2)a^2 = 0.08. \quad (4.23)$$

She suggests that the true flavor symmetric theory has Goldstone pseudoscalar mesons that are that much heavier than the staggered Goldstone pseudoscalar mesons. This could be true for the baryons (although it is not clear in staggered calculations whether it is the lightest or heaviest baryon that is measured) and could also be true for the ρ mesons. Figure 4.11 (top) shows figure 4.8 for the nucleon replotted with the shifted pseudoscalar meson mass. Figure 4.11 (bottom) shows a similar plot for the ρ meson mass on the $am_l = 0.03$, $am_s = 0.05$ dataset. The open symbols are the ρ, K^* and ϕ measured by the MILC collaboration [90] on their corresponding full ensembles. It can be seen that the shifted points in figures 4.11 top and bottom match almost perfectly the Ginsparg-Wilson data. The data seems to support this additive mass shift much more than a multiplicative one assumed previously. This suggests that the overlap operator "sees" the taste-singlet pseudoscalar meson in the sea rather than the Goldstone pseudoscalar meson that the staggered valence operator "sees". It would therefore be interesting to carry out the quark matching discussed in section 4.3 to see whether this too shows up the additive shift in quark mass.

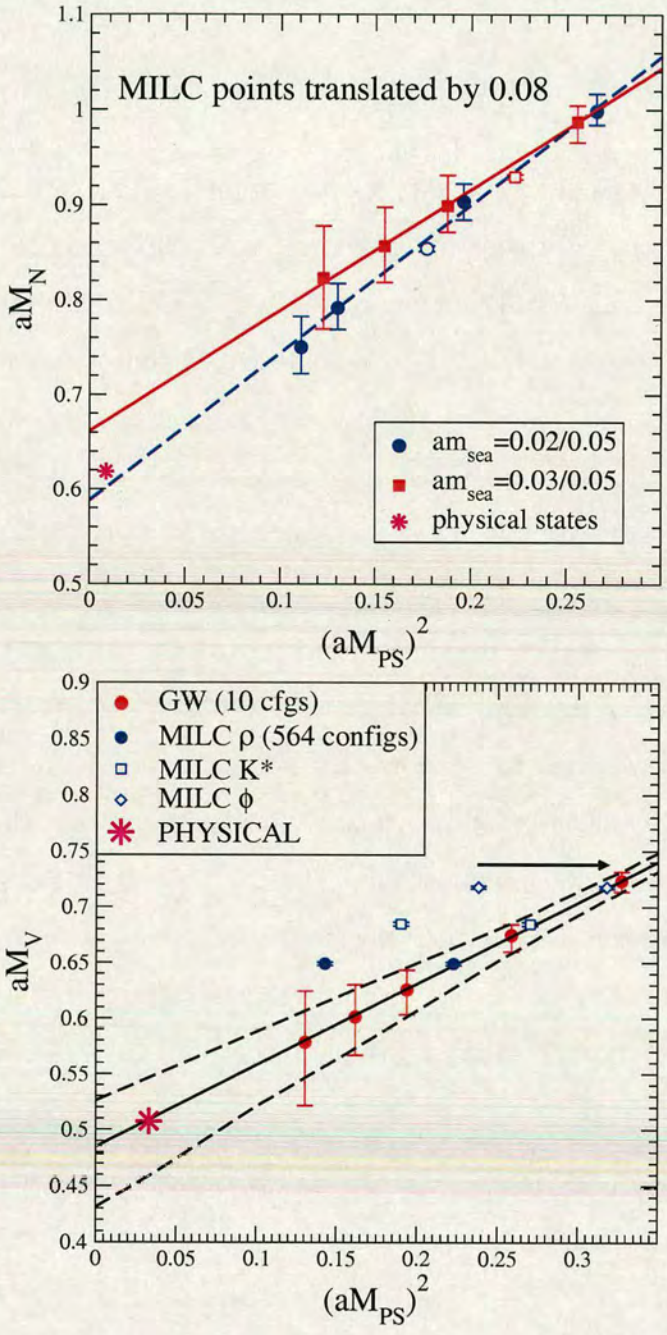

Figure 4.11: **TOP:** Figure 4.8 replotted with the staggered Goldstone pseudoscalar meson mass squared points shifted to the right by 0.08 as described in the text. **BOTTOM:** ρ meson mass vs pseudoscalar meson mass squared for the $am_{sea} = 0.03/0.05$ dataset. The arrow indicates that the values calculated by the MILC collaboration [90] have been shifted to the right by 0.08 as described in the text.

4.11 Tables

Valence quarks	Timeslices	Results			
$(m_1 : m_2)$	$t_{min} - t_{max}$	Z_{PP}	Z_{AA}	am_{PS}	χ^2/dof
(0.0476 : 0.0476)	13-30	0.36(2)	0.088(5)	0.333(4)	4.190/51
(0.0476 : 0.056)	13-30	0.35(2)	0.092(5)	0.346(4)	4.380/51
(0.0476 : 0.084)	13-30	0.36(1)	0.108(4)	0.391(4)	4.799/51
(0.0476 : 0.112)	13-30	0.38(2)	0.124(6)	0.432(4)	5.332/51
(0.0476 : 0.14)	13-30	0.39(2)	0.140(6)	0.471(5)	5.743/51
(0.0476 : 0.476)	10-16	0.52(3)	0.30(2)	0.853(8)	1.425/18
(0.0476 : 0.7)	10-16	0.62(5)	0.40(3)	1.09(1)	0.681/18
(0.0476 : 0.84)	10-16	0.71(6)	0.49(4)	1.24(1)	0.718/18
(0.0476 : 0.896)	10-16	0.76(6)	0.53(4)	1.31(2)	0.695/18
(0.0476 : 0.896)	10-16	0.76(6)	0.53(4)	1.31(2)	0.695/18
(0.056 : 0.056)	13-30	0.36(2)	0.098(5)	0.361(4)	4.450/51
(0.056 : 0.084)	13-30	0.37(2)	0.113(5)	0.403(4)	4.967/51
(0.056 : 0.112)	13-30	0.38(2)	0.129(5)	0.444(4)	5.516/51
(0.056 : 0.14)	13-30	0.39(2)	0.145(5)	0.482(4)	5.912/51
(0.056 : 0.476)	10-16	0.52(3)	0.31(1)	0.859(8)	1.175/18
(0.056 : 0.7)	10-16	0.62(4)	0.41(3)	1.094(9)	0.514/18
(0.056 : 0.84)	10-16	0.72(5)	0.50(3)	1.25(1)	0.561/18
(0.056 : 0.896)	10-16	0.76(6)	0.54(4)	1.31(1)	0.552/18
(0.084 : 0.084)	13-30	0.38(1)	0.129(5)	0.443(4)	5.546/51
(0.084 : 0.112)	13-30	0.39(1)	0.145(5)	0.480(4)	5.962/51
(0.084 : 0.14)	13-30	0.40(1)	0.160(6)	0.516(4)	6.108/51
(0.084 : 0.476)	10-16	0.54(3)	0.33(1)	0.883(7)	0.621/18
(0.084 : 0.7)	10-16	0.64(4)	0.43(3)	1.116(7)	0.225/18
(0.084 : 0.84)	10-16	0.74(4)	0.52(4)	1.269(8)	0.267/18
(0.084 : 0.896)	10-16	0.78(5)	0.56(4)	1.332(9)	0.279/18

Valence quarks	Timeslices	Results			
$(m_1 : m_2)$	$t_{min} - t_{max}$	Z_{PP}	Z_{AA}	am_{PS}	χ^2/dof
(0.112 : 0.112)	13-30	0.40(1)	0.160(5)	0.515(3)	6.051/51
(0.112 : 0.14)	13-30	0.42(1)	0.176(6)	0.550(3)	5.840/51
(0.112 : 0.476)	10-16	0.55(2)	0.34(1)	0.907(6)	0.340/18
(0.112 : 0.7)	10-16	0.67(4)	0.46(2)	1.138(6)	0.122/18
(0.112 : 0.84)	10-16	0.76(4)	0.54(3)	1.290(7)	0.143/18
(0.112 : 0.896)	10-16	0.81(5)	0.58(4)	1.352(7)	0.159/18
(0.14 : 0.14)	13-30	0.43(1)	0.192(6)	0.582(2)	5.393/51
(0.14 : 0.476)	10-16	0.57(2)	0.36(1)	0.931(5)	0.192/18
(0.14 : 0.7)	10-16	0.69(3)	0.48(2)	1.161(5)	0.082/18
(0.14 : 0.84)	10-16	0.79(4)	0.57(3)	1.312(5)	0.090/18
(0.14 : 0.896)	10-16	0.84(5)	0.61(4)	1.373(6)	0.106/18
(0.476 : 0.476)	10-16	0.83(3)	0.60(3)	1.237(6)	0.472/18
(0.7 : 0.7)	10-15	1.32(5)	1.01(4)	1.658(4)	12.886/15

Table 4.3: Pseudoscalar meson masses from degenerate and non-degenerate combinations of valence quark masses on the $m_{sea} = 0.02/0.05$ dataset.

Valence quarks	Timeslices	Results			
$(m_1 : m_2)$	$t_{min} - t_{max}$	Z_{PP}	Z_{AA}	am_{PS}	χ^2/dof
(0.056 : 0.056)	12-30	0.37(3)	0.089(4)	0.350(5)	15.223/54
(0.056 : 0.07)	12-30	0.37(3)	0.096(4)	0.372(5)	14.376/54
(0.056 : 0.084)	12-30	0.37(3)	0.104(5)	0.394(5)	13.600/54
(0.056 : 0.112)	12-30	0.38(2)	0.118(6)	0.434(5)	12.301/54
(0.056 : 0.14)	12-30	0.39(2)	0.133(8)	0.472(6)	11.178/54
(0.056 : 0.644)	10-16	0.58(4)	0.37(2)	1.028(9)	0.392/18
(0.056 : 0.7)	10-16	0.60(5)	0.39(3)	1.09(1)	0.386/18

Valence quarks	Timeslices	Results			
$(m_1 : m_2)$	$t_{min} - t_{max}$	Z_{PP}	Z_{AA}	am_{PS}	χ^2/dof
(0.056 : 0.84)	10-16	0.67(5)	0.45(4)	1.23(1)	0.392/18
(0.056 : 0.896)	10-16	0.69(6)	0.48(5)	1.29(2)	0.400/18
(0.056 : 0.98)	10-16	0.74(9)	0.52(6)	1.38(2)	0.664/18
(0.07 : 0.07)	12-30	0.37(3)	0.104(5)	0.393(4)	13.593/54
(0.07 : 0.084)	12-30	0.38(2)	0.111(5)	0.414(5)	12.857/54
(0.07 : 0.112)	12-30	0.38(2)	0.126(6)	0.453(5)	11.582/54
(0.07 : 0.14)	12-30	0.39(2)	0.140(7)	0.489(5)	10.473/54
(0.07 : 0.644)	10-16	0.59(4)	0.38(2)	1.040(8)	0.384/18
(0.07 : 0.7)	10-16	0.62(4)	0.40(3)	1.099(9)	0.380/18
(0.07 : 0.84)	10-16	0.69(5)	0.47(3)	1.25(1)	0.377/18
(0.07 : 0.896)	10-16	0.72(7)	0.50(4)	1.31(2)	0.361/18
(0.07 : 0.98)	10-16	0.77(9)	0.55(6)	1.40(2)	0.446/18
(0.084 : 0.084)	12-30	0.38(2)	0.118(6)	0.433(5)	12.143/54
(0.084 : 0.112)	12-30	0.39(2)	0.133(6)	0.470(4)	10.879/54
(0.084 : 0.14)	12-30	0.40(2)	0.147(7)	0.506(4)	9.778/54
(0.084 : 0.644)	10-16	0.61(4)	0.39(2)	1.053(8)	0.378/18
(0.084 : 0.7)	10-16	0.63(4)	0.42(2)	1.111(9)	0.375/18
(0.084 : 0.84)	10-16	0.70(5)	0.49(3)	1.26(1)	0.368/18
(0.084 : 0.896)	10-16	0.74(6)	0.52(4)	1.32(1)	0.340/18
(0.084 : 0.98)	10-16	0.80(8)	0.57(6)	1.41(2)	0.336/18
(0.112 : 0.112)	12-30	0.40(2)	0.147(7)	0.505(4)	9.623/54
(0.112 : 0.14)	12-30	0.40(1)	0.161(7)	0.539(3)	8.539/54
(0.112 : 0.644)	10-16	0.63(4)	0.41(2)	1.077(8)	0.361/18
(0.112 : 0.7)	10-16	0.66(4)	0.44(2)	1.136(8)	0.360/18
(0.112 : 0.84)	10-16	0.74(5)	0.52(3)	1.28(1)	0.349/18
(0.112 : 0.896)	10-16	0.78(6)	0.55(3)	1.35(1)	0.313/18
(0.112 : 0.98)	10-16	0.85(7)	0.61(5)	1.44(2)	0.251/18

Valence quarks	Timeslices	Results			
$(m_1 : m_2)$	$t_{min} - t_{max}$	Z_{PP}	Z_{AA}	am_{PS}	χ^2/dof
(0.14 : 0.14)	12-30	0.41(2)	0.175(8)	0.571(3)	7.481/54
(0.14 : 0.644)	10-16	0.66(4)	0.44(2)	1.102(8)	0.339/18
(0.14 : 0.7)	10-16	0.69(4)	0.47(3)	1.160(8)	0.339/18
(0.14 : 0.84)	10-16	0.77(5)	0.55(3)	1.308(10)	0.328/18
(0.14 : 0.896)	10-16	0.81(6)	0.59(3)	1.37(1)	0.290/18
(0.14 : 0.98)	10-16	0.89(7)	0.65(5)	1.46(1)	0.226/18

Table 4.4: Pseudoscalar meson masses from degenerate and non-degenerate combinations of valence quark masses on the $m_{sea} = 0.03/0.05$ dataset.

Sea quarks	Valence quarks	Timeslices	Results	
$(m^1_{sea} : m^2_{sea})$	$(m_1 : m_2)$	$t_{min} - t_{max}$	am_N	χ^2/dof
(0.02 : 0.05)	(0.0476 : 0.0476)	10-16	0.75(3)	0.014/5
(0.02 : 0.05)	(0.056 : 0.056)	10-16	0.79(3)	0.021/5
(0.02 : 0.05)	(0.084 : 0.084)	10-16	0.90(2)	0.040/5
(0.02 : 0.05)	(0.112 : 0.112)	10-16	1.00(2)	0.067/5
(0.02 : 0.05)	(0.14 : 0.14)	10-16	1.08(2)	0.097/5
(0.02 : 0.05)	$m_q \to 0$	0.58(4)		0.285/2
(0.03 : 0.05)	(0.056 : 0.056)	10-15	0.82(6)	0.040/5
(0.03 : 0.05)	(0.07 : 0.07)	10-15	0.86(4)	0.010/5
(0.03 : 0.05)	(0.084 : 0.084)	10-15	0.90(3)	0.009/5
(0.03 : 0.05)	(0.112 : 0.112)	10-15	0.99(2)	0.016/5
(0.03 : 0.05)	(0.14 : 0.14)	10-15	1.07(2)	0.021/5
(0.03 : 0.05)	$m_q \to 0$	0.65(8)		0.024/2

Table 4.5: Nucleon masses for the $m_{sea} = 0.02/0.05$ and $m_{sea} = 0.03/0.05$ datasets.

Sea quarks	Valence quarks	Timeslices	Results	
$(m^1_{sea} : m^2_{sea})$	$(m_1 : m_2)$	$t_{min} - t_{max}$	am_Δ	χ^2/dof
(0.02 : 0.05)	(0.0476 : 0.0476)	8-16	0.94(9)	0.672/5
(0.02 : 0.05)	(0.056 : 0.056)	8-16	0.97(8)	0.990/5
(0.02 : 0.05)	(0.084 : 0.084)	8-16	1.06(7)	0.540/5
(0.02 : 0.05)	(0.112 : 0.112)	8-16	1.13(5)	0.123/5
(0.02 : 0.05)	(0.14 : 0.14)	8-16	1.20(4)	0.124/5
(0.02 : 0.05)	$m_q \to 0$	0.8(1)		0.022/2
(0.03 : 0.05)	(0.056 : 0.056)	8-16	0.95(7)	3.95/5
(0.03 : 0.05)	(0.07 : 0.07)	8-16	1.01(5)	2.65/5
(0.03 : 0.05)	(0.084 : 0.084)	8-16	1.05(4)	1.85/5
(0.03 : 0.05)	(0.112 : 0.112)	8-16	1.13(3)	1.19/5
(0.03 : 0.05)	(0.14 : 0.14)	8-16	1.19(2)	1.01/5
(0.03 : 0.05)	$m_q \to 0$	0.8(1)		0.094/2

Table 4.6: Decuplet masses for the $m_{sea} = 0.02/0.05$ and $m_{sea} = 0.03/0.05$ datasets.

Sea Quarks	$\hat{m}$	m_s	$(aM_{PS})^2\big\|_{m_q=0}$
$am_{\text{sea}} = 0.03/0.05$	0.008(1)	0.092(2)	-0.011(3)
$am_{\text{sea}} = 0.02/0.05$	0.005(1)	0.088(1)	-0.004(3)

Table 4.7: Normal and strange quark masses and the intercept of the pseudoscalar meson mass squared versus quark mass.

Valence quarks	Results	
$(m_1 : m_2)$	A_{PP}	af_{PS}
(0.0476 : 0.0476)	0.19(2)	0.109(7)
(0.0476 : 0.056)	0.18(2)	0.109(7)
(0.0476 : 0.084)	0.17(2)	0.112(6)
(0.0476 : 0.112)	0.16(1)	0.115(4)
(0.0476 : 0.14)	0.16(1)	0.118(4)
(0.056 : 0.056)	0.18(2)	0.110(6)
(0.056 : 0.084)	0.17(1)	0.113(5)
(0.056 : 0.112)	0.16(1)	0.116(4)
(0.056 : 0.14)	0.16(1)	0.118(4)
(0.084 : 0.084)	0.16(1)	0.115(4)
(0.084 : 0.112)	0.16(1)	0.118(4)
(0.084 : 0.14)	0.157(9)	0.121(3)
(0.112 : 0.112)	0.157(9)	0.121(3)
(0.112 : 0.14)	0.158(8)	0.124(3)
(0.14 : 0.14)	0.160(8)	0.128(3)
$m_q \to 0$	0.099(9)	
$af_{PS}(m_q = \hat{m})$	0.100(9)	
$af_{PS}(m_q = m_s)$	0.108(7)	

Table 4.8: Pseudoscalar meson decay constant from degenerate and non-degenerate combinations of valence quark masses on the $m_{sea} = 0.02/0.05$ dataset.

Valence quarks	Results	
$(m_1 : m_2)$	A_{PP}	af_{PS}
(0.056 : 0.056)	0.19(3)	0.119(9)
(0.056 : 0.07)	0.18(3)	0.120(8)
(0.056 : 0.084)	0.18(3)	0.120(8)
(0.056 : 0.112)	0.17(2)	0.122(7)
(0.056 : 0.14)	0.16(2)	0.123(6)
(0.07 : 0.07)	0.18(3)	0.120(8)
(0.07 : 0.084)	0.17(2)	0.121(7)
(0.07 : 0.112)	0.16(2)	0.122(7)
(0.07 : 0.14)	0.16(1)	0.124(6)
(0.084 : 0.084)	0.17(2)	0.121(7)
(0.084 : 0.112)	0.16(1)	0.123(6)
(0.084 : 0.14)	0.16(1)	0.124(5)
(0.112 : 0.112)	0.15(1)	0.124(5)
(0.112 : 0.14)	0.15(1)	0.124(5)
(0.14 : 0.14)	0.15(1)	0.127(5)
$m_q \to 0$	0.115(13)	
$af_{PS}(m_q = \hat{m})$	0.115(12)	
$af_{PS}(m_q = m_s)$	0.119(9)	

Table 4.9: Pseudoscalar meson decay constant from degenerate and non-degenerate combinations of valence quark masses on the $m_{sea} = 0.03/0.05$ dataset.

Sea quarks	Valence quarks	Results		
$(m^1_{sea} : m^2_{sea})$	m_h	Intercept	Gradient	aM_{Hs}
(0.02 : 0.05)	0.7	1.05(1)	0.80(8)	1.119(7)
(0.02 : 0.05)	0.84	1.21(2)	0.73(8)	1.273(7)
(0.02 : 0.05)	0.896	1.27(2)	0.7(1)	1.335(9)
(0.03 : 0.05)	0.7	1.04(1)	0.88(5)	1.12(1)
(0.03 : 0.05)	0.84	1.18(2)	0.89(7)	1.27(1)
(0.03 : 0.05)	0.896	1.24(2)	0.9(1)	1.33(1)

Table 4.10: Intercept and gradient for the extrapolation of aM_{Hl} versus m_h and the interpolated value aM_{Hs} at the strange quark mass for both the $m_{sea} = 0.02/0.05$ and $m_{sea} = 0.03/0.05$ datasets.

Sea quarks	Valence quarks	Results		
$(m^1_{sea} : m^2_{sea})$	m_h	Intercept	Gradient	af_{Hs}
(0.02 : 0.05)	0.7	0.13(1)	0.16(4)	0.146(6)
(0.02 : 0.05)	0.84	0.14(1)	0.16(5)	0.152(7)
(0.02 : 0.05)	0.896	0.14(1)	0.15(6)	0.155(8)
(0.03 : 0.05)	0.7	0.13(1)	0.18(4)	0.145(8)
(0.03 : 0.05)	0.84	0.13(1)	0.22(4)	0.148(9)
(0.03 : 0.05)	0.896	0.128(9)	0.24(5)	0.15(1)

Table 4.11: Intercept and gradient for the extrapolation of af_{Hl} versus m_h and the interpolated value af_{Hs} at the strange quark mass for both the $m_{sea} = 0.02/0.05$ and $m_{sea} = 0.03/0.05$ datasets.

Chapter 5

2+1 flavour domain wall QCD

In this chapter results for hadron masses and pseudoscalar meson decay constants in 2+1 flavour domain wall QCD with the DBW2 and Iwasaki gauge actions are presented. The lattices used have linear sizes in the range 1.6 to 2.2fm and u and d quark masses as low as one quarter of the strange quark mass.

5.1 Simulation Parameters

Section 2.10 describes the domain wall fermion action used in this work whilst the DBW2 and Iwasaki gluonic actions are described in section 2.13. The analysis was carried out on 2+1 flavour domain wall fermion configurations generated on the QCDOC machines. In the DBW2 case the ensembles have three different β values: 0.72, 0.764 and 0.78, while for the Iwasaki case they have two: 2.13 and 2.2. All ensembles were generated using the RHMC algorithm [50, 51] with a trajectory length of 0.5, volume of 16^3x32, fifth dimension length of 8, and a domain wall height of 1.8. Two different ensembles were generated at each β value, one with a light isodoublet with mass $m_{ud} = \frac{1}{2}m_s$ and one where the light sea quark masses are both equal to a rough estimate of the strange quark mass,

m_s. An additional DBW2 ensemble with a light isodoublet mass $m_{ud} = \frac{1}{4}m_s$ at β=0.72 was generated. The number of trajectories in each ensemble and the mnemonics that will be used subsequently to describe the different ensembles are given in table 5.1. The ensembles had $am_{ud} = 0.01$, 0.02 or 0.04 and $am_s = 0.04$. Non-degenerate mesons were created on the $\beta = 0.72$ ensembles where the light quark mass in the correlators was fixed to be equal to the light quark mass in the sea.

5.2 Computation

The $(0.72, 0.01/0.04)$ configurations, the $(0.764, 0.04/0.04)$ MC8 configurations and the $(2.2, 0.04/0.04)$ MC1 configurations (see table 5.4 and discussions in section 5.6) were generated on the QCDOC machines at Brookhaven National Laboratory. All other configurations and measurement data used in this chapter were generated on the QCDOC machines at the University of Edinburgh. The amount of compute time required to generate the ensembles and perform the required analysis depends on the parameters of the ensemble. However, as a guide, the $(0.72, 0.01/0.04)$ ensemble was generated on 1024 nodes of QCDOC at a rate of 3.75 configurations per hour while for the $(2.13, 0.02/0.04)$ ensemble this increases to 4.2 configurations per hour and to 4.5 configurations per hour for the $(2.13, 0.04/0.04)$ ensemble. In going from 1024 nodes to 2048 nodes of QCDOC the compute time required for the $(2.13, 0.02/0.04)$ ensemble decreases to 6.9 configurations per hour. The measurement for the $(0.72, 0.01/0.04)$ ensemble was carried out on 2048 nodes of QCDOC. For the $m_q = 0.01$ quark 1200-1300 CG iterations were required per spin-colour component which took 8-9 seconds per component. For the $m_q = 0.04$ quark this drops to 450 CG iterations which took 3-3.5 seconds per spin-colour component.

5.3 Autocorrelation length and thermalisation

Figure 5.2 shows a typical Monte-Carlo history for the ensembles. The values plotted are the average plaquette and the fourteenth timeslice of the pseudoscalar meson, ρ meson and nucleon correlator. It can be seen from the figure that, as expected, different observables take different amounts of evolution time in order to reach thermalisation. Beyond $\sim$ 800 trajectories there is no visible trend above the noise in any of the observables studied. With more statistics it may be possible to see longer term trends in some observables. A cut for thermalisation is imposed at at least 800 trajectories except for the $(0.764, 0.04/0.04)$ case discussed in section 5.6.

In this section we attempt to measure the autocorrelation times on our ensembles (Table 5.1). This work closely follows [57] while further discussion of similar methods may be found in [45, 58, 44, 8] and [106]. The importance of the autocorrelation time is that it gives insight into the statistical quality of the configurations. This is essential as the more independent the configurations the closer our sample average will be to being normally distributed around the mean value. Ideally we would like our configurations to be completely decorrelated with one another. However, in practice, the correlation length depends on the observable we wish to measure and often requires a very large ensemble. Estimators of the autocorrelation time are noisy and this makes accurate evaluation of the autocorrelation time difficult.

To obtain reliable estimates for the exponential, τ_{exp}, and cumulative, τ_A^{cum}, autocorrelation time defined in section 2.18, autocorrelations should be measured using ensembles containing many more configurations than the value of the integrated autocorrelation time, τ_A^{int}. Figure 5.3 shows example plots for the autocorrelation function (top) and the integrated cumulative autocorrelation time (bottom) on the $\beta = 0.72$ ensembles. The statistical errors plotted for $\rho(t)$ and

τ_{cum} were estimated using a jackknife procedure. In order to take into account the effects of autocorrelations in the error estimates for $\rho(t)$ and τ_{cum} themselves, the original data for $\rho(t)$ and τ_{cum} were grouped in bins of size b. Jackknife averages were then formed for varying bin size. The error bands shown in figures 5.3 top and bottom were calculated by increasing the bin size, b, until the jackknife errors stabilised.

The plot of $\ln\rho(t)$, e.g. figure 5.3 (top), was used to obtain the exponential autocorrelation time and then a plateau was sought in the graph of the cumulative autocorrelation time, e.g. figure 5.3 (bottom), in order to give an estimate of the integrated autocorrelation time.

Table 5.2 shows results for the autocorrelation time on the datasets composed of single long chains. Due to the relatively small ensemble size of all the datasets the autocorrelation time could not be measured precisely. Indeed, for the datasets with smaller chains than those shown in table 5.2 realistic measurements for autocorrelation times were not possible. For these datasets, the autocorrelation time was assumed to be similar to that of the longer chains.

5.3.1 Binning

The analysis in section 3.17 of autocorrelation times shows that statistically independent configurations for a quantity A are separated by $2\tau_A^{int}$. Due to the high computational cost of generating the dynamical configurations, and subsequent limited ensemble size, using independent configurations separated by $2\tau_A^{int}$ would significantly degrade the statistical quality of the Monte-Carlo estimate of the quantity $\bar{A}$. An alternative way of obtaining the correct error estimate from an updating sequence with autocorrelations is by binning. Assuming that the sequence of gauge configurations is long enough, they are 'binned' into blocks of sequential configurations on which the measurements are then averaged. The

bin averages are considered as results of a single measurement on an independent configuration and a full correlated analysis is performed with the binned data as input. The error estimate is obtained from

$$\sigma_{\bar{A}}^2 = \frac{\overline{A^2} - \overline{A}^2}{N-1} = \frac{\overline{\left(A - \bar{A}\right)^2}}{N-1}. \tag{5.1}$$

If the bins are large enough, larger than the autocorrelation time, then the average values in different bins are practically uncorrelated and the error estimate from $\sigma_{\bar{A}}$ is correct. Therefore, if the bins are further increased, beyond the autocorrelation time, the error estimates remain constant.

Figure 5.4 (top) shows a comparison of binning and sampling. In the binning case the 12^{th} timeslice of the ρ correlator is oversampled and averaged into bins of increasing size. In the sampling case $\frac{N_{cfgs}}{h}$ configurations where N_{cfg} is the total number of configurations in the ensemble and h is the separation between configurations are used. In both the binning and sampling case the errors and average value are obtained by a jackknife analysis. Sampling every configuration and binning with a bin size of 1 are equivalent and therefore produce the same value.

Figure 5.4 (bottom) shows the magnitude of the binned jackknifed error versus bin size. The observed errors stabilised with a bin size of $\gtrsim 20$. This is in good agreement with the calculated integrated auto-correlation time for the pseudoscalar meson (table 5.2).

In all the analysis that follows correlators were oversampled and averaged into bins in order to deal with autocorrelation effects. A full correlated analysis was then performed with the binned data as input.

5.4 Measurement Analysis

Table 5.3 lists the measurements performed on each dataset. The (0.78,0.04/0.04) and (0.78,0.02/0.04) datasets have very limited statistics compared to the other datasets. Measurements were made on every fifth or tenth configuration with a valence quark mass equal to the light quark mass in the sea. On some of the ensembles correlators were measured with sources on multiple time planes (N_{tp} in table 5.3) to improve statistics.

5.5 Smearing Analysis

Several types of smearing were used in the analysis (see table 5.3). In particular, point sources (LL-LL), wall sources (WL-WL), and gauge fixed hydrogen-like wavefunction smearing where one (SL-LL) or two (SL-SL) of the quark propagators in a meson correlator were smeared at the source. The hydrogen-like wavefunction smearing is very similar to that described in [67, 66]. For all smearing cases the aim was to create an operator that had as large an overlap as possible with the ground state of the observable in question. Qualitatively, this can be seen in the early plateau of the effective mass, allowing fits to the ground state to start at early timeslices. In the case of the gauge fixed hydrogen-like wavefunction smearing, the effectiveness of the smearing depends on the smearing radius in the smearing function. The radius governs the shape of the hydrogen like smearing function. Figure 5.5 shows an effective mass plot for the vector meson comparing the different types of smearing considered. In the case of the hydrogen-like wavefunction smearing, several different radii were compared. By examining the onset of the plateau in effective mass plots for the pseudoscalar meson and the vector meson a radius of 3.0 was chosen for the hydrogen-like smearing which seemed to be optimal for both states.

In the case of the baryons, correlators were generated with point sources (LL-LL-LL), wall sources (WL-WL-WL) and gauge fixed hydrogen-like wavefunction smearing where two of the quark propagators in the baryon correlator were smeared at the source (SL-SL-LL).

Figure 5.6 shows the fitted value of the pseudoscalar meson mass for various different types of smearing. The analysis was performed on the (0.72,0.02/0.04) dataset where there were equal numbers of correlators with different types of smearing. It is observed that fitting to a single smearing type produces a larger error than fits to two of the smeared correlators using a fit function which includes the first excited state. Single cosh fits starting on timeslice 6 are observed to be systematically higher than those starting on timeslice 10 where t_{max} is held fixed and equal to 16. It can be seen that all of the smeared correlators produce a slightly smaller mass than the local-local correlator over the same fit range. This may hint that the local-local correlator is still being affected by excited states and, in order to remove this, one ought to fit the local-local correlator at later times.

5.6 Farming

The ensembles generated for this analysis were produced primarily for a search of parameter space to guide larger production runs. In many cases subsequent choice of parameters to explore depended on ensembles running at that time, so it was very important to generate ensembles as quickly as possible. Computational constraints meant that several smaller machines were available for this exploration work rather than one (or more) larger machines. Due to the computational time cost for generating single long chain Monte-Carlo ensembles of a reasonable size, several short chains were 'spawned' from an original Monte-Carlo chain (see figure 5.1).

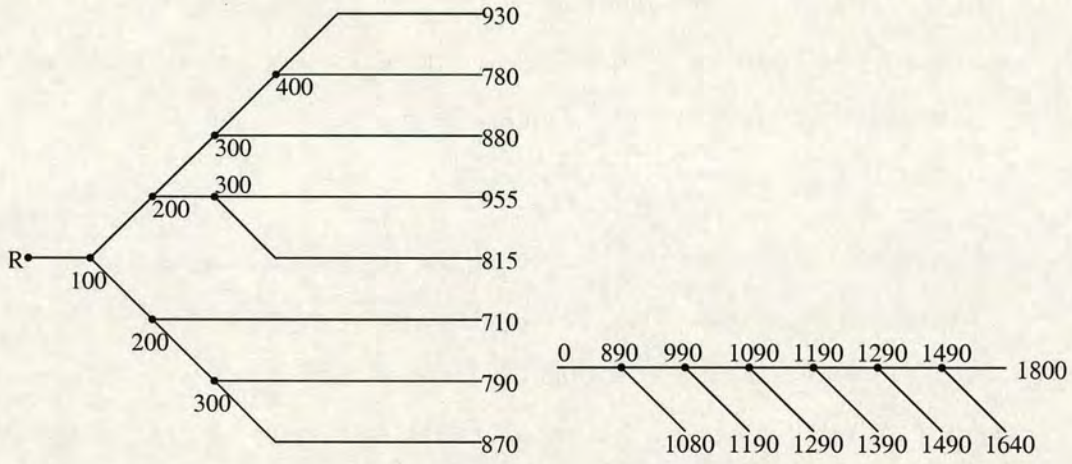

Figure 5.1: β=0.764 datasets were 'farmed' from an original dataset. **LEFT:** (0.764,0.04/0.04) started from a thermalised R-algorithm configuration. **RIGHT:** (0.764,0.02/0.04) was started from an ordered configuration which was allowed to thermalise and was then 'farmed'.

Starting from a configuration in the original chain, a second distribution of random numbers (different from those in the original evolution) were generated and these were subsequently used to evolve another chain or branch. These branches were 'farmed' on several smaller machines, using trivial parallelism to maximum effect. This had the advantage of increasing statistics to an acceptable level while keeping the 'wall clock' time required to a minimum. Table 5.4 shows the separate branches of the $\beta = 0.764$ and $\beta = 2.2$ ensembles used in this analysis.

Figure 5.7 (top) shows three timeslices of the pseudoscalar meson correlator averaged over each Monte-Carlo branch compared to aggregating all the branches together. The errors are obtained by the jackknife method. For comparison, figure 5.7 (bottom) shows the same, but on separate blocks of one long chain Monte-Carlo ensemble, which are approximately the same size as one of the MC branches. The long chain was measured on only one time-plane per configuration whereas the branches had four time-planes per configuration. This accounts

for the slightly larger fluctuations on the bottom figure. The aggregation of the branches leads to improved error estimation and no systematic trends are observed across the chains. However, one disadvantage of this process is that autocorrelation information is limited.

5.7 Fitting the data

The following sections discuss the results of the analysis procedure used to extract the lattice masses of various hadronic observables. As far as possible the analysis was carried out in the same way across all the datasets. All fits to masses were correlated fits and used 100 bootstrap samples to estimate the error. Effective mass plots were studied in order to determine the onset of the ground-state plateau. Final values for the fits were decided on minimising χ^2/dof while at the same time trying to obtain a timeslice interval over which fitted values were stable when the timeslices fitted over were moved by one or two timeslices.

5.8 Residual mass

The residual mass is a measure of the violation of chiral symmetry [107]. In all the ensembles the length of the fifth dimension is relatively short, hence there is a significant left-right coupling between the quark fields on opposite walls. The residual mass (see section 2.11) was calculated from the ratio of the point-split pseudoscalar density $\mathcal{J}_5^a$ at the middle of the fifth dimension to the pseudoscalar density P built from the fields on the walls [107]

$$am_{\text{res}} = \frac{\Sigma_{\vec{x},\vec{y}}\langle \mathcal{J}_5^a(\vec{y},t,\frac{L_s}{2})P^a(\vec{x},0)\rangle}{\Sigma_{\vec{x},\vec{y}}\langle P^a(\vec{y},t)P^a(\vec{x},0)\rangle}. \tag{5.2}$$

The value of m_{res} is obtained by fitting the above ratio to a plateau. For most datasets good signals for the value of am_{res} were observed, as can be seen in

figure 5.8 (top).

For the (0.72,0.01/0.04) ensemble, shown in figure 5.8 (bottom), which has the smallest light quark mass and is the coarsest lattice of all the ensembles, there is a clear "wiggle" in all the different smearing types available on this dataset. This made obtaining a value for am_{res} with an acceptable χ^2/dof difficult. Fitting the dip in the wiggle produces an acceptable χ^2/dof but clearly a value for am_{res} which is too small. On the other hand, fitting only the last few timeslices (i.e. ignoring the wiggle), gives a value of am_{res} which is too large. As the "wiggle" was apparent in all the different smearings a simultaneous fit to two of the smearings produced a large χ^2/dof. A fit from $t_{min} = 5$ to $t_{max} = 16$ to only the $SL - SL$ correlator, although having a relatively large χ^2/dof, gives a value in the middle and was finally chosen. In the process of attaining a final value it was observed that increasing (or decreasing) the bin size and changing the thermalisation point had little effect on the outcome of the fit. Similar fluctuations have also been observed in high statistics runs [102].

For all the other ensembles the value of am_{res} was obtained by a simultaneous fit to two correlators with different smearings. Due to the small value of am_{res} and because the errors are of $\mathcal{O}(10^{-4} - 10^{-5})$ it might be hoped that any slight deviation in am_{res} from the fit will have little effect on other quantities. The fitted values can be seen in table 5.5.

5.9 Pseudoscalar and ρ meson masses

As with the residual mass, good signals for the pseudoscalar meson and ρ meson were observed for most datasets. The masses were obtained by simultaneously fitting a pair of correlators with different smearings to the ground and first excited

state using the function

$$\begin{aligned} C_1(t) &= A_1^G \left(e^{-m_G t} + e^{-m_G(T-t)}\right) + A_1^E \left(e^{-m_E t} + e^{-m_E(T-t)}\right) \\ C_2(t) &= A_2^G \left(e^{-m_G t} + e^{-m_G(T-t)}\right) + A_2^E \left(e^{-m_E t} + e^{-m_E(T-t)}\right). \end{aligned} \tag{5.3}$$

In general, the pseudoscalar and ρ meson mass fits were found to be quite stable under small variations of the fitting range. Figure 5.9 (top) shows a typical pseudoscalar meson effective mass plot for the (0.764,0.02/0.04) ensemble.

Figure 5.9 (bottom) shows the effective mass plot for the (0.72,0.01/0.04) dataset. The plateau "wiggles" and it is therefore difficult to get a reliable fit value for the mass. Several fits were attempted: removing the excited state from the fit (this is equivalent to setting $A_1^E = A_2^E = m_E = 0$ in equation (5.3)), fitting a single cosh to one of the correlators, adjusting the bin size and adjusting the thermalisation point, however, the fit did not improve with any of these. Once again a fit range was chosen, which although giving a relatively large χ^2/dof, gives a fitted value at about the median of all the different possibilities. It may be the case that for this dataset, although there is a relatively long chain, there is still not enough statistics. The slight deviation of the data from the fit lines at early timeslices in figures 5.9 and 5.10 is due to the inclusion of the excited state in the fit and the fit lines should be used to 'guide the eye' at later timeslices. It is perhaps worth noting that the effective mass is not fitted to a plateau but rather it is the correlators that are fitted to the functional form.

Due to the lack of statistics on the (0.78,0.02/0.04) and (0.78,0.04/0.04) datasets simultaneous fits to the LL-LL and WL-WL correlators were not reliable. In the (0.78,0.02/0.04) case the WL-WL correlator was fitted to a single cosh in order to extract the ground state, while for the (0.78,0.04/0.04) case the LL-LL correlator was fitted the same way. Table 5.6 gives the values extracted for the pseudoscalar effective mass from these fits.

Figure 5.10 (top) shows a typical effective mass plot for the ρ meson. For most

datasets, including the (0.72,0.01/0.04) dataset, simultaneous fits were performed and the fits were found to be quite stable under small variations of the fitting range. For the (2.13,0.02/0.04) dataset the simultaneous fit to two of the correlators was not as stable. In this case the SL-SL correlator was fitted to a single cosh (see figure 5.10 (bottom)). Due to the lack of statistics on the (0.78,0.04/0.04) dataset in order to produce a more stable fit, the excited state was removed from the fit. Table 5.7 shows the results obtained from these fits.

5.10 Baryon masses

The standard baryon interpolating operator is given by

$$\Omega(x) = \epsilon_{ijk} \left[\psi_i(x) C\Gamma \psi_j(x)\right] \psi_k(x) \tag{5.4}$$

where C is the charge conjugation matrix. For the $I = \frac{1}{2}$ baryons, $\Gamma = \gamma_5$. Another operator, with $\Gamma = 1$, which projects onto the negative parity $I = \frac{1}{2}$ state was also used. For baryon correlators in a finite box with periodic boundary conditions, the backward propagating state is the negative parity partner, that is

$$C_B(t) = A_+ e^{-m_+ t} + A_- e^{-m_-(T-t)}. \tag{5.5}$$

For the $I = \frac{1}{2}$ baryon, the masses of the positive and negative parity states were determined by a simultaneous fit to equation (5.5) using the standard operator ($\Gamma = \gamma_5$), and a single exponential to the negative parity correlator ($\Gamma = 1$),

$$\begin{aligned} C_{B_1}(t) &= A_+ e^{-m_+ t} + A_- e^{-m_-(T-t)} \\ C_{B_2}(t) &= A_- e^{-m_- t} \end{aligned} \tag{5.6}$$

as the backward propagating state of the $\Gamma = 1$ correlator was very noisy and doesn't couple to the m_+ or m_- state. Typically this was computed for the smeared correlator only, as the local correlator had a poor signal. Figure 5.11

(top) shows a typical effective mass plot for the nucleon. The backwards propagating, positive parity state has been reflected about the middle of the time axis. On the (0.72,0.02/0.04) dataset there are two types of smearing: wall-point and gauge fixed hydrogen-like wavefunction smearing at source. Both of these are shown in figure 5.11(bottom). Fits to either type of smearing produces the same nucleon mass within errors, however, the mass of the negative parity partner is less well determined due to the poor signal and has some dependence on the type of smearing chosen. The ensembles have a small volume, too small certainly for excited states such as the $N^{\star}$, but this can be used, eventually in combination with larger volumes runs to try to estimate the size of the finite volume effects on the remaining spectrum.

The statistics on the $\beta = 0.78$ datasets were too poor to attempt a meaningful fit. For the $\beta = 0.764$ datasets and the $\beta = 2.2$ datasets the wall smearing correlators were used, while for the $\beta = 0.72$ and $\beta = 2.13$ datasets gauge fixed hydrogen wavefunction smearing was chosen. The results of the nucleon fits are given in table 5.8. The three fit ranges given are for the forwards propagating state (N_+), the backwards propagating state (N_-), and the negative parity correlator (N'_-).

5.11 Pseudoscalar decay constant

In this section the results for measurements of the pseudoscalar meson decay constant obtained using the three different methods outlined in section 3.11 will be presented.

5.11.1 Results from Method A

This method requires fitting the form

$$C_{PP}(t) \approx \frac{|\langle 0|P|P\rangle|^2}{2m_{PS}} e^{-m_{PS}\frac{T}{2}} \cosh(m_{PS}(\frac{T}{2} - t)) \tag{5.7}$$

to the point-point pseudoscalar density correlator, which is equivalent to

$$C_{PP}(t) = A^{PP}\left(e^{-m_G t} + e^{-m_G(T-t)}\right), \tag{5.8}$$

and allows the evaluation of the amplitude,

$$A_{PP} = \frac{|\langle 0|P|P\rangle|^2}{2m_{PS}} = \frac{Z_{PP}^2}{2m_{PS}}, \tag{5.9}$$

and mass, m_{PS}. After fitting, the pseudoscalar decay constant is found from

$$f_{PS}^{PP} = \frac{2\sqrt{2}(m_q + m_{\text{res}})\sqrt{A_{PP}}}{m_{PS}^{3/2}} \tag{5.10}$$

where the input from the pseudoscalar density correlator fit are A_{PP} and m_{PS}. Due to the partial chiral symmetry the quark mass must be shifted by the additive mass renormalisation m_{res}

$$m_q \to (m_q + m_{\text{res}}). \tag{5.11}$$

In this work the fermion fields are normalised by

$$\psi \to \kappa_5 \psi, \quad \kappa_5 = \frac{1}{\sqrt{(N_d - M_5)}} \tag{5.12}$$

where $N_d = 5$ and the domain wall height, $M_5 = 1.8$.

The values of the residual mass used can be found in table 5.5. As the amplitude of the correlator is important only the local-local correlator was fitted. This was done in two ways. Firstly, the pseudoscalar meson mass evaluated using the smeared correlators in table 5.6 was held fixed and a one parameter fit performed to extract the amplitude. Secondly a two parameter fit was performed where both the mass and amplitude were allowed to vary. It was observed that both methods

give equivalent values for f_{PS}^{PP}. Figure 5.12 (top and bottom) shows typical fits to the point-point pseudoscalar density correlator for the Iwasaki $\beta = 2.13$ and DBW2 $\beta = 0.764$ datasets used to extract the amplitude for f_{PS}^{PP}.

As can be observed from figure 5.9(bottom) for the (0.72,0.01/0.04) dataset, there is a "wiggle" which made obtaining a reliable value for the pseudoscalar meson mass difficult. This is clearly equally true for the extracting the amplitude from the local-local correlator. The "wiggle" manifests itself with the large χ^2/dof for f_{PS}^{PP} on this dataset. Table 5.9 gives the fitted values.

5.11.2 Z_A

For the remaining two methods of calculating f_{PS} an explicit calculation of the Z_A factor in equation (3.81) is required. The calculation of Z_A is described in section 3.11.2. The ratio of correlators

$$Z_A(t) = \frac{C(t+\frac{1}{2}) + C(t-\frac{1}{2})}{4L(t)} + \frac{C(t+\frac{1}{2})}{(L(t)+L(t+1))} \tag{5.13}$$

is fitted to a constant for suitably large t. Good signals were observed on all datasets for Z_A, as can be seen in figure 5.13. In all cases a fit to the wall-point or smeared-point correlators was sufficient to extract this ratio. The results of these fits can be found in table 5.10.

5.11.3 Results from Method B

In this case we fit the axial-axial correlator

$$C_{A_4A_4}(t) \approx \frac{|\langle 0|A_4|P\rangle|^2}{2m_{PS}} e^{-m_{PS}\frac{T}{2}} \cosh(m_{PS}(\frac{T}{2} - t)) \tag{5.14}$$

to

$$C_{A_4A_4}(t) = A_{A_4A_4}\left(e^{-m_G t} + e^{-m_G(T-t)}\right). \tag{5.15}$$

This allows the evaluation of the amplitude,

$$A_{A_4A_4} = \frac{|\langle 0|A_4|P\rangle|^2}{2m_{PS}} = \frac{Z^2_{A_4P}}{2m_{PS}}, \tag{5.16}$$

and mass m_{PS}. The axial-axial correlator has an overlap with the pseudoscalar meson ground state so the fit was performed both by holding the pseudoscalar meson mass fixed from table 5.6, and by allowing it to vary. In all cases the outcome of the fit did not depend on which of the two choices was made. As the amplitude was important, only the local-local correlator was fitted in this way. Example effective mass plots for these fits can be seen in figure 5.14. Table 5.11 gives the values for the amplitude, $A_{A_4A_4}$, from these fits. The amplitude was then used together with the values of Z_A (see table 5.10) in equation (3.81) to extract the pseudoscalar meson decay constant

$$\begin{aligned} f_{PS}^{AA} &= \frac{Z_A|\langle 0|A_4|P\rangle|}{m_{PS}} \\ &= Z_A\sqrt{\frac{2A_{A_4A_4}}{m_{PS}}}. \end{aligned} \tag{5.17}$$

The fermion fields required to be rescaled as in equation (5.12).

5.11.4 Results from Method C

In this method the ratio of the two-point local axial current

$$C_{A_4P}(t) \approx \frac{\langle 0|A_4|P\rangle\langle 0|P|P\rangle}{2m_{PS}} e^{-m_{PS}\frac{T}{2}} \sinh(m_{PS}(\frac{T}{2} - t)) \tag{5.18}$$

to the pseudoscalar density correlator (5.7) was fitted to the form

$$\frac{C_{AP}(t)}{C_{PP}(t)} = \frac{\langle 0|A_4|P\rangle\langle P|P|0\rangle}{\langle 0|P|P\rangle\langle P|P|0\rangle} \approx \frac{|\langle 0|A_4|P\rangle|}{|\langle 0|P|P\rangle|} \tanh(m_{PS}(\frac{T}{2} - t)). \tag{5.19}$$

The local axial correlator has an overlap with the pseudoscalar meson ground state so the fit was performed both by holding the pseudoscalar mass fixed from the previous fits (see table 5.6) and by allowing the pseudoscalar mass to vary in the fit. The amplitude

$$A_{A_4P} = \frac{|\langle 0|A_4|P\rangle|}{|\langle 0|P|P\rangle|} \tag{5.20}$$

and mass, m_{PS}, was obtained. Substituting this into equation (3.81) and using the amplitude from the fit to the pseudoscalar density correlator (equation(5.9)) together with the value of Z_A (see table 5.10) we obtain an expression for the pseudoscalar decay constant as

$$f_{PS}^{AP} = Z_A \sqrt{\frac{2A_{PP}}{m_{PS}}} A_{A_4P}. \tag{5.21}$$

In all cases holding the pseudoscalar meson mass fixed or allowing it to vary had no effect on the result for f_{PS}^{AP}. Due to the very limited statistics on the (0.78,0.04/0.04) dataset the fit changed by 1 to 2 σ depending on the fit range. Figure 5.15 shows typical example fits to the ratio $\frac{C_{AP}(t)}{C_{PP}(t)}$ for the Iwasaki $\beta = 2.13$ datasets. Table 5.12 gives the values of f_{PS}^{AP} obtained from the ratio fits.

For the (0.72,0.01/0.04) dataset it was again difficult to obtain reliable fit values as can be seen by the large error on the value of f_{PS}^{AP} given in table 5.12. This was probably due to the observed "wiggle" in this dataset mentioned in previous sections. This may be due to a lack of statistics resulting in the error estimation from the covariance matrix being underestimated. The resultant effect of this is the observed large error bars in the pseudoscalar decay constant fit in figure 5.15 (bottom) when compared with the fits on the datasets with the same β value but heavier quark masses.

The fermion fields required to be rescaled as in equation (5.12).

5.12 Setting the scale

The lattice spacing and the volume of the box are determined from the quark-antiquark static potential in [108] using the Sommer scale [109] r_0, where it has been assumed $r_0 = 0.5$fm. The value of r_0/a and the lattice spacing calculated in [108] is given in table 5.13 along with the size of the box. The determination of r_0/a is well defined for each ensemble, and thus it is a good quantity to use

to examine scaling behaviour. As the value of r_0 in the continuum is unknown, rather than setting the absolute scale with r_0, a better strategy is to predict dimensionless ratios of physical quantities in the continuum, while using r_0 just to examine the scaling behaviour. The choice of r_0 to set the scale does, however, impact some quantities indirectly through their dependence on the strange quark mass.

5.13 Chiral extrapolations of light meson masses

The quark mass is defined using the axial Ward identity definition of quark mass through

$$am_q \equiv a(m_f + m_{\text{res}}(m_f)), \tag{5.22}$$

where am_f is the valence quark mass and $m_{\text{res}}(m_f)$ is the residual mass measured using quark propagators generated with a valence quark mass equal to m_f. Chiral extrapolations were performed by taking $am_q \to 0$ using the points where the valence quark mass is equal to the u and d quark masses in the sea.

Other than in the DBW2 β=0.72 case, where a linear fit to three points was performed, straight lines were drawn through the two available points. The values of the residual mass obtained in the chiral limit are shown in table 5.14. These values correspond to a residual mass of ~5-30 MeV. Figure 5.16 (top) shows the residual mass chiral extrapolations on all the datasets. It can be seen that there is little change in the residual mass with decreasing quark mass.

The pseudoscalar mass chiral extrapolations were performed in an analogous way to the residual mass by extrapolating the results to $m_q = 0$. The extrapolations take the form

$$(am_{PS})^2 = B(am_q^{val=sea}) + A \tag{5.23}$$

where the value of A is not constrained to go through zero. Given the low

statistics, an acceptable slight deviation of A from zero, typically less than 2σ, is observed (see table 5.15). Figure 5.16 shows typical example chiral extrapolations for both the Iwasaki datasets. The errors on the points at the chiral limit in figure 5.16 were obtained by drawing straight lines to obtain the maximum and minimum error.

The lattice spacing from the quark-antiquark potential may be compared to that obtained from m_ρ in the chiral limit by performing a linear chiral extrapolation of the vector meson mass

$$am_V = C(am_q^{val=sea}) + D. \tag{5.24}$$

Table 5.16 shows results for the lattice spacing obtained from m_ρ. It can be seen from the table that the lattice spacing obtained from the $\beta = 0.764$ and $\beta = 2.13$ ensembles with different actions are equivalent. These lattice spacings may be compared with those in table 5.13 obtained from the quark-antiquark static potential. Figure 5.17 (top) shows chiral extrapolations for the vector meson for the DBW2 ensembles.

The value of the strange quark mass (table 5.17) was obtained from the physical kaon mass by substituting $am_q^{val=sea} \rightarrow 1/2(am_{q_1} + am_{q_2})$ in eq.(5.23) and setting $am_{q_1} = am_{ud} = 0$ and $am_{q_2} = am_s$. Figure 5.16 (bottom) shows pseudoscalar chiral extrapolation for the Iwasaki datasets. The horizontal dotted lines are the physical kaon mass using the lattice spacing from the quark-antiquark static potential, while the vertical dotted lines are at half the strange quark mass in lattice units.

The determination of the strange quark mass depends on the input of the lattice spacing. Table 5.17 shows additional strange quark mass determinations where the kaon mass required used the lattice spacing from m_ρ and f_{PS} in the chiral limit. It can be seen from table 5.17 that there is a dependence on the value of the strange quark mass on the quantity chosen to set the scale. This may

reduce with improved statistics. However, in this analysis subsequent quantities depending on the strange quark mass will indirectly depend on which quantity is chosen to set the scale. Unless otherwise stated the strange mass used will be that from the quark-antiquark static potential.

The mass of the K^* in table 5.18 was evaluated from the vector meson chiral extrapolation using am_s and the lattice spacing

$$am_{K^*} = C\left(\frac{am_s}{2}\right) + D \tag{5.25}$$

where it has been assumed $am_{q_1} = am_{ud} = 0$. This is shown by the dotted lines in figure 5.17 (top).

5.14 Baryon chiral extrapolations

The nucleon (N) and its negative parity partner ($N^\star$) were extrapolated to the chiral limit $m_q = 0$ using

$$am_X = Eam_q + F \tag{5.26}$$

where $X = \{N, N^\star\}$. Results for this can be seen in table 5.19. Figure 5.17 (bottom) shows typical chiral extrapolations for the baryons on the DBW2 $\beta = 0.72$ and $\beta = 0.764$ datasets. The masses of the baryons on the lightest (0.72,0.01/0.04) ensemble were difficult to obtain reliably and therefore were not included in the chiral extrapolations.

5.15 Chiral extrapolation of f_{PS}

Table 5.20 shows the results of the chiral extrapolation of the three pseudoscalar decay constants: f_{PS}^{PP}, f_{PS}^{AA} and f_{PS}^{AP}. These were extrapolated using the form

$$af_{PS} = Gam_q + H. \tag{5.27}$$

The value of f_{PS} in the chiral limit (H) was used with the physical value f_π to extract the lattice spacing from the datasets. These are shown in table 5.20 and can be compared with the lattice spacing from the quark-antiquark potential and from m_ρ. The lattice spacing obtained from the pseudoscalar meson decay constant was consistently higher than that from the ρ meson (see table 5.16). Good agreement between all methods of calculating f_{PS} was observed. Figure 5.18 (top) shows typical chiral extrapolations of the pseudoscalar meson decay constant for the three methods on the Iwasaki β=2.2 ensemble. Excellent agreement was observed between the three methods on this dataset. Figure 5.18 (bottom) shows the chiral extrapolations of the pseudoscalar decay constant on the Iwasaki β=2.13 ensembles. This dataset has good agreement for f_{PS}^{PP} and f_{PS}^{AP} but only moderate agreement for f_{PS}^{AA} which is slightly higher. The Iwasaki β=2.2 dataset has approximately eight times the statistics of the Iwasaki β=2.13 dataset and this may account for the not quite so good agreement on the β=2.13 dataset. The only moderate agreement on the DBW2 β=0.78 dataset (see table 5.20) is probably due to the lack of statistics. The horizontal dotted lines show the value of af_K obtained from the strange quark mass (vertical lines) using r_0

$$af_K = G\left(\frac{am_s}{2}\right) + H. \tag{5.28}$$

The slight discrepancy between the different method for the Iwasaki β=2.13 dataset leads to the systematic error in the obtained value of af_K. The values of af_{PS} and af_K used in the following sections were obtained from the f_{PS}^{PP} chiral extrapolations on all the datasets.

5.16 Scaling

The ensembles generated for this analysis with several different lattice spacings and two different gauge actions have $\mathcal{O}(a^2)$ discretisation errors. The determination of r_0/a is well defined for each ensemble, and thus it is a good quantity to use

to examine scaling behaviour. As the value of r_0 in the continuum is unknown, rather than setting the absolute scale with r_0, a better strategy is to predict dimensionless ratios of physical quantities in the continuum, while using r_0 to just examine the scaling behaviour. Figures 5.19 and 5.20 show the dependence of various light mesonic quantities, in dimensionless units, on the lattice spacing. The $\beta = 0.78$ points (furthest left red points) on these figures have very large error bars due to the poor statistics on the datasets. For the furthest right β =0.72 points a fit to the chiral behaviour was possible, rather than drawing straight lines, and hence their errors are better estimated. Since m_ρ and m_{K^*} both come from the chiral extrapolation of the vector meson the points on figure 5.19 top and bottom follow the same trend. Similarly figure 5.20 top and bottom both come from the pseudoscalar decay constant chiral extrapolation (f_{PS}^{PP}).

Figures 5.21 and 5.22 show the ratios of various quantities. The different colour symbols correspond to the different gauge actions, Iwasaki in blue and DBW2 in red. Again the furthest two points to the right are the DBW2 β=0.72 points where a chiral fit was performed so their errors are better estimated. Even with the large and crude error estimate for the other results, it may be concluded that there is an indication of scaling. Table 5.21 gives the numerical values for these ratios.

Shown in Figure 5.23 is the dependence of the baryon spectrum, in dimensionless units, on the lattice spacing. A continuum extrapolation cannot be attempted with these ensembles. The data for the ground state nucleon, $\{N\}$, shows reasonable scaling, albeit with large errors. These large uncertainties are due to the crude nature of the chiral extrapolation and the limited statistics available.

The negative parity partner of the nucleon, the $N^\star$ is expected to become degenerate with the nucleon in a small enough box. This effect can be clearly seen from figure 5.23; the $N^\star$ mass drops as the volume is reduced. This suggests that finite size effects may also be beginning to affect the ground states for the ensembles at

finest lattice spacing. These finite size effects would tend to increase the mass of the ground states. The slight upward tendency in the scaling plot as the lattice spacing decreases is consistent with the finite size effects spoiling otherwise very good scaling, or a small scaling violation for the nucleon mass. Although these initial ensembles have a small volume (see table 5.13), too small certainly for excited states such as the $N^{\star}$, this can be used eventually, in combination with the production runs on larger volumes, to estimate the size of the finite volume effects.

5.17 The Edinburgh plot

Shown in figure 5.24 is the Edinburgh plot [110]. This is a useful way of comparing results for different actions without the need for any extrapolations of the data. Shown on the graph are the experimental ratios and the values obtained in the static quark limit, where the hadron mass is equal to the sum of the valence quark masses. The data is compared with the curve obtained from the phenomenological model for the hadron masses described in [111]. The model predicts the hadron masses from the following equations

$$\begin{aligned} M_{\text{baryon}} &= M_b + \sum_{i=1}^{3} m_i + \zeta_b \sum_{i>j} \frac{\mathbf{S_i}.\mathbf{S_j}}{m_i m_j} \\ M_{\text{meson}} &= M_m + \sum_{i=\bar{q},q} m_i + \zeta_m \sum_{i>j} \frac{\mathbf{S_{\bar{q}}}.\mathbf{S_q}}{m_{\bar{q}} m_q} \end{aligned} \tag{5.29}$$

where the constants are taken to have the values, $M_b = 0.077\text{GeV}$, $M_m = -0.057\text{GeV}$, $\zeta_b = 0.02205\text{GeV}^3$ and $\zeta_m = 0.0715\text{GeV}^3$. These formula then depend on the masses, m_i, and spins, $\mathbf{s_i}$, of the constituent quarks of the hadron. The curve is shown as a guide for the eye. It is reassuring that, even at relatively coarse lattice spacing, with a small fifth dimension and consequently moderate chiral symmetry breaking, the data follows the phenomenological curve very well. The only exception is the lightest Iwasaki $\beta = 2.2$ datum which seems slightly

high. Naively, one might expect this to be a finite size effect, especially, examining table 5.13, given that the lattice spacing and thus the box size are rather small. However, the value of Lm_P is not significantly smaller than the other data sets and, critically, $Lm_P > 4$, suggesting that the box is big enough as measured by the pseudoscalar meson.

For comparison the green points in figure 5.24 are from simulations with two dynamical flavours of domain wall fermions [112]. These simulations were performed on $16^3 \times 32$ lattices with a fifth dimension length of 12. They employ the DBW2 gauge action with $\beta = 0.8$ and a domain wall height of $M_5 = 1.8$. The lattice spacing is measured to be $\sim 1.7GeV$ and the dynamical quark masses are in the range $m_{\text{strange}}/2 \lesssim m_{\text{sea}} \lesssim m_{\text{strange}}$. It is pleasing to note that when compared with two flavour simulations the 2+1 flavour simulations show good agreement.

5.18 The J parameter

Since data from different gauge actions and lattice spacings need to be combined, it is worthwhile to look for observables which are independent. This was the motivation, for example, for the Edinburgh plot. The J parameter [113] is defined as

$$J = m_v \frac{dm_V}{dm_{PS}^2} \tag{5.30}$$

and is determined at the experimental ratio

$$\frac{M_{K^*}}{M_K} = 1.8. \tag{5.31}$$

The values of the vector and pseudoscalar masses are defined at this quark mass as m_v and m_{ps}. This allows comparison of lattice results with experimental results without the need for a chiral extrapolation. Using the simplest assumption that the meson masses are given by a Taylor series in the quark masses

$$m_V(q_1, q_2) = d + c(q_1 + q_2) \tag{5.32}$$

$$m_{PS}^2(q_1, q_2) = b(q_1 + q_2) \tag{5.33}$$

implies that a plot of m_V versus m_{PS}^2 will be a straight line for varying quark masses. Here we are working along the 'unitary trajectory' where $m_{\text{sea}} = m_{\text{val}}$. Figure 5.25 (top) shows a plot of am_V versus am_{PS}^2 for the DBW2 β=0.72 and Iwasaki β=2.13 cases and, indeed, for the β =0.72 case, where there are three points, approximate linear behaviour is seen. The intersection of this line with $m_V = 1.8m_{PS}$ (starred points) determines the reference value m_v which is to be multiplied by the slope to yield J. Figure 5.25 (bottom) shows the value of the J parameter on all the datasets. Within the large errors, mostly due to the limited statistics and the crude nature of the extrapolations, good agreement with the experimental value is observed.

5.19 Non-degenerate analysis

On the DBW2 β=0.72 ensembles non-degenerate correlators were created. The light quark mass in the correlator was fixed to be equal to the light quark mass in the sea and the heavy quark mass was varied from 0.04 to 0.06 in steps of 0.01. These correlators had one of the quark propagators in the meson correlator smeared at source using a gauge fixed hydrogen-like wavefunction smearing. Additional correlators with two heavy quarks equal to 0.04, 0.05 or 0.06 were calculated. These additional correlators were used to measure the residual mass (see table 5.22).

Figure 5.26 shows typical pseudoscalar meson effective mass plots for the case of the (0.72,0.02/0.04) dataset (top) and the (0.72,0.04/0.04) dataset (bottom). For the (0.72,0.02/0.04) dataset the light quark mass in the correlator was fixed to be 0.02 while for the (0.72,0.04/0.04) dataset the light quark mass was fixed to be 0.04. The lines shown on the plots are from a single exponential fit to the smeared-local correlator. The results of the fits to these correlators are given in

table 5.23.

For the points where both the quarks in the correlator have a mass equal to the light quark mass in the sea the results from the simultaneous fits presented in section 5.9 were used.

There are four quark masses: two valence quark masses in the correlator and two sea quark masses. These will be denoted $am^V_{q_1}$, $am^V_{q_2}$, $am^S_{q_1}$ and $am^S_{q_2}$ respectively. The chiral extrapolation of the pseudoscalar meson mass squared and the vector meson mass will in principle be functions of all four quark masses

$$(am_{PS})^2 = g_1(am^V_{q_1}, am^V_{q_2}, am^S_{q_1}, am^S_{q_2}) \quad (5.34)$$

$$am_V = g_2(am^V_{q_1}, am^V_{q_2}, am^S_{q_1}, am^S_{q_2}). \quad (5.35)$$

Here we will consider g_1 and g_2 to be linear functions of the quark masses. The heavy quark mass in the sea is fixed equal to 0.04 and therefore the functions g_1 and g_2 will not depend on the heavy quark mass in the sea. Ordering the quark masses so that $am^{S/V}_{q_1} \leq am^{S/V}_{q_2}$ equation (5.34) may be rewritten as

$$(am_{PS})^2 = g_1(am^V_{q_1}, am^V_{q_2}, am^S_{q_1}) \quad (5.36)$$

$$am_V = g_2(am^V_{q_1}, am^V_{q_2}, am^S_{q_1}). \quad (5.37)$$

A two-dimensional fit was performed to the pseudoscalar meson mass squared. The x-axis was equal to the light quark mass in the sea, $am^S_{q_1}$, while the y-axis was given by the average of the two valence quark masses in the correlator

$$(am_{PS})^2 = \delta + \frac{L}{2}\left(am^V_{q_1} + am^V_{q_2}\right) + Mam^S_{q_1}. \quad (5.38)$$

Here M gives the sea quark mass dependence and L the valence quark mass dependence. Denoting the light valence quark mass as $am^V_{q_1}$ it should be noted that for this data $am^V_{q_1} = am^S_{q_1}$. All the quark masses in equation (5.38) have been shifted by the appropriate residual mass. As $am^S_{q_1}$ is the light quark mass in the sea it has been shifted

$$am^S_{q_1} \rightarrow \left(am^S_{f_1} + am^{ll}_{\text{res}}\right) \quad (5.39)$$

where am_{res}^{ll} is the value of the residual mass obtained from the correlator with both quarks equal to the light quark mass in the sea. Similarly for $am_{q_1}^V$ and $am_{q_2}^V$

$$am_{q_1}^V \rightarrow \left(am_{f_1}^V + am_{\text{res}}^{ll}\right) \tag{5.40}$$

$$am_{q_2}^V \rightarrow \left(am_{f_2}^V + am_{\text{res}}^{hh}\right) \tag{5.41}$$

where am_{res}^{hh} is the residual mass value obtained from the correlator with both quarks equal to the heavy valence quark mass.

The normal quark mass, m_n, was evaluated by setting $am_{q_1}^V = am_{q_2}^V = am_n$ and $am_q^S = am_n$ in equation (5.38) and using the physical pseudoscalar meson mass. Figure 5.27 (top) shows the pseudoscalar meson mass squared plotted against the average quark mass $m_q^{ave} = \frac{1}{2}\left(am_{q_1}^V + am_{q_2}^V\right)$. The different colours in the plot correspond to the different ensembles (or light quark masses in the correlator). The fit is not constrained to go through zero and, as in table 5.15 for the degenerate case, a slight deviation of δ from the origin, of order 2σ, is observed. The values obtained can be found in table 5.25 where the lattice spacing has been set in two ways: from the ρ meson mass in the chiral limit (ρ), or by the quark-antiquark static potential (r_0), for comparison.

Figure 5.27 (bottom) shows the dependence of the pseudoscalar meson mass squared on the sea quark mass $am_{q_1}^S$ (or light quark mass in the correlator). The different colours correspond to the different ensembles or light quark masses. It was observed that there was little dependence of the pseudoscalar meson mass squared on the light quark mass in the sea. The horizontal lines on the plot are drawn to guide the eye as these points have equal average valence quark mass.

The strange quark mass is obtained from the physical kaon mass by substituting $am_{q_1}^V = am_n$, $am_{q_2}^V = am_s$ and $am_{q_1}^S = am_n$ in equation (5.38). The values obtained for the strange quark mass are given in table 5.25. The lattice spacing was set from the ρ meson mass in the chiral limit, (ρ), or from the quark-antiquark static potential, (r_0).

Non-degenerate vector mesons were computed and the results of the fits can be seen in table 5.24. Chiral extrapolations of the vector mesons were performed in a similar way to the pseudoscalar meson squared using

$$am_V = P + \frac{Q}{2}\left(am_{q_1}^V + am_{q_2}^V\right) + Ram_{q_1}^S. \tag{5.42}$$

The lattice spacing was calculated by comparing the value in the chiral limit to the experimental value of the ρ meson mass. The value of M_{K^*} was calculated by substituting the values of the strange and normal quark masses into equation (5.42)

$$am_{K^*} = P + \frac{Q}{2}\left(am_n + am_s\right) + Ram_n. \tag{5.43}$$

The lattice spacing required was calculated from the ρ meson mass in the chiral limit (see table 5.25). The value of M_{K^*} compares favourably with the experimental value of 892(1)MeV [70].

Good agreement was observed between the non-degenerate values of am_s, am_ρ and am_{K^*} obtained and given in table 5.25 and the values obtained by the degenerate analysis given in tables 5.16, 5.17 and 5.18.

5.20 Tables

Action	β	$\frac{m_{ud}}{m_s}$	Mnemonic	N_{traj}	Therm
DBW2	0.72	0.01/0.04	(0.72 , 0.01/0.04)	6000	1000
DBW2	0.72	0.02/0.04	(0.72 , 0.02/0.04)	6000	1000
DBW2	0.72	0.04/0.04	(0.72 , 0.04/0.04)	3395	1000
DBW2	0.764	0.02/0.04	(0.764 , 0.02/0.04)	2940*	800
DBW2	0.764	0.04/0.04	(0.764 , 0.04/0.04)	5320*	100**
DBW2	0.78	0.02/0.04	(0.72 , 0.02/0.04)	1505	800
DBW2	0.78	0.04/0.04	(0.72 , 0.04/0.04)	1620	800
Iwasaki	2.13	0.02/0.04	(2.13 , 0.02/0.04)	3595	1000
Iwasaki	2.13	0.04/0.04	(2.13 , 0.04/0.04)	3595	1000
Iwasaki	2.2	0.02/0.04	(2.2 , 0.02/0.04)	5900*	800
Iwasaki	2.2	0.04/0.04	(2.2 , 0.04/0.04)	5800*	800

Table 5.1: RHMC 2+1 flavour datasets. A * denotes that the dataset was obtained by farming (see section 5.6). A ** denotes that the dataset was farmed from a thermalised R algorithm dataset.

Dataset	Ensemble size		$\overline{Plaq}$		PS	
$(\beta : \frac{m_l}{m_s})$	N_{traj}	N_{cfgs}	τ^{cum}	τ^{exp}	τ^{cum}	τ^{exp}
(0.72 , 0.01/0.04)	6000	1000	20^{+10}_{-7}	> 4	13^{+10}_{-8}	> 8
(0.72 , 0.02/0.04)	6000	1000	10^{+5}_{-5}	> 5	15^{+10}_{-10}	> 12
(2.13 , 0.02/0.04)	3595	520	6^{+3}_{-3}	> 6	5^{+3}_{-3}	> 5
(2.13 , 0.04/0.04)	3595	520	6^{+2}_{-4}	> 4	7^{+3}_{-3}	> 9

Table 5.2: Estimates of autocorrelation times for the average plaquette and the pseudoscalar meson on timeslice 14. Note plaquettes are separated by 1 trajectory while pseudoscalar meson correlators by 5 trajectories.

Dataset	N_{traj}	Therm	Separation	N_{tp}	N_{meas}	Smearing
(0.72 , 0.01/0.04)	6000	1000	5	1	1000	L,S
(0.72 , 0.02/0.04)	6000	1000	5	1	1000	L,W,S
(0.72 , 0.04/0.04)	3395	1000	5	1	475	L,W,S
(0.764 , 0.02/0.04)	2940*	800	10	4	215	L,W
(0.764 , 0.04/0.04)	5320*	100**	10	4	541	L,W
(0.78 , 0.02/0.04)	1505	800	5	1	142	L,W
(0.78 , 0.04/0.04)	1620	800	5	1	165	L,W
(2.13 , 0.02/0.04)	3590	1000	5	1	520	L,S
(2.13 , 0.04/0.04)	3590	1000	5	1	520	L,S
(2.2 , 0.02/0.04)	5900*	800	5	4	1026	L,W
(2.2 , 0.04/0.04)	5800*	800	5	4	1004	L,W

Table 5.3: Measurements performed on RHMC 2+1 flavour datasets. A * denotes that the dataset was obtained by farming (see section 5.6). A ** denotes that the dataset was farmed from a thermalised R algorithm dataset. Several types of smearing were used (see section 5.5), in particular, point sources (L), wall sources (W), and hydrogen-like wavefunction smearing (S) where one or two of the quark propagators in a meson correlator were smeared at the source.

Dataset	Branch	N_{traj}	Dataset	Branch	N_{traj}
(0.764, 0.04/0.04)	MC0	100-930	(0.764, 0.02/0.04)	MC0	0-1800
(0.764, 0.04/0.04)	MC1	100-870	(0.764, 0.02/0.04)	MC1	990-1190
(0.764, 0.04/0.04)	MC2	200-800	(0.764, 0.02/0.04)	MC2	890-1080
(0.764, 0.04/0.04)	MC3	200-710	(0.764, 0.02/0.04)	MC3	1290-1490
(0.764, 0.04/0.04)	MC4	300-810	(0.764, 0.02/0.04)	MC4	1190-1390
(0.764, 0.04/0.04)	MC5	300-790	(0.764, 0.02/0.04)	MC5	1090-1290
(0.764, 0.04/0.04)	MC6	400-780	(0.764, 0.02/0.04)	MC6	1490-1640
(0.764, 0.04/0.04)	MC7	300-880	(2.2, 0.02/0.04)	MC0	800-3175
(0.764, 0.04/0.04)	MC8	960-1616	(2.2, 0.02/0.04)	MC1	800-1365
(2.2, 0.04/0.04)	MC0	800-2965	(2.2, 0.02/0.04)	MC2	800-1355
(2.2, 0.04/0.04)	MC1	2760-4320	(2.2, 0.02/0.04)	MC3	800-1330
(2.2, 0.04/0.04)	MC2	1045-1675	(2.2, 0.02/0.04)	MC4	800-1360
(2.2, 0.04/0.04)	MC3	1245-1890	(2.2, 0.02/0.04)	MC6	800-1350

Table 5.4: Farmed Monte-Carlo chain branches aggregated to give the full ensemble.

Dataset	Fit range	Results			
$(\beta, m_{ud}/m_s)$	$t_{min} - t_{max}$	m_{val}	am_{res}	χ^2/dof	Q
(0.72 , 0.01/0.04)	5-16	0.01	0.01089^{+4}_{-4}	51.296/11	0.000
(0.72 , 0.02/0.04)	9-16	0.02	0.01092^{+7}_{-6}	18.176/15	0.254
(0.72 , 0.04/0.04)	9-16	0.04	0.01105^{+9}_{-5}	23.4817/15	0.074
(0.764 , 0.02/0.04)	9-15	0.02	0.00535^{+2}_{-2}	18.249/13	0.148
(0.764 , 0.04/0.04)	10-14	0.04	0.00540^{+1}_{-1}	12.402/9	0.192
(0.78 , 0.02/0.04)	11-15	0.02	0.00428^{+1}_{-2}	6.206/4	0.184
(0.78 , 0.04/0.04)	4-15	0.04	0.00427^{+1}_{-2}	8.933/11	0.628
(2.13 , 0.02/0.04)	10-15	0.02	0.01127^{+3}_{-3}	12.023/11	0.362
(2.13 , 0.04/0.04)	9-15	0.04	0.01175^{+5}_{-3}	20.231/13	0.090
(2.2 , 0.02/0.04)	10-15	0.02	0.00688^{+2}_{-2}	18.584/11	0.069
(2.2 , 0.04/0.04)	12-16	0.04	0.00711^{+2}_{-2}	16.614/9	0.055

Table 5.5: Residual mass values for the datasets.

Dataset	Fit range	Results				
$(\beta, m_{ud}/m_s)$	$t_{min} - t_{max}$	m_{val}	am_{PS}	χ^2/dof	Q	smear
(0.72 , 0.1/0.04)	4-14	0.01	0.303^{+2}_{-3}	66.227/16	0.000	SL,SS
(0.72 , 0.02/0.04)	5-16	0.02	0.3742^{+9}_{-8}	34.3113/18	0.012	LL,WL
(0.72 , 0.04/0.04)	6-16	0.04	0.4864^{+9}_{-10}	31.865/16	0.010	LL,WL
(0.764 , 0.02/0.04)	7-15	0.02	0.311^{+1}_{-1}	20.034/12	0.066	LL,WL
(0.764 , 0.04/0.04)	6-16	0.04	0.4203^{+7}_{-6}	23.275/16	0.107	LL,WL
(0.78 , 0.02/0.04)	11-16	0.02	0.288^{+6}_{-6}	4.516/4	0.341	WL
(0.78 , 0.04/0.04)	11-16	0.04	0.400^{+7}_{-5}	7.807/4	0.099	LL
(2.13 , 0.02/0.04)	10-16	0.02	0.362^{+2}_{-1}	10.061/8	0.261	LL,SL
(2.13 , 0.04/0.04)	9-16	0.04	0.4665^{+8}_{-9}	14.208/10	0.164	SL,SS
(2.2 , 0.02/0.04)	5-16	0.02	0.315^{+2}_{-2}	28.828/18	0.051	LL,WL
(2.2 , 0.04/0.04)	6-16	0.04	0.425^{+1}_{-1}	20.639/16	0.193	LL,WL

Table 5.6: Fitted pseudoscalar meson masses.

Dataset	Fit range	Results				
$(\beta, m_{ud}/m_s)$	$t_{min} - t_{max}$	m_{val}	am_ρ	χ^2/dof	Q	smear
(0.72 , 0.01/0.04)	6-14	0.01	0.580^{+10}_{-10}	13.159/12	0.358	LL,SL
(0.72 , 0.02/0.04)	6-16	0.02	0.635^{+3}_{-4}	27.183/16	0.039	LL,WL
(0.72 , 0.04/0.04)	6-13	0.04	0.703^{+5}_{-4}	10.708/10	0.381	LL,WL
(0.764 , 0.02/0.04)	8-14	0.02	0.543^{+5}_{-4}	13.098/8	0.109	LL,WL
(0.764 , 0.04/0.04)	7-15	0.04	0.607^{+3}_{-3}	21.223/12	0.047	LL,WL
(0.78 , 0.02/0.04)	10-15	0.02	0.48^{+1}_{-2}	1.859/4	0.762	WL
(0.78 , 0.04/0.04)	8-15	0.04	0.575^{+5}_{-5}	23.912/13	0.032	LL,WL
(2.13 , 0.02/0.04)	5-14	0.02	0.581^{+4}_{-3}	14.376/8	0.072	SS
(2.13 , 0.04/0.04)	6-14	0.04	0.661^{+3}_{-2}	20.786/12	0.054	SS,SL
(2.2 , 0.02/0.04)	7-16	0.02	0.493^{+5}_{-6}	11.455/14	0.650	LL,WL
(2.2 , 0.04/0.04)	7-15	0.04	0.586^{+5}_{-4}	18.868/12	0.092	LL,WL

Table 5.7: Fitted values for the mass of the ρ meson.

Dataset	$t_{min} - t_{max}$			Results				
$(\beta, m_{ud}/m_s)$	N_+	N_-	N'_-	m_{val}	am_N	am_{N_-}	χ^2/dof	Q
(0.72 , 0.02/0.04)	10-16	20-27	6-11	0.02	0.904^{+8}_{-8}	1.18^{+1}_{-2}	25.663/16	0.059
(0.72 , 0.04/0.04)	8-14	23-25	4-8	0.04	1.021^{+4}_{-3}	1.28^{+2}_{-1}	13.166/10	0.215
(0.764 , 0.02/0.04)	11-15	20-23	6-10	0.02	0.76^{+2}_{-1}	0.96^{+1}_{-2}	15.845/9	0.070
(0.764 , 0.04/0.04)	10-16	20-23	7-12	0.04	0.888^{+3}_{-2}	1.17^{+1}_{-1}	22.616/12	0.031
(2.13 , 0.02/0.04)	9-14	21-25	7-9	0.02	0.82^{+1}_{-1}	1.14^{+2}_{-2}	11.305/9	0.255
(2.13 , 0.04/0.04)	8-12	24-25	6-11	0.04	0.984^{+5}_{-5}	1.28^{+2}_{-2}	8.203/8	0.414
(2.2 , 0.02/0.04)	8-16	21-25	6-10	0.02	0.729^{+2}_{-3}	0.90^{+1}_{-1}	15.204/14	0.364
(2.2 , 0.04/0.04)	10-15	21-26	6-11	0.04	0.860^{+4}_{-3}	1.051^{+5}_{-5}	18.675/13	0.134

Table 5.8: Results of fits to the nucleon as described in the text.

Dataset	Fit range	Results				
$(\beta, m_{ud}/m_s)$	$t_{min} - t_{max}$	m_{val}	A_{PP}	af_{PS}^{PP}	χ^2/dof	Q
(0.72 , 0.01/0.04)	11-16	0.01	0.76^{+5}_{-4}	0.097^{+3}_{-2}	18.486/5	0.002
(0.72 , 0.02/0.04)	8-16	0.02	0.93^{+3}_{-3}	0.115^{+2}_{-2}	6.627/8	0.577
(0.72 , 0.04/0.04)	10-16	0.04	0.96^{+4}_{-4}	0.129^{+3}_{-3}	9.367/5	0.095
(0.764 , 0.02/0.04)	10-16	0.02	0.49^{+1}_{-1}	0.0884^{+8}_{-9}	11.915/5	0.036
(0.764 , 0.04/0.04)	11-16	0.04	0.55^{+1}_{-1}	0.108^{+1}_{-1}	6.705/4	0.152
(0.78 , 0.02/0.04)	11-16	0.02	0.36^{+2}_{-3}	0.080^{+3}_{-3}	1.457/4	0.834
(0.78 0.04/0.04)	11-16	0.04	0.35^{+2}_{-2}	0.089^{+3}_{-3}	6.472/4	0.167
(2.13 , 0.02/0.04)	10-16	0.02	0.53^{+2}_{-2}	0.092^{+1}_{-1}	8.160/5	0.148
(2.13 , 0.04/0.04)	9-16	0.04	0.60^{+1}_{-2}	0.112^{+1}_{-2}	7.439/7	0.385
(2.2 , 0.02/0.04)	9-16	0.02	0.39^{+1}_{-1}	0.0833^{+8}_{-7}	10.377/7	0.168
(2.2 , 0.04/0.04)	11-16	0.04	0.48^{+1}_{-1}	0.1033^{+8}_{-9}	7.561/4	0.109

Table 5.9: Fitted values for the pseudoscalar meson decay constant using the residual mass and the pseudoscalar density correlator.

Dataset	Fit range	Results			
$(\beta, m_{ud}/m_s)$	$t_{min} - t_{max}$	m_{val}	Z_A	χ^2/dof	Q
(0.72 , 0.01/0.04)	5-11	0.01	0.7335^{+2}_{-2}	18.089/13	0.154
(0.72 , 0.02/0.04)	5-11	0.02	0.7347^{+2}_{-2}	18.673/13	0.134
(0.72 , 0.04/0.04)	8-13	0.04	0.7393^{+9}_{-6}	18.878/11	0.063
(0.764 , 0.02/0.04)	6-12	0.02	0.75521^{+5}_{-5}	24.922/13	0.024
(0.764 , 0.04/0.04)	6-14	0.04	0.75722^{+6}_{-7}	21.059/17	0.224
(0.78 , 0.02/0.04)	8-14	0.02	0.7625^{+3}_{-3}	14.377/13	0.348
(0.78 , 0.04/0.04)	8-14	0.04	0.7662^{+2}_{-2}	17.443/13	0.180
(2.13 , 0.02/0.04)	7-14	0.02	0.73376^{+10}_{-7}	27.921/15	0.022
(2.13 , 0.04/0.04)	6-11	0.04	0.7357^{+1}_{-1}	21.777/11	0.026
(2.2 , 0.02/0.04)	10-15	0.02	0.74563^{+8}_{-9}	12.967/11	0.295
(2.2 , 0.04/0.04)	10-15	0.04	0.74820^{+7}_{-7}	23.028/11	0.017

Table 5.10: Fitted values for Z_A.

Dataset	Fit range	Results				
$(\beta, m_{ud}/m_s)$	$t_{min} - t_{max}$	m_{val}	$A_{A_4A_4}$	af_{PS}^{AA}	χ^2/dof	Q
(0.72 , 0.01/0.04)	9-15	0.01	0.028^{+2}_{-2}	0.099^{+3}_{-3}	9.088/6	0.169
(0.72 , 0.02/0.04)	9-15	0.02	0.044^{+1}_{-1}	0.111^{+2}_{-2}	10.720/6	0.097
(0.72 , 0.04/0.04)	9-15	0.04	0.075^{+3}_{-3}	0.128^{+2}_{-3}	11.376/6	0.077
(0.764 , 0.02/0.04)	8-16	0.02	0.0219^{+5}_{-3}	0.0890^{+8}_{-7}	14.410/7	0.044
(0.764 , 0.04/0.04)	8-15	0.04	0.043^{+1}_{-1}	0.107^{+1}_{-1}	7.650/6	0.265
(0.78 , 0.02/0.04)	11-16	0.02	0.016^{+1}_{-2}	0.083^{+3}_{-3}	9.350/4	0.053
(0.78 , 0.04/0.04)	12-16	0.04	0.026^{+2}_{-1}	0.086^{+2}_{-1}	4.809/4	0.307
(2.13 , 0.02/0.04)	5-16	0.02	0.0307^{+7}_{-7}	0.096^{+1}_{-1}	12.881/11	0.301
(2.13 , 0.04/0.04)	10-16	0.04	0.057^{+2}_{-2}	0.114^{+2}_{-2}	3.250/6	0.777
(2.2 , 0.02/0.04)	9-16	0.02	0.0195^{+5}_{-5}	0.0825^{+10}_{-9}	9.846/6	0.131
(2.2 , 0.04/0.04)	10-16	0.04	0.0407^{+7}_{-7}	0.1024^{+8}_{-9}	14.060/6	0.029

Table 5.11: Fitted values for the pseudoscalar meson decay constant using the value of Z_A and the axial-axial correlator.

Dataset	Fit range	Results			
$(\beta, m_{ud}/m_s)$	$t_{min} - t_{max}$	m_{val}	af_{PS}^{AP}	χ^2/dof	Q
(0.72 , 0.01/0.04)	10-16	0.01	0.11^{+2}_{-1}	1.319/6	0.971
(0.72 , 0.02/0.04)	10-16	0.02	0.113^{+2}_{-2}	7.267/6	0.201
(0.72 , 0.04/0.04)	12-16	0.04	0.127^{+3}_{-2}	5.274/4	0.260
(0.764 , 0.02/0.04)	11-16	0.02	0.089^{+1}_{-1}	4.159/4	0.385
(0.764 , 0.04/0.04)	11-16	0.04	0.107^{+1}_{-1}	5.970/4	0.201
(0.78 , 0.02/0.04)	12-16	0.02	0.076^{+2}_{-3}	8.347/4	0.080
(0.78 , 0.04/0.04)	10-16	0.04	0.088^{+3}_{-3}	0.287/5	0.998
(2.13 , 0.02/0.04)	11-16	0.02	0.092^{+1}_{-1}	4.396/5	0.494
(2.13 , 0.04/0.04)	10-16	0.04	0.111^{+1}_{-2}	2.731/5	0.741
(2.2 , 0.02/0.04)	11-16	0.02	0.0830^{+7}_{-8}	7.434/5	0.190
(2.2 , 0.04/0.04)	10-16	0.04	0.102^{+1}_{-1}	9.932/5	0.077

Table 5.12: Fitted values for the pseudoscalar meson decay constant using the Z_A and the local axial correlator.

β	am_l/am_s	r_0/a	a^{-1}(GeV)	L(fm)	Lm_{PS}	m_{PS}/m_V
0.72	0.04/0.04				7.8(1)	0.692(5)
0.72	0.02/0.04	4.3(1)	1.7(1)	1.9(1)	6.0(1)	0.589(3)
0.72	0.01/0.04				4.9(1)	0.52(3)
0.764	0.04/0.04	5.1(2)	2.0(1)	1.6(1)	6.7(1)	0.699(4)
0.764	0.02/0.04				5.1(1)	0.619(4)
0.78	0.04/0.04	5.2(3)	2.0(1)	1.5(1)	6.4(1)	0.69(1)
0.78	0.02/0.04				4.6(1)	0.60(1)
2.13	0.04/0.04	4.6(2)	1.8(1)	1.8(1)	7.5(1)	0.700(8)
2.13	0.02/0.04				5.8(1)	0.615(5)
2.2	0.04/0.04	5.3(1)	2.1(1)	1.5(1)	6.8(1)	0.726(2)
2.2	0.02/0.04				5.1(1)	0.667(8)

Table 5.13: Properties of the ensembles used in this study. The value of r_0/a was determined in [108]. The lattice spacing, and thus the volume are set by choosing $r_0 = 0.5$ fm.

Dataset	Results		
β	$am_{res}(m_q \to 0)$	χ^2/dof	Q
0.72	0.01077^{+6}_{-9}	0.068/1	0.794
0.764	0.00529^{+5}_{-5}	-	-
0.78	0.00430^{+3}_{-4}	-	-
2.13	0.0105^{+1}_{-1}	-	-
2.2	0.00656^{+5}_{-6}	-	-

Table 5.14: Residual mass values for the datasets in the chiral limit ($m_q \to 0$).

Dataset	Results		
β	$am_{PS}(m_q \to 0)$	χ^2/dof	Q
0.72	-0.008^{+2}_{-2}	0.006/1	0.936
0.764	-0.004^{+2}_{-2}	-	-
0.78	-0.011^{+8}_{-10}	-	-
2.13	-0.002^{+4}_{-3}	-	-
2.2	-0.008^{+3}_{-3}	-	-

Table 5.15: Pseudoscalar meson mass in the chiral limit ($m_q \to 0$).

Dataset	Results			
β	$am_\rho(m_q \to 0)$	a^{-1} (GeV)	χ^2/dof	Q
0.72	0.52^{+1}_{-1}	1.49^{+3}_{-3}	1.175/1	0.278
0.764	0.45^{+2}_{-1}	1.71^{+5}_{-6}	-	-
0.78	0.38^{+3}_{-4}	2.1^{+2}_{-2}	-	-
2.13	0.46^{+1}_{-1}	1.68^{+4}_{-4}	-	-
2.2	0.37^{+1}_{-2}	2.08^{+9}_{-6}	-	-

Table 5.16: ρ meson mass in the chiral limit ($m_q \to 0$).

Dataset	Results		
β	$am_s(m_\rho)$	$am_s(f_{PS})$	$am_s(r_0)$
0.72	0.049^{+2}_{-2}	0.042^{+5}_{-3}	0.039^{+2}_{-2}
0.764	0.044^{+3}_{-3}	0.031^{+2}_{-2}	0.032^{+2}_{-3}
0.78	0.036^{+5}_{-4}	0.040^{+9}_{-7}	0.036^{+5}_{-4}
2.13	0.042^{+2}_{-2}	0.027^{+2}_{-3}	0.036^{+4}_{-3}
2.2	0.032^{+2}_{-2}	0.027^{+2}_{-2}	0.032^{+2}_{-1}

Table 5.17: Strange quark mass evaluated using the physical Kaon mass. The physical value of f_{PS} and m_ρ in the chiral limit and r_0 were used to set the scale on the datasets.

Dataset	Results						
β	$r_0 m_\rho$	am_{K^*}	$r_0 m_{K^*}$	af_{PS}	$r_0 f_{PS}$	af_K	$r_0 f_K$
0.72	2.22^{+6}_{-8}	0.588^{+7}_{-7}	2.53^{+4}_{-5}	0.080^{+5}_{-4}	0.34^{+2}_{-2}	0.099^{+3}_{-2}	0.43^{+1}_{-1}
0.764	2.3^{+1}_{-1}	0.51^{+1}_{-1}	2.6^{+1}_{-1}	0.064^{+2}_{-2}	0.33^{+2}_{-2}	0.079^{+2}_{-2}	0.41^{+1}_{-1}
0.78	2.0^{+2}_{-2}	0.46^{+2}_{-2}	2.4^{+1}_{-1}	0.068^{+8}_{-8}	0.35^{+5}_{-5}	0.077^{+4}_{-4}	0.40^{+3}_{-3}
2.13	2.1^{+1}_{-1}	0.529^{+10}_{-10}	2.43^{+9}_{-8}	0.062^{+3}_{-2}	0.28^{+2}_{-2}	0.079^{+2}_{-2}	0.36^{+1}_{-1}
2.2	1.96^{+6}_{-8}	0.443^{+8}_{-9}	2.35^{+5}_{-6}	0.057^{+2}_{-2}	0.30^{+1}_{-1}	0.073^{+1}_{-1}	0.385^{+10}_{-7}

Table 5.18: Values of am_{K^*}, af_{PS} and af_K together with dimensionless values of m_ρ, m_{K^*} and f_K. The values of am_ρ are given in table 5.16.

Dataset	Results	
β	$am_N(m_q \to 0)$	$am_{N^*}(m_q \to 0)$
0.72	0.73^{+2}_{-2}	1.02^{+3}_{-5}
0.764	0.59^{+4}_{-3}	0.80^{+3}_{-3}
2.13	0.58^{+3}_{-3}	0.92^{+5}_{-5}
2.2	0.554^{+6}_{-9}	0.71^{+3}_{-2}

Table 5.19: Nucleon and negative parity partner masses in the chiral limit ($m_q \to 0$).

Dataset	Results					
β	af_{PS}^{PP}	a^{-1} (GeV)	af_{PS}^{AA}	a^{-1} (GeV)	af_{PS}^{AP}	a^{-1} (GeV)
0.72	0.080^{+5}_{-4}	1.6^{+1}_{-1}	0.082^{+4}_{-4}	1.59^{+8}_{-8}	0.082^{+4}_{-4}	1.59^{+8}_{-8}
0.764	0.064^{+2}_{-2}	2.04^{+6}_{-6}	0.067^{+2}_{-2}	1.94^{+7}_{-7}	0.065^{+3}_{-3}	1.99^{+9}_{-8}
0.78	0.068^{+8}_{-8}	1.9^{+3}_{-2}	0.07^{+1}_{-1}	1.8^{+3}_{-2}	0.062^{+6}_{-8}	2.1^{+3}_{-2}
2.13	0.062^{+3}_{-2}	2.10^{+9}_{-9}	0.067^{+3}_{-5}	1.9^{+1}_{-1}	0.061^{+3}_{-3}	2.1^{+1}_{-1}
2.2	0.057^{+2}_{-2}	2.29^{+8}_{-8}	0.056^{+3}_{-2}	2.31^{+10}_{-10}	0.057^{+2}_{-3}	2.3^{+1}_{-1}

Table 5.20: Pseudoscalar meson decay constant in the chiral limit ($m_q \to 0$) and corresponding lattice spacing from the physical value of f_π.

Dataset	Results			
β	m_{K^*}/m_ρ	f_{PS}/m_ρ	f_K/f_{PS}	f_K/m_ρ
0.72	1.14^{+2}_{-1}	0.15^{+1}_{-1}	1.25^{+5}_{-4}	0.192^{+9}_{-6}
0.764	1.12^{+2}_{-2}	0.141^{+6}_{-6}	1.25^{+4}_{-3}	0.176^{+6}_{-6}
0.78	1.2^{+1}_{-1}	0.18^{+3}_{-2}	1.13^{+9}_{-6}	0.20^{+3}_{-2}
2.13	1.15^{+2}_{-2}	0.135^{+6}_{-7}	1.28^{+4}_{-4}	0.172^{+6}_{-6}
2.2	1.20^{+3}_{-2}	0.153^{+9}_{-7}	1.28^{+2}_{-3}	0.196^{+10}_{-7}

Table 5.21: Ratios of various quantities on the datasets.

Dataset	Fit range	Results				
$(\beta, m_{ud}/m_s)$	$t_{min} - t_{max}$	$m^1_{\rm val}$	$m^2_{\rm val}$	$am_{\rm res}$	χ^2/dof	Q
(0.72 , 0.01/0.04)	5-16	0.01	0.01	0.01089^{+8}_{-8}	45.679/11	0.000
(0.72 , 0.01/0.04)	5-16	0.04	0.04	0.01036^{+8}_{-8}	58.238/11	0.000
(0.72 , 0.01/0.04)	5-16	0.05	0.05	0.01024^{+7}_{-8}	58.862/11	0.000
(0.72 , 0.01/0.04)	5-16	0.06	0.06	0.01013^{+7}_{-8}	58.708/11	0.000
(0.72 , 0.02/0.04)	9-16	0.02	0.02	0.01092^{+7}_{-6}	18.176/15	0.254
(0.72 , 0.02/0.04)	6-16	0.04	0.04	0.01063^{+3}_{-3}	11.607/10	0.312
(0.72 , 0.02/0.04)	6-16	0.05	0.05	0.01049^{+4}_{-3}	13.131/10	0.216
(0.72 , 0.02/0.04)	6-16	0.06	0.06	0.01038^{+4}_{-3}	13.572/10	0.193
(0.72 , 0.04/0.04)	9-16	0.04	0.04	0.01105^{+9}_{-5}	23.4817/15	0.074
(0.72 , 0.04/0.04)	6-14	0.05	0.05	0.0108^{+2}_{-1}	16.646/8	0.034
(0.72 , 0.04/0.04)	6-14	0.06	0.06	0.0106^{+2}_{-1}	15.491/8	0.050

Table 5.22: Non-degenerate residual mass values for the datasets.

Dataset	Fit range	Results				
$(\beta, m_{ud}/m_s)$	$t_{min} - t_{max}$	m^1_{val}	m^2_{val}	am_{PS}	χ^2/dof	Q
(0.72 , 0.01/0.04)	7-16	0.01	0.01	0.306^{+3}_{-3}	42.892/8	0.000
(0.72 , 0.01/0.04)	7-16	0.01	0.04	0.399^{+3}_{-3}	31.648/8	0.000
(0.72 , 0.01/0.04)	7-16	0.01	0.05	0.426^{+2}_{-3}	27.822/8	0.001
(0.72 , 0.01/0.04)	7-16	0.01	0.06	0.452^{+2}_{-2}	24.420/8	0.002
(0.72 , 0.02/0.04)	7-16	0.02	0.02	0.374^{+2}_{-2}	7.558/8	0.478
(0.72 , 0.02/0.04)	7-16	0.02	0.04	0.430^{+2}_{-2}	8.490/8	0.387
(0.72 , 0.02/0.04)	7-16	0.02	0.05	0.455^{+2}_{-1}	9.377/8	0.311
(0.72 , 0.02/0.04)	7-16	0.02	0.06	0.480^{+1}_{-1}	10.214/8	0.250
(0.72 , 0.04/0.04)	6-16	0.04	0.04	0.4864^{+9}_{-10}	31.865/16	0.010
(0.72 , 0.04/0.04)	6-16	0.04	0.05	0.509^{+2}_{-2}	19.979/9	0.018
(0.72 , 0.04/0.04)	6-16	0.04	0.06	0.532^{+2}_{-2}	20.164/9	0.017

Table 5.23: Non-degenerate pseudoscalar meson mass for the datasets.

Dataset	Fit range	Results				
$(\beta, m_{ud}/m_s)$	$t_{min} - t_{max}$	$m^1_{\rm val}$	$m^2_{\rm val}$	am_ρ	χ^2/dof	Q
(0.72 , 0.01/0.04)	8-16	0.01	0.01	0.59^{+1}_{-1}	10.029/7	0.187
(0.72 , 0.01/0.04)	8-16	0.01	0.04	0.633^{+7}_{-6}	11.443/7	0.120
(0.72 , 0.01/0.04)	8-16	0.01	0.05	0.648^{+6}_{-6}	10.890/7	0.144
(0.72 , 0.01/0.04)	8-16	0.01	0.06	0.664^{+6}_{-6}	10.202/7	0.177
(0.72 , 0.02/0.04)	10-16	0.02	0.02	0.63^{+1}_{-1}	6.810/5	0.235
(0.72 , 0.02/0.04)	10-16	0.02	0.04	0.655^{+8}_{-9}	8.372/5	0.137
(0.72 , 0.02/0.04)	10-16	0.02	0.05	0.671^{+7}_{-8}	8.114/5	0.150
(0.72 , 0.02/0.04)	10-16	0.02	0.06	0.687^{+6}_{-7}	7.557/5	0.182
(0.72 , 0.04/0.04)	6-13	0.04	0.04	0.703^{+5}_{-4}	10.708/10	0.381
(0.72 , 0.04/0.04)	10-16	0.04	0.05	0.718^{+9}_{-8}	6.137/5	0.293
(0.72 , 0.04/0.04)	10-16	0.04	0.06	0.733^{+8}_{-8}	5.394/5	0.370

Table 5.24: Non-degenerate ρ meson mass for the datasets.

δ	$m_n(\rho)$	$m_s(\rho)$	am_ρ	$am_{K^*}(\rho)$	$M_{K^*}(\rho)$	$m_n(r_0)$	$m_s(r_0)$	$am_{K^*}(r_0)$
-0.008^{+3}_{-2}	0.0070^{+8}_{-11}	0.043^{+3}_{-3}	0.051^{+2}_{-2}	0.59^{+1}_{-1}	0.893^{+7}_{-8}	0.0062^{+8}_{-11}	0.034^{+2}_{-1}	0.58^{+1}_{-1}

Table 5.25: Quark masses, ρ meson and K^* meson masses obtained from the non-degenerate analysis on the DBW2 β=0.72 ensembles. Brackets correspond to whether the lattice spacing was set with m_ρ in the chiral limit or by r_0.

5.21 Figures

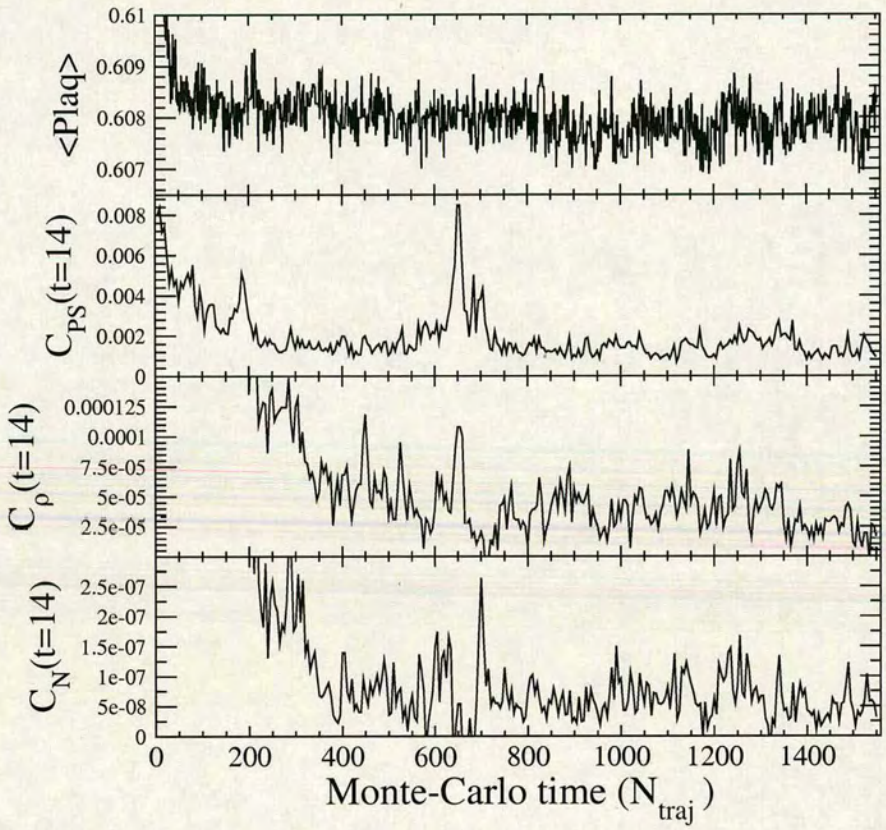

Figure 5.2: Monte-Carlo time history of Iwasaki $\beta = 2.2$ ensemble with $m_{ud} = m_s = 0.04$.

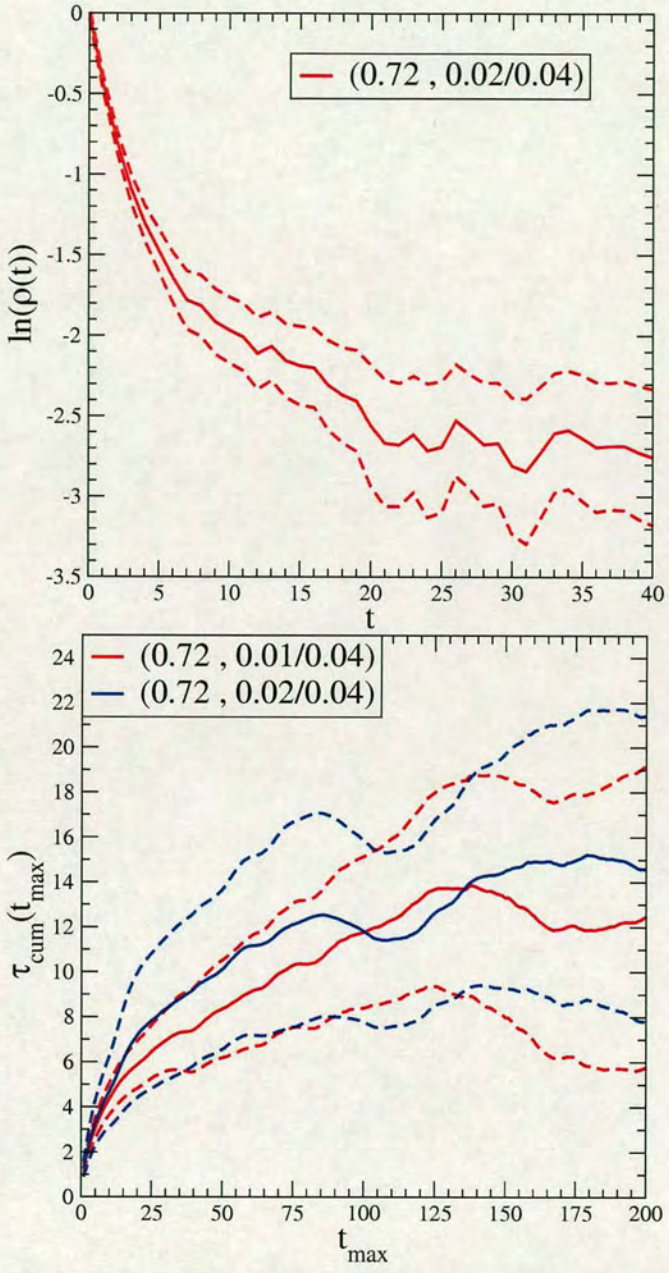

Figure 5.3: **TOP:** Logarithm of the normalised autocorrelation function for the plaquette on the (0.72 , 0.02/0.04) dataset. τ_{exp} is found from the slope at early t. **BOTTOM:** Integrated autocorrelation time for the pseudoscalar meson on the DBW2 β=0.72 datasets with the longest single Monte-Carlo chains. The separation for decorrelated configurations should be $2\tau_{cum}$ and the measurement is made every 5 trajectories.

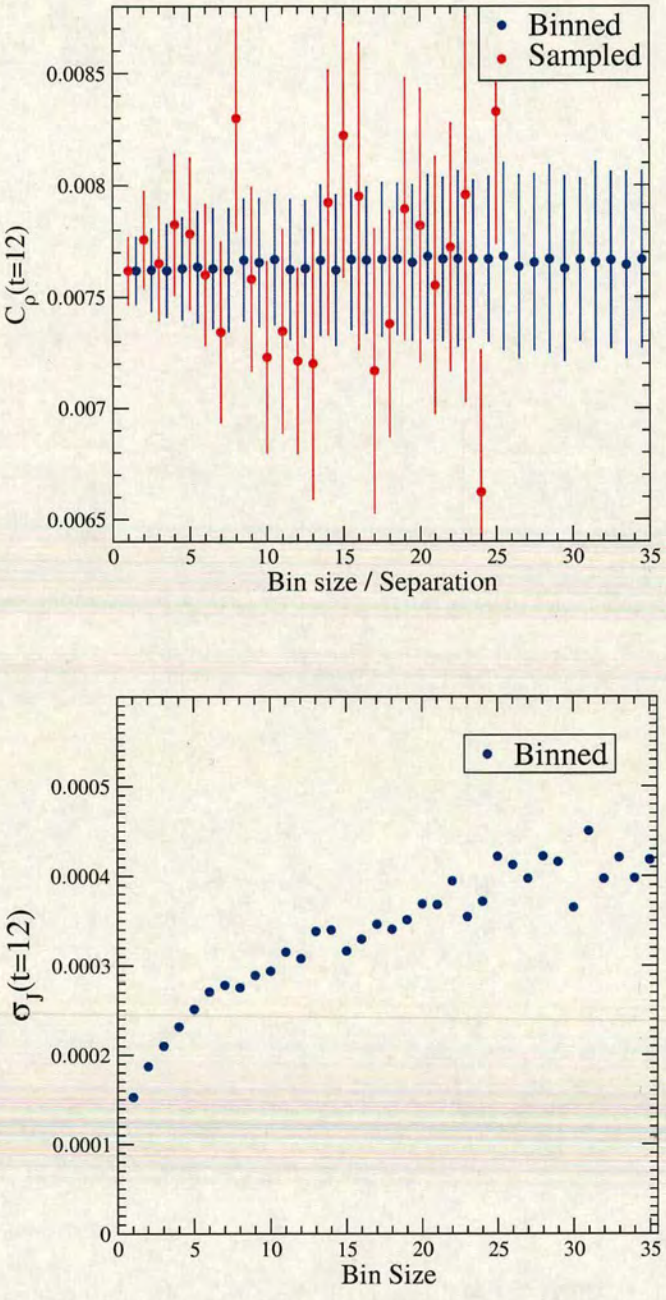

Figure 5.4: **TOP:** Comparison of binning and sampling on the 12^{th} timeslice of the ρ correlator and **BOTTOM:** Jackknife error versus bin size. Analysis carried out on Iwasaki $\beta = 2.13$ ensemble with $m_{ud} = m_s = 0.04$. Measurements are separated by five trajectories for this ensemble (bin size$= 20 \Rightarrow 100$ trajectories per bin).

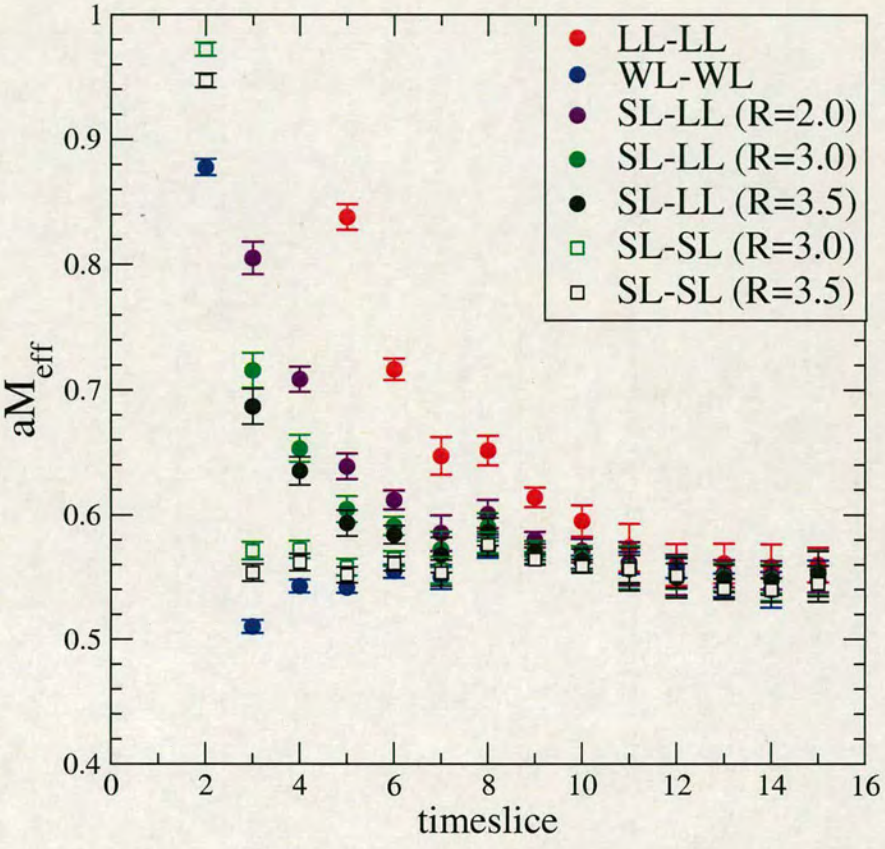

Figure 5.5: Comparison of smearing functions for a valence quark with mass $m_{val} = 0.04$ using 72 Iwasaki $\beta = 2.2$ configurations with $m_{ud} = 0.02$ and $m_s = 0.04$. 10 configurations were averaged into each bin and then a full correlated analysis performed on the binned data.

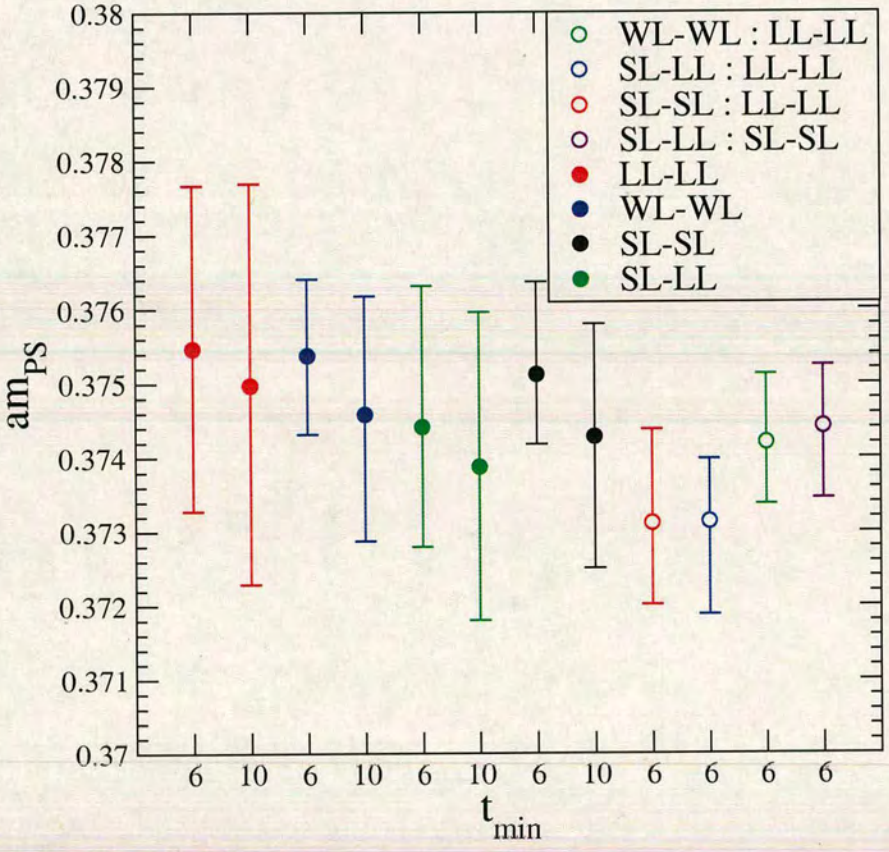

Figure 5.6: Comparison of smearing functions for a valence quark with mass $m_{val} = 0.02$ using 1000 DBW2 $\beta = 0.72$ configurations with $m_{ud} = 0.02$ and $m_s = 0.04$. 20 configurations were averaged into each bin and then a full correlated analysis performed on the binned data.

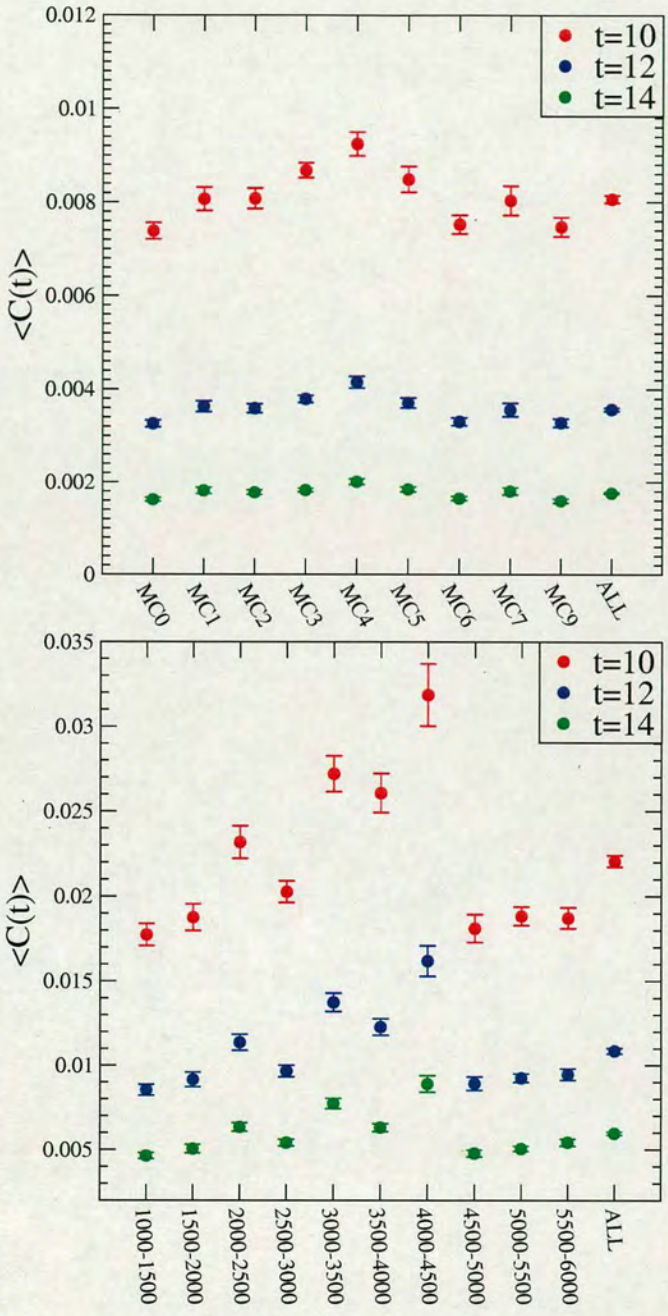

Figure 5.7: **TOP:** 10^{th}, 12^{th} and 14^{th} timeslice of the pseudoscalar meson correlator on each of the 'farmed chains' for the (0.764,0.04/0.04) dataset. On this dataset, each pseudoscalar meson correlator was measured on four timeplanes. **BOTTOM:** Same as top but measured on separate slices of the long chain (0.72,0.02/0.04) dataset that are approximately the same size as one of the 'farmed' chains. Each pseudoscalar meson correlator was measured on one timeplane.

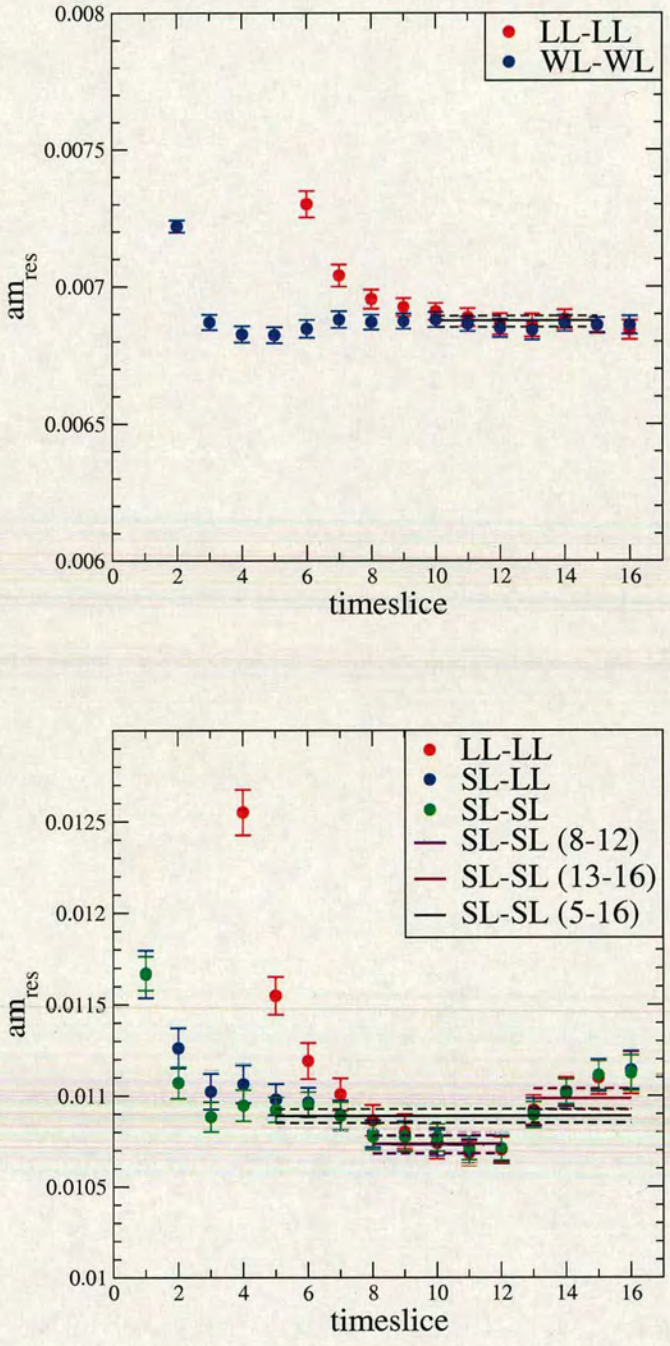

Figure 5.8: **TOP:** Residual mass for (2.2,0.02/0.04) dataset. Different colours correspond to different smearings. The lines shown are best fit lines using a simultaneous fit to both smearings. **BOTTOM:** Residual mass for (0.72,0.01/0.04) dataset. Three fits over different timeslices to the *SL-SL* correlator are shown.

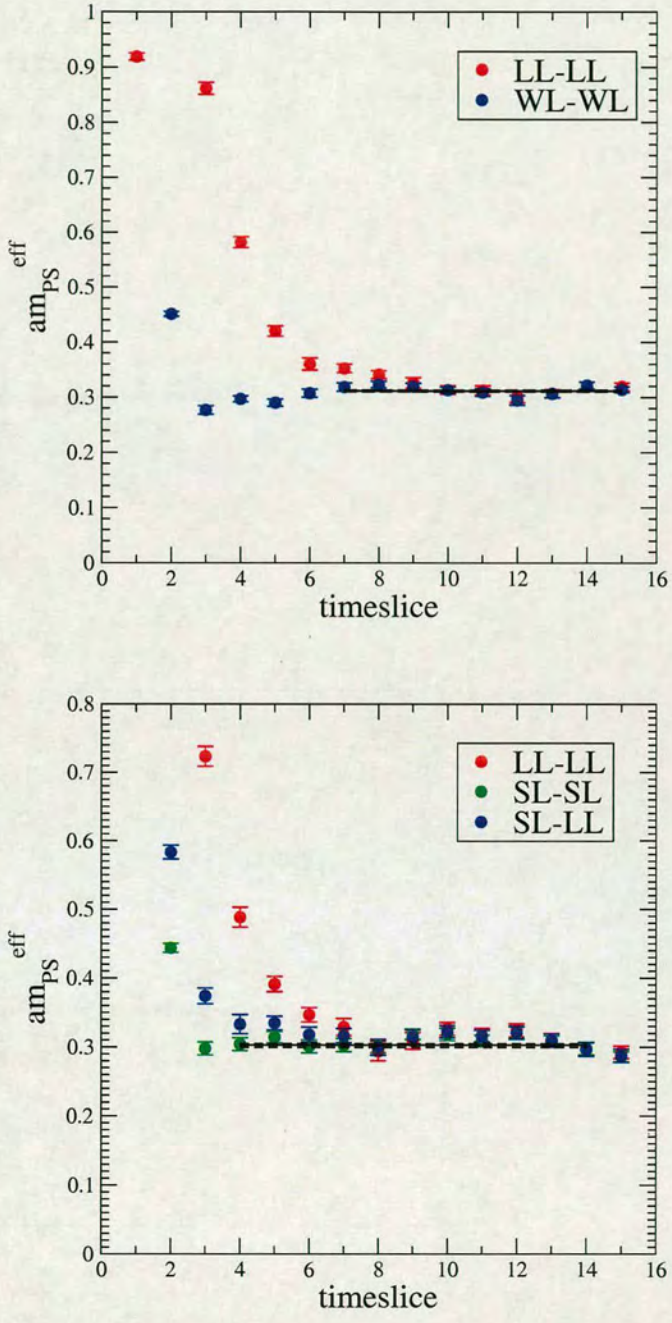

Figure 5.9: **TOP:** Pseudoscalar meson effective mass plot for the (0.764,0.02/0.04) dataset. Different colours correspond to different smearings. The lines shown are best fit lines using a simultaneous fit to both smearings. **BOTTOM:** Pseudoscalar meson effective mass plot for the (0.72,0.01/0.04) dataset. Different colours correspond to different smearings.

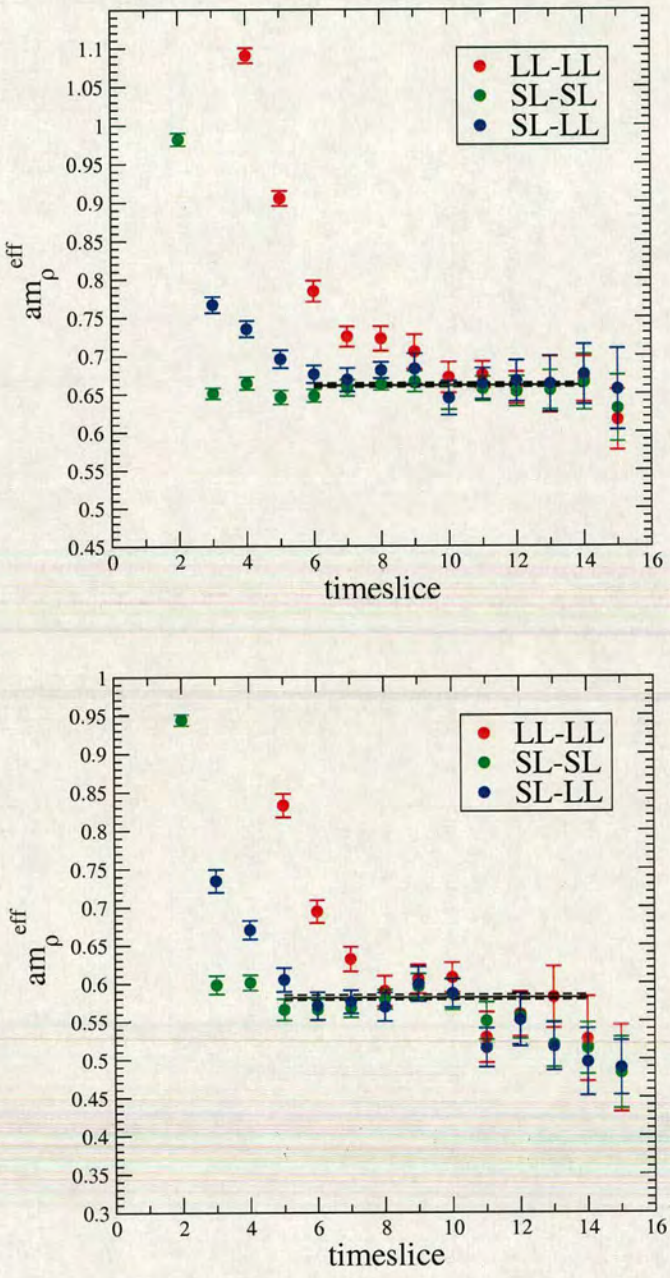

Figure 5.10: **TOP:** ρ meson effective mass plot for the (2.13,0.04/0.04) dataset. Different colours correspond to different smearings. The lines shown are best fit lines using a simultaneous fit to both smearings. **BOTTOM:** ρ meson effective mass plot for the (2.13,0.02/0.04) dataset. Different colours correspond to different smearings. The lines shown are best fit lines for fitting a single cosh to the SL-SL correlator.

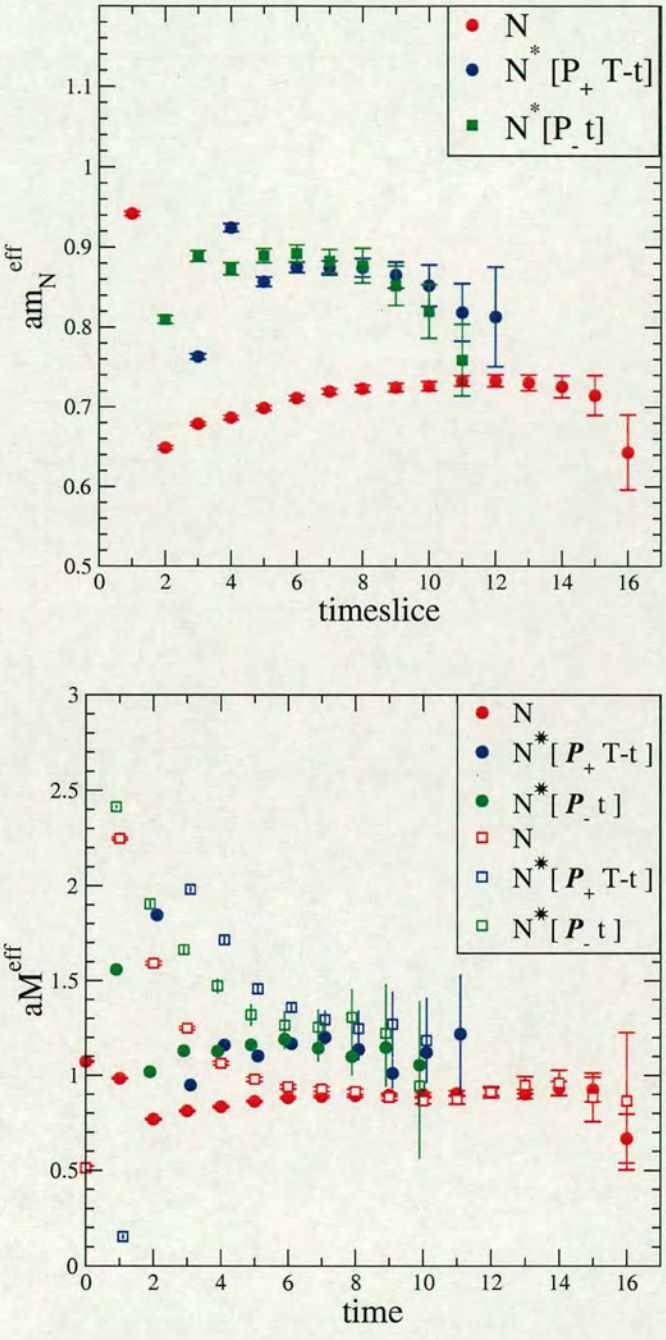

Figure 5.11: **TOP:** Nucleon effective mass plot for the (2.2,0.02/0.04) dataset. The square symbols are from the $\Gamma = 1$ correlator while the circles are from $\Gamma = \gamma_5$. Correlators are wall smeared at source. **BOTTOM:** Nucleon effective mass plot for the (0.72,0.02/0.04) dataset. Circles correspond to wall-point smearing, the squares are gauge fixed hydrogen-like wavefunction smeared at source.

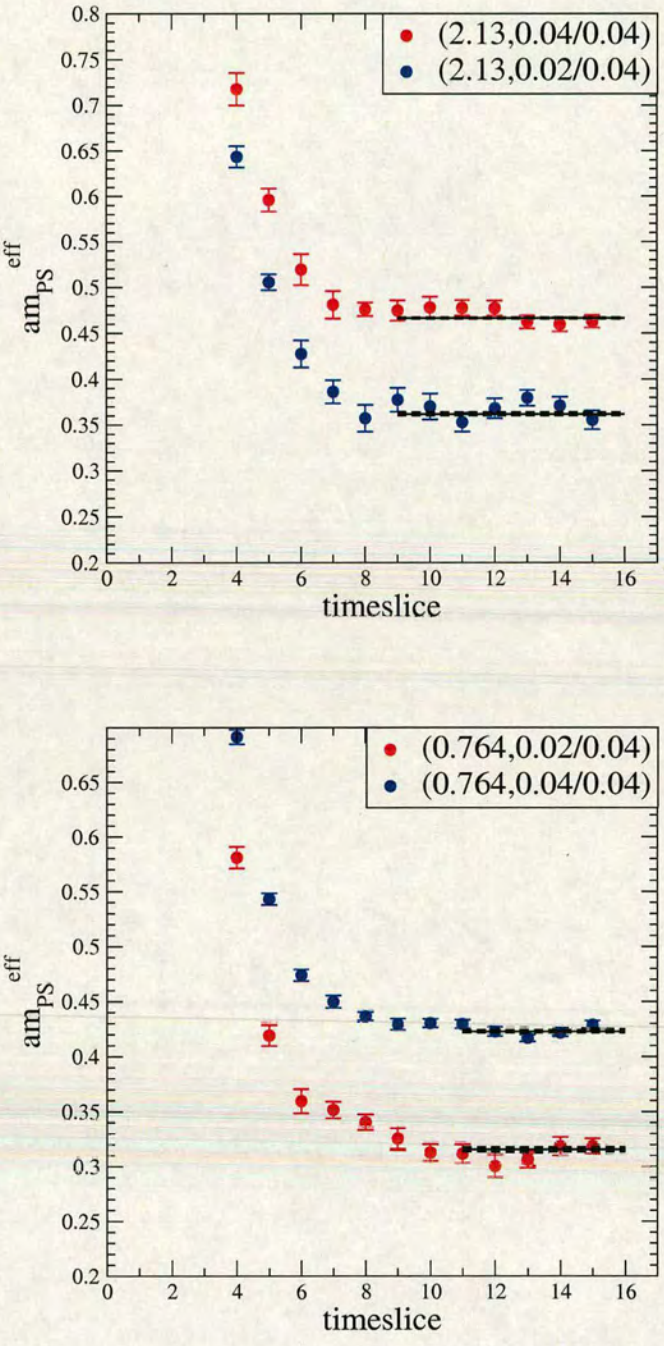

Figure 5.12: **TOP:** Pseudoscalar meson effective mass plots for the (2.13,0.02/0.04) and (2.13,0.04/0.04) datasets. The lines are from a single cosh fit to the point-point correlator. **BOTTOM:** The same as top but for the (0.764,0.02/0.04) and (0.764,0.04/0.04) datasets.

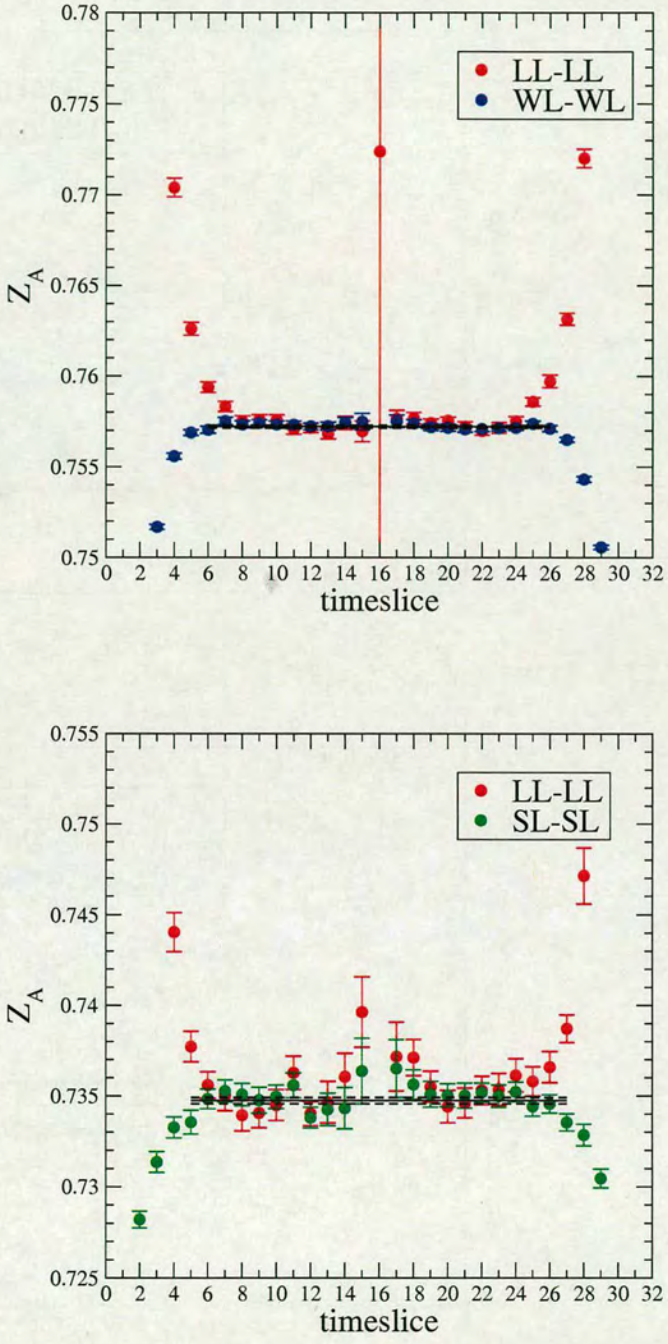

Figure 5.13: **TOP:** Z_A for the (0.764,0.04/0.04) dataset. Different colours correspond to the different smearings. The lines shown are a fit to the WL-WL plateau. **BOTTOM:** The same as top but for the (0.72,0.02/0.04) dataset with different smearings.

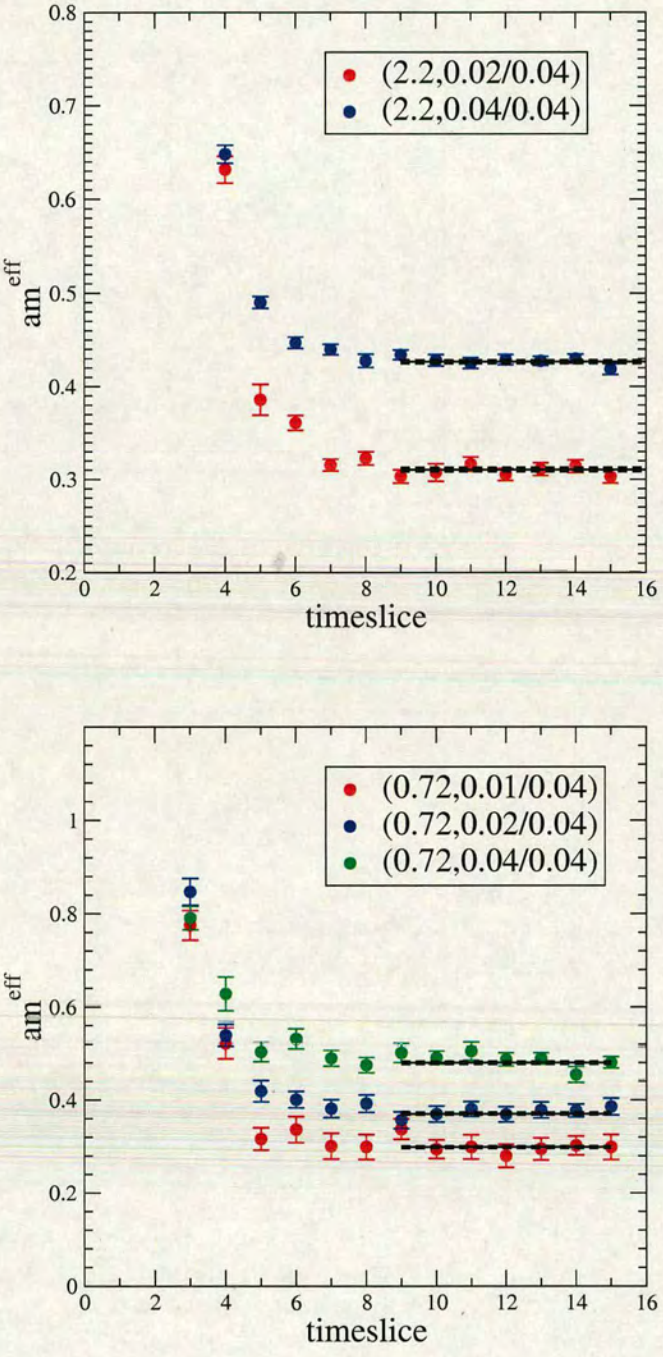

Figure 5.14: **TOP:** Effective mass plot for the axial-axial correlator on the (2.2,0.02/0.04) and (2.2,0.04/0.04) datasets. The lines shown are a fit to the LL-LL correlators. **BOTTOM:** The same as top but for the (0.72,0.01/0.04), (0.72,0.02/0.04) and (0.72,0.04/0.04) datasets.

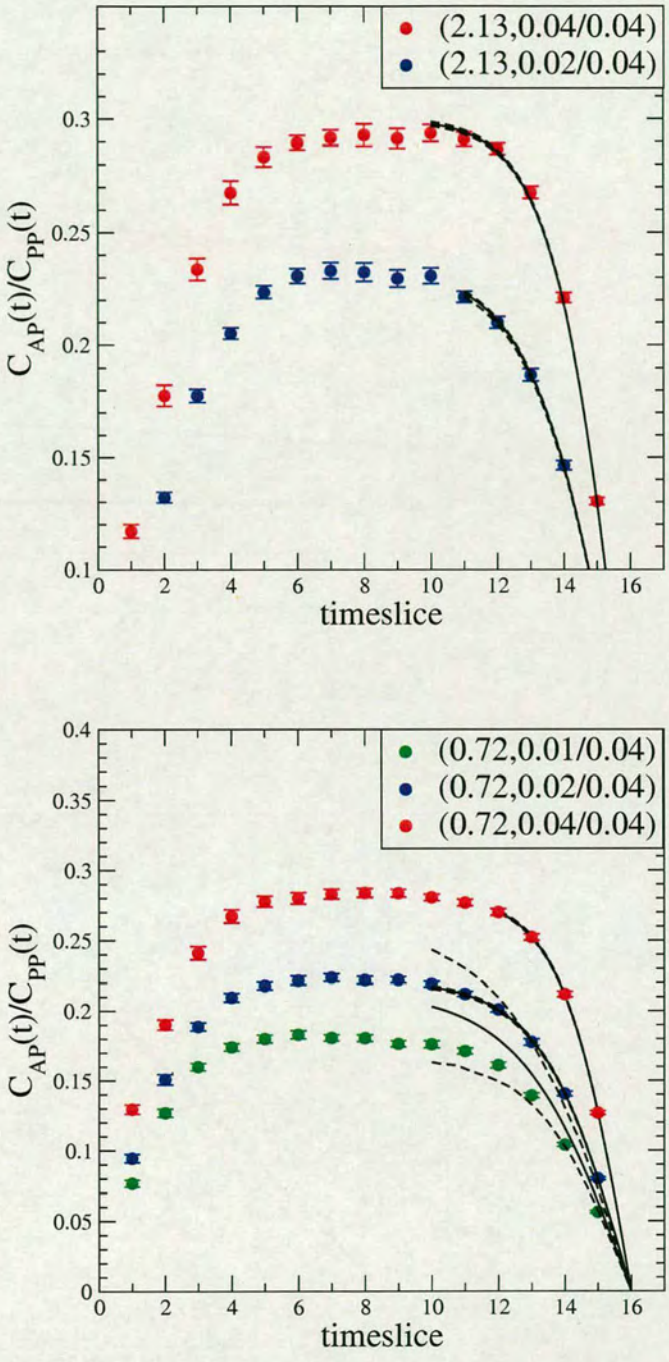

Figure 5.15: **TOP:** The ratio $C_{AP}(t)/C_{PP}(t)$ versus time for the (2.13,0.02/0.04) and (2.13,0.04/0.04) datasets. The lines shown are the tanh fit to the LL-LL correlators. **BOTTOM:** The same as top but for the (0.72,0.01/0.04), (0.72,0.02/0.04) and (0.72,0.04/0.04) datasets.

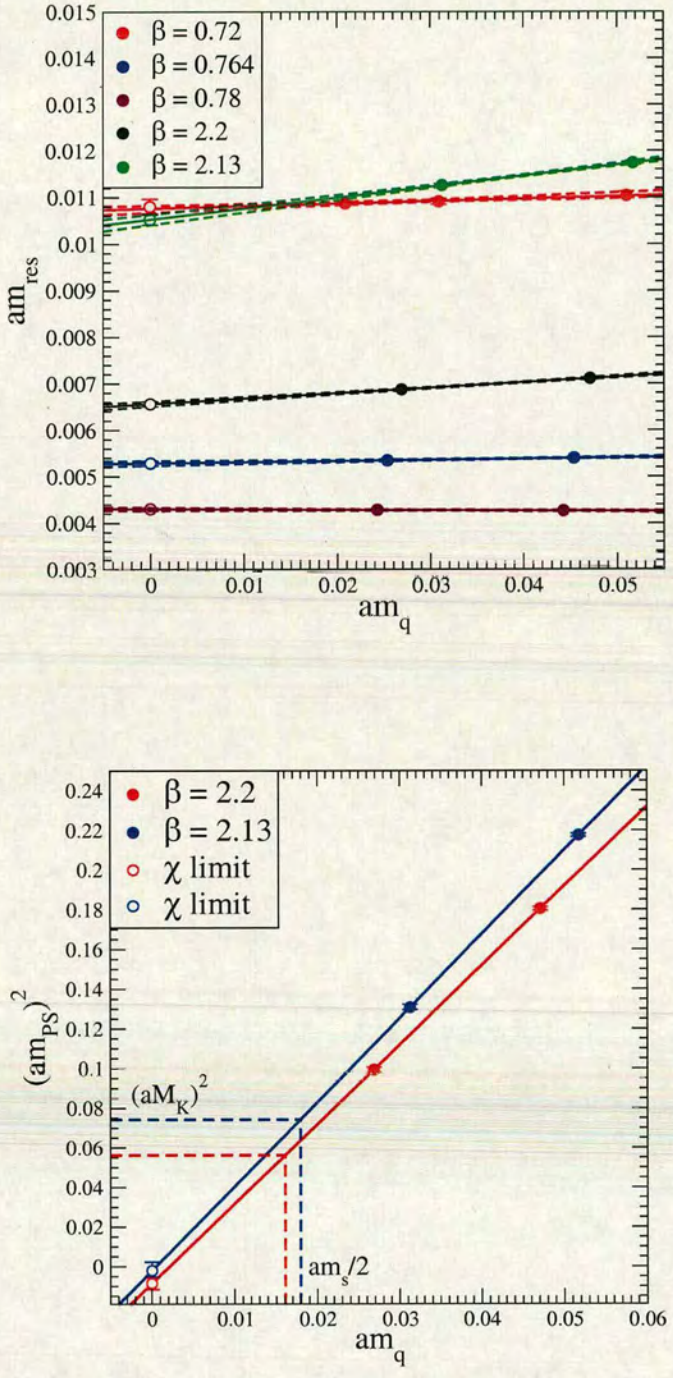

Figure 5.16: **TOP:** Chiral extrapolation of residual mass for all datasets. **BOTTOM:** Chiral extrapolation of the pseudoscalar meson mass squared for the Iwasaki datasets.

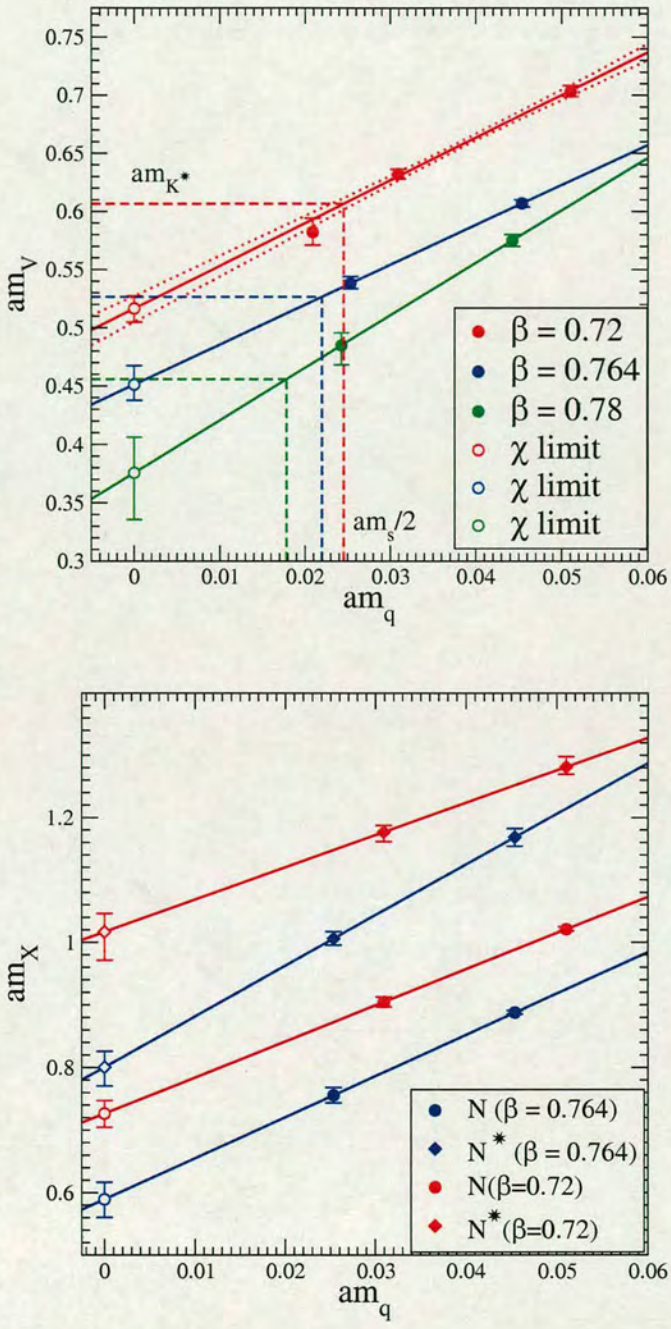

Figure 5.17: **TOP:** Chiral extrapolation of the vector meson for the DBW2 datasets. Dotted lines show the value of am_{K*} obtained from the strange quark set from r_0. **BOTTOM:** Nucleon and negative parity partner chiral extrapolations on the $\beta = 0.72$ and $\beta = 0.764$ DBW2 datasets. Open symbols are the values in the chiral limit ($m_q \to 0$).

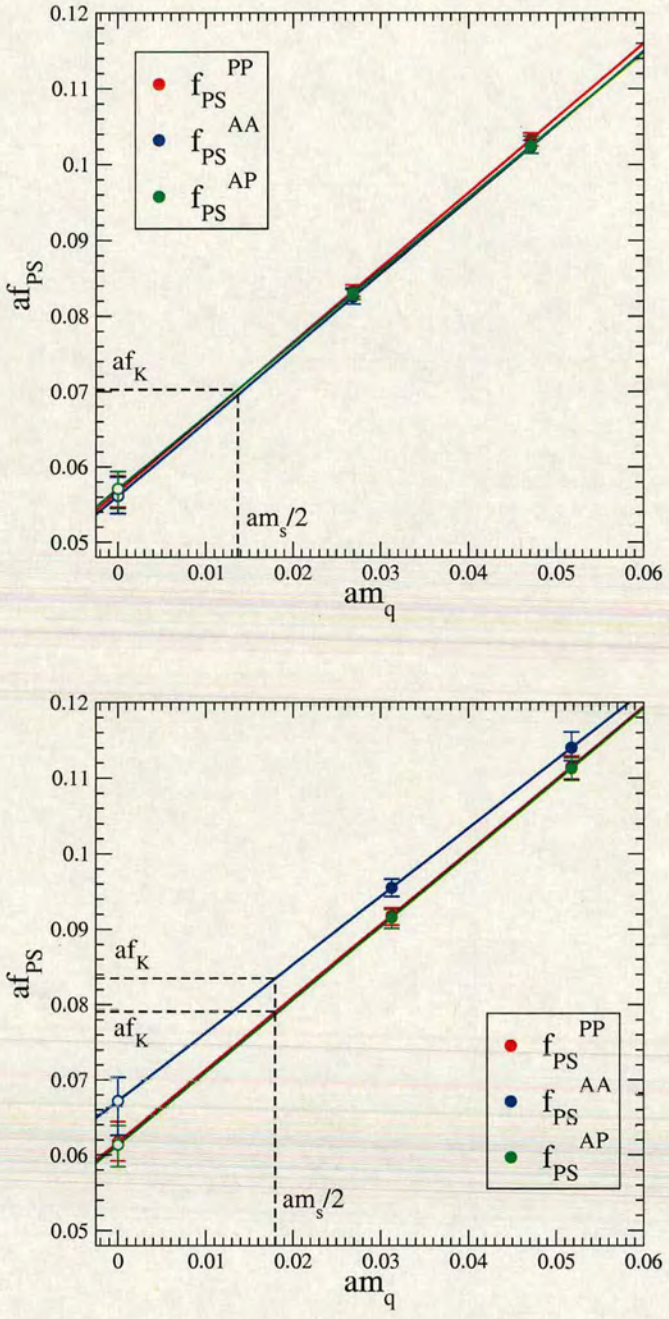

Figure 5.18: Chiral extrapolation of the pseudoscalar meson decay constant using three different methods for **TOP:** the Iwasaki β=2.2 dataset and **BOTTOM:** the Iwasaki β=2.13 dataset. Open symbols are chiral limit values. The errors on the points in the chiral limit are obtained by drawing straight lines. Dotted lines show the value of af_K obtained from the strange quark mass set by r_0.

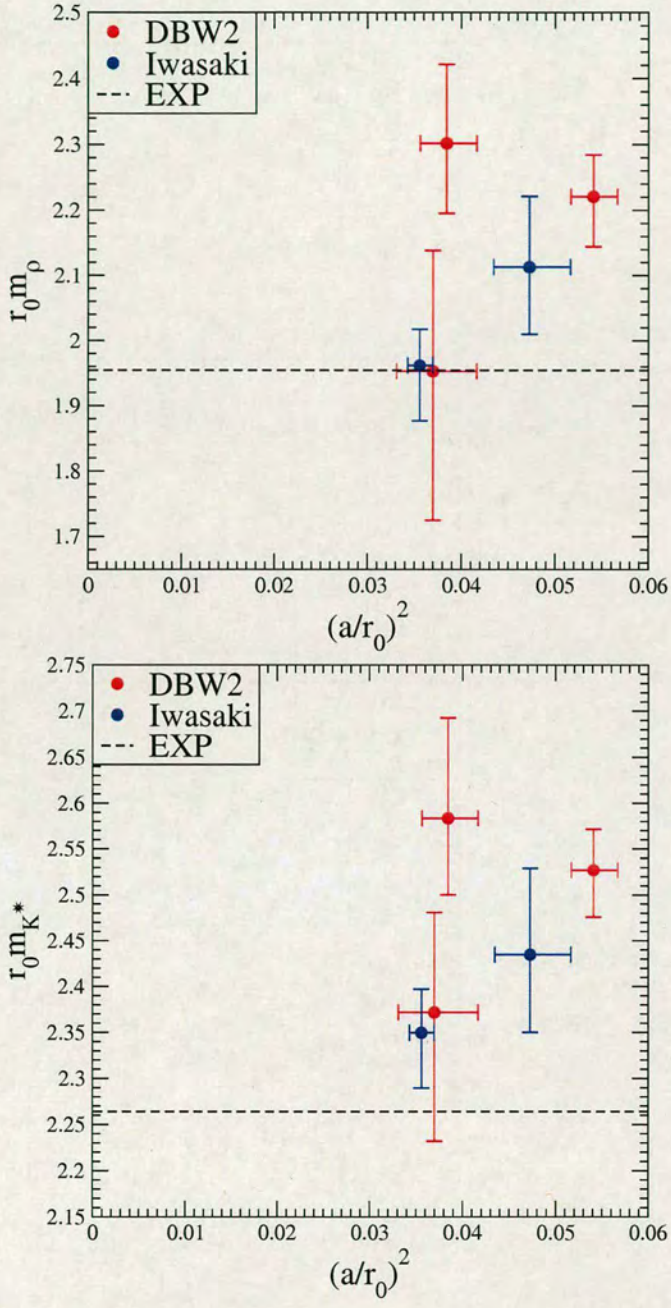

Figure 5.19: Dimensionless values of **TOP:** $r_0 m_\rho$ and **BOTTOM:** $r_0 m_{K^*}$ versus $(a/r_0)^2$ for all the datasets. The dotted lines are the experimentally obtained values scaled by appropriate factors of r_0.

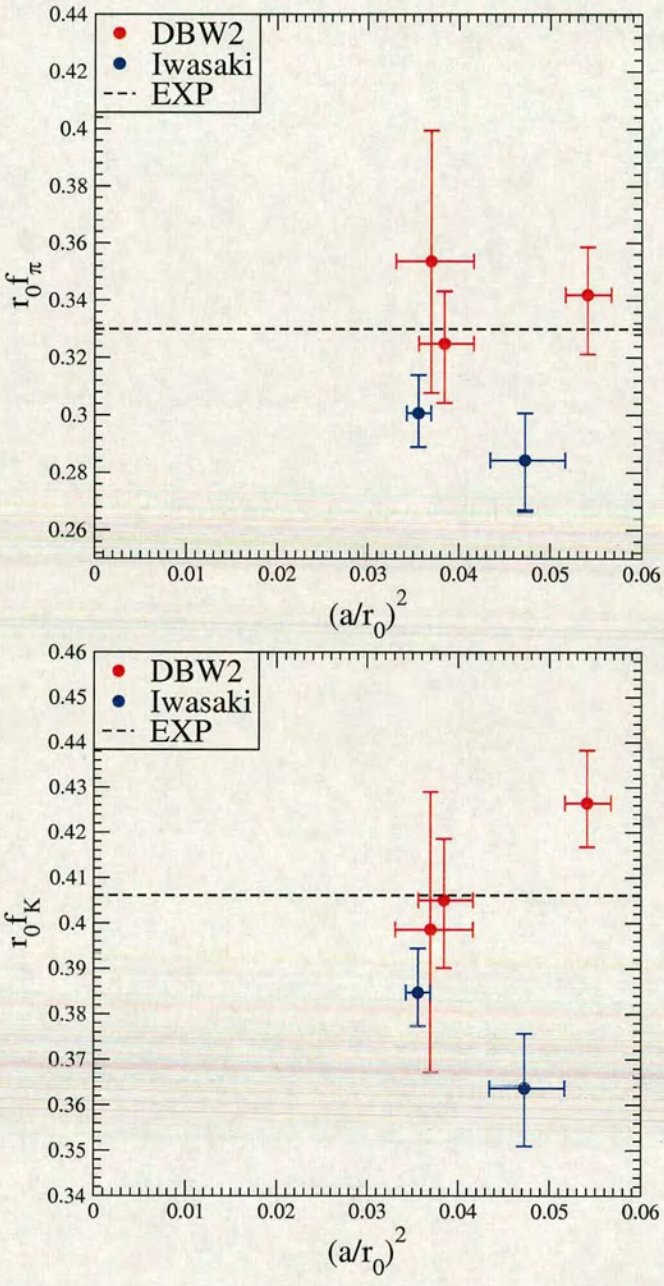

Figure 5.20: Dimensionless values of **TOP:** $r_0 f_\pi$ and **BOTTOM:** $r_0 f_K$ versus $(a/r_0)^2$ for all the datasets. The dotted lines are the experimentally obtained values scaled by appropriate factors of r_0.

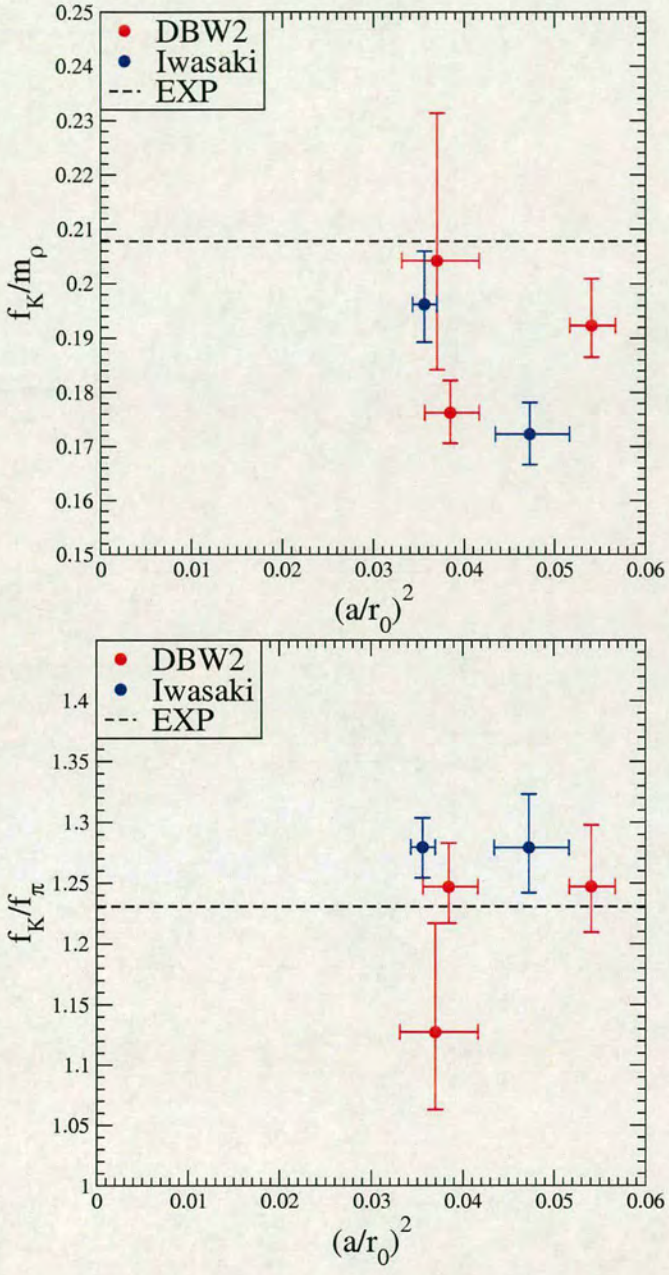

Figure 5.21: Ratios of **TOP:** f_K/m_ρ and **BOTTOM:** f_K/f_{PS} for plotted against $(a/r_0)^2$ for all the β values. The dotted lines are calculated from the ratio of the experimental values.

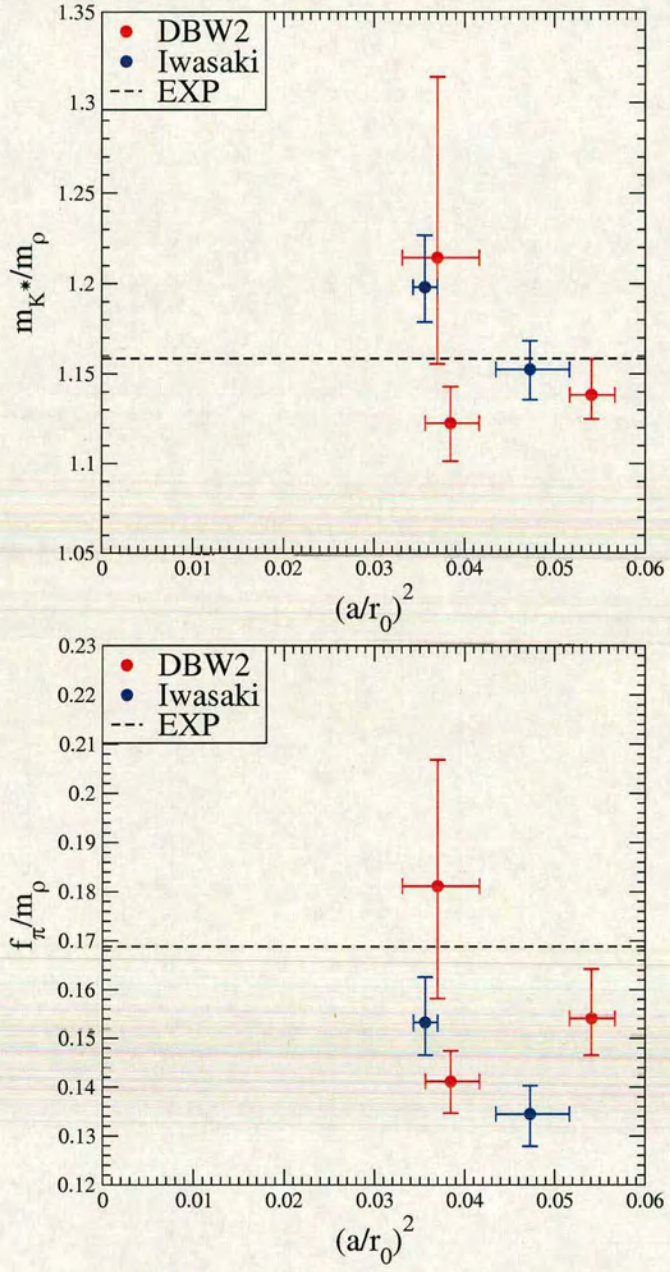

Figure 5.22: Ratios of **TOP:** m_{K^*}/m_ρ and **BOTTOM:** f_{PS}/m_ρ plotted against $(a/r_0)^2$ for all the β values. The dotted lines are calculated from the ratio of the experimental values.

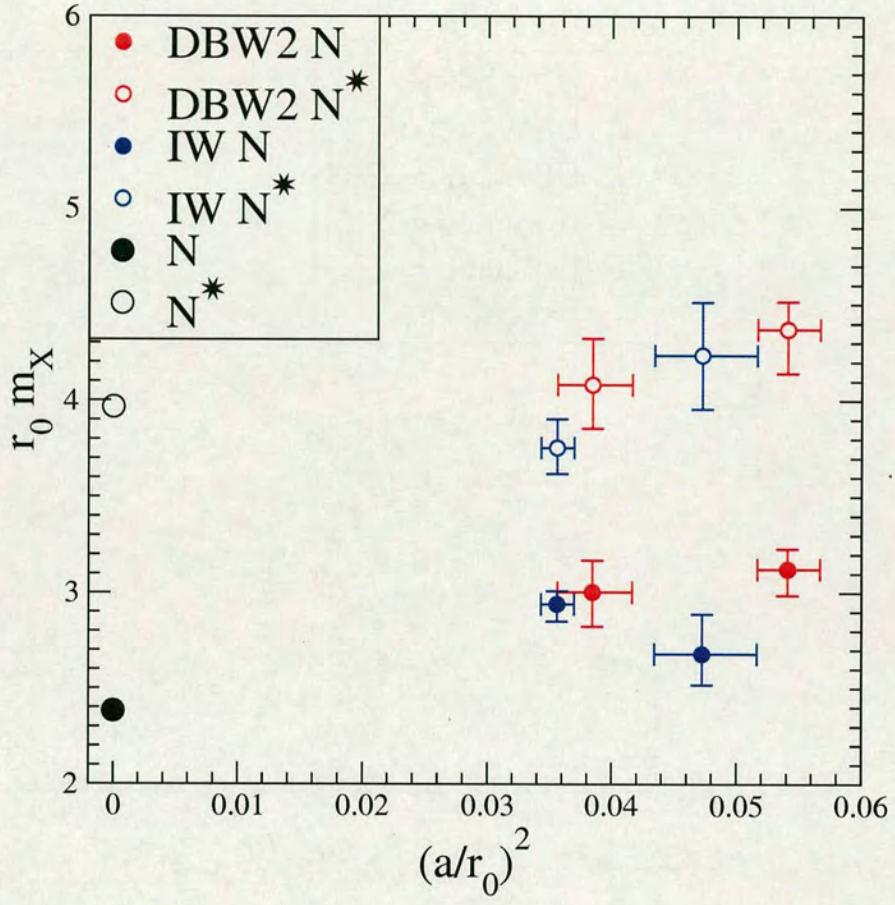

Figure 5.23: Scaling of the baryon spectrum with lattice spacing squared. Closed circles denote the nucleon, N, and open circles the negative parity partner, $N^{\star}$. Black symbols denote the experimental values scaled by appropriate factors of r_0, red symbols the DBW2 ensembles and blue symbols the Iwasaki ensembles. The value of $r_0 = 0.5$fm was chosen to give an indication of the experimental spectrum in these units.

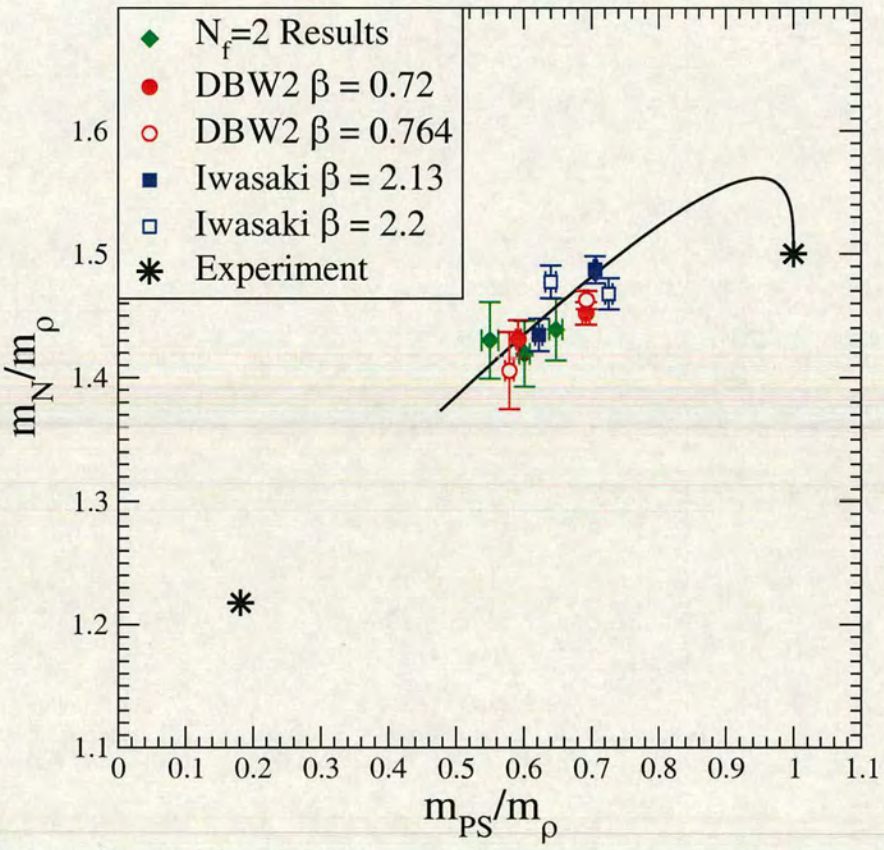

Figure 5.24: The Edinburgh plot. Red symbols denote the DBW2 ensembles and blue symbols the Iwasaki ensembles. The phenomenological curve derived from [111] has been shown to guide the eye. Experimental ratios and the values obtained in the static quark limit, where the hadron mass is equal to the sum of the valence quark masses, are given by the starred points. For comparison the green points are from 2 flavour simulations described in [112].

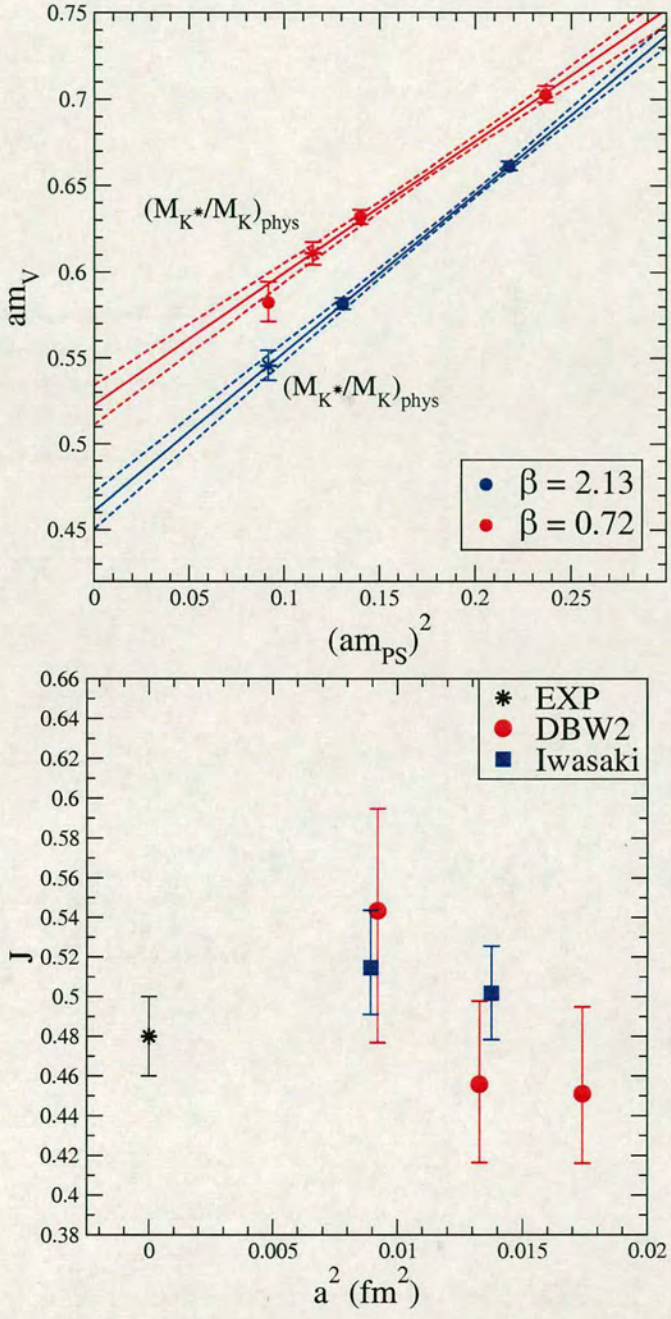

Figure 5.25: **TOP** Linear dependence of am_V on $(am_{PS})^2$. **BOTTOM** The J parameter on all the datasets.

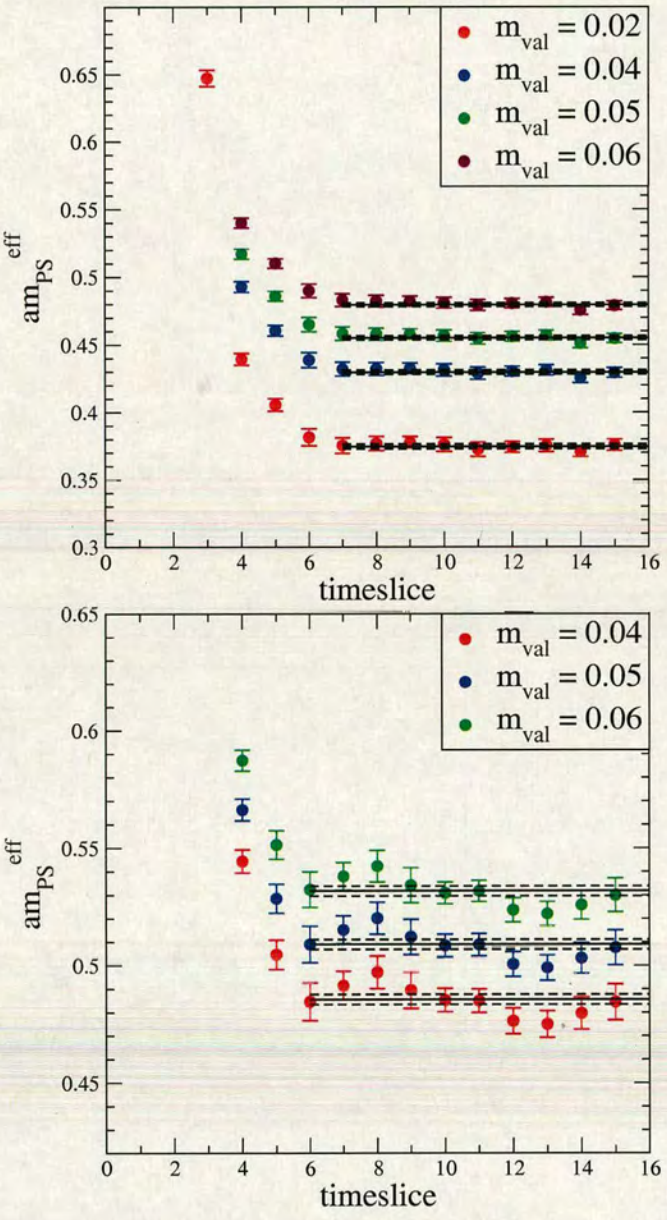

Figure 5.26: **TOP:** Pseudoscalar meson effective masses for the (0.72,0.02/0.04) dataset. All correlators had one quark smeared at source. **BOTTOM:** Pseudoscalar meson effective masses for the (0.72,0.04/0.04) dataset. All correlators had one quark smeared at source.

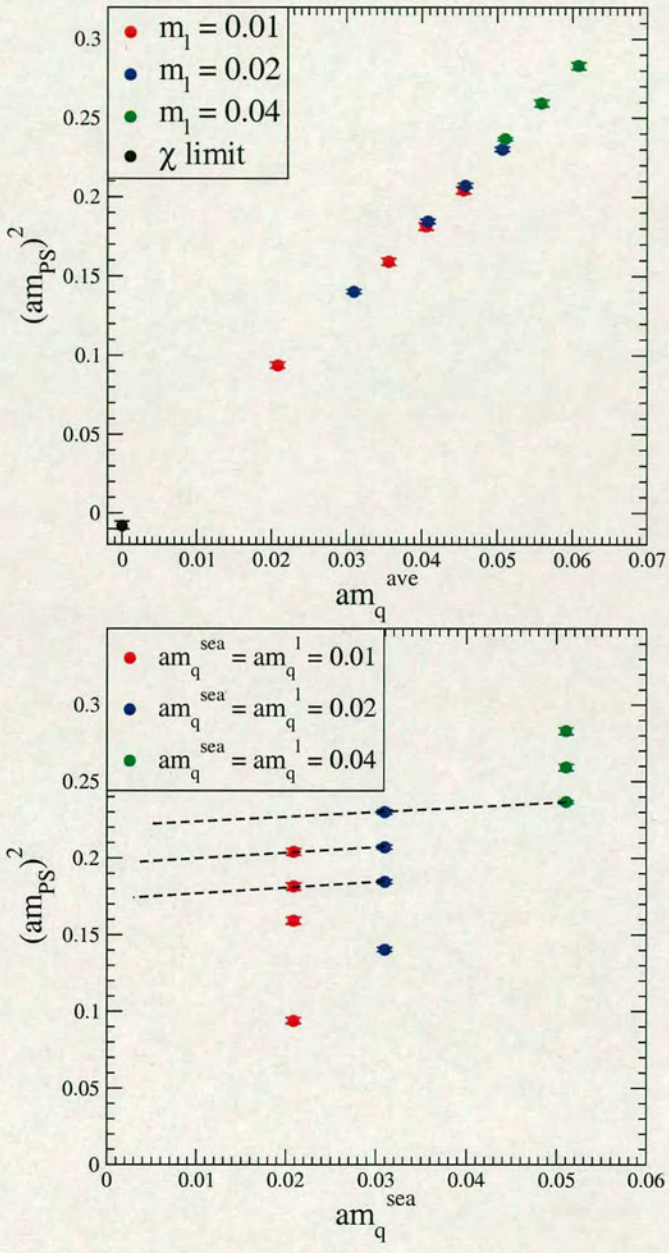

Figure 5.27: **TOP:** Pseudoscalar mass squared versus average quark mass. **BOTTOM:** Sea quark mass dependence of the pseudoscalar mass squared. The dotted lines go through points of equal average quark mass.

Chapter 6

Conclusion

This thesis has presented results on the light hadron spectrum from numerical simulations of Lattice QCD. Chapters 2 and 3 introduce the basics of the theory. In chapter 4 a mixed action formalism is introduced and exploratory results are presented. In chapter 5 results from calculations using the domain wall quark action and one of a class of improved gauge actions with 2+1 flavours of dynamical light quarks are presented. This chapter summarises the results of these numerical calculations.

6.1 Summary of the mixed action analysis

While staggered quarks appear to offer the most cost effective way of simulating light dynamical quarks today, they require the use of a mixed action formulation of QCD. Outside the chiral regime of both valence and sea quarks, it is necessary to implement a matching procedure for the quark masses for the model to be in the same universality class as QCD. (Within the chiral regime, the partially quenched results may be matched to chiral perturbation theory and thence to QCD low energy constants.) Indeed, in chapter 4 it has been shown numeri-

cally that the partially quenched theory with $m_{\text{val}} < m_{\text{sea}}$ has similar negative metric pathologies to those observed by Bardeen *et al.* in quenched QCD. In principle, this observation provides a matching condition, but, just like the alternative approach of determining m_{sea} by matching a flavour singlet quantity to experiment, suffers from a poor signal-to-noise ratio in practice. Despite these practical problems with matching, encouragingly good signals for flavour non-singlet hadron masses and decay constants using overlap valence quarks on a staggered sea quark ensemble have been obtained. The potential gain from the simplicity of valence quarks with the correct flavour and chiral symmetries, together with the clean statistical signals, particularly for baryons, and the recent comments on an additive shift to the quark mass is good motivation for trying to improve on these exploratory attempts to match valence and sea quark masses.

6.2 Summary of the domain wall analysis

The domain wall formulation of quark fields is now understood as one of a wider class of lattice fermion actions that obey the Ginsparg-Wilson relation. Several ensembles have been generated on the QCDOC machines with 2+1 flavours of quark using the domain wall fermion formulation with two different gauge actions, several β values and multiple sea quark masses. These ensembles have a relatively small volume and limited statistics as they were primarily generated to search parameter space for a larger production run. A fifth dimension size of eight produces a residual mass larger than would be acceptable for such a production run. Even with these drawbacks it is still possible to calculate the light hadron spectrum and pseudoscalar decay constants obtaining results which are consistent with experiment and show some scaling within large errors. The nucleon and negative parity partner masses have been determined for several of the ensembles. With limited statistics, and only two different sea quark masses,

we qualitatively reproduce the experimental spectrum. There is limited evidence that finite size effects may be influencing the ground state baryons on the smaller volumes. The 2+1 flavour simulations show good agreement when compared to previous 2 flavour simulations. Within the relatively low statistics available it is however, difficult to observe any effect in the data due to the addition of the heavy quark such as those observed in [114] for example. Indeed, for the case of quark masses in the chiral limit, good agreement was observed between 2 and 2+1 flavour improved Wilson simulations [115]. Both the Edinburgh plot, and the scaling analysis suggest that a programme of baryon physics on larger volumes and at lighter quark mass will yield very interesting results.

Appendix A

Grassmann Variables

The fundamental matter fields in nature are believed to carry spin $\frac{1}{2}$. In contrast to the bosonic case, these fields anticommute, and hence are elements of a Grassmann algebra. The path integral built from fermionic fields will therefore involve the integration of anticommuting (Grassmann) variables. A Grassmann algebra, $\mathcal{G}$, is an associative algebra generated by a unit (denoted 1) and a set of generators $\{\theta_i\}$ that satisfy the anticommutation relations

$$\{\theta_i, \theta_j\} = \theta_i\theta_j + \theta_j\theta_i = 0 \quad i, j = 1, \ldots, N \tag{A.1}$$

As a consequence, it follows that $\theta_i^2 = 0$ and hence, if the number n of generators is finite then all elements of the algebra may be written as a linear combination of the elements 1 and $\{\theta_{i_1}\theta_{i_2}\ldots\theta_{i_p}\}$ with $i_1 < i_2 < \ldots < i_p$, $1 \leq p \leq n$. Therefore, we may write a general Grassmann element as a power series in the $\{\theta_i\}$

$$A(\theta) = A_0 + \sum_i A_i\theta + \sum_{i\neq j} A_{ij}\theta_i\theta_j + \cdots + A_{12\ldots N}\theta_i\theta_j\cdots\theta_N. \tag{A.2}$$

Since the Grassmann variables anti-commute, the function A can only be a polynomial of a finite degree. In quantum mechanics we often require Grassmann algebras with an even number of generators which can be divided into two subsets $\{\theta_i\}$ and $\{\bar{\theta}_i\}$, $i, j = 1, \ldots, n$. One can define the algebra generated by $\{\theta_i\bar{\theta}_i\}$

the analogue of usual complex conjugation

$$\theta^\dagger = \bar{\theta}, \quad \bar{\theta}^\dagger = \theta \tag{A.3}$$

and as a consequence $(\theta\bar{\theta})^\dagger = \theta\bar{\theta}$.

A.1 Differentiation of Grassmann algebras

In Grassmann algebras, it is possible to define a generalised derivative, however, a too naive definition would be inconsistent with the non-commutative nature of the algebra. Consider as an example some general function $A = A_1 + \theta_i A_2$, where A_1 and A_2 do not depend on θ_i. We define the derivative with respect to θ_i as

$$\frac{\partial A}{\partial \theta_i} = A_2. \tag{A.4}$$

As in usual differentiation it is a linear operation, however, $(\frac{\partial}{\partial \theta_i})^2 = 0$. Similarly we may define a right derivative $\frac{\overleftarrow{\partial}}{\partial \theta_i}$ by commuting θ_i to the left before suppressing it

$$\theta_i \frac{\overleftarrow{\partial}}{\partial \theta_i} = 1 \tag{A.5}$$

so for example

$$\frac{\partial}{\partial \theta_i}\theta_j\theta_i = -\theta_j = 0_i\theta_j\frac{\overleftarrow{\partial}}{\partial \theta_i} \quad (i \neq j). \tag{A.6}$$

A.2 Integration of Grassmann algebras

The main thing that we want to do with anticommuting numbers is integrate over them. We define the integral of a general function f of a Grassmann variable θ as

$$\int d\theta f(\theta) \tag{A.7}$$

over the whole range θ. To perform integrations of functions of Grassmann variables is suffices to define the rules

$$\begin{aligned} \int d\theta_i &= 0 \\ \int d\theta_i \theta_i &= 1 \end{aligned} \tag{A.8}$$

where for multiple integrals the integration measures $\{d\theta_j\}$ anti-commute with themselves and the $\{\theta_i\}$

$$\{\theta_i, d\theta_j\} = \{d\theta_i, d\theta_j\} = 0 \ \forall i, j. \tag{A.9}$$

A.3 Gaussian integration

We now define gaussian integration over two families of generators $\{\theta_i, \bar{\theta}_i\}$, $i = 1, \ldots, n$. This result is important in quantum field theories.

We first consider the integral

$$\mathcal{Z}[M] = \int d\theta_1 d\bar{\theta}_1 d\theta_2 d\bar{\theta}_2 \ldots d\theta_n d\bar{\theta}_n \exp\left(\sum_{\mathrm{i,j}=1}^{\mathrm{n}} \bar{\theta}_{\mathrm{i}} \mathrm{M}_{\mathrm{ij}} \theta_{\mathrm{j}}\right). \tag{A.10}$$

According to the rules of Grassmann integration, the result is simply the coefficient of the product $\bar{\theta}_n \theta_n \ldots \bar{\theta}_1 \theta_1$ in the expansion of the integrand. The argument of the exponential contains only terms belonging to the Grassmann algebra $\mathcal{G}$, which commute. The integrand can thus be written as

$$\begin{aligned} \exp\left(\sum_{\mathrm{i,j}=1}^{\mathrm{n}} \bar{\theta}_{\mathrm{i}} \mathrm{M}_{\mathrm{ij}} \theta_{\mathrm{j}}\right) &= \prod_{i=1}^{n} \exp\left(\bar{\theta}_{\mathrm{i}} \sum_{\mathrm{j}=1}^{\mathrm{n}} \mathrm{M}_{\mathrm{ij}} \theta_{\mathrm{j}}\right) \\ &= \prod_{i=1}^{n} \left(1 + \bar{\theta}_i \sum_{j_i=1}^{n} M_{i j_i} \theta_{j_i}\right) \end{aligned} \tag{A.11}$$

where in the last step we have used the fact that since $\bar{\theta}_i^2 = 0$ only the first two terms in the expansion of the exponential will contribute. Expanding the product

one observes that in each factor only the term proportional to $\bar{\theta}_i$ contributes to the integral. It thus remains to integrate

$$\prod_{i=1}^{n} \bar{\theta}_i \left(\sum_{j_i=1}^{n} M_{ij_i} \theta_{j_i} \right). \tag{A.12}$$

The terms giving non-vanishing contribution to the integral are those that contain the product $\theta_n \ldots \theta_2 \theta_1$ up to a permutation of the factors θ_j since repeated θ's give zero. They have the form

$$\sum_{\substack{\text{permutations} \\ \{j_1 \ldots j_n\}}} M_{nj_n} M_{n-1 j_{n-1}} \ldots M_{1j_1} \bar{\theta}_n \theta_{j_n} \ldots \bar{\theta}_1 \theta_{j_1}. \tag{A.13}$$

As the product of the Grassmann variables is antisymmetric under the exchange of any pair of indices i_l, $i_{l'}$ we can write the expression A.13 in some standard order as

$$\bar{\theta}_n \theta_n \ldots \bar{\theta}_1 \theta_1 \sum_{j_1 \ldots j_n} \epsilon_{j_1 j_2 \ldots j_n} M_{1j_1} M_{2j_2} \ldots M_{nj_n}, \tag{A.14}$$

where $\epsilon_{j_1 j_2 \ldots j_n}$ is the epsilon tensor in n dimensions. Recalling the definition of the determinant of a matrix

$$\det M = \sum_{j_1 \cdots j_n} \epsilon_{j_1 \cdots j_n} M_{1j_1} \cdots M_{nj_n}. \tag{A.15}$$

Thus we can finally evaluate the integral A.10 and obtain

$$\begin{aligned} \mathcal{Z}[M] &= \prod_{i=1}^{n} \int d\theta_i d\bar{\theta}_i \exp\left(\sum_{\mathrm{i,j=1}}^{\mathrm{n}} \bar{\theta}_{\mathrm{i}} \mathrm{M}_{\mathrm{ij}} \theta_{\mathrm{j}} \right) \\ &= \prod_{i=1}^{n} \int d\theta_i d\bar{\theta}_i \bar{\theta}_i \theta_i \det M \\ &= \det M \end{aligned} \tag{A.16}$$

With the definition of complex conjugation given in equation A.3, θ_i and $\bar{\theta}_i$ are conjugate. Moreover, the conjugate of a quadratic form is

$$\sum_{i,j=1}^{n} \left(\bar{\theta}_i M_{ij} \theta_j \right)^\dagger = \sum_{i,j=1}^{n} \bar{\theta}_j \bar{M}_{ij} \theta_i = \sum_{i,j=1}^{n} \bar{\theta}_i M^\dagger_{ij} \theta_j. \tag{A.17}$$

Then, the result of the integral is real since

$$\det M = \det M^{\dagger} = \overline{\det M}. \tag{A.18}$$

Introducing a further copy of the Grassmann algebra $\mathcal{G}$, whose generators we denote by η_i and $\bar{\eta}_i$, and consider the Grassmann algebra generated by the set $\{\theta, \bar{\theta}, \eta, \bar{\eta}\}$. We first evaluate the integral

$$\mathcal{Z}_{\mathrm{G}}(\eta, \bar{\eta}) = \int \prod_i d\theta_i d\bar{\theta}_i \mathrm{exp} \mathrm{E}_{\mathrm{G}}(\theta, \bar{\theta}, \eta, \bar{\eta}) \tag{A.19}$$

with

$$E_G(\theta, \bar{\theta}, \eta, \bar{\eta}) = \sum_{i,j=1}^{n} \bar{\theta}_i M_{ij} \theta_j + \sum_{i=1}^{n} \left(\bar{\eta}_i \theta_i + \bar{\theta}_i \eta_i \right), \tag{A.20}$$

where E_G, thus is an element of the direct sum of the two copies of the initial Grassmann algebra. Provided $\det M \neq 0$ we can introduce the inverse matrix

$$\Delta = M^{-1} \tag{A.21}$$

and make the change of variable

$$\theta_i = \theta'_i - \sum_j \Delta_{ij} \eta_j, \quad \bar{\theta}_i = \bar{\theta}'_i - \sum_j \bar{\eta}_j \Delta_{ji}. \tag{A.22}$$

After this change of variables the integral takes the form

$$\begin{aligned} \mathcal{Z}_{\mathrm{G}}(\eta, \bar{\eta}) &= \int \prod_i d\theta_i d\bar{\theta}_i \mathrm{exp} \left(\sum_{\mathrm{i,j=1}}^{\mathrm{n}} \bar{\theta}'_{\mathrm{i}} \mathrm{M}_{\mathrm{ij}} \theta'_{\mathrm{j}} \right) \mathrm{exp} \left(- \sum_{\mathrm{i,j=1}}^{\mathrm{n}} \bar{\eta}_{\mathrm{i}} \Delta_{\mathrm{ij}} \eta_{\mathrm{j}} \right) \\ &= \det M \mathrm{exp} \left(- \sum_{\mathrm{i,j=1}}^{\mathrm{n}} \bar{\eta}_{\mathrm{i}} \Delta_{\mathrm{ij}} \eta_{\mathrm{j}} \right) \end{aligned} \tag{A.23}$$

where the invariance of the integration measure is ensured by the Grassmann integration rules. See e.g. /refZinn-Justin

Notice that in contrast to the bosonic case the generating functional is proportional to $\det M$ rather than $(\det M)^{-\frac{1}{2}}$ which may be seen many text books (name a few for refs).

A.4 Gaussian expectation values

Using the rules of Grassmann differentiation we note that

$$\begin{aligned} \frac{\partial}{\partial\bar{\eta}_i}e^{E_G(\theta,\bar{\theta},\eta,\bar{\eta})} &= \theta_i e^{E_G(\theta,\bar{\theta},\eta,\bar{\eta})} \\ \frac{\partial}{\partial\eta_i}e^{E_G(\theta,\bar{\theta},\eta,\bar{\eta})} &= -\bar{\theta}_i e^{E_G(\theta,\bar{\theta},\eta,\bar{\eta})}. \end{aligned} \tag{A.24}$$

Denoting $\langle\bullet\rangle_\eta$ as the expectation value of $\bullet$ with respect to the gaussian weight corresponding to the integrand A.19 from the definitions A.19 and A.20 and the Grassmann derivatives, it follows that

$$\begin{aligned} \langle\theta_i\rangle_\eta &= \mathcal{Z}_G^{-1}\frac{\partial}{\partial\bar{\eta}_i}\mathcal{Z}_G, \\ \langle\bar{\theta}_i\rangle_\eta &= -\mathcal{Z}_G^{-1}\frac{\partial}{\partial\eta_i}\mathcal{Z}_G. \end{aligned} \tag{A.25}$$

Another useful identity obtained by differentiating twice (note the order) is

$$\langle\bar{\theta}_i\theta_j\rangle_\eta = \mathcal{Z}_G^{-1}\frac{\partial}{\partial\bar{\eta}_j}\frac{\partial}{\partial\eta_i}\mathcal{Z}_G - \left(\mathcal{Z}_G^{-1}\frac{\partial}{\partial\bar{\eta}_j}\mathcal{Z}_G\right)\left(\mathcal{Z}_G^{-1}\frac{\partial}{\partial\eta_i}\mathcal{Z}_G\right). \tag{A.26}$$

Since in general we are interested in two-point correlation functions of the form

$$\langle\bar{\theta}_i\theta_j\rangle = \frac{\int\left(\prod_i d\theta_i d\bar{\theta}_i\right)\bar{\theta}_i\theta_j\exp\left(\sum_{\mathrm{i,j}=1}^{\mathrm{n}}\bar{\theta}_{\mathrm{i}}\mathrm{M}_{\mathrm{ij}}\theta_{\mathrm{j}}\right)}{\mathcal{Z}_G} \tag{A.27}$$

we note that $\mathcal{Z}_G^{-1}|_{\eta=\bar{\eta}=0} = \det M$ from equation A.23. Using the rules of differentiation,

$$\begin{aligned} &\int\left(\prod_i d\theta_i d\bar{\theta}_i\right)\bar{\theta}_i\theta_j\exp\left(\sum_{\mathrm{i,j}=1}^{\mathrm{n}}\bar{\theta}_{\mathrm{i}}\mathrm{M}_{\mathrm{ij}}\theta_{\mathrm{j}} + \sum_{\mathrm{i}=1}^{\mathrm{n}}\left(\bar{\eta}_{\mathrm{i}}\theta_{\mathrm{i}} + \bar{\theta}_{\mathrm{i}}\eta_{\mathrm{i}}\right)\right) \\ &= \int\left(\prod_i d\theta_i d\bar{\theta}_i\right)\frac{\partial}{\partial\bar{\eta}_j}\frac{\partial}{\partial\eta_i}\exp\left(\sum_{\mathrm{i,j}=1}^{\mathrm{n}}\bar{\theta}_{\mathrm{i}}\mathrm{M}_{\mathrm{ij}}\theta_{\mathrm{j}} + \sum_{\mathrm{j}=1}^{\mathrm{n}}\bar{\eta}_{\mathrm{j}}\theta_{\mathrm{j}} + \sum_{\mathrm{i}=1}^{\mathrm{n}}\bar{\theta}_{\mathrm{i}}\eta_{\mathrm{i}}\right) \\ &= \frac{\partial}{\partial\bar{\eta}_j}\frac{\partial}{\partial\eta_i}\mathcal{Z}_G. \end{aligned} \tag{A.28}$$

Replacing $\mathcal{Z}_G$ by the expression in A.23 and evaluating at $\eta = \bar{\eta} = 0$

$$\begin{aligned} \frac{\partial}{\partial\bar{\eta}_j}\frac{\partial}{\partial\eta_i}\mathcal{Z}_G\Big|_{\eta=\bar{\eta}=0} &= \frac{\partial}{\partial\bar{\eta}_j}\frac{\partial}{\partial\eta_i}\left(\det M\exp\left(-\sum_{\mathrm{i,j}=1}^{\mathrm{n}}\bar{\eta}_{\mathrm{j}}\Delta_{\mathrm{ji}}\eta_{\mathrm{i}}\right)\right)\Big|_{\eta=\bar{\eta}=0} \\ &= \det M\Delta_{ji} \end{aligned} \tag{A.29}$$

and using the relations A.28 and A.29 in equation A.27 gives

$$\langle \bar{\theta}_i \theta_j \rangle = \frac{1}{\det M} \det M \Delta_{ji} = \Delta_{ji} = M_{ji}^{-1}. \tag{A.30}$$

Hence we note also that equation A.26 in the limit $\eta = \bar{\eta} = 0$ yields

$$\langle \bar{\theta}_i \theta_j \rangle = \Delta_{ji} = M_{ji}^{-1}. \tag{A.31}$$

These results can be expanded to include n-point functions of Grassmann variables. See for example [7, 116].

Appendix B

Baryon operators

B.1 General 3 Quark Operators

The aim of this appendix is to show that the form of the interpolating operators used to describe baryons has the correct symmetry properties. We will make the general ansatz that the tri-quark operator takes the form

$$O^{ijk}(x) = \psi_\alpha^{ia}(x) A_{\alpha\beta} \psi_\beta^{jb}(x) \psi_\gamma^{kc}(x) \epsilon_{abc} \tag{B.1}$$

where α, β, γ are the quark spinor indices, i, j, k are the quark flavour indices, a, b, c are the colour indices and A is the matrix given by

$$A_{\alpha\beta} = (C\Gamma)_{\alpha\beta} \tag{B.2}$$

where Γ is a member of the Clifford algebra. It will then be shown that operators of this type do indeed take the form required to describe firstly the the proton and secondly the decuplet baryon for particular choices of the matrix A.

The proton is an $I = \frac{1}{2}$ particle. The operator O^{ijk} that we choose to describe the proton is therefore required to have $I = \frac{1}{2}$. The quarks that make up the proton contain $I = \frac{1}{2}$ and have component of isospin $I_3 = \pm\frac{1}{2}$. The problem

then becomes that of putting two "up" type quarks and one "down" type quark together to create a bound state that has $I = \frac{1}{2}$.

Isospin is an SU(2) symmetry. Consider the case of two quarks each with $I = \frac{1}{2}$. The combined system can have a total isospin that is equal to 1 or 0. These states are referred to as triplet or singlet states respectively, because in the former there are three possible values for the isospin component quantum number, $I_3 = 1, 0, -1$, whereas in the latter there is only one such value, $I_3 = 0$. Using the notation χ_{I,I_3} to denote a state with total isospin I and isospin component, I_3, the possible states for the combined system are

$$\chi_{1,1} = \alpha_1\alpha_2 \tag{B.3}$$

$$\chi_{1,0} = \sqrt{\frac{1}{2}}(\alpha_1\beta_2 + \beta_1\alpha_2) \tag{B.4}$$

$$\chi_{1,-1} = \beta_1\beta_2 \tag{B.5}$$

$$\chi_{0,0} = \sqrt{\frac{1}{2}}(\alpha_1\beta_2 - \beta_1\alpha_2) \tag{B.6}$$

where we have used α_1 as quark 1 having $I_3 = +\frac{1}{2}$ and β_2 is quark 2 having $I_3 = -\frac{1}{2}$. The singlet state, $\chi_{0,0}$, is totally antisymmetric under interchange of quarks 1 and 2. In the baryon ground state, where orbital angular momentum $l = 0$, all the angular momentum of the baryon comes from the combined spins of the three quarks. Three $I = \frac{1}{2}$ quarks can be combined into a system with *total isospin* $= \frac{1}{2}$ or $\frac{3}{2}$, or in SU(2) group theory language

$$2 \otimes 2 \otimes 2 = 4 \oplus 2 \oplus 2 \tag{B.7}$$

or

$$\frac{1}{2} \otimes \frac{1}{2} \otimes \frac{1}{2} = (1 \oplus 0) \otimes \frac{1}{2} = \frac{3}{2} \oplus \frac{1}{2} \oplus \frac{1}{2}. \tag{B.8}$$

There are two distinct ways of making an overall $I = \frac{1}{2}$ system composed of three quarks

- couple an isospin $\frac{1}{2}$ quark to the isosinglet state ($\chi_{0,0}$)

- couple an isospin $\frac{1}{2}$ quark to a total isospin 1 combination of two quarks ($\chi_{1,1}, \chi_{1,0}, \chi_{1,-1}$) using the appropriate Clebsch Gordan coefficients.

Coupling to the isosinglet state can be accomplished in two distinct ways. Specifically

$$\begin{aligned} |\frac{1}{2}\frac{1}{2}\rangle_{12} &= \sqrt{\frac{1}{2}}(\alpha_1\beta_2 - \beta_1\alpha_2)\alpha_3 \\ |\frac{1}{2}-\frac{1}{2}\rangle_{12} &= \sqrt{\frac{1}{2}}(\alpha_1\beta_2 - \beta_1\alpha_2)\beta_3 \end{aligned} \tag{B.9}$$

$$\begin{aligned} |\frac{1}{2}\frac{1}{2}\rangle_{23} &= \sqrt{\frac{1}{2}}\alpha_1(\alpha_2\beta_3 - \beta_2\alpha_3) \\ |\frac{1}{2}-\frac{1}{2}\rangle_{23} &= \sqrt{\frac{1}{2}}\beta_1(\alpha_2\beta_3 - \beta_2\alpha_3) \end{aligned} \tag{B.10}$$

and

$$\begin{aligned} |\frac{1}{2}\frac{1}{2}\rangle_{13} &= \sqrt{\frac{1}{2}}(\alpha_1\alpha_2\beta_3 - \beta_1\alpha_2\alpha_3) \\ |\frac{1}{2}-\frac{1}{2}\rangle_{13} &= \sqrt{\frac{1}{2}}(\alpha_1\beta_2\beta_3 - \beta_1\beta_2\alpha_3) \end{aligned} \tag{B.11}$$

where the subscript on the ket (e.g. $|I, I_3\rangle_{ij}$) denotes that this is antisymmetric under interchange of i and j. Only (B.9) and (B.10) are independent as

$$|\rangle_{13} = |\rangle_{12} + |\rangle_{23}. \tag{B.12}$$

In the second case a third quark may be coupled to the $I = 1$ di-quark combination in two ways to produce an $I = \frac{1}{2}$ three quark state

$$\begin{aligned} |\frac{1}{2}\frac{1}{2}\rangle &= \sqrt{\frac{2}{3}}\alpha_1\alpha_2\beta_3 - \sqrt{\frac{1}{3}}\cdot\sqrt{\frac{1}{2}}(\alpha_1\beta_2 + \beta_1\alpha_2)\alpha_3 \qquad \text{(B.13)} \\ &= \sqrt{\frac{1}{6}}(2\alpha_1\alpha_2\beta_3 - \alpha_1\beta_2\alpha_3 - \beta_1\alpha_2\alpha_3) \\ |\frac{1}{2}-\frac{1}{2}\rangle &= \sqrt{\frac{1}{3}}\cdot\sqrt{\frac{1}{2}}(\alpha_1\beta_2 + \beta_1\alpha_2)\beta_3 - \sqrt{\frac{2}{3}}\beta_1\beta_2\alpha_3 \qquad \text{(B.14)} \\ &= \sqrt{\frac{1}{6}}(\alpha_1\beta_2\beta_3 + \beta_1\alpha_2\beta_3 - 2\beta_1\beta_2\alpha_3). \end{aligned}$$

The operator for the proton is given by replacing $A_{\alpha\beta}$ by the combination $C\gamma_5$ or $C\gamma_4\gamma_5$ and using the appropriate flavours of quarks - $i = u, j = d, k = u$ in equation(B.1). In order to have an overlap with the proton groundstate we require this operator to have isospin quantum numbers $|\frac{1}{2}, \frac{1}{2}\rangle$. If the matrix A in equation(B.1) satisfies $A^T = -A$ we have

$$O^{udu} = \left(u^a_\alpha A_{\alpha\beta} d^b_\beta\right) u^c_\gamma \epsilon_{abc} \tag{B.15}$$

and then

$$\begin{aligned}
O^{duu} &= \left(d^a_\alpha A_{\alpha\beta} u^b_\beta\right) u^c_\gamma \epsilon_{abc} && \text{(B.16)}\\
&= \left(d^a_\alpha (A^T)_{\beta\alpha} u^b_\beta\right) u^c_\gamma \epsilon_{abc} && \text{(B.17)}\\
&= -\left(d^a_\alpha A_{\beta\alpha} u^b_\beta\right) u^c_\gamma \epsilon_{abc} \quad A^T = -A && \text{(B.18)}\\
&= \left(u^b_\beta A_{\beta\alpha} d^a_\alpha\right) u^c_\gamma \epsilon_{abc} && \text{(B.19)}\\
&= \left(u^a_\alpha A_{\alpha\beta} d^b_\beta\right) u^c_\gamma \epsilon_{bac} && \text{(B.20)}\\
&= -\left(u^a_\alpha A_{\alpha\beta} d^b_\beta\right) u^c_\gamma \epsilon_{abc} && \text{(B.21)}\\
&= -O^{udu} && \text{(B.22)}
\end{aligned}$$

where in (B.19) interchanging any two quarks gives a minus sign as they are Grassmann valued variables, in (B.20) the indices have been relabelled and in (B.21) the anti-symmetry of ϵ_{ijk} under interchange of indices has been used. O^{udu} is antisymmetric under interchange of u and d. For an matrix A, such that $A^T = -A$, the di-quark piece of the operator is completely antisymmetric and must belong to the isosinglet state with $I = 0$ and $I_3 = 0$. The isospin of the baryon (nucleon here) is given by the isospin of the third quark which is either $u = |\frac{1}{2}, \frac{1}{2}\rangle$ for the proton or $d = |\frac{1}{2}, -\frac{1}{2}\rangle$ for the neutron. The operator O^{udu} will have the correct isospin for the proton provided the matrix in the operator has the property $A^T = -A$.

Using the representation independent relations

$$C\gamma_\mu C^{-1} = -\gamma_\mu^T \tag{B.23}$$

$$C\gamma_5 C^{-1} = \gamma_5^T \tag{B.24}$$

$$C^\dagger = C^{-1} = C^T = -C \tag{B.25}$$

$$C\sigma_{\mu\nu} C^{-1} = -\sigma_{\mu\nu}^T \tag{B.26}$$

and the commutation relations between the gamma matrices we require to show that the choice $C\gamma_5$ or $C\gamma_4\gamma_5$ for A for a proton satisfies $A^T = -A$. Relation (B.24) gives

$$(C\gamma_5)^T = \gamma_5^T C^T = -\gamma_5^T C = -C\gamma_5 \tag{B.27}$$

and from relation (B.23)

$$(C\gamma_\mu\gamma_5)^T = \gamma_5^T\gamma_\mu^T C^T = \gamma_5\gamma_\mu^T C^T = -\gamma_5\gamma_\mu^T C = \gamma_5 C\gamma_\mu = -C\gamma_\mu\gamma_5. \tag{B.28}$$

Constructing operators as in equation(B.15) with $A = \{C\gamma_5, C\gamma_\mu\gamma_5\}$ therefore gives an operator with $I = \frac{1}{2}$ as is required for a proton.

Another way of looking at this is to consider the action of the isospin raising operator I_+ on our interpolating operators. The action of I_+ on the u and d quarks is given by

$$I_+|u\rangle = I_+|\frac{1}{2}\frac{1}{2}\rangle = 0 \tag{B.29}$$

$$I_+|d\rangle = I_+|\frac{1}{2}-\frac{1}{2}\rangle = |\frac{1}{2}\frac{1}{2}\rangle = |u\rangle. \tag{B.30}$$

Applying I_+ to the proton interpolating operators

$$I_+(u^{Ta}(x)C\gamma_5 d^b(x))u^c(x)\epsilon^{abc} = (u^{Ta}(x)C\gamma_5 u^b(x))u^c(x)\epsilon^{abc} \tag{B.31}$$

$$= (u^{Ta}(x)C\gamma_5 u^b(x))^T u^c(x)\epsilon^{abc} \tag{B.32}$$

$$= -(u^{Ta}(x)C\gamma_5 u^b(x))u^c(x)\epsilon^{abc} \tag{B.33}$$

$$= 0 \tag{B.34}$$

and similarly

$$I_+(u^{Ta}(x)C\gamma_\mu\gamma_5 u^b(x))u^c(x)\epsilon^{abc} = (u^{Ta}(x)C\gamma_\mu\gamma_5 u^b(x))u^c(x)\epsilon^{abc} \tag{B.35}$$

$$= (u^{Ta}(x)C\gamma_\mu\gamma_5 u^b(x))^T u^c(x)\epsilon^{abc} \quad \text{(B.36)}$$

$$= -(u^{Ta}(x)C\gamma_5\gamma_\mu u^b(x))u^c(x)\epsilon^{abc} \quad \text{(B.37)}$$

$$= 0 \quad \text{(B.38)}$$

so all these operators must have $I = \frac{1}{2}$. Now that we have checked that the interpolating operator for the baryon(nucleon) gives the correct isospin quantum number we consider the symmetries properties of the interpolating operator under the Lorentz transformations.

B.2 Lorentz Invariance

Under a Lorentz transformation, $S(\Lambda)$, the spinor fields transform like

$$\begin{aligned} u \to u' &= S(\Lambda)u \\ \bar{u} \to \bar{u'} &= \bar{u}S^{-1}(\Lambda) \end{aligned} \quad \text{(B.39)}$$

with

$$S(\Lambda)\gamma^\mu S^{-1}(\Lambda) = \Lambda^\mu_\nu \gamma^\nu. \quad \text{(B.40)}$$

Mesons therefore transform as Lorentz scalars

$$\bar{u}u \to \bar{u'}u' = \bar{u}S^{-1}(\Lambda)S(\Lambda)u. \quad \text{(B.41)}$$

Under a Lorentz transformation the baryon operator

$$p_\alpha = \left(\psi^{Ta}C\gamma_5\psi^b\right)\psi^c_\alpha\epsilon^{abc} \quad \text{(B.42)}$$

transforms to

$$p_\alpha \to \left(\psi^{Ta}S^T(\Lambda)C\gamma_5 S(\Lambda)\psi^b\right)S(\Lambda)\psi^c_\alpha\epsilon^{abc}. \quad \text{(B.43)}$$

Using the relations [117]

$$S^T(\Lambda)C = CS^{-1}(\Lambda) \quad \text{(B.44)}$$

$$S^{-1}(\Lambda)\gamma_5 S(\Lambda) = \gamma_5 \quad \text{(B.45)}$$

the operator in equation(B.43) transforms like a spinor

$$p_\alpha \to S(\Lambda) p_\alpha \tag{B.46}$$

under Lorentz transformations. This operator is therefore a good operator for the spin-$\frac{1}{2}$ baryon octet and could be used (with the correct quark flavours) to describe the proton.

B.3 Parity

Similar considerations hold for the parity operator. Applying the parity operator, $\mathcal{P} = \gamma_4$, to the baryon operator B.42 gives

$$p_\alpha \to \left(\psi^{Ta} \mathcal{P}^T C \gamma_5 \mathcal{P} \psi^b\right) \mathcal{P} \psi^c_\alpha \epsilon^{abc}. \tag{B.47}$$

Applying the relations

$$\mathcal{P}^T C = -C\mathcal{P}^{-1} \tag{B.48}$$

$$\mathcal{P}^{-1} \gamma_5 \mathcal{P} = -\gamma_5 \tag{B.49}$$

to equation(B.47) the operator transforms like a spinor under parity

$$p_\alpha \to \mathcal{P} p_\alpha. \tag{B.50}$$

This operator has the transformation properties required to describe particles belonging to the spin-$\frac{1}{2}$ octet provided they have the correct flavour content.

Considerations of the Lorentz, isospin and parity transformation properties of the operator

$$p_\gamma(x) = \left(u^{Ta}_\alpha(x)(C\gamma_5)_{\alpha\beta} d^b_\beta(x)\right) u^c_\gamma(x) \epsilon_{abc} \tag{B.51}$$

lead us to the conclusion that this operator would be suitable to describe a nucleon (proton) state. Note that the positions of the u and d quarks in the above currents are there for convenience and would need to appropriately antisymmetrised.

Appendix C

Nucleon two point function

There are several different possible choices for the proton operator

$$p^1_\alpha = \left(u^a C\gamma_5 d^b\right) u^c_\alpha \epsilon^{abc} \tag{C.1}$$

$$p^2_\alpha = \left(u^a C\gamma_4\gamma_5 d^b\right) u^c_\alpha \epsilon^{abc} \tag{C.2}$$

where a, b, c are the colour indices and α is the free spinor index. These operators may be written more explicitly as

$$p_{\gamma,k} = \left(\psi^a_{\alpha,i}\Gamma_{P\alpha\beta}\psi^b_{\beta,j}\right)\psi^c_{\gamma,k}\epsilon^{abc}\epsilon^{ij} \tag{C.3}$$

where ϵ^{ij} is the totally antisymmetric tensor on two indices. ($\epsilon^{11} = \epsilon^{22} = 0$, $\epsilon^{12} = 1$ and $\epsilon^{21} = -1$.) This ensures the operators have the correct flavour content in order that they describe the proton. i, j, k now label the flavour indices and Γ_P $= \{C\gamma_5, C\gamma_4\gamma_5\}$.

The barred operator is defined by

$$\bar{p}_{\phi,l} = \bar{\psi}^f_{\phi,l}\left(\bar{\psi}^e_{\epsilon,e}\left(\bar{\Gamma}_P\right)_{\epsilon\delta}\bar{\psi}^d_{\delta,n}\right)\epsilon^{def}\epsilon^{nm}. \tag{C.4}$$

The nucleon two point function $\langle p_{\gamma,k}\bar{p}_{\phi,l}\rangle$ follows from

$$\langle p_{\gamma,k}\bar{p}_{\phi,l}\rangle = \epsilon^{abc}\epsilon^{ij}\epsilon^{def}\epsilon^{nm}\left(\Gamma_P\right)_{\alpha\beta}\left(\bar{\Gamma_P}\right)_{\epsilon\delta}\langle\psi^a_{i\alpha}\psi^b_{j\beta}\psi^c_{k\gamma}\bar{\psi}^f_{l\phi}\bar{\psi}^e_{m\epsilon}\bar{\psi}^d_{n\delta}\rangle. \tag{C.5}$$

Recalling that interchanging any of the quark fields introduces a minus sign (as they are Grassmann valued variables) and contracting quark fields such that

$$\overbrace{\psi^a_{i\alpha}(x)\bar{\psi}^f_{l\phi}}(y) = \delta_{il}G^{af}_{\alpha\phi}(x,y;U) \tag{C.6}$$

gives

$$\begin{aligned}
\langle p_{\gamma,k}\bar{p}_{\phi,l}\rangle = \epsilon^{abc}\epsilon^{def}\left(\Gamma_P\right)_{\alpha\beta}\left(\bar{\Gamma_P}\right)_{\epsilon\delta}[\; & - \; \delta_{il}G^{af}_{\alpha\phi}\delta_{jm}G^{be}_{\beta\epsilon}\delta_{kn}G^{cd}_{\gamma\delta}\epsilon^{ij}\epsilon^{nm} && \text{(C.7)}\\
& + \; \delta_{il}G^{af}_{\alpha\phi}\delta_{jn}G^{bd}_{\beta\delta}\delta_{km}G^{ce}_{\gamma\epsilon}\epsilon^{ij}\epsilon^{nm} && \text{(C.8)}\\
& - \; \delta_{im}G^{ae}_{\alpha\epsilon}\delta_{jn}G^{bd}_{\beta\delta}\delta_{kl}G^{cf}_{\gamma\phi}\epsilon^{ij}\epsilon^{nm} && \text{(C.9)}\\
& + \; \delta_{im}G^{ae}_{\alpha\epsilon}\delta_{jl}G^{bf}_{\beta\phi}\delta_{kn}G^{cd}_{\gamma\delta}\epsilon^{ij}\epsilon^{nm} && \text{(C.10)}\\
& + \; \delta_{in}G^{ad}_{\alpha\delta}\delta_{jm}G^{be}_{\beta\epsilon}\delta_{kl}G^{cf}_{\gamma\phi}\epsilon^{ij}\epsilon^{nm} && \text{(C.11)}\\
& - \; \delta_{in}G^{ad}_{\alpha\delta}\delta_{jl}G^{bf}_{\beta\phi}\delta_{km}G^{ce}_{\gamma\epsilon}\epsilon^{ij}\epsilon^{nm}]. && \text{(C.12)}
\end{aligned}$$

This operator will have an overlap with both the proton and the nucleon if we make the flavour index association $k = l = 1$ and $\epsilon^{12} = 1$, $\epsilon^{21} = -1$ where 1 and 2 label the different flavours of quark - either u or d.

Performing the contractions gives

$$\begin{aligned}
\delta_{il}\delta_{jm}\delta_{kn}\epsilon^{ij}\epsilon^{nm} &= \epsilon^{1j}\epsilon^{1j} = +1, && \text{(C.13)}\\
\delta_{il}\delta_{jn}\delta_{km}\epsilon^{ij}\epsilon^{nm} &= \epsilon^{1j}\epsilon^{j1} = -1, && \text{(C.14)}\\
\delta_{im}\delta_{jn}\delta_{kl}\epsilon^{ij}\epsilon^{nm} &= \epsilon^{mn}\epsilon^{nm} = -2, && \text{(C.15)}\\
\delta_{im}\delta_{jl}\delta_{kn}\epsilon^{ij}\epsilon^{nm} &= \epsilon^{m1}\epsilon^{1m} = -1, && \text{(C.16)}\\
\delta_{in}\delta_{jm}\delta_{kl}\epsilon^{ij}\epsilon^{nm} &= \epsilon^{nm}\epsilon^{nm} = +2, && \text{(C.17)}\\
\delta_{in}\delta_{jl}\delta_{km}\epsilon^{ij}\epsilon^{nm} &= \epsilon^{n1}\epsilon^{n1} = +1 && \text{(C.18)}
\end{aligned}$$

and hence

$$\begin{aligned}
\langle p_{\gamma,k}\bar{p}_{\phi,l}\rangle = \epsilon^{abc}\epsilon^{def}\left(\Gamma_P\right)_{\alpha\beta}\left(\bar{\Gamma_P}\right)_{\epsilon\delta}\{ \; & - \; G^{af}_{\alpha\phi}G^{be}_{\beta\epsilon}G^{cd}_{\gamma\delta} && \text{(C.19)}\\
& - \; G^{af}_{\alpha\phi}G^{bd}_{\beta\delta}G^{ce}_{\gamma\epsilon} && \text{(C.20)}\\
& + \; 2G^{ae}_{\alpha\epsilon}G^{bd}_{\beta\delta}G^{cf}_{\gamma\phi} && \text{(C.21)}
\end{aligned}$$

$$- \; G^{ae}_{\alpha\epsilon} G^{bf}_{\beta\phi} G^{cd}_{\gamma\delta} \tag{C.22}$$

$$+ \; 2G^{ad}_{\alpha\delta} G^{be}_{\beta\epsilon} G^{cf}_{\gamma\phi} \tag{C.23}$$

$$- \; G^{ad}_{\alpha\delta} G^{bf}_{\beta\phi} G^{ce}_{\gamma\epsilon}\}. \tag{C.24}$$

The set of Γ's are antisymmetric in spin indices

$$\Gamma^T = -\Gamma \tag{C.25}$$

$$\Gamma_{\alpha\beta} = -\Gamma_{\beta\alpha}. \tag{C.26}$$

Interchanging spin indices introduces a minus sign. Due to the colour antisymmetric epsilon tensor interchanging colour indices introduce a minus sign. The terms C.19 and C.20 are equal under the simultaneous interchange $d \leftrightarrow e$ and $\delta \leftrightarrow \epsilon$. Terms C.21 and C.23 are equal under the same transformation. Under the transformation $a \leftrightarrow b$ $\alpha \leftrightarrow \beta$ the term C.22 transforms to

$$G^{ae}_{\alpha\epsilon} G^{bf}_{\beta\phi} G^{cd}_{\gamma\delta} \rightarrow G^{af}_{\alpha\phi} G^{be}_{\beta\epsilon} G^{cd}_{\gamma\delta} \tag{C.27}$$

and C.23 to

$$G^{ad}_{\alpha\delta} G^{bf}_{\beta\phi} G^{ce}_{\gamma\epsilon} \rightarrow G^{af}_{\alpha\phi} G^{bd}_{\beta\delta} G^{ce}_{\gamma\epsilon}. \tag{C.28}$$

Applying the additional permutation $d \leftrightarrow e$ $\delta \leftrightarrow \epsilon$ to C.28 it becomes equal to C.27.

A final expression for the nucleon correlator is then given by

$$\langle p_{\gamma,k} \bar{p}_{\phi,l} \rangle = \epsilon^{abc} \epsilon^{def} \left(\Gamma_P\right)_{\alpha\beta} \left(\bar{\Gamma}_P\right)_{\epsilon\delta} [G^{ad}_{\alpha\delta} G^{be}_{\beta\epsilon} G^{cf}_{\gamma\phi} - G^{af}_{\alpha\phi} G^{be}_{\beta\epsilon} G^{cd}_{\gamma\delta}]. \tag{C.29}$$

The overall sign by defining the barred gamma matrices $\bar{\Gamma}_P$

$$\overline{C\gamma_5} = \gamma_4 (C\gamma_5)^\dagger \gamma_4 = \gamma_4 \gamma_5^\dagger C^\dagger \gamma_4 = \gamma_4 \gamma_5 C^\dagger \gamma_4 = -\gamma_5 \gamma_4 C^\dagger \gamma_4 \tag{C.30}$$

$$= -\gamma_5 C \tag{C.31}$$

$$\overline{C} = \gamma_4 C^\dagger \gamma_4 = C \tag{C.32}$$

$$\overline{\gamma_5} = \gamma_4 \gamma_5^\dagger \gamma_4 = \gamma_4 \gamma_5 \gamma_4 = -\gamma_5 \gamma_4 \gamma_4 = -\gamma_5 \tag{C.33}$$

$$\overline{C\gamma_4\gamma_5} = \gamma_4 \gamma_5^\dagger \gamma_4^\dagger C^\dagger \gamma_4 = \gamma_4 \gamma_5 \gamma_4^\dagger C^\dagger \gamma_4 = \gamma_4 \gamma_5 \gamma_4 C^\dagger \gamma_4 = \gamma_4 \gamma_5 \gamma_4^2 \gamma_2 \gamma_4 \tag{C.34}$$

$$= \gamma_4 \gamma_5 \gamma_2 \gamma_4 = \gamma_4 \gamma_2 \gamma_4 \gamma_5 = \gamma_2 \gamma_4 \gamma_4 \gamma_5 = C\gamma_4\gamma_5. \tag{C.35}$$

Appendix D

Spin $\frac{1}{2}$ or Spin $\frac{3}{2}$ Projection

The spin $\frac{3}{2}$ interpolating field defined in table 3.3 has an overlap with both spin-$\frac{3}{2}$ and spin-$\frac{1}{2}$ states. A spin projection can be used to isolate the individual contributions. Let the vector-spinor be written as follows:

$$\eta_\mu^\alpha = \underbrace{\Delta_\mu^\alpha}_{\text{pure spin } \frac{3}{2}\text{piece}} + p_\mu v_1^\alpha + \gamma_\mu^{\alpha\beta} v_2^\beta \tag{D.1}$$

The Rarita-Schwinger equations [63] are given by

$$\gamma_\mu \psi^\mu = 0 \tag{D.2}$$

$$p_\mu \psi^\mu = 0 \tag{D.3}$$

where the second follows from $\partial_\mu \psi^\mu = 0$ for ψ^μ a pure spin $\frac{3}{2}$ vector-spinor. Therefore $\gamma^\mu \Delta_\mu = 0$ and $p^\mu \Delta_\mu = 0$. Applying γ^μ and p^μ to equation(D.1)

$$p^\mu \eta_\mu = p^2 v_1 + \not{p} v_2 \tag{D.4}$$

$$\gamma^\mu \eta_\mu = \not{p} v_1 + 4 v_2 \tag{D.5}$$

which can then solve for v_1 and v_2. Multiplying equation (D.4) by 4 and equation (D.5) by $\not{p}$ gives

$$4 p^\mu \eta_\mu = 4 p^2 v_1 + 4 \not{p} v_2 \tag{D.6}$$

$$\not{p}\gamma^\mu\eta_\mu = p^2 v_1 + 4\not{p}v_2. \tag{D.7}$$

Subtracting (D.7) from (D.6) gives

$$v_1 = \frac{1}{3p^2}\{4p^\mu\eta_\mu - \not{p}\gamma^\mu\eta_\mu\} \tag{D.8}$$

and (D.4) from (D.7) gives

$$v_2 = \frac{1}{3}\gamma^\mu\eta_\mu - \frac{1}{3p^2}\not{p}p^\mu\eta_\mu. \tag{D.9}$$

Substituting these values into equation (D.1) and rearranging gives

$$\Delta_\mu = \eta_\mu - \frac{p_\mu}{3p^2}[4p^\nu\eta_\nu - \not{p}\gamma^\nu\eta_\nu] - \frac{1}{3}\gamma_\mu[\gamma^\nu\eta_\nu - \frac{1}{p^2}\not{p}p^\nu\eta_\nu]. \tag{D.10}$$

Moving to the rest frame

$$\vec{p} = 0 \;\Rightarrow\; p_\mu = (0, m) \tag{D.11}$$

$$\Rightarrow \not{p} \;=\; \gamma^\mu p_\mu \to \gamma^4 p_4 = \gamma^4 m \tag{D.12}$$

the spatial component of equation(D.10) becomes

$$\Delta_i = \eta_i - \frac{1}{3}\gamma_i[\underbrace{\gamma^4\eta_4 + \gamma^j\eta_j}_{\gamma^\nu\eta_\nu} - \frac{1}{m^2}\gamma^4 mm\eta_4] \tag{D.13}$$

The second term in Δ_μ disappears as it is multiplied by p_μ and $p_i = 0$.

Hence

$$\Delta_i = \eta_i - \frac{1}{3}\gamma_i[\gamma^j\eta_j]. \tag{D.14}$$

As an aside it may be noted that if $\gamma^\mu\eta_\mu = \gamma^4\eta_4 + \gamma^j\eta_j = 0$ automatically, then

$$\Delta_i = \eta_i + \frac{1}{3}\gamma_i\gamma^4\eta_4 \tag{D.15}$$

Given $\Delta_i = \eta_i - \frac{1}{3}\gamma_i[\gamma^j\eta_j]$ a projector $[\delta_i^j - \frac{1}{3}\gamma_i\gamma^j]$ having the property that when it acts on η_j it gives back the pure spin $\frac{3}{2}$ state Δ_i may be constructed. The projection operator

$$P_i^j = [\delta_i^j - \frac{1}{3}\gamma_i\gamma^j] \tag{D.16}$$

has the generic property

$$P_i^{j(l)} P_j^{k(l)} = P_i^{k(l)} \tag{D.17}$$

as

$$\begin{aligned} P_i^j P_j^k &= [\delta_i^j - \frac{1}{3}\gamma_i\gamma^j][\delta_j^k - \frac{1}{3}\gamma_j\gamma^k] && \text{(D.18)} \\ &= \delta_i^k - \frac{1}{3}\gamma_i\gamma^k - \frac{1}{3}\gamma_i\gamma^k + \frac{1}{9}\gamma_i\gamma^j\gamma_j\gamma^k && \text{(D.19)} \\ &= [\delta_i^k - \frac{1}{3}\gamma_i\gamma^k] = P_i^k && \text{(D.20)} \end{aligned}$$

The other component, Δ_4, is given by:

$$\Delta_4 = \eta_4 - \frac{p_4}{3p^2}[4p^\nu\eta_\nu - \not{p}\gamma^\nu\eta_\nu] - \frac{1}{3}\gamma_4[\gamma^\nu\eta_\nu - \frac{1}{p^2}\not{p}p^\nu\eta_\nu]. \tag{D.21}$$

In the rest frame where $p_i = 0$, $p_4 = m$, $p^2 = m^2$

$$\begin{aligned} \Delta_4 &= \eta_4 - \frac{1}{3m}[4m\eta_4 - \gamma_4 m\not{\eta}] - \frac{1}{3}\gamma_4\not{\eta} + \frac{1}{3}\gamma_4\gamma_4\eta_4 && \text{(D.22)} \\ &= \eta_4 - \frac{4}{3}\eta_4 + \frac{1}{3}\gamma_4\not{\eta} - \frac{1}{3}\gamma_4\not{\eta} + \frac{1}{3}\eta_4 = 0. && \text{(D.23)} \end{aligned}$$

Therefore η_4 is pure spin $\frac{1}{2}$. For the baryons, this means that the current

$$\eta_4(x) = u_\alpha^a(x)(C\gamma_4)_{\alpha\beta}u_\beta^b(x)u_\gamma^c(x)\epsilon_{abc} \tag{D.24}$$

is the spin-$\frac{1}{2}$ piece of the spin-$\frac{3}{2}$ operator

$$\eta_\mu(x) = u_\alpha^a(x)(C\gamma_\mu)_{\alpha\beta}u_\beta^b(x)u_\gamma^c(x)\epsilon_{abc}. \tag{D.25}$$

Bibliography

[1] J. F. Donoghue, E. Golowich and B. R. Holstein, *Dynamics of the Standard Model.* Cambridge University Press, Cambridge, 1992.

[2] K. G. Wilson, *Confinement of Quarks*, *Phys. Rev.* **D10** (1974) 2445–2459.

[3] **CP-PACS** Collaboration, S. Aoki *et. al.*, *Quenched Light Hadron Spectrum*, *Phys. Rev. Lett.* **84** (2000) 238–241 [hep-lat/9904012].

[4] K. I. Ishikawa, *Hadron Spectrum from Dynamical Lattice QCD Simulations*, *Nucl. Phys. Proc. Suppl.* **140** (2005) 20–33 [hep-lat/0410050].

[5] P. H. Ginsparg and K. G. Wilson, *A remnant of chiral symmetry on the lattice*, *Phys. Rev.* **D25** (1982) 2649.

[6] M. Creutz, *Quarks, gluons and lattices.* Cambridge University Press, Cambridge, 1983.

[7] H. J. Rothe, *Lattice Gauge Theories.* World Scientific, Singapore, 1992.

[8] I. Montvay and G. Münster, *Quantum Fields on a Lattice.* Cambridge University Press, Cambridge, 1994.

[9] J. Smit, *Introduction to Quantum Fields on a Lattice.* Cambridge University Press, Cambridge, 2002.

[10] R. Gupta, *Introduction to Lattice QCD*, `hep-lat/9807028`.

[11] M. Luscher, *Advanced Lattice QCD*, `hep-lat/9802029`.

[12] S. R. Sharpe, *Phenomenology from the Lattice*, `hep-ph/9412243`.

[13] C. Davies, *Lattice QCD - a guide for people who want results*, `hep-lat/0509046`.

[14] G. P. Lepage, *Lattice QCD for Novices*, `hep-lat/0506036`.

[15] R. P. Feynman, *Space-time Approach to Nonrelativistic Quantum Mechanics*, *Rev. Mod. Phys.* **20** (1948) 367–387.

[16] R. P. Feynman and A. R. Hibbs, *Quantum Mechanics and Path Integrals.* McGraw-Hill, New York, 1965.

[17] M. Peskin and D. Schroeder, *An Introduction to Quantum Field Theory.* Addison-Wesley, New York, 1995.

[18] D. Griffiths, *Introduction to Elementary Particles.* John Wiley & Sons, New York, 1987.

[19] I. Aitchison and A. Hey, *Gauge Theories in Particle Physics, Volume II: QCD and the Electroweak Theory.* Institute of Physics, Bristol and Philadelphia, 2004.

[20] H. B. Nielsen and M. Ninomiya, *Absence of Neutrinos on a Lattice. 1. proof by Homotopy Theory*, *Nucl. Phys.* **B185** (1981) 20.

[21] B. Sheikholeslami and R. Wohlert, *Improved Continuum Limit Lattice Action for QCD with Wilson Fermions*, *Nucl. Phys.* **B259** (1985) 572.

[22] J. B. Kogut and L. Susskind, *Hamiltonian Formulation of Wilson's Lattice Gauge Theories*, *Phys. Rev.* **D11** (1975) 395.

[23] L. Susskind, *Lattice Fermions*, *Phys. Rev.* **D16** (1977) 3031–3039.

[24] H. Neuberger, *A Practical Implementation of the Overlap-Dirac Operator*, *Phys. Rev. Lett.* **81** (1998) 4060–4062 [hep-lat/9806025].

[25] D. B. Kaplan, *A Method for Simulating Chiral Fermions on the Lattice*, *Phys. Lett.* **B288** (1992) 342–347 [hep-lat/9206013].

[26] Y. Shamir, *Chiral Fermions from Lattice Boundaries*, *Nucl. Phys.* **B406** (1993) 90–106 [hep-lat/9303005].

[27] R. Narayanan and H. Neuberger, *Infinitely Many Regulator Fields for Chiral Fermions*, *Phys. Lett.* **B302** (1993) 62 [hep-lat/9212019].

[28] R. Narayanan and H. Neuberger, *Chiral Fermions on the Lattice*, *Phys. Rev. Lett.* **71** (1993) 3251–3254 [hep-lat/9308011].

[29] V. Furman and Y. Shamir, *Axial Symmetries in Lattice 'QCD' with Kaplan Fermions*, *Nucl. Phys.* **B439** (1995) 54 [hep-lat/9405004].

[30] P. Vranas, *Domain Wall Fermions and MC Simulations of Vector Theories*, *Nucl. Phys. Proc. Suppl.* **53** (1997) 278–282 [hep-lat/9608078].

[31] P. M. Vranas, *Chiral Symmetry Restoration in the Schwinger Model with Domain Wall Fermions*, *Phys. Rev.* **D57** (1998) 1415–1432 [hep-lat/9705023].

[32] Y. Kikukawa and T. Noguchi, *Low Energy Effective Action of Domain-Wall Fermion and the Ginsparg-Wilson Relation*, hep-lat/9902022.

[33] A. Borici, *Computational Methods for the Fermion Determinant and the Link Between Overlap and Domain Wall Fermions*, hep-lat/0402035.

[34] T. Blum *et. al.*, *Non-Perturbative Renormalisation of Domain Wall Fermions: Quark Bilinears*, *Phys. Rev.* **D66** (2002) 014504 [hep-lat/0102005].

[35] T. Blum *et. al.*, *Quenched Lattice QCD with Domain Wall Fermions and the Chiral Limit*, *Phys. Rev.* **D69** (2004) 074502 [hep-lat/0007038].

[36] T. Blum, *Domain Wall Fermions in Vector Gauge Theories*, *Nucl. Phys. Proc. Suppl.* **73** (1999) 167–179 [hep-lat/9810017].

[37] S. Aoki, T. Izubuchi, Y. Kuramashi and Y. Taniguchi, *Lattice QCD with Domain-Wall Fermions*, *Nucl. Phys. Proc. Suppl.* **83** (2000) 624–626 [hep-lat/9909154].

[38] T. Takaishi, *Heavy Quark Potential and Effective Actions on Blocked Configurations*, *Phys. Rev.* **D54** (1996) 1050–1053.

[39] **QCD-TARO** Collaboration, P. de Forcrand *et. al.*, *Renormalization Group Flow of SU(3) Lattice Gauge Theory: Numerical Studies in a Two Coupling Space*, *Nucl. Phys.* **B577** (2000) 263–278 [hep-lat/9911033].

[40] Y. Iwasaki, *Renormalization Group Analysis of Lattice Theories and Improved Lattice Action. 2. Four-Dimensional Nonabelian SU(n) Gauge Model*, . UTHEP-118.

[41] Y. Iwasaki and T. Yoshie, *Renormalization Group Improved Action for SU(3) Lattice Gauge Theory and the String Tension*, *Phys. Lett.* **B143** (1984) 449.

[42] N. Metropolis, A. W. Rosenbluth, M. N. Rosenbluth, A. H. Teller and E. Teller, *Equation of State Calculations by Fast Computing Machines*, *J. Chem. Phys.* **21** (1953) 1087–1092.

[43] S. Duane, A. D. Kennedy, B. J. Pendleton and D. Roweth, *Hybrid Monte Carlo*, *Phys. Lett.* **B195** (1987) 216–222.

[44] B. Joó, *Efficient Monte Carlo Simulation of Lattice QCD.* PhD thesis, University of Edinburgh, 1999.

[45] Z. Sroczynski, *Taking Lattice QCD Beyond the Quenched Approximation.* PhD thesis, University of Edinburgh, 1998.

[46] S. A. Gottlieb, W. Liu, D. Toussaint, R. L. Renken and R. L. Sugar, *Hybrid Molecular Dynamics Algorithms for the Numerical Simulation of Quantum Chromodynamics, Phys. Rev.* **D35** (1987) 2531–2542.

[47] P. de Forcrand and T. Takaishi, *Fast Fermion Monte Carlo, Nucl. Phys. Proc. Suppl.* **53** (1997) 968–970 [hep-lat/9608093].

[48] R. Frezzotti and K. Jansen, *A Polynomial Hybrid Monte Carlo Algorithm, Phys. Lett.* **B402** (1997) 328–334 [hep-lat/9702016].

[49] A. D. Kennedy, I. Horvath and S. Sint, *A New Exact Method for Dynamical Fermion Computations with Non-Local Actions, Nucl. Phys. Proc. Suppl.* **73** (1999) 834–836 [hep-lat/9809092].

[50] M. A. Clark, A. D. Kennedy and Z. Sroczynski, *Exact 2+1 Flavour RHMC Simulations*, hep-lat/0409133.

[51] M. Clark, *The Rational Hybrid Monte Carlo Algorithm.* PhD thesis, University of Edinburgh, 2005.

[52] E. Y. Remez, *General Computational Methods of Chebyshev Approximation, US Atomic Energy Commision* (1962).

[53] E. I. Zolotarev *Zap. Imp. Akad. Nauk. St. Petersburg* **30** (1877) 5.

[54] Y. Saad, *Iterative Methods for Sparse Linear Systems.* PWS-Publishing, U.S.A., 1996.

[55] H. van der Vorst, *Iterative Krylov Methods for Large Linear Systems.* Cambridge University Press, Cambridge, 2003.

[56] B. Jegerlehner, *Krylov Space Solvers for Shifted Linear Systems*, hep-lat/9612014.

[57] **UKQCD** Collaboration, C. R. Allton *et. al.*, *Light Hadron Spectroscopy with O(a) Improved Dynamical Fermions*, *Phys. Rev.* **D60** (1999) 034507 [hep-lat/9808016].

[58] P. Brockwell and R. Davis, *Time Series: Theory and Methods.* Springer Verlag, New York, 1987.

[59] P. Rowland, *Light Hadron Spectroscopy in Quenched QCD.* PhD thesis, University of Edinburgh, 1997.

[60] F. Fucito *et. al.*, *Hadron Spectroscopy in Lattice QCD*, *Nucl. Phys.* **B210** (1982) 407.

[61] B. L. Ioffe, *Calculation of Baryon Masses in Quantum Chromodynamics*, *Nucl. Phys.* **B188** (1981) 317–341.

[62] D. B. Leinweber, T. Draper and R. M. Woloshyn, *Decuplet Baryon Structure from Lattice QCD*, *Phys. Rev.* **D46** (1992) 3067–3085 [hep-lat/9208025].

[63] W. Rarita and J. S. Schwinger, *On a Theory of Particles with Half Integral Spin*, *Phys. Rev.* **60** (1941) 61.

[64] D. Lurié, *Partices and Fields.* John Wiley & Sons, London, 1968.

[65] G. Kilcup, *Weak Interaction Matrix Elements with Staggered Fermions*, . IN *BATAVIA 1988, PROCEEDINGS, LATTICE 88* 201-206.

[66] **UKQCD** Collaboration, P. Boyle, *A Novel Gauge Invariant Multi-State Smearing Technique*, *J. Comput. Phys.* **179** (2002) 349–370 [hep-lat/9903033].

[67] P. Boyle, *Heavy Meson Spectroscopy from the Lattice.* PhD thesis, University of Edinburgh, 1997.

[68] C. Alexandrou, E. Follana, H. Panagopoulos and E. Vicari, *One-Loop Renormalization of Fermionic Currents with the Overlap-Dirac Operator, Nucl. Phys.* **B580** (2000) 394–406 [hep-lat/0002010].

[69] S. Chandrasekharan and U. J. Wiese, *An Introduction to Chiral Symmetry on the Lattice, Prog. Part. Nucl. Phys.* **53** (2004) 373–418 [hep-lat/0405024].

[70] **Particle Data Group** Collaboration, S. Eidelman *et. al.*, *Review of Particle Physics, Phys. Lett.* **B592** (2004) 1.

[71] W. H. Press, S. A. Teukolsky, W. T. Vetterling and B. P. Flannery, *Numerical Recipes in C.* Cambridge University Press, Cambridge, 1992.

[72] B. Efron and R. J. Tibshirani, *An Introduction to the Bootstrap.* Chapman and Hall, New York, 1993.

[73] S. B. K. F. Riley, M. P. Hobson, *Mathematical Methods for Physics and Engineering.* Chapman and Hall, Cambridge University Press, 2002.

[74] A. D. Kennedy and B. Pendleton, *Cost of the Generalised Hybrid Monte Carlo Algorithm for Free Field Theory, Nucl. Phys.* **B607** (2001) 456–510 [hep-lat/0008020].

[75] **HPQCD** Collaboration, C. T. H. Davies *et. al.*, *High-Precision Lattice QCD Confronts Experiment, Phys. Rev. Lett.* **92** (2004) 022001 [hep-lat/0304004].

[76] B. Bunk, M. Della Morte, K. Jansen and F. Knechtli, *Locality with Staggered Fermions, Nucl. Phys.* **B697** (2004) 343–362 [hep-lat/0403022].

[77] B. Bunk, M. Della Morte, K. Jansen and F. Knechtli, *The Locality Problem for Two Tastes of Staggered Fermions*, hep-lat/0408048.

[78] A. Hart and E. Muller, *The Locality of the Square-Root Method for Improved Staggered Quarks*, *Phys. Rev.* **D70** (2004) 057502 [hep-lat/0406030].

[79] O. Bar, G. Rupak and N. Shoresh, *Simulations with Different Lattice Dirac Operators for Valence and Sea Quarks*, *Phys. Rev.* **D67** (2003) 114505 [hep-lat/0210050].

[80] A. Morel, *Chiral Logarithms in Quenched QCD*, *J. Phys. (France)* **48** (1987) 1111–1119.

[81] S. R. Sharpe and N. Shoresh, *Partially Quenched Chiral Perturbation Theory without Phi0*, *Phys. Rev.* **D64** (2001) 114510 [hep-lat/0108003].

[82] P. Hasenfratz, V. Laliena and F. Niedermayer, *The Index Theorem in QCD with a Finite Cut-Off*, *Phys. Lett.* **B427** (1998) 125–131 [hep-lat/9801021].

[83] M. Luscher, *Exact Chiral Symmetry on the Lattice and the Ginsparg-Wilson Relation*, *Phys. Lett.* **B428** (1998) 342–345 [hep-lat/9802011].

[84] W. A. Bardeen, A. Duncan, E. Eichten, N. Isgur and H. Thacker, *Chiral Loops and Ghost States in the Quenched Scalar Propagator*, *Phys. Rev.* **D65** (2002) 014509 [hep-lat/0106008].

[85] W. A. Bardeen, E. Eichten and H. Thacker, *Chiral Lagrangian Parameters for Scalar and Pseudoscalar Mesons*, *Phys. Rev.* **D69** (2004) 054502 [hep-lat/0307023].

[86] S. Prelovsek, C. Dawson, T. Izubuchi, K. Orginos and A. Soni, *Scalar Meson in Dynamical and Partially Quenched Two-Flavor QCD: Lattice Results and Chiral Loops*, *Phys. Rev.* **D70** (2004) 094503 [hep-lat/0407037].

[87] **UKQCD** Collaboration, C. R. Allton *et. al.*, *Effects of Non-Perturbatively Improved Dynamical Fermions in QCD at Fixed Lattice Spacing*, *Phys. Rev.* **D65** (2002) 054502 [hep-lat/0107021].

[88] **UKQCD** Collaboration, C. R. Allton *et. al.*, *Improved Wilson QCD Simulations with Light Quark Masses*, *Phys. Rev.* **D70** (2004) 014501 [hep-lat/0403007].

[89] K. Jansen *et. al.*, *Non-Perturbative Renormalization of Lattice QCD at All Scales*, *Phys. Lett.* **B372** (1996) 275–282 [hep-lat/9512009].

[90] C. W. Bernard *et. al.*, *The QCD Spectrum with Three Quark Flavors*, *Phys. Rev.* **D64** (2001) 054506 [hep-lat/0104002].

[91] P. Hernandez, K. Jansen and M. Luscher, *Locality Properties of Neuberger's Lattice Dirac Operator*, *Nucl. Phys.* **B552** (1999) 363–378 [hep-lat/9808010].

[92] A. Hasenfratz and F. Knechtli, *Flavor Symmetry and the Static Potential with Hypercubic Blocking*, *Phys. Rev.* **D64** (2001) 034504 [hep-lat/0103029].

[93] T. DeGrand, A. Hasenfratz and T. G. Kovacs, *Improving the Chiral Properties of Lattice Fermions*, *Phys. Rev.* **D67** (2003) 054501 [hep-lat/0211006].

[94] S. Durr and C. Hoelbling, *Staggered Versus Overlap Fermions: A Study in the Schwinger Model with N(f) = 0,1,2*, *Phys. Rev.* **D69** (2004) 034503 [hep-lat/0311002].

[95] S. Durr, C. Hoelbling and U. Wenger, *Staggered Eigenvalue Mimicry*, hep-lat/0406027.

[96] S. Durr, C. Hoelbling and U. Wenger, *A Comparative Study of Overlap and Staggered Fermions in QCD*, hep-lat/0409108.

[97] M. Teper, *Cooling and Confinement in Lattice Gauge Theory*, *Nucl. Phys.* **B411** (1994) 855–874.

[98] S. Durr, *Gauge Action Improvement and Smearing*, hep-lat/0409141.

[99] http://www.jlab.org/~edwards/szin/.

[100] S. J. Dong *et. al.*, *Chiral Properties of Pseudoscalar Mesons on a Quenched 20**4 Lattice with Overlap Fermions*, *Phys. Rev.* **D65** (2002) 054507 [hep-lat/0108020].

[101] **UKQCD** Collaboration, K. C. Bowler, B. Joo, R. D. Kenway, C. M. Maynard and R. J. Tweedie, *Exploratory Spectrum Calculations Using Overlap Valence Quarks on a Staggered Sea*, hep-lat/0408043.

[102] **JLQCD** Collaboration, S. Aoki *et. al.*, *Analysis of Hadron Propagators with One Thousand Configurations on a* $24\ 3 \times 64$ *Lattice at* $\beta = 6.0$, *Nucl. Phys. Proc. Suppl.* **47** (1996) 354–357 [hep-lat/9510013].

[103] A. Hasenfratz, *Universality and Quark Masses of the Staggered Fermion action*, hep-lat/0511021.

[104] B. Billeter, C. DeTar and J. Osborn, *Topological Susceptibility in Staggered Fermion Chiral Perturbation Theory*, *Phys. Rev.* **D70** (2004) 077502 [hep-lat/0406032].

[105] **MILC** Collaboration, C. Aubin *et. al.*, *Light Pseudoscalar Decay Constants, Quark Masses, and Low Energy Constants from Three-Flavor Lattice QCD*, *Phys. Rev.* **D70** (2004) 114501 [hep-lat/0407028].

[106] S. Pickles, *Algorithms in Lattice QCD.* PhD thesis, University of Edinburgh, 1998.

[107] V. Furman and Y. Shamir, *Axial Symmetries in Lattice QCD with Kaplan Fermions, Nucl. Phys.* **B439** (1995) 54–78 [hep-lat/9405004].

[108] **RBC-UKQCD** Collaboration, K. Hashimoto, T. Izubuchi and J. Noaki, *The Static Quark Potential in 2+1 Flavour Domain Wall QCD from QCDOC*, hep-lat/0510079.

[109] R. Sommer, *A New Way to Set the Energy Scale in Lattice Gauge Theories and its Applications to the Static Force and Alpha-s in SU(2) Yang-Mills Theory, Nucl. Phys.* **B411** (1994) 839–854 [hep-lat/9310022].

[110] K. C. Bowler *et. al.*, *A Critique of Quenched Hadron Mass Calculations, Phys. Lett.* **B162** (1985) 354.

[111] S. Ono, *States of Hadrons with Five Quarks, Phys. Rev.* **D17** (1978) 888.

[112] Y. Aoki *et. al.*, *Lattice QCD with Two Dynamical Flavors of Domain Wall Fermions, Phys. Rev.* **D72** (2005) 114505 [hep-lat/0411006].

[113] **UKQCD** Collaboration, P. Lacock and C. Michael, *Is the Quenched Spectrum in Agreement with Experiment?, Phys. Rev.* **D52** (1995) 5213–5219 [hep-lat/9506009].

[114] **CP-PACS** Collaboration, T. Ishikawa *et. al.*, *Light Hadron Spectrum in 2+1 Flavor Full QCD by CP-PACS and JLQCD Collaborations, Nucl. Phys. Proc. Suppl.* **140** (2005) 225–227 [hep-lat/0409124].

[115] **JLQCD** Collaboration, CP-PACS *et. al.*, *Light Hadron Spectrum and Quark Masses in 2+1 Flavor QCD, PoS* **LAT2005** (2005) 057 [hep-lat/0509142].

[116] J. Zinn-Justin, *Path Integrals in Quantum Mechanics.* Oxford University Press, Oxford, 2005.

[117] A. B. Henriques, B. H. Kellett and R. G. Moorhouse, *General Three Spinor Wave Functions and the Relativistic Quark Model, Ann. Phys.* **93** (1975) 125.